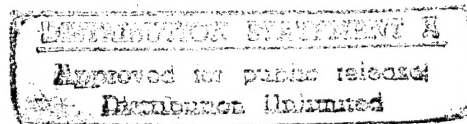


Semiannual Technical Report

Interface Properties of Wide Bandgap Semiconductor Structures

Supported under Grant #N00014-92-J-1477
Office of the Chief of Naval Research
Report for the period 1/1/96-6/30/96



R. F. Davis, S. Bedair*, J. Bernholc†, R. J. Nemanich†, and Z. Sitar
c/o Materials Science and Engineering Department,
*Electrical and Computer Engineering Department
and †Department of Physics
North Carolina State University
Campus Box 7907
Raleigh, NC 27695-7907

19960809 071

June, 1996

REPORT DOCUMENTATION PAGE			Form Approved OMB No. 0704-0188	
Public reporting burden for this collection of information is estimated to average 1 hour per response, including the time for reviewing instructions, searching existing data sources, gathering and maintaining the data needed, and completing and reviewing the collection of information. Send comments regarding this burden estimate or any other aspect of this collection of information, including suggestions for reducing this burden to Washington Headquarters Services, Directorate for Information Operations and Reports, 1215 Jefferson Davis Highway, Suite 1204, Arlington, VA 22202-4302, and to the Office of Management and Budget Paperwork Reduction Project (0704-0188), Washington, DC 20503.				
1. AGENCY USE ONLY (Leave blank)		2. REPORT DATE June, 1996		3. REPORT TYPE AND DATES COVERED Semiannual Technical 1/1/96-6/30/96
4. TITLE AND SUBTITLE Interface Properties of Wide Bandgap Semiconductor Structures			5. FUNDING NUMBERS uri41114a-01 1114SS N00179 N66005 4B855	
6. AUTHOR(S) Robert F. Davis and R. J. Nemanich				
7. PERFORMING ORGANIZATION NAME(S) AND ADDRESS(ES) North Carolina State University Hillsborough Street Raleigh, NC 27695			8. PERFORMING ORGANIZATION REPORT NUMBER N00014-92-J-1477	
9. SPONSORING/MONITORING AGENCY NAME(S) AND ADDRESS(ES) Sponsoring: ONR, 800 N. Quincy, Arlington, VA 22217-5660 Monitoring: Administrative Contracting Officer, Office of Naval Research Regional Office Atlanta, 101 Marietta Tower, Suite 2805 101 Marietta Street Atlanta, GA 30323-6145			10. SPONSORING/MONITORING AGENCY REPORT NUMBER	
11. SUPPLEMENTARY NOTES				
12a. DISTRIBUTION/AVAILABILITY STATEMENT Approved for Public Release; Distribution Unlimited			12b. DISTRIBUTION CODE	
13. ABSTRACT (Maximum 200 words) Page 1 of 2 Nuclear transmutation of B to Li is being investigated for donor doping of diamond. Homoepitaxial ^{10}B enriched diamond films have been grown, characterized using Hall measurements and Raman and PL spectroscopies and neutron-irradiated at a dose of $3 \times 10^{20} \text{ n/cm}^2$. The field emission energy distribution was measured from a Mo field emitter before and after diamond coating. After coating, the Mo needle had a lower "turn-on" voltage that was attributed to the diamond crystals acting as micro-tips which enhanced the field. The "turn-on" voltage further decreased after <i>in vacuo</i> annealing. Comparisons between the wetting characteristics of 6H-SiC(0001) $_{\text{Si}}$ and Si(111) surfaces in various acids and bases were conducted. The 10:1 HF dipped Si(111) surfaces were hydrophobic; the (0001) $_{\text{Si}}$ 6H-SiC surfaces were hydrophilic. Annealing of Si capped (0001) $_{\text{Si}}$ 6H-SiC surfaces in UHV at 1100°C for 5 min. caused thermal desorption of the Si capping layer and the formation of (3x3) Si rich, oxygen free (0001) $_{\text{Si}}$ 6H-SiC surfaces. As-deposited (at RT) NiAl, Au, and Ni contacts were rectifying on p-type 6H-SiC (0001) with very low leakage current densities ($\sim 1 \times 10^{-8} \text{ A/cm}^2$ at 10 V). The Schottky barrier heights showed a reduced dependence on the metal work functions. Ni/NiAl contacts on p^+ ($1 \times 10^{19} \text{ cm}^{-3}$) SiC were ohmic after annealing for 10–80 s at 1000°C in a N_2 ambient. The estimated specific contact resistivity was $2\text{--}3 \times 10^{-2} \Omega \cdot \text{cm}^2$. Cr-B contacts were semi-ohmic on p-type SiC ($1 \times 10^{18} \text{ cm}^{-3}$) after annealing at 1000°C for 60–300 s in Ar; oxidation of these latter contacts did not occur. Thin Zr films were deposited on natural single crystal diamond (100) substrates by e-beam evaporation in ultra-high vacuum. Field emission current-voltage measurements resulted in a threshold field of 79 V/ μm for positive electron affinity diamond surfaces and values as low as 20 V/ μm for Zr on diamond. Different material systems were investigated for solution (flux) growth of AlN. Single crystal needles of AlN were achieved using SiO_2 . Thin films of GaN and $\text{Al}_x\text{Ga}_{1-x}\text{N}$ ($0.05 < x < 0.96$) were deposited directly on both vicinal and on-axis 6H-SiC(0001) substrates. The FWHM of the XRCs and the density of defects for GaN were narrower and lower, respectively, for films on the on-axis substrates. A linear relationship was found between the lattice parameter <i>c</i> and the bound exciton energy ($E_{\text{BX}} = (-14.76 + 3.561 \cdot c(\text{\AA})) \text{ eV}$), confirming that the range of reported E_{BX} values is due to a variation in film strain. Some of the films tested were in compression, indicating that the residual stress due to lattice mismatch was not fully relieved by defect formation. The lack of steps on the SiC limits the formation of inversion-domain boundaries (IDBs), which may act to relieve lattice mismatch. Initial results show that the strain in the AlN buffer layer varies with that				
14. SUBJECT TERMS diamond, films, doping, donor, nuclear transmutation, ^{10}B , Hall, Raman spectroscopy, photoluminescence, gamma ray spectroscopy, neutron-irradiation, field emission, energy distribution, molybdenum, molybdenum carbide, annealing, hydrogen termination, wetting, hydrophobic, hydrophilic, thermal desorption, 6H-SiC, silicon carbide, ohmic contacts, Schottky barrier heights, work function, NiAl, Cr-B, contact			15. NUMBER OF PAGES 166	
			16. PRICE CODE	
17. SECURITY CLASSIFICATION OF REPORT UNCLAS	18. SECURITY CLASSIFICATION OF THIS PAGE UNCLAS	19. SECURITY CLASSIFICATION OF ABSTRACT UNCLAS	20. LIMITATION OF ABSTRACT SAR	

Table of Contents

I. Introduction	1
Carbon-based Materials	
II. Donor Doping of Diamond Using Nuclear Transmutation <i>S. P. Bozeman, R. J. Nemanich, and R. F. Davis</i>	3
III. Spectral Analysis of Field Emitted Electrons from Diamond-Coated Nanoscale Molybdenum Emitters <i>M. T. McClure, R. Schlessner, W. B. Choi, J. J. Hren, and Z. Sitar</i>	6
IV. <i>Ex Situ</i> and <i>In Situ</i> Methods for Complete Oxygen and Non-Carbidic Carbon Removal from (0001) _{Si} 6H-SiC Surfaces <i>S. W. King, M. C. Benjamin, R. S. Kern, R. J. Nemanich and R. F. Davis</i>	11
V. Rectifying and Ohmic Contacts for P-type Alpha (6H) Silicon Carbide <i>L. Porter and R. F. Davis</i>	18
VI. Characterization of Zirconium-Diamond Interfaces <i>P. K. Baumann, S. P. Bozeman, B. L. Ward, and R. J. Nemanich</i>	27
Nitrogen-based Materials	
VII. Solvent Systems for Solution Growth of Single Crystal Aluminum Nitride <i>C. Balkas and R. F. Davis</i>	35
VIII. Growth, Doping and Characterization of Al _x Ga _{1-x} N Thin Film Alloys on 6H-SiC(0001) Substrates <i>M. D. Bremser, W. G. Perry, T. Zheleva, N. V. Edwards, O. H. Nam, N. Parikh, D. E. Aspnes, and R. F. Davis</i>	45
IX. Structural Characterization of Group III-Nitride Films and Their Interfaces by XRD and TEM <i>T. Zheleva and R. F. Davis</i>	59
X. Luminescence and XRD Studies of Stresses in GaN Films Grown on 6H-SiC(0001) Substrates via MOVPE <i>W. G. Perry and R. F. Davis</i>	78
XI. UV Photoemission Study of Heteroepitaxial AlN Films Grown on 6H-SiC Non-Polar Surfaces <i>M. C. Benjamin, M. D. Bremser, T. W. Weeks, Jr., S. W. King, R. F. Davis, and R. J. Nemanich</i>	88
XII. New Buffer Layers for GaN on Sapphire by Atomic Layer and Molecular Stream Epitaxy <i>E. L. Piner, Y. W. He, K. S. Boutros, F. G. McIntosh, J. C. Roberts, S. M. Bedair, and N. A. El-Masry</i>	94

XIII.	Growth of High Quality InGaN Films by Metalorganic Chemical Vapor Deposition <i>J. C. Roberts, F. G. McIntosh, K. S. Boutros, S. M. Bedair, M. Moussa, E. L. Piner, Y. He, and N. A. El-Masry</i>	101
XIV.	AlGaInN Quaternary Alloys by MOCVD <i>F. G. McIntosh, E. Piner, K. Boutros, J. C. Roberts, Y. He, M. Moussa, N. El-Masry, and S. M. Bedair</i>	107
XV.	Theory of Surfaces and Interfaces in the Wide-Gap Nitrides <i>K. Rapcewicz, M. Buongiorno Nardelli, B. Chen, Z. Zhang, and J. Bernholc</i>	112
XVI.	Theory of Defects, Doping, Surfaces and Interfaces in Wide Gap Nitrides <i>J. Bernholc, P. Boguslawski, E. L. Briggs, M. Buongiorno Nardelli, B. Chen, K. Rapcewicz, and Z. Zhang</i>	123
XVII.	Strain Effects on the Interface Properties of Nitride Semiconductors <i>M. Buongiorno Nardelli, K. Rapcewicz, and J. Bernholc</i>	133
XVIII.	Photothermally Assisted Dry Etching of GaN <i>R. T. Leonard and S. M. Bedair</i>	146
XIX.	Ohmic Contact Formation to GaN <i>L. Smith and R. F. Davis</i>	152
XX.	III-V Nitrides for Use in Semiconductor Microelectronic Device Applications <i>R. Therrien and R. F. Davis</i>	160
XXI.	Distribution List	166

I. Introduction

Heteroepitaxy is the growth of a crystal (or a film) on a foreign crystalline substrate that determines its orientation. Such oriented growth requires that lattice planes in both materials have similar structure. In general, an epitaxial relationship is probable whenever the orientation of the substrate and overgrowth produces an interface with a highly coincident atomic structure having low interfacial energy relative to a random arrangement.

During the past decade, nonequilibrium techniques have been developed for the growth of epitaxial semiconductors, superconductors, insulators and metals which have led to new classes of artificially structured materials. In many cases, the films were deposited on substrates having a different chemistry from that of the film, and heteroepitaxy was achieved. Moreover, layered structures with a periodicity of a few atomic layers have also been produced by the sequential heteroepitaxial deposition of a film of one type on another. Metastable structures can be generated which possess important properties not present in equilibrium systems. A consideration of the materials under consideration for next generation electronic and optoelectronic devices, e.g., the III-V nitrides show that only a few of them can currently be grown in bulk, single crystal form having a cross-sectional area of $>3\text{cm}^2$. Thus other, commercially available substrates must be used. This introduces a new set of challenges for the successful growth of device quality films which are not present in homoepitaxial growth and which must be surmounted if these materials are to be utilized in device structures.

In addition to providing structures which do not exist in nature, applications of advanced heteroepitaxial techniques permit the growth of extremely high quality heterostructures involving semiconductors, metals, and insulators. These heterostructures offer the opportunity to study relationships between the atomic structure and the electrical properties of both the film itself and the interface between the two dissimilar materials. They also allow the study of epitaxial growth between materials exhibiting very different types (ionic, covalent, or metallic) of bonding.

While the potential of heteroepitaxial deposition has been demonstrated, significant advances in theoretical understanding, experimental growth and control of this growth, and characterization are required to exploit the capabilities of this process route. It is particularly important to understand and control the principal processes which control heteroepitaxy at the atomic level. It is this type of research, as well as the chemistry of dry etching via laser and plasma processing, which forms the basis of the research in this grant.

The materials of concern in this report are classified as wide bandgap semiconductors and include diamond, SiC and the III-V nitrides of Al, Ga, and In and their alloys. The extremes in electronic and thermal properties of diamond and SiC allow the types and numbers of current and conceivable applications of these materials to be substantial. However, a principal driving force for the interest in the III-V nitrides is their potential for solid-state optoelectronic devices

for light emission and detection from the visible through the far ultraviolet range of the spectrum.

The principal objectives of the research program are the determination of (1) the fundamental physical and chemical processes ongoing at the substrate surface and substrate/film interface during the heteroepitaxial deposition of both monocrystalline films of the materials noted above, as well as metal contacts on these materials, (2) the mode of nucleation and growth of the materials noted in (1) on selected substrates and on each other in the fabrication of multilayer heterostructures, (3) the resulting properties of the individual films and the layered structures and the effect of interfacial defects on these properties, (4) the development and use of theoretical concepts relevant to the research in objectives (1-3) to assist in the fabrication of improved films and structures and (5) the determination of process chemistry which leads to the laser assisted and plasma etching of these wide bandgap compound semiconductors.

This is the eighth bi-annual report since the initiation of the project. The following sections introduce each topic, detail the experimental approaches, report the latest results and provide a discussion and conclusion for each subject. Each major section is self-contained with its own figures, tables and references.

Carbon-based Materials

II. Donor Doping of Diamond Using Nuclear Transmutation

A. Introduction

This report provides an update on an ongoing project at NCSU investigating Li incorporation into diamond via nuclear transmutation. This doping mechanism is of interest in diamond because of difficulties encountered in attempts to incorporate Li by more conventional means such as diffusion or incorporation during CVD. Additional background for this work has been described in previous quarterly reports.

Our approach has been to investigate transmutation in well characterized homoepitaxial films grown by established techniques. Growth and electrical measurements have been performed at Kobe Steel USA by researchers with extensive experience in electrical measurements on homoepitaxial and polycrystalline diamond film. Our isotopically-enriched boron source is diborane, one of the most common doping sources of boron for CVD diamond growth. The carrier concentration and mobility have been measured as a function of temperature prior to irradiation. The quality of the films and diamond substrates prior to irradiation has also been evaluated using Raman and photoluminescence spectroscopy. In addition, our experiments include control samples with no boron and with the natural abundance of boron to separate the effects of irradiation damage from the effects of Li production. Irradiation has been performed by Dr. S. Mirzadeh of the Nuclear Medicine group at Oak Ridge National Laboratory.

B. Experimental Procedure

Homoepitaxial boron doped films have been grown using microwave CVD with diborane as the dopant source. Table I shows the target boron concentrations for each of the five films. All films are grown on (100) oriented type 2a natural diamond substrates and range from 3 to 8 microns in thickness. The films were grown over a $3 \times 3 \text{ mm}^2$ area on the $4 \times 4 \text{ mm}^2$ substrates to isolate the films from the edges of the wafers. The isotopically enriched diborane is 96% ^{10}B and 4% ^{11}B . Films with the natural abundance of the two boron isotopes are included to aid in separating the effects of Li production from the effects of damage. The natural isotopic abundance of boron is 19% ^{10}B and 81% ^{11}B , so the maximum possible conversion of the natural abundance samples (#1 and #2) is 19%. Samples 4 and 5 have the same boron content to provide a duplicate experiment. In addition, measurements can be made of the back surfaces of the diamond wafers to analyze the effects of neutron irradiation on diamond which is free of boron. Metal contacts consisting of Ti and Au were applied. The carrier concentration and mobility were measured at several temperatures from 300 to 600 K using the Hall effect in a van der Pauw geometry.

Table I. Samples and Target Boron Content

Sample	Boron content (Target value, cm ⁻³)	Isotopic Composition
1	10 ¹⁸	natural abundance
2	10 ²⁰	natural abundance
3	10 ¹⁸	¹⁰ B enriched
4	10 ²⁰	¹⁰ B enriched
5	10 ²⁰	¹⁰ B enriched

Raman and photoluminescence spectroscopy were used to provide a baseline measurement of the quality and defects in the films and substrates. It is expected that the films will be damaged during the irradiation process, so it is important to measure the quality of the films before irradiation. Raman measurements were made using the 5145Å line of an Argon laser, and photoluminescence measurements using the 4579Å line (2.71eV). The incident light was focused to a 10 µm spot size using a microscope, and the scattered light was analyzed using an ISA U-1000 scanning double monochromator.

Samples were irradiated by Dr. S. Mirzadeh of the Nuclear Medicine Group at Oak Ridge National Laboratory. The total dose was 9×10²⁰n/cm².

C. Results and Discussion

The diamond samples were irradiated at a dose of 9×10²⁰ n/cm². The previously reported target dose of 3×10²⁰ n/cm² was increased. Calculations performed by Dr. Mirzadeh indicate that this dose will convert 95% of the ¹⁰B to ⁷Li (Fig. 1). The samples exhibited a greater radioactivity than expected when removed from the reactor. As of 2/26/96, the package read 1 R/h unshielded and ~64 mR/h shielded with 1" lead. The samples were retested on 4/29/96 after removal from the packaging and a lower but still significant activity was detected. Gamma ray spectroscopy indicated that the remaining activity consisted of approximately 5µCi of ¹¹⁰Ag. The samples have now been returned to NCSU, where they will be cleaned to remove the remaining silver.

D. Conclusions

In summary, nuclear transmutation is being investigated as a means for donor doping of diamond. To date samples have been prepared for irradiation, baseline electrical measurements and optical measurements have been performed, and samples have been irradiated at a dose of 9×10²⁰n/cm².

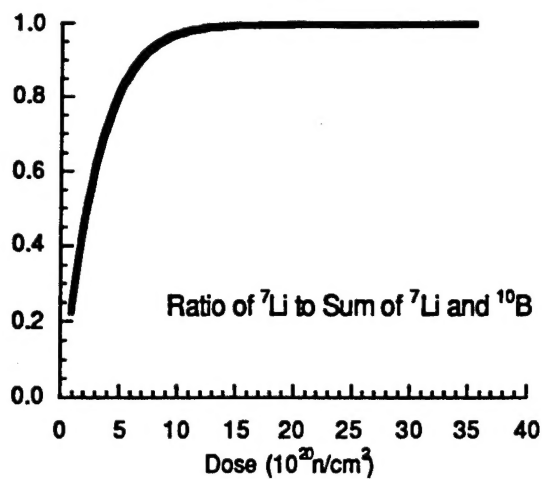


Figure 1. Percentage of ${}^{10}\text{B}$ converted to ${}^7\text{Li}$ as a function of neutron dose.

E. Future Research Plans and Goals

Following cleaning of the samples, post irradiation studies will begin with optical assessment of the damage via Raman and photoluminescence spectroscopy. We will then attempt to remove the damage via annealing. If the damage can be recovered, additional Hall measurements will be performed.

III. Spectral Analysis of Field Emitted Electrons from Diamond-Coated Nanoscale Molybdenum Emitters

A. Introduction

For several years, the study of field emitters has been of interest as the possibility of flat panel displays and vacuum microelectronics has appeared feasible [1]. One drawback to traditional field emitter materials, Si and Mo, has been contamination of surface and surface degradation through back sputtering by the ambient ions. One approach to counteract these drawbacks has been coating the emitters with diamond to protect the surface from oxidation and ion bombardment. Diamond has an additional attraction of negative electron affinity under certain conditions [2]. However, traditional Fowler-Nordheim analysis of I-V measurements is not well suited for curved surfaces and low work function materials [3, 4]. On the other hand, field emission energy distribution analysis of the emitted electrons is ideally suited for the detection of materials with a negative electron affinity and would reveal any other effects a diamond coating would have on the emitter. Also, this analysis technique would indicate the energy relationship between the applied voltage and the emitted electrons.

This report relates the experimental results measuring the field emission energy distribution of a diamond coated Mo emitter. The data was compared to the same Mo emitter before coating and several *in vacuo* thermal treatments were performed to determine their effects on electron emission. The analyzer used was a hemispherical energy analyzer typically used for x-ray photoelectron spectroscopy or Auger electron spectroscopy.

B. Experimental Approach

Mo Needle Preparation and Diamond Powder Coating. A single emitter tip was made from 99.95% pure Mo wire with a diameter of 0.125mm. The wire was held in a Cu tube and then electrochemically etched in a concentrated KOH solution. This technique has consistently produced needles with a radius of curvature approximately 500 μm .

After the initial data was collected, the needle was coated with diamond powder via a dielectrophoresis method. The diamond powder (size range: 0-0.25 μm) was suspended in a ethanol solution and voltage was applied between the Mo needle and the container. The non-uniform field generated by the needle created an impelling force driving the diamond particles toward the region of highest field (i.e. the tip end). SEM observation after coating revealed the entire tip end was covered by diamond powder.

Testing Configuration. The Mo needle was set into the holder and centered within a circular gate where the needle was the "cold cathode" and the gate was the "extraction grid." The gate was electrically grounded and had a 500 μm opening and a tip-to-gate separation distance of 400 μm . A negative voltage was applied to the tip, see Fig. 1. The energy analyzer used was a CLAM II hemispherical energy analyzer from Vacuum Generators, Ltd., typically used in

x-ray photoelectron spectroscopy or Auger electron spectroscopy. Both the gate and analyzer were at the same ground potential. Typical data collection conditions included a dwell time of 100 ms, an energy step of 0.025 eV, and 3 scans were taken over the desired energy range.

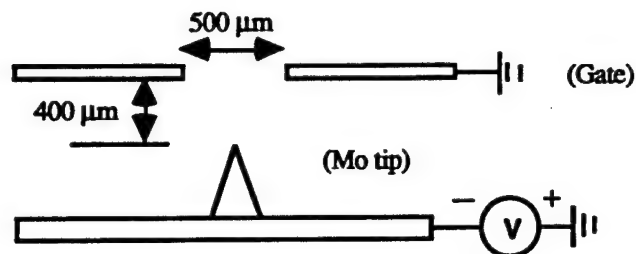


Figure 1. Schematic drawing of sample holder and voltage connections.

Experimental Procedure. After the sample was placed into the vacuum chamber, an initial thermal desorption treatment was performed. The sample holder was heated to 500°C for 1 hour and the chamber pressure was in the 10^{-7} Torr range. All emission data was collected under UHV conditions (typically 10^{-9} Torr). Next, the sample was removed from the chamber and coated with diamond powder via the dielectrophoresis method. To remove any atmospheric contaminants and desorb any solvent, the sample holder was heated *in vacuo* to 400°C for 3 hours before taking any measurements. Next, a thermal annealing treatment was performed by heating *in vacuo* to 600°C for 90 minutes. For the final heat treatment, the sample was transferred to a microwave plasma diamond CVD system (ASTeX, Inc.) for the H_2 plasma treatment. The sample was heated to 620°C for 30 minutes downstream from the plasma, then the sample was transferred back to the analysis chamber and data was collected. After this series, the sample was imaged in a scanning electron microscope.

C. Results

Table I summarizes the observed energy shift between the applied voltage and the peak maximum and the voltage for which there was perceptible signal (i. e. count rates $> 10s^{-1}$), hereafter termed "turn-on" voltage. Figure 2 displays spectra of similar count rate for the different treatments. The spectra typically had a rapid increase on the high energy side of the peak and a less rapid decay on the lower energy side of the peak. The "turn-on" voltage for the bare Mo needle was -450 V. After diamond coating the "turn-on" voltage decreased to -350 V and it decreased to -280 V after annealing the diamond coated needle. The "turn-on" voltage increased to -650 V after attempting to hydrogen terminate the diamond coating.

The energy difference between the applied voltage and the peak maximum for the Mo tip was -4.1 eV for all voltages and the peak FWHM was 0.7 ± 0.1 eV. After diamond coating, the energy difference increased to -5.4 eV for the "turn-on" voltage and increased with applied voltage to -11 eV for -525 V with a FWHM of 0.7 ± 0.1 eV. Two peaks appeared after

annealing the diamond coated needle at an energy difference of -4.6 eV and -3.4 eV. The second peak appeared only above voltages of -400 V. The peak FWHM for both peaks was 0.8 ± 0.1 eV. After attempting to hydrogen terminate the diamond coating, only one peak was observed and the energy difference was -3.4 eV with a FWHM of 0.7 ± 0.1 eV.

SEM micrographs taken after the H_2 plasma treatment revealed that the diamond powder coating near the tip of the needle had been removed. The tip had partially melted and bent away from the gate.

Table I. Summary Table of Energy Separation Between the Applied Voltage and Emission Peak and "Turn-on" Voltages for the Different Treatments

Treatment	Energy Shift (eV)	"Turn-on" Voltage (V)
bare Mo	-4.1	-450
Diamond coated Mo	-5.4 to -11 increased with voltage	-350
Diamond coated Mo - annealed	-4.6 and -3.4	-280
Diamond coated Mo - H_2 plasma	-3.4	-650

D. Discussion

The energy difference between the applied voltage and the peak maximum for different treatments is summarized in Table I. For the uncoated Mo needle, the peak maximum was observed to be 4.25 ± 0.25 eV below the applied voltage, which is in agreement with the reported effective work function for Mo (4.2-4.4 eV) [1]. While no reported values for molybdenum carbide could be found, the following trends were noted. TiC had an effective work function 0.7 eV less than Ti and TaC had an effective work function 0.9 eV less than Ta. Since the refractory metals share many common attributes, it is reasonable to assume that the effective work function of molybdenum carbide is lower than that of Mo [1]. Therefore, the peaks recorded that were around 3.4 eV below the applied voltage may be attributed to emission from the carbide phase, while the peaks approximately 4.25 ± 0.25 eV below the applied voltage can be attributed to emission from Mo. However, the presence of Mo_xC cannot be confirmed until further analysis of the needle is done. The reported work function values for diamond are either 1.0 eV or negative electron affinity depending on surface termination. No peaks were observed corresponding to those values.

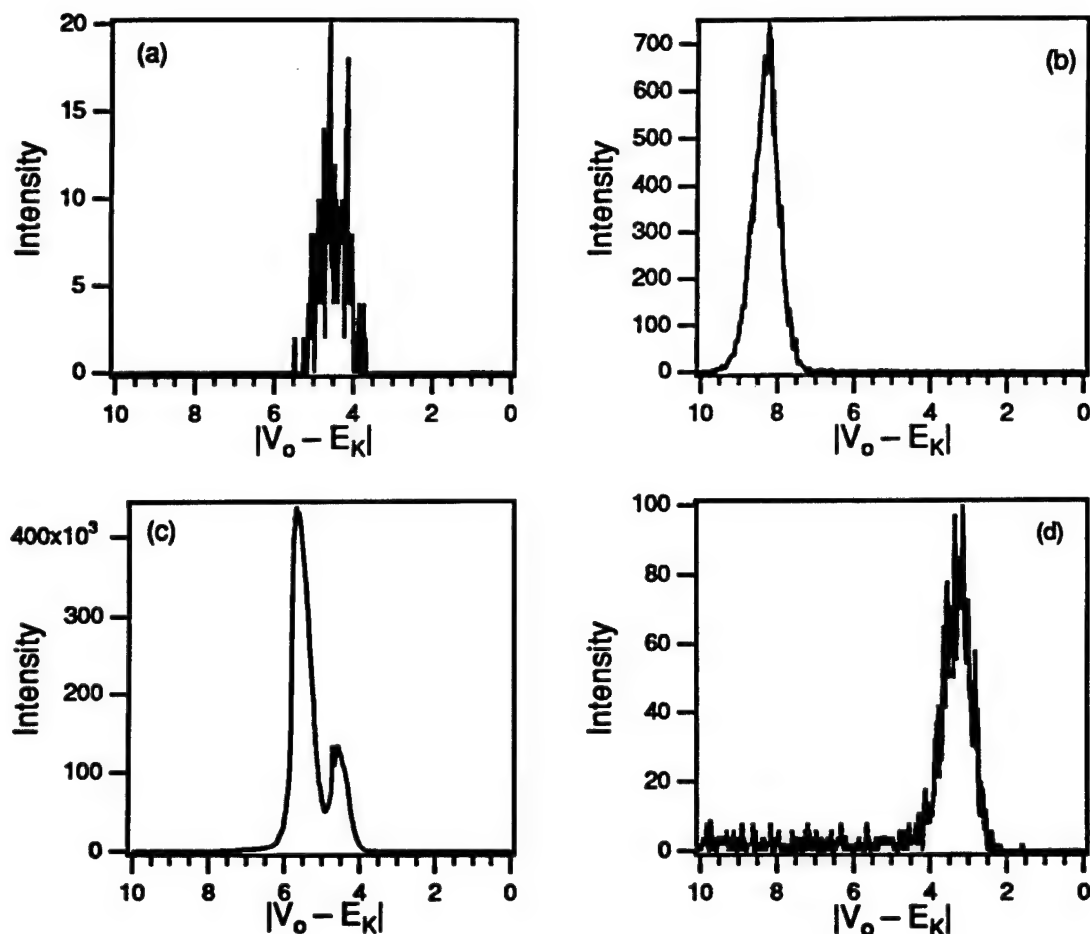


Figure 2. Typical energy distribution spectra for the (a) Mo needle (-450 V), (b) after diamond coating (-450 V), (c) after annealing (-450 V), and (d) after H₂ plasma treatment (-700 V).

The decrease in "turn-on" voltage after coating the Mo needle with diamond powder probably resulted in a change in the field distribution to enhance emission; however, the large work functions observed suggest that the emission did not emanate from the diamond coating. After annealing the diamond coated Mo needle, the morphology of the coating may have changed and modified the field distribution at the emitting area. SEM micrographs after the H₂ plasma treatment revealed that the tip was no longer covered with diamond and the needle had bent. The increase in radius of curvature caused an increase in the "turn-on" voltage.

After those treatments that resulted in the formation of a carbide phase, it would be reasonable to assume that the lower work function areas would begin to emit at lower voltages. This supposition is counter to what was observed. One possible explanation is that the carbide phase formed only where there was significant contact between the Mo needle and diamond crystals. It is unlikely that the entire crystal was consumed in the formation of the carbide,

therefore, the remaining diamond crystal would have been a scattering barrier to electrons emitted from the carbide phase. At higher voltages, where emission appeared to have come from the carbide phase, the voltage may have been sufficient to cause ballistic transport of electrons from the carbide through the obstructing diamond particle.

E. Conclusions

The field emission energy distribution was successfully measured from a diamond powder coated, nanoscale Mo needle, after several thermal treatments, using a hemispherical energy analyzer. Examination of the field emission energy distribution (FEED) spectra yielded valuable information not gained during standard I-V measurements. Measuring the energy difference between the applied voltage and the field emission peak provided information regarding the work function of the emission area. The variation in this energy difference for the diamond coated Mo needle indicated that diamond did not emit under the conditions investigated. The FEED spectra also indicated that both Mo and possibly Mo_xC regions emitted after annealing the diamond powder coated needle.

F. Future Research Plans and Goals

These initial experiments revealed that the energy distribution of field emission electrons provided important information not obtained in I-V measurements. Several questions were also raised. For instance, although Mo_xC probably has a lower work function than Mo a higher voltage was required to induce emission from these regions. To determine whether the lower work function of diamond is of relevance, or whether the lowering of the "turn-on" voltage is exclusively due to topographic effects leading to further field enhancements, graphite coated needles will be investigated. Comparison experiments between Mo and Si needles will also be performed to investigate the differences in these two commonly used emitter materials.

G. References

1. S. Iannazzo, Solid State Electronics 36 (3), 301-20 (1993).
2. J. van der Weide and R. J. Nemanich, Applied Physics Letters 62 (16), 1878-80 (1993).
3. D. Nicolaescu, J. Vac. Sci. Technol. B 11 (2), 392-395 (1993).
4. R. H. Fowler and L. W. Nordheim, Proc. R. Soc. London Ser. A 119, 173 (1928).

IV. *Ex Situ* and *In Situ* Methods for Complete Oxygen and Non-Carbide Carbon Removal from (0001)_{Si} 6H-SiC Surfaces

A. Introduction

For SiC to succeed as the substrate/semiconductor of choice for high-frequency, high-temperature, high-power devices and III-N heteroepitaxy, a considerable reduction in defects (line, planar, point, etc.) must be achieved. Following Si technology, where surface cleaning and preparation are critical first step in all processes [1], a continued reduction in defects in SiC should be expected as a result of improved SiC wafer surface cleaning techniques. In Si technology for example, improper removal of surface contamination and oxides prior to Si homoepitaxy has been shown to result in an increase in the density of line and planar defects in epitaxial films from $< 10^4/\text{cm}^2$ to $> 10^{10}/\text{cm}^2$ [2-5] and an associated drop in device yield [2].

Typically, SiC *ex situ* cleaning consists of solvent degreasing and RCA cleaning with the last step usually a 5-10 min. dip in an HF solution (composition ranging from 0.1-50%) [6-8]. The HF dip is intended to remove any native or intentionally grown (dry or thermal) oxides formed on the SiC surface. For silicon, the HF etch has been found to be beneficial in that it not only removes oxides (SiO_2 or SiO_x) from the surface but also passivates the surface by terminating all the dangling bonds with hydrogen [9-11]. The hydrogen termination inhibits re-oxidation of the silicon surface on removal from the HF solution and produces a hydrophobic surface [11]. For (0001)_{Si} 6H-SiC, this has not been found to be the case. Surface analysis by the authors and others (see Fig. 1a) has revealed that the SiC surface is still terminated with an $\approx 10 \text{ \AA}$ layer of carbonaceous material (consisting of C-C, C-O, C=O, and C-H bonding) after HF dipping [7-9]. Thermal desorption of this non-carbide carbon can be easily achieved by annealing at temperatures as low as 500-700°C. However, unlike Si, approximately 1/2 to 3/4 monolayer of oxide remains at the surface (see Fig. 2a-b), and thermal desorption of this oxide in UHV requires temperatures in excess of 1000°C [12]. In Fig. 1c, removal of the oxide by this method can result in the formation of some non-carbide/graphitic carbon at the SiC surface. To combat this, others have followed the pioneering work of Kaplan [13] and employed *in situ* techniques in which the SiC surface is annealed in a flux of Si (solid or gas source) which allows thermal desorption of the oxide at lower temperatures ($< 900^\circ\text{C}$) while maintaining a Si-rich surface [12,14]. This section reports efforts to use a Si capping layer to provide both a hydrophobic surface during *ex situ* processing and a Si-rich surface during *in situ* processing.

B. Experimental

The vicinal n-type (typically $N_d = 10^{18}/\text{cm}^3$) (0001)_{Si} 6H-SiC wafers used in these experiments contained an n type epilayer (typically $N_d = 10^{17}/\text{cm}^3$) and 500-1000 Å of thermally

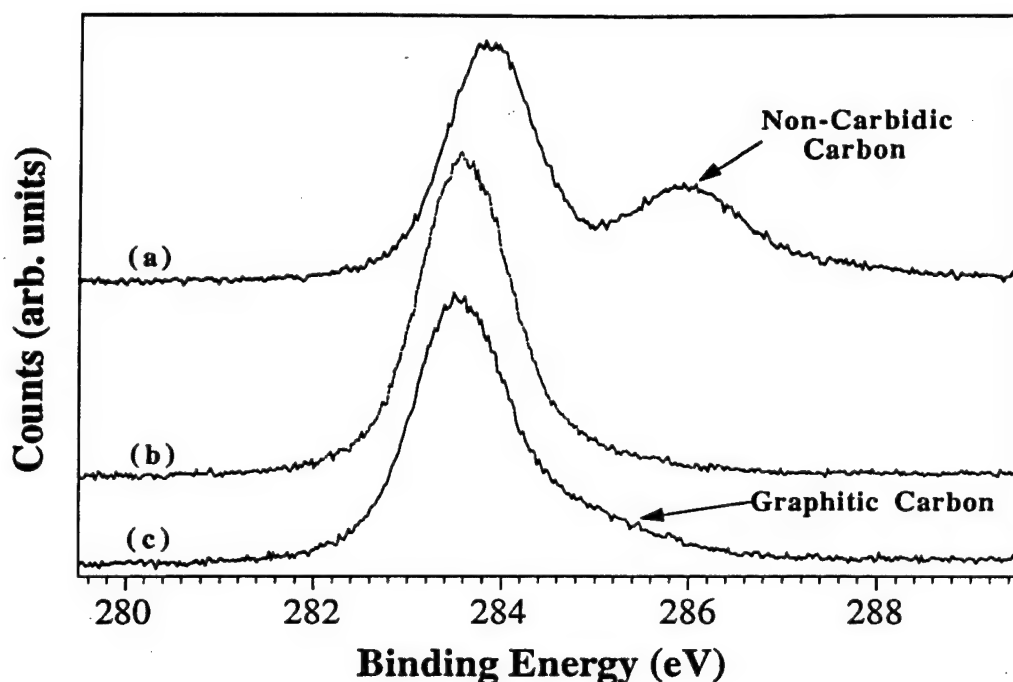


Figure 1. XPS of C 1s from (0001)_{Si} 6H-SiC surface after: (a) 5 min. 10:1 HF dip, (b) after thermal annealing at 800°C, and (c) after annealing at 1200°C in UHV [8].

grown oxide. They were supplied by Cree Research, Inc. The thermal oxide was removed using a 5-10 min. dip in a 10:1 HF dip (CMOS grade, J. T. Baker). Further cleaning of this surface was then investigated by immersion in other acid/base solutions or by reoxidizing the SiC surface using a UV/O₃ treatment followed by a wet chemical treatment. The UV/O₃ treatments described in this study employed a box in which was positioned a high intensity Hg lamp in close proximity to the SiC wafer. The details of this process have been described previously [15]. The wet chemistries examined included 10:1 HF, 10:1 buffered HF (7:1 NH₄F:HF), 40% NH₄F, HCl:HF, and NH₃OH:HF solutions, HNO₃, H₂SO₄, acetic, and lactic acid. Except where noted, after all wet chemical cleans the samples were rinsed in DI water (18 MΩ) and blown dry with N₂ (UHP). All wet chemicals were of CMOS grade purity (J. T. Baker).

The *in situ* cleaning and the surface analyses of the samples subjected to *ex situ* and *in situ* cleaning were conducted in a unique ultra-high vacuum (UHV) system consisting of a 36 ft. long UHV transfer line to which were connected several surface analysis and thin film deposition units. The details of each and the transfer line have been described elsewhere [15]. Surfaces prepared in the above manner were then subsequently mounted to a molybdenum sample holder and loaded into the loadlock for subsequent analysis by AES, XPS, EELS, and LEED. XPS analysis was performed using the Al anode ($h\nu = 1486.6$ eV) at 20 mA and 10kV. AES spectra were obtained using a beam voltage of 3 keV and an emission current of

1 mA. LEED was performed using rear view optics, a beam voltage of approximately 100 eV, and an emission current of 1 mA. Calibration of the XPS binding energy scale was performed by measuring the position of the Au 4f_{7/2} and shifting the spectra such that the peak position occurred at 83.98 eV. All sample temperatures quoted here were measured using an optical pyrometer and an emissivity of 0.5.

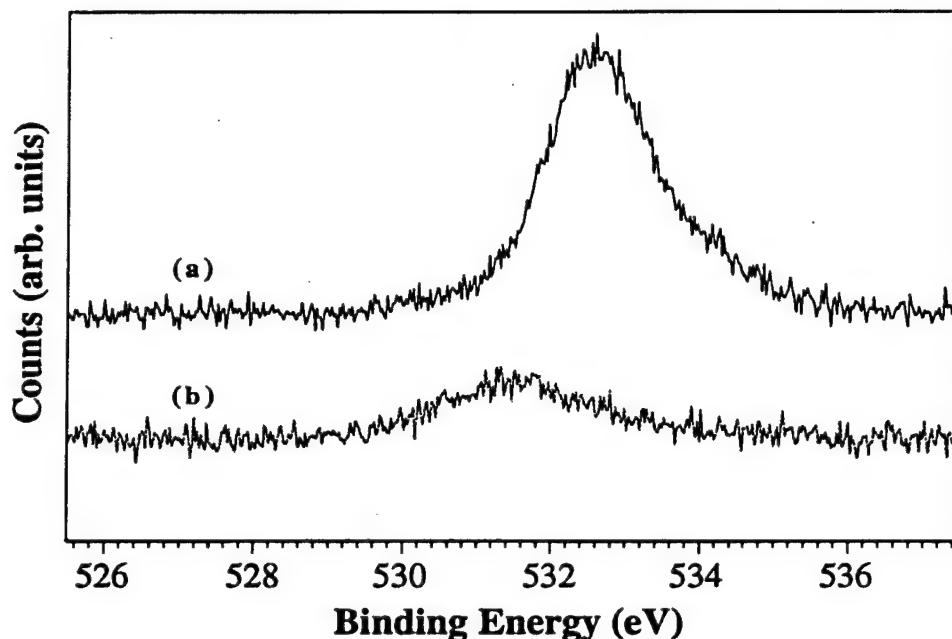


Figure 2. XPS of O 1s from (a) (0001)_{Si} 6H-SiC and (b) Si (111) wafers after dipping in 10:1 HF for 5 min [12].

C. Results

Si and SiC Wetting Experiments. As previously mentioned, oxide removal from (0001) 6H-SiC surfaces using HF leaves a hydrophilic surface containing significant amounts of oxide surface (see Fig. 3a). To determine a wet chemistry which produces a more hydrophobic SiC surface, several (0001)_{Si} 6H-SiC wafers were dipped in HF, NH₄F, NH₃OH, HCl, HNO₃, H₂O₂, H₂SO₄, acetic acid, and lactic acid and the wetting characteristics of these surfaces in these acids and bases and de-ionized water monitored visually. For comparison purposes, Si (111) and Si (100) wafers were also dipped simultaneously in each acid with the SiC wafer. All wafers (Si or SiC) were initially dipped in 10% HF to remove any native oxides from the surfaces before dipping in the acids and bases of interest. For Si, the surfaces remained hydrophobic when dipped in NH₃OH, HCl, or H₂O₂. Dipping the Si wafers in HNO₃ or H₂SO₄ removed the hydrophobic nature of the surface. Dipping Si in the organic acids resulted in a strongly adhering thin film of the acid to the silicon surface which could be removed in DI H₂O leaving a hydrophobic surface. For SiC, all acids and bases wetted the surface and none

were found to produce a hydrophobic SiC surface. 10% HF solutions with pH's adjusted from strongly acidic, neutral, and to strongly basic using HCl, NH_4F , and NH_3OH , respectively, were also examined as they have been reported to produce better hydrogen termination of Si (111) surfaces [17,18]. In these experiments, the dipping times were held constant at 10 min. No changes in the wetting characteristics of the $(0001)_{\text{Si}}$ SiC surface in HF solutions with the different pH's were found. In an additional experiment, the dipping time was varied from 5 min. to 1 hr.; however, no difference was found. Additionally, neither XPS nor AES indicated a significant change (within AES and XPS experimental accuracy) in the amount of surface oxygen on $(0001)_{\text{Si}}$ SiC wafers after dipping in HF solutions of various pH. No differences were observed between on axis and vicinal surfaces, as well.

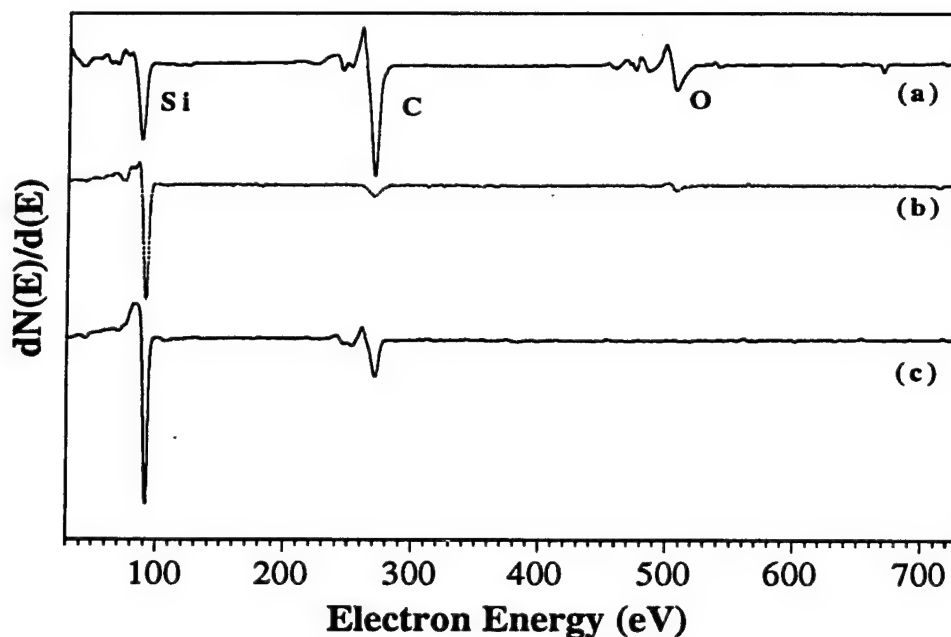


Figure 3. (a) AES of $(0001)_{\text{Si}}$ 6H-SiC surface after dipping in 10:1 HF for 5 min., (b) $(0001)_{\text{Si}}$ 6H-SiC with a 20Å Si capping layer after dipping in 10:1 HF, 5 min., (c) $(0001)_{\text{Si}}$ 6H-SiC after thermal desorption of the Si capping layer at 1100°C for 5 min.

Si Capping Layer. A new technique for *in situ* oxide removal rapidly gaining acceptance consists of annealing SiC in a flux of silicon at temperatures $> 900^\circ\text{C}$ [13,14]. Since wet chemical cleaning of Si was found to more readily produce hydrophobic and cleaner surfaces, the use of a 20Å Si capping layer on $(0001)_{\text{Si}}$ 6H-SiC was investigated. The following procedure was used to prepare the Si capping layer. Firstly, the (0001) 6H-SiC wafer was given a 5 min. dip in 10:1 HF, DI rinsed, N_2 blow dried and loaded into vacuum. The 6H-SiC was then degassed and annealed in a SiH_4 flux (10^{-6} Torr) at 950°C for 20 min. in the

GSMBE. This produced an oxygen free Si rich (1×1) SiC surface. Next, a Si-Ge electron beam MBE was used to deposit 200Å of Si on the SiC at room temperature *in situ*. The Si/SiC sample was then given two UV/O₃ treatments followed by dips in 10:1 HF to thin the Si capping layer down to 20Å. After each HF dip, the polished face of the Si/SiC wafer was found to be hydrophobic as with Si wafers. AES of this surface after HF dipping showed only small amounts of oxygen and carbon contamination (see Fig. 3b). XPS of this surface after HF exposure showed a Si 2p peak at 99.5 eV with a shoulder at 101.5 eV indicating that the surface consisted of an ≈ 20 Å Si film on top of the SiC. On annealing this surface to desorb the Si capping layer, it was observed that the outgassing from the wafer was several orders of magnitude lower than that typical for other HF dipped SiC wafers (10^{-7} Torr ax vs. 10^{-5} Torr typical). In fact, the outgassing levels were typical for those observed from Si (111) wafers. The reason's for these higher and lower outgassing rates will be discussed later.

Following annealing of the Si/SiC wafer at 1100°C for 5 min., LEED showed a sharp (3×3) reconstructed surface commonly observed for surfaces prepared via annealing in Si fluxes [12]. XPS of this surface, now shows a Si 2p peak located at 101.5 eV with a shoulder at 99.5 eV indicating that the 3×3 surface is due to the presence of a Si bilayer. Continued annealing at 1100°C resulted in further desorption of Si which resulted in first a (1×1) and then a ($\sqrt{3}\times\sqrt{3}$)R30° LEED pattern. AES of the (3×3) surface showed no oxygen within the detection limits of AES and a Si/C ratio of 3/1. It should be pointed out that (3×3) surfaces

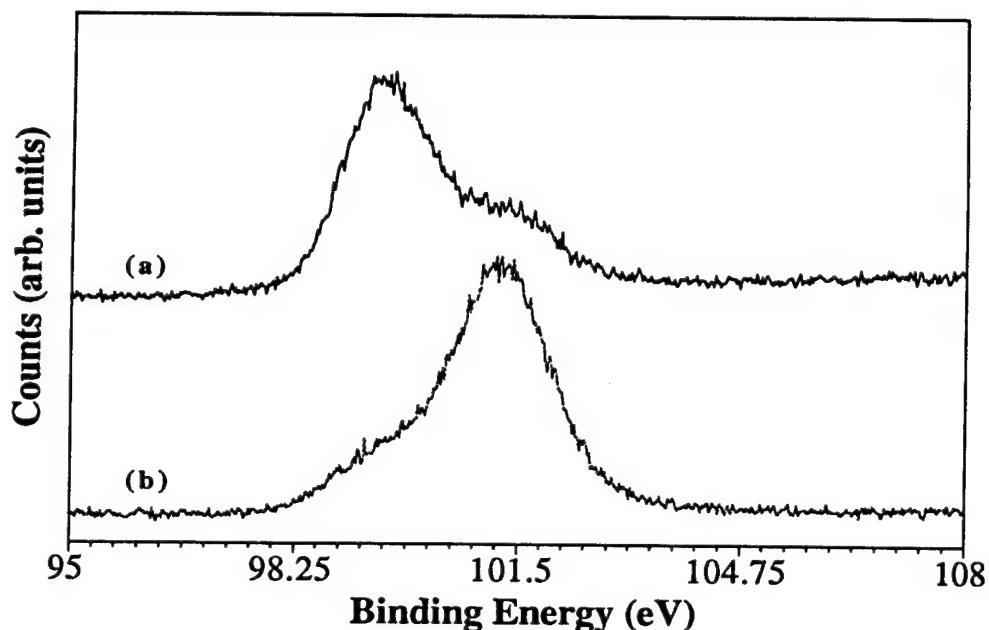


Figure 4. XPS of Si 2p from a (0001)_{Si} 6H-SiC with a 20Å Si capping layer after: (a) 5 min. dip in 10:1 HF, and (b) after thermal desorption of the Si capping layer at 1100°C for 5 min.

have been previously prepared, removed from vacuum, dipped in HF, and the wetting characteristics observed. In this case, the surfaces were hydrophilic indicating that the Si bilayer is readily removed by the combination of air exposure and HF dipping. As such, 15-20 Å probably represents the optimum thickness for the Si capping layer.

D. Discussion

One frequently noted problem with (0001) 6H-SiC wafers is the existence of internal micro-pipes. Aside from being potential device killers, the authors have frequently experienced other problems during processing of SiC wafers which can be attributed to the micro-pipes as well. The authors have frequently observed that these entities can harbor HF and H₂O after HF dipping and N₂ drying. Presumably, this is due to capillary action. This conclusion is based primarily on the observation that during annealing/thermal desorption in UHV of HF dipped SiC wafers phenomenally high outgassing rates have been observed (i.e. 10⁻⁵ Torr). RGA analysis of the background vacuum during thermal annealing of the SiC wafer reveals that HF and H₂O are the two main constituents outgassing from the wafers. As outgassing rates for Si wafers which have experienced an HF dip & N₂ dry are several orders of magnitude lower (10⁻⁸ to 10⁻⁷ Torr), we suggest that HF/H₂O trapped in the micro-pipes due to capillary action are the source of the extremely high outgassing. The importance of this observation is that the high outgassing can lead to difficulties in completely removing the oxide from the SiC surface as well as creating a large background of H₂O and HF in the growth system. The H₂O/HF levels can subsequently result in an increase of background oxygen or fluorine in epitaxial films. Owing to the observed change from a hydrophilic to a hydrophobic surface with the addition of the Si capping layer, it is not surprising that lower outgassing rates were observed for the SiC surface with the Si capping layer.

In addition to the oxide removal and the lower outgassing rates, another advantage of the use of the Si capping layer is the potential for its incorporation into already existing processing routes. Potentially, the Si capping layer could be deposited during cooling from SiC thin film CVD epitaxy. Currently, the SiC wafer/film assemblies are cooled in H₂ which produces a carbon rich layer which must be removed by a second processing step of thermal oxidation [9,18]. Unfortunately, high quality SiC CVD epitaxial deposition typically occurs at temperatures higher than the Si melting point (1440°C) and hence results in the deposition of Si droplets instead of a continuous film of Si [19]. However, the authors have initially found that this approach can still eliminate the need for oxidation as the Si droplets can be etched away (15 HNO₃: 2 HF: 5 CH₃COOH) leaving a surface concentration equal (by XPS and AES) to that produced by thermal oxidation and oxide removal by HF. Perhaps, the Si capping layer can best be utilized with 3C-SiC surfaces where epitaxy can occur at lower temperatures.

E. Conclusions

The wetting characteristics of (0001) 6H-SiC surfaces in HF and other acids were found to be hydrophilic. Hydrophobic surfaces could be achieved by use of a thin 20 Å Si capping layer. The use of the capping layer also resulted in lower outgassing rates during thermal annealing during *in situ* processing. Annealing the Si capping layer/SiC wafer at 1100°C for 5 min. resulted in the desorption of the excess silicon and a (3×3) reconstructed SiC surface.

F. Acknowledgments

The authors would like to express appreciation to Dr. Ja-Hum Ku for assistance with the deposition of the Si capping layer and input into these experiments. Appreciation is also expressed to Cree Research, Inc. for the 6H-SiC wafers. The work described herein was supported by the Office of Naval Research under contract N00014-95-1-1080.

G. References

1. W. Kern, J. Electrochem. Soc. **137** (6), 1887 (1990).
2. R. Williams, *Modern GaAs Processing Methods*, 2nd ed. (Artech House, Inc., New York, 1990), pp. 81-114.
3. G. R. Srinivasan and B. S. Meyerson, J. Electrochem. Soc. **134** (6), 1518 (1987).
4. B. S. Meyerson, E. Ganin, D. A. Smith, and T. N. Nguyen, J. Electrochem. Soc. **133** (6), 1232 (1986).
5. M. K. Sanganeria, M. C. Ozturk, G. Harris, K. E. Violette, I. Ban, C. A. Lee, and D. M. Maher, J. Electrochem. Soc. **142** (11), 3961 (1995).
6. Y. Mizokawa, S. Nakanishi, O. Komoda, S. Miyase, H. S. Diang, C. Wang, N. Li, and C. Jiang, J. Appl. Phys. **67** (1), 264 (1990).
7. H. Tsuchida, I. Kamata, and K. Izumi, Jpn. J. Appl. Phys. **34**, 6003 (1995).
8. L. M. Porter, R. F. Davis, J. S. Bow, M. J. Kim, R. W. Carpenter, R. C. Glass, J. Mater. Res. **10** (3), 668 (1995).
9. B. S. Meyerson, F. J. Himpsel, and K. J. Uram, Appl. Phys. Lett. **57**, 1034 (1990).
10. M. Grundner and H. Jacob, Appl. Phys. A **39**, 73 (1986).
11. Y. J. Chabal, G. S. Higashi, K. Raghavachari, and V. A. Burrows, J. Vac. Sci. Technol. A **7** (3), 2104 (1989).
12. R. S. Kern, S. W. King, and R. F. Davis, to be published.
13. R. Kaplan, Surf. Sci. **215**, 111 (1989).
14. A. Fissel, B. Schroter, E. Ducke, B. Schroter, and W. Richter, J. Cryst. Growth **154**, 72 (1995).
15. J. A. McClintock, R. A. Wilson, and N. E. Byer, J. Vac. Sci. Technol. **20**, 241 (1982).
16. J. van der Weide and R. J. Nemanich, Appl. Phys. Lett. **62**, 1878 (1985).
17. G. S. Higashi, R. S. Becker, Y. J. Chabal, A. J. Becker, Appl. Phys. Lett. **58**, 1656 (1991).
18. G. S. Higashi, Y. J. Chabal, G. W. Trucks, and K. Raghavachari, Appl. Phys. Lett. **56**, 656 (1990).
19. L. Rowland, Northrop-Grumman. Private communication.

V. Rectifying and Ohmic Contacts for P-type Alpha (6H) Silicon Carbide

A. Introduction

While the wide band gap of SiC is responsible for its use in optoelectronic, high power, and high temperature devices, this property also adds to the difficulty of controlling the electrical properties at the metal-semiconductor contacts in these devices. The primary parameter used to quantify the electrical relationship at these interfaces is the Schottky barrier height (SBH), or the energy barrier for electrons traversing the interface. A small SBH is desired for a good ohmic, while a relatively large SBH is necessary to create a good rectifying contact.

The formation of low resistivity and thermally stable ohmic contacts to 6H-SiC remains a serious problem in the development of SiC device technology. For SiC power devices to have the advantage over Si, the contact resistivities must be below $1 \times 10^{-5} \Omega\text{-cm}^2$ [1]. The thermal stability of ohmic contacts is of particular concern for p-type SiC, which have traditionally contained Al to dope the SiC surface below the contacts. While the fabrication of ohmic contacts to SiC also has usually depended on very heavily-doped surfaces, the introduction of high levels of dopants in the near surface device region of the epilayer prior to the deposition of the contact or by ion implantation through the contact makes probable the introduction of point and line defects as a result of the induced strain in the lattice. Based on all of these issues and experiments already performed at NCSU, our goals are to produce contacts which are thermally stable and have low contact resistivities while also reducing the need for doping by ion implantation.

Low resistance contacts to p-type SiC remain a substantial challenge for high temperature and high-power devices. An Al-Ti alloy [2] annealed at 1000°C for 5 min. was reported to yield contact resistances ranging from $2.9 \times 10^{-2} \Omega\text{ cm}^2$ for a carrier concentration of $5 \times 10^{15} \text{ cm}^{-3}$ to $1.5 \times 10^{-5} \Omega\text{ cm}^2$ for $2 \times 10^{19} \text{ cm}^{-3}$. The thermal stability of these contacts was not reported. Aluminum deposited on a heavily-doped 3C-SiC interlayer on a 6H-SiC substrate and subsequently annealed at 950°C for 2 min. reportedly yielded contact resistivities of $2\text{--}3 \times 10^{-5} \Omega\text{ cm}^2$ [3]. Because of its low melting point (660°C), however, pure Al would be unsuitable for high temperature applications. Platinum contacts annealed from 450 to 750°C in 100°C increments were also used as ohmic contacts to p-type SiC [4]. These contacts, which rely on the combination of a highly-doped surface and the high work function of Pt, have not been known to yield contact resistivities as low as those for contacts containing Al.

B. Experimental Procedure

Vicinal, single-crystal 6H-SiC (0001) wafers provided by Cree Research, Inc. were used as substrates in the present research. The wafers were doped with N or Al during growth to

create n- or p-type material, respectively, with carrier concentrations of $1\text{--}5 \times 10^{18} \text{ cm}^{-3}$. Homoepitaxial layers ($1\text{--}5 \text{ }\mu\text{m}$ thick) grown by chemical vapor deposition (CVD) were Al-doped with carrier concentrations ranging from 1×10^{16} to $1 \times 10^{19} \text{ cm}^{-3}$. The surfaces were oxidized to a thickness of $500\text{--}1000 \text{ \AA}$ in dry oxygen. The substrates were cleaned using a 10 min. dip in 10% hydrofluoric acid, transferred into the vacuum system, and heated at 700°C for 15 min. to remove any residual hydrocarbon contamination.

A UHV electron beam evaporation system was used to deposit the NiAl, Ni, Au, Pt, and Cr-B films. After depositing 1000 \AA of NiAl, $500\text{--}1000 \text{ \AA}$ of Ni was deposited as a passivating layer. Pure Ni (99.99%) and pure Al (99.999%) pellets were arc melted to form alloyed pellets of 50:50 atomic concentration for evaporation of NiAl. The films were deposited onto unheated substrates at a rate of $10\text{--}20 \text{ \AA/s}$. Chromium and B were evaporated simultaneously from separate evaporation sources. The pressure during the depositions was between 5×10^{-9} and 5×10^{-8} Torr.

Circular contacts of $500 \text{ }\mu\text{m}$ diameter were fabricated for electrical characterization by depositing the metal films through a Mo mask in contact with the substrate. Silver paste served as the large area back contact. For contact resistance measurements, TLM patterns [5] were fabricated by photolithography. The Ni/NiAl films were etched in phosphoric acid : acetic acid : nitric acid (12 : 2 : 3) at 50°C (etch rate $\approx 30 \text{ \AA/s}$). The contact pads were $300 \times 60 \text{ }\mu\text{m}$ with spacings of 5, 10, 20, 30 and $50 \text{ }\mu\text{m}$. Mesas in the substrate were not fabricated. All annealing was conducted in a N_2 ambient in a rapid annealing furnace.

Electrical characteristics were obtained from current-voltage and capacitance-voltage measurements. Current-voltage (I-V) measurements were obtained with a Rucker & Kolls Model 260 probe station in tandem with an HP 4145A Semiconductor Parameter Analyzer. Capacitance-voltage (C-V) measurements were taken with a Keithley 590 CV Analyzer using a measurement frequency of 1 MHz.

Auger electron spectroscopy (AES) was performed with a JEOL JAMP-30 scanning Auger microprobe. The films were sputtered with Ar ions at a beam current and voltage of $0.3 \text{ }\mu\text{A}$ and 3 kV, respectively, to obtain composition profiles through the thickness of the films.

C. Results and Discussion

Chemical Characterization of As-deposited Films. An Auger depth profile of a film deposited from the NiAl source showed that the overall composition remained relatively stable. The relative compositions of Ni and Al were calculated by referencing to pure Ni and pure Al standards and accounting for their corresponding sensitivity factors. The average atomic composition was approximately 50:50. With reference to Cr and B standards, the Cr-B film was determined to be comprised of approximately 20% Cr and 80% B (CrB_4). While a thin

oxide layer was detected at the surface of the NiAl film, no O was detected within either of the films.

Schottky Contacts. In the as-deposited condition the Ni/NiAl contacts were rectifying on p-type SiC with carrier concentrations of 1.6×10^{16} and $3.8 \times 10^{18} \text{ cm}^{-3}$ in the epilayer. The sample with the lower carrier concentration displayed leakage current densities of $\sim 1 \times 10^{-8} \text{ A/cm}^2$ at 10 V and ideality factors between 1.4 and 2.4, while the latter sample displayed approximately five orders of magnitude higher leakage current densities and similar ideality factors. The average Schottky barrier heights (SBH's) calculated for the samples with the lower and higher carrier concentrations were 1.37 and 1.26 eV, respectively. The lower SBH calculated for the former sample is likely due to enhanced thermionic field emission through the upper energy region of the barrier because of the narrower depletion region. Hence, the 1.37 eV value is believed to be more accurate.

Similar results were obtained for as-deposited Ni, Au, and Pt contacts on p-type ($2.1\text{--}4.5 \times 10^{16} \text{ cm}^{-3}$) 6H-SiC (0001). These samples displayed similar leakage currents and ideality factors of 1.3–2.1 and <1.1 , respectively. From these measurements SBH's of 1.31 eV for the Ni contacts and 1.27 eV for the Au contacts were calculated. In comparison, as-deposited Ni on n-type ($4.1 \times 10^{16} \text{ cm}^{-3}$) 6H-SiC (0001) yielded ideality factors below 1.1, similar leakage current densities to those stated above, and SBH's of 1.14 eV and 1.21 eV calculated from I-V and C-V measurements, respectively.

Our measurements on p-type SiC have shown consistent differences from measurements on n-type 6H-SiC. The SBH's tended to be higher on p-type than on n-type material. While leakage currents for Au, NiAl, and Ni contacts on p-type 6H-SiC were comparable to Ni contacts on n-type 6H-SiC, the ideality factors were higher on p-type SiC. These ideality factors and SBH's are higher than for Ni contacts (and other previously studied contacts) on n-type 6H-SiC (0001). The higher ideality factors indicates that thermionic emission was not the dominant current transport mechanism in the p-type SiC and may indicate the occurrence of recombination at deep levels.

On the other hand, the relationship between the SBH's of the metals on p-type SiC and their respective work functions was similar to that which we previously found for n-type SiC. The calculated SBH's on p-type SiC are plotted vs. the metal work functions in Fig. 1. The work function for NiAl was taken to be the average of the work functions for pure Ni and pure Al since a value was not found in the literature for NiAl. The slope of the line fit to the empirical data was -0.28 as compared to a slope of -1.0 for the theoretical data. These results indicate that surface states on p-type 6H-SiC (0001) cause a partial pinning of the Fermi level, in agreement with the results of our previous, extensive study on n-type SiC.

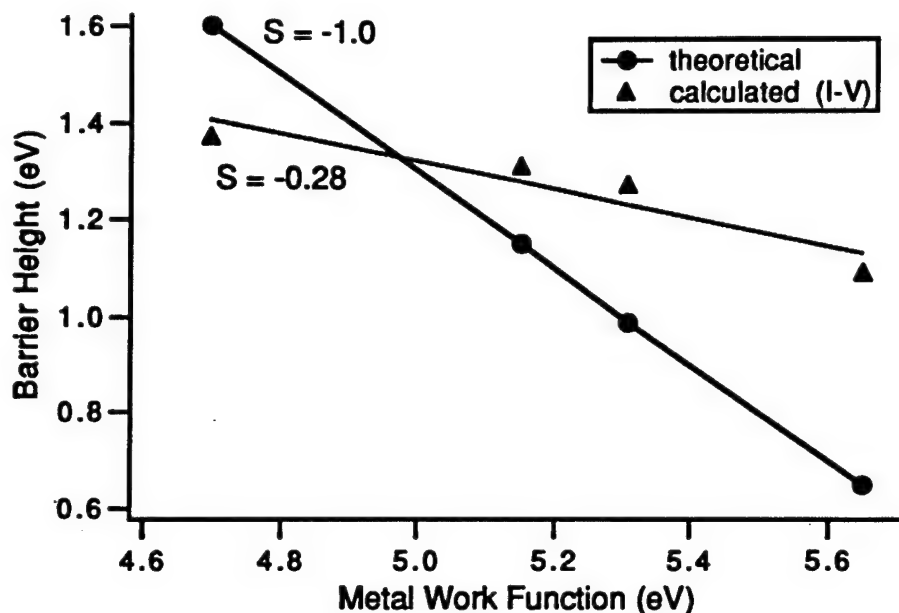


Figure 1. Graph of calculated and theoretical barrier heights of as-deposited NiAl, Au, Ni, and Pt contacts on p-type 6H-SiC vs. metal work function. The calculated values were determined from I-V measurements, and the theoretical values were calculated according to the Schottky-Mott limit. The slopes, S , of the lines fit to each set of data are indicated on the graph.

Ohmic Contacts. The Ni/NiAl contacts were sequentially annealed for total times of 10–80 s at 1000 °C in a N_2 ambient. This temperature was used because (1) limited intermixing of Al and SiC was reported at 900°C [6] and (2) other papers report annealing in this temperature range for Al-based ohmic contacts on p-type SiC [2,3,7]. Because of the extremely high thermodynamic driving force for Al to form an insulating oxide layer ($\Delta G_f(Al_2O_3) \sim -1300$ kJ/mol at 1000 °C [JANAF - Chase, M., et al., JANAF Thermochem. Tables, 3d Ed. J. Phys. Chem. Ref. Data, 1985. 14(Supp. 1)]), 1000 Å of Ni was deposited on top of the NiAl contacts to slow the oxidation process.

Table I summarizes the results of I-V measurements taken at selected intervals through the annealing series for three samples with various carrier concentrations in the SiC epitaxial layer (1.4×10^{18} , 5.7×10^{18} , and 1.5×10^{19} cm^{-3}). The two samples with the lower carrier concentrations were not truly ohmic but became ohmic-like after annealing for 80 s. The additional force on the probes needed to obtain consistent results indicates that an oxide began to form at the surface which would likely cause more severe problems if the samples were annealed further. The sample with the higher carrier concentration was ohmic after annealing for 10 s. The calculated specific contact resistivity remained approximately 2.0×10^{-2} Ωcm^2 through annealing for 60 s. A slight increase to 3.1×10^{-2} Ωcm^2 was calculated after annealing for 80 s. This increase is believed to be due to the surface oxide layer.

Table I. Estimated specific contact resistivities / electrical behavior of Ni (1000 Å) / NiAl (1000 Å) / p-SiC after annealing at 1000 °C for 20, 40, 60, and 80 s for three samples with the carrier concentrations indicated. The specific contact resistivities were calculated from non-mesa etched linear TLM patterns.

Annealing Time	20 s	40 s	60 s	80 s
$1.4 \times 10^{18} \text{ cm}^{-3}$	non-ohmic	non-ohmic	non-ohmic	almost ohmic
$5.7 \times 10^{18} \text{ cm}^{-3}$	non-ohmic	non-ohmic	non-ohmic	almost ohmic
$1.5 \times 10^{19} \text{ cm}^{-3}$	$2.0 \times 10^{-2} \Omega \text{ cm}^2$	$1.9 \times 10^{-2} \Omega \text{ cm}^2$	$2.2 \times 10^{-2} \Omega \text{ cm}^2$	$3.1 \times 10^{-2} \Omega \text{ cm}^2$

An Auger depth profile (Fig. 2b) of Ni/NiAl/SiC annealed at 1000°C for 80 s shows that the surface oxide is thicker than that on the as-deposited sample (Fig. 2a). After sputtering for a couple of minutes, the O concentration dropped to below detectable limits; however, the data shows a decreasing Al concentration in the direction toward the SiC interface. This indicates that the kinetics are more favorable for the Al to diffuse toward the surface and react with O than for the Al to react with the SiC. Some of the Ni has probably reacted with Si at the interface to form a silicide, as indicated by the local maximum in the Ni intensity near the SiC interface, while the peak in the C intensity indicates the presence of an adjacent C-rich layer.

The demonstrated oxidation problem with Al necessitates the development of ohmic contacts which do not consist of substantial concentrations of Al. To reduce this problem we have chosen to investigate contacts which contain B.

The main reasons for choosing B are that it is also a p-type dopant in SiC, its oxide is not as stable, and it is a much faster diffusant in SiC. Table II compares some important properties of B, Al, and their associated oxides. Recent reports [8,9] show that the 'shallow' activation energy for B in SiC is significantly less than previously reported. Boron compounds tend to be more stable at high temperatures than aluminum compounds which suffer from the low melting point of Al. Also, the diffusion coefficient of B is at least three orders of magnitude greater than that of Al. Therefore, more B than Al will diffuse into the SiC at lower temperatures. As discussed in this report, a major problem with Al-based contacts is the strong driving force for forming an insulating oxide layer. This situation is shown by the extremely low equilibrium partial pressure, p_{O_2} , for Al_2O_3 formation. While B_2O_3 also has a low p_{O_2} , it is significantly higher than that for Al_2O_3 , indicating that the driving force for B to form an oxide is significantly lower. There is also a larger number of metals which would reduce the oxide formed with B than that formed with Al, a fact which is encouraging when one is trying to diffuse free B into SiC. Another advantage is that the melting point of boron oxide is notably low.

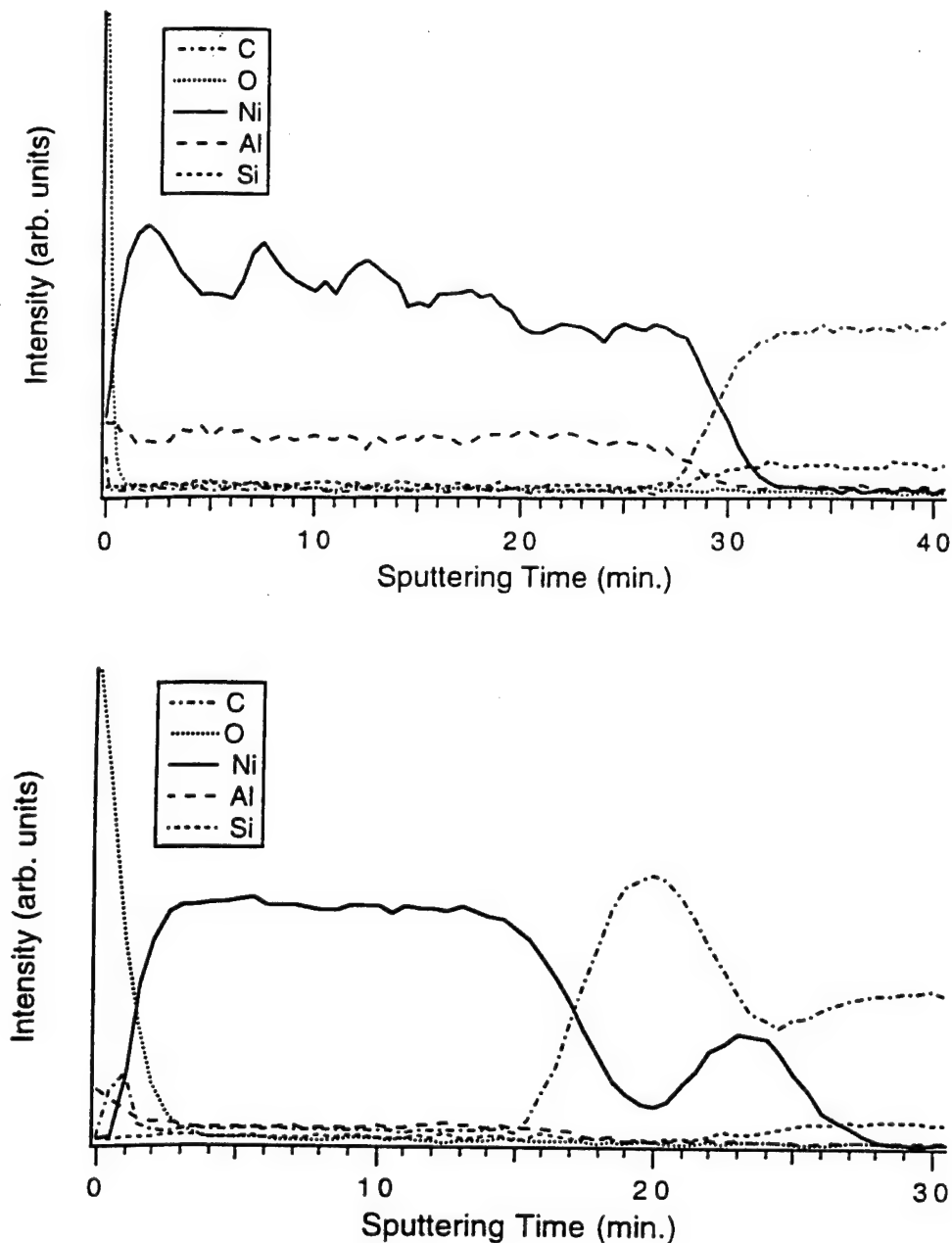


Figure 2. AES composition profile of (a) NiAl (1000 Å) deposited at room temperature on (0001) 6H-SiC and (b) Ni (1000 Å) / NiAl (1000 Å) / 6H-SiC annealed at 1000 °C for 80 s in N₂.

Several boron compounds which possess reasonably low resistivities and high melting temperatures are listed in Table III. We have chosen to investigate Cr-B contacts because of the relative ease to deposit these materials by electron beam evaporation and the demonstrated use of Cr in metallization schemes for diffusion barriers. The refractory nature of these materials increases the probability of forming ohmic contacts which will be stable at high temperatures.

Table II. Selected Properties of B, Al, and Their Associated Oxides

Element	Activation Energy in 6H-SiC (meV)	Solid Source Diffusion, D_{SiC} @ 1800°C (cm ² /s)	Equilibrium partial pressure of O ₂ , pO ₂ @ 700°C (torr)	Melting temp. of the associated oxide, T _{melt} (°C)
B	700	10 ⁻¹¹ [10-11]	10 ⁻³⁵	450
Al	240	<10 ⁻¹⁴ [12]	10 ⁻⁴⁷	2040

Table III. Resistivities and Melting Points of Selected Boron Compounds

Compound	Electrical Resistivity (μΩ-cm) 298 K [13]	Melting Temperature (°C) [14]
CrB ₂	30	2200
GdB ₄	31	2650
MoB	45	2600
NbB ₂	26	3000
TaB ₂	33	3037
VB ₂	23	2747
ZrB ₂	10	2972

Cr and B were simultaneously deposited on p-type 6H-SiC epitaxial layers, some of which had not been oxidized to prevent the reduction of the Al dopant near the surface during oxidation. The carrier concentrations in the epitaxial layers ranged from 1×10^{18} to 8×10^{18} cm⁻³. The as-deposited contacts for the sample with a carrier concentration of 1×10^{18} cm⁻³ displayed rectifying behavior with low leakage currents ($\sim 4 \times 10^{-8}$ at 10 V) and ideality factors between 1.5 and 1.9. Rectification was expected since the contacts had not been annealed, and large SBH's normally exist for as-deposited contacts on p-type SiC.

The samples were annealed at 1000°C for total times varying from 60 to 300 s in an Ar ambient. A subsequent anneal for 60 s at 1100°C in Ar was also performed. After 60 s at 1000°C, the contacts showed substantial changes in their electrical characteristics. The contacts became very leaky, or semi-ohmic. As the annealing time increased, the contacts became more ohmic-like and the resistivity decreased. A slight increase in resistivity of many of the contacts was displayed after annealing at 1100°C. An insulating oxide at the surface, which was a problem after annealing Ni/NiAl/SiC at 1000°C for 60-80 s, has not been a problem during electrical probing of the annealed Cr-B contacts.

D. Conclusions

Nickel-aluminum was investigated primarily as an ohmic contact for p-type 6H-SiC because of the p-type doping of Al in SiC, the high melting point of NiAl (as compared to Al), and the tendency of Ni to form silicides but not carbides. This latter property potentially could have resulted in extraction of Si from the SiC lattice in exchange for Al, thereby enhancing the p-type carrier concentration at the surface. Although the I-V measurements indicate that some Al may be diffusing into the SiC after the longest annealing time performed (80 s at 1000°C), this potential for reaction between Al and SiC appears to be exceeded by the driving force for Al to diffuse to the surface and react with O. A concentration profile obtained from AES analysis shows that Al has diffused through the 1000 Å Ni overlayer to form a thin (200 Å estimated) oxide layer.

In addition to the ohmic behavior resulting from annealing the NiAl contacts, as-deposited Ni, NiAl, and Au contacts deposited at room temperature on p-type ($N_A < 5 \times 10^{16} \text{ cm}^{-3}$) 6H-SiC (0001) were rectifying with low leakage currents, ideality factors between 1.3 and 2.4, and SBH's of 1.31, 1.27, and 1.37 eV, respectively. These results indicate that the Fermi level is partially pinned at p-type SiC surface, in agreement with our previous results on n-type SiC.

As an alternative to Al for fabricating ohmic contacts to p-type 6H-SiC, Cr-B contacts were investigated because of its low resistivity, high melting temperature, and reduced tendency for oxidation of B (compared to that of Al). In the as-deposited condition these contacts were rectifying with low leakage currents. After annealing at 1000 °C for 60 s, the contacts displayed semi-ohmic behavior and became less resistive with successive 60 s anneals to a total time of 300 s. This annealing series will be continued.

E. References

1. D. Alok, B. J. Baliga, and P. K. McLarty, IEDM Technical Digest IEDM 1993, 691 (1993).
2. J. Crofton, P. A. Barnes, J. R. Williams, and J. A. Edmond, Appl. Phys. Lett. 62 (4), 384 (1993).
3. V. A. Dmitriev, K. Irvine, and M. Spencer, Appl. Phys. Lett. 64 (3), 318 (1994).
4. R. C. Glass, J. W. Palmour, R. F. Davis, and L. S. Porter, U.S. Patent No. 5,323,022 (1994).
5. H. H. Berger, Solid State Electron. 15 (2), 145 (1972).
6. V. M. Bermudez, J. Appl. Phys. 63 (10), 4951 (1988).
7. T. Nakata, K. Koga, Y. Matsushita, Y. Ueda, and T. Niina, in *Amorphous and Crystalline Silicon Carbide and Related Materials II*, M. M. Rahman, C. Y.-W. Yang, and G. L. Harris (eds.), Vol. 43, (Springer-Verlag, Berlin, 1989).
8. W. Suttrop, G. Pensl, and P. Lanig, Appl. Phys. Lett. A 51, 231 (1990).
9. W. C. Mitchel, M. Rogh, A. O. Ewvaraye, P. W. Yu, and S. R. Smith, J. Electronic Mater. 25 (5), 863 (1996).
10. E. N. Mokhov, Y. A. Vodakov, G. A. Lomakina, V. G. Oding, G. F. Kholuanov, and V. V. Semenov, Soviet Physics - Semiconductors 6 (3), 414 (1972).
11. G. Pensl and W. J. Choyke, Phys. B 185, 264 (1993).

12. E. N. Mokhov, Y. A. Vodakov, and G. A. Lomakina, *Soviet Physics - Solid State* **11** (2), 415 (1969).
13. C. van Opdorp, *Solid State Electronics* **14**, 613 (1971).
14. G. V. Samsonov and I. M. Vinitskii, *Handbook of Refractory Borides* (Plenum Press, New York, 1980).
15. *Binary Alloy Phase Diagrams, 2nd Edn.*, T. B. Massalski (ed.), (ASM International, Materials Park, Ohio, 1990).
16. R. F. Davis, R. J. Nemanich, M. O. Abeolfotoh, J. P. Barnak, M. C. Benjamin, R. S. Kern, S. W. King, and L. M. Porter, Semiannual Technical Report, Office of Naval Research, Grant #N00014-92-J-1500, June, 1995.

VI. Characterization of Zirconium-Diamond Interfaces

A. Introduction

Negative electron affinity (NEA) surfaces based on wide bandgap semiconductors like diamond could enable the development of cold cathodes. So far n-type doping of diamond remains a major challenge. The electron affinity of a semiconductor corresponds to the energy difference between the vacuum level and the conduction band minimum. Usually the conduction band minimum lies below the vacuum level resulting in a positive electron affinity surface. For wide bandgap semiconductors like diamond the conduction band minimum is likely to be close to the vacuum level. For a NEA surface the electrons from the conduction band minimum have sufficient energy to overcome the surface potential and can be emitted into vacuum. Various surface treatments can induce or inhibit a NEA on diamond surfaces [1-6]. Such treatments include plasma cleaning as well as annealing in ultra high vacuum (UHV). Subsequent to a wet chemical etch the diamond surfaces are terminated by oxygen. This chemisorbed oxygen layer forms a surface dipole that results in an increase in the surface workfunction. It is found that such a surface exhibits a positive electron affinity. For the diamond (100) surface an anneal to 900-1050°C or a H-plasma clean results in a NEA and a 2×1 reconstructed, oxygen free surface [3, 5, 6]. The different threshold temperatures are related to different wet chemical pre-treatments [3]. However for all these treatments a positive electron affinity and a 2×1 reconstruction are observed following a 1150°C anneal [6]. The diamond (100) surface has been proposed to be terminated by a monohydride subsequent to a 900-1050°C anneal or a H-plasma exposure. *Ab initio* calculations for the 2×1 reconstructed surface predict a NEA for a monohydride terminated surface and a positive electron affinity for an adsorbate free surface [5].

Depositing a few Å of a metal like Ti, Ni, Co or Cu on diamond can induce a NEA [7, 8, 9, 10, 3]. The presence of a NEA or positive electron affinity has been correlated with different structures of the metal-diamond interface. Metal-diamond structures with a NEA have been found to exhibit lower Schottky barrier heights than those with a positive electron affinity. Schottky barrier height measurements have been reported for metals deposited on (100), (111) and polycrystalline diamond surfaces [3, 7-20]. No significant dependence of the Schottky barrier height on the metal work function has been found. Lower Schottky barrier heights have been reported for metal films deposited on adsorbate free surfaces than for surfaces terminated by species such as hydrogen or oxygen.

Photoemission spectroscopy is found to be a very sensitive method to distinguish between a NEA or positive electron affinity. Electrons get photoexcited from the valence band into states in the conduction band and can quasi thermalize to the conduction band minimum. Secondary electrons from the conduction band minimum appear as a sharp peak at the low kinetic energy

end of photoemission spectra for NEA surfaces [14, 21]. While photoemission spectroscopy determines the emission properties of the surface itself, field emission data reflect a combination of carrier injection, transport and emission processes. In this study diamond (100) surfaces have been cleaned by anneals to 500°C or 1050°C. Thin Zr films were deposited on these diamond substrates. The surface properties were analyzed before and after Zr deposition.

B. Experimental Procedure

Several natural p-type single crystal semiconducting diamond (100) substrates were used in this study. To remove nondiamond carbon and metal contaminants an electrochemical etch has been employed. Details of this technique have been described earlier [22, 3]. The samples were then loaded into a UHV system consisting of several interconnected chambers featuring capabilities for annealing, metal deposition, ARUPS and AES. Two different *in vacuo* cleaning processes were used to study the effect of surface treatment on the characteristics of the zirconium - diamond interface. One procedure involved annealing the wafers to 500°C for 10 minutes. And the other involved a 1150°C anneal for 10 minutes. The base pressure in the annealing chamber was $\sim 1 \times 10^{-10}$ Torr and rose to $\sim 8 \times 10^{-10}$ Torr and $\sim 7 \times 10^{-9}$ Torr during the anneals, respectively. Subsequent to the anneal a Zr e-beam evaporator was employed to deposit 2 Å thick films. A quartz crystal monitor was used to measure the thickness. During deposition the pressure was $\sim 2 \times 10^{-9}$ Torr. Following each annealing and deposition step, UPS and AES were used to characterize the samples.

The presence of a Zr film was confirmed by means of AES. AFM images of the diamond wafers clearly display linear grooves with a depth of ~ 20 Å. This surface structure is due to polishing the samples with diamond grit. No island structures were observed in AFM measurements after 2 Å of deposition, indicating a uniform 2D layer.

A discharge lamp was employed to excite HeI (21.21 eV) radiation to facilitate the photoemission and a 50 mm hemispherical analyzer with an energy resolution of 0.15 eV was used to detect the emitted electrons. To overcome the workfunction of the analyzer a bias of 2 V was applied to the sample. It was, therefore, possible to detect the low energy electrons emitted from the NEA surface as a sharp peak at the low energy end of UPS spectra. The position of this feature corresponds to the energy position of the conduction band minimum, E_C . Electrons emitted from E_C appear at $E_V + E_G$ in the spectra, where E_V is the energy of the valence band maximum and E_G the bandgap energy. Furthermore, electrons from E_V get photoexcited to an energy level at $E_V + h\nu$ in the conduction band and are obviously detected at $E_V + h\nu$ in UPS spectra. This corresponds to the high kinetic energy end of the spectra. Therefore the spectral width for a NEA surface is $h\nu - E_G$. Using the value of $h\nu = 21.21$ eV for HeI radiation and $E_G = 5.47$ eV for the bandgap of diamond, a spectral width of ~ 15.7 eV is obtained. For a surface with a positive electron affinity the low energy cutoff is determined

by the vacuum level. This results in a smaller value for the spectral width as compared to the case of a NEA.

Photoemission spectra that exhibit features from both the semiconductor and the metal can be used to determine the Schottky barrier height Φ_B (Fig. 1).

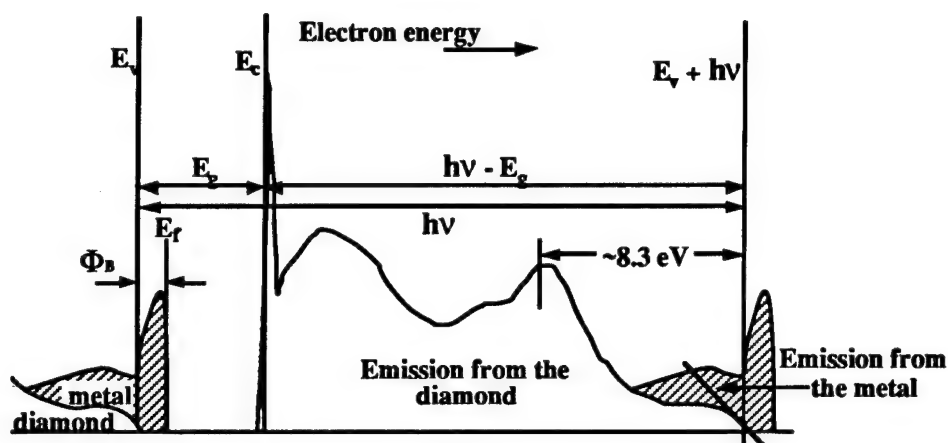


Figure 1. Schematic diagram of photoemission spectra for metal deposited on diamond. The Schottky barrier height Φ_B is determined from the difference between the position of the valence band edge of diamond E_v and the metal Fermi level E_f .

This method is only suitable for metal films with thicknesses equal to or less than the electron mean free path ($\leq 5 \text{ \AA}$). For p-type semiconductors like diamond, Φ_B corresponds to the difference between the position of the valence band edge, E_v , of the semiconductor and the Fermi level of the metal, E_f . But the relatively weak onset of emission at E_v may, however, be obscured by the metal Fermi level even for metal layers thinner than the mean free path. As an independent method E_v can be referenced to some strong features in the diamond spectrum before metal deposition. In our case a feature positioned at 8.3 eV below E_v has been chosen. For a NEA the position of the low energy turnon (which corresponds to E_c) can also be used as a reference to find E_v (which is the high energy turnon of the spectrum). The difference between E_c and E_v has to be $h\nu - E_g$.

The base pressure in the field emission chamber was $\sim 2 \times 10^{-7}$ Torr. To determine the current - voltage characteristics a bias of 0 to 1100V was applied between the sample and a 2 mm diameter platinum anode with a rounded tip. The distances were varied between 2 and 20 μm .

C. Results and Discussion

AES spectra of the as-loaded samples clearly exhibited oxygen peaks. Following a 500°C anneal the oxygen feature was only slightly reduced. Upon heating the samples to 1150°C oxygen could no longer be detected by means of AES. By employing UPS a positive electron

affinity of $\chi \equiv 1.4$ eV and of $\chi \equiv 0.7$ eV were observed for the crystals annealed to 500°C and 1150°C, respectively. These values correspond to previous results [5, 9] Oxygen chemisorbed to diamond is expected to induce a stronger surface dipole and therefore cause an increase in the workfunction compared to a clean surface. Our results are consistent with this. Depositing 2Å of Zr onto oxygen terminated diamond (100) samples resulted in a NEA (Fig. 2a). A Schottky barrier height of $\Phi_B \equiv 0.9$ eV was determined by UPS. Subsequent to deposition of 2Å of Zr on clean diamond (100) surfaces a NEA was observed and the spectrum shifted ~ 0.3 eV toward lower energies (Fig. 2b). A lower Schottky barrier height of $\Phi_B \equiv 0.7$ eV was measured. This structure exhibited emission even below the conduction band minimum E_C . A summary of these results is shown in Table I. The averages and standard deviations of the field emission measurements at different distances are shown as the field emission threshold and the barrier height. The threshold current is 0.1 μ A. (PEA: positive electron affinity, NEA: negative electron affinity.) The electron affinity of a p-type semiconductor following metal deposition is given by equation (1) [21].

$$\chi = (\Phi_M + \Phi_B) - E_G \quad (1)$$

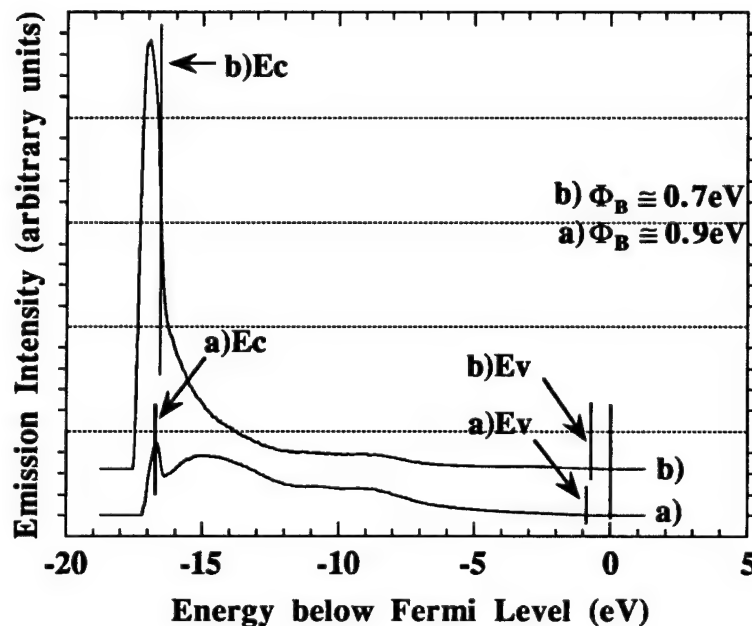


Figure 2. UV photoemission spectra of 2Å of Zr deposited on a diamond (100) surface annealed to a) 500°C b) 1150°C. Metal induced NEA's are observed upon deposition of Zr for both a) and b). For b) emission below E_C is detected.

Using the bandgap of diamond $E_G = 5.47$ eV, the workfunction of Zr $\Phi_M = 4.05$ eV and the measured Schottky barrier heights one can calculate electron affinities of $\chi \equiv -0.52$ eV for the oxygen terminated surface and $\chi \equiv -0.72$ eV for the clean surface. These results are in agreement with the detection of metal induced NEA's by means of UPS. The emission detected below E_C for the clean surface is consistent with the calculated value of $\chi \equiv -0.72$ eV. The fact that no emission below E_C was observed for Zr on oxygen terminated diamond may be due to a different interface structure.

Table I. Results of Electron Emission Measurements.

Sample	UPS	Field Emission Threshold (V/ μ m)	Barrier Height (eV)
C(100)	after 500°C anneal PEA, $\chi \equiv 1.4$ eV	after 1150°C anneal PEA, $\chi \equiv 0.7$ eV	
		79 ± 7	0.23 ± 0.01
Zr/C(100) oxygen	NEA, $\chi < 0$, $\Phi_B \equiv 0.9$ eV	49 ± 4	0.20 ± 0.01
Zr/C(100) clean	NEA, $\chi < 0$, $\Phi_B \equiv 0.7$ eV	20 ± 3	0.09 ± 0.01

This simple workfunction model has been used successfully to explain NEA or positive electron affinity effects for systems like Ti or Ni layers on diamond (111) surfaces [7, 8] and Co or Cu films on diamond (100) surfaces [9, 10]. It has been found that Ni deposited on Ar plasma cleaned diamond (111) substrates induced a NEA. An Ar plasma or a 950°C anneal result in a (111) surface free of adsorbates [4]. In comparison, a positive electron affinity and a larger Schottky barrier were observed for thin Ni films on (111) surfaces terminated by hydrogen. Theoretical results of the Ni - diamond interface have been reported by Erwin and Pickett [24-27] and Pickett, Pederson and Erwin [28]. The most stable configuration for clean (111) and (100) surfaces resulted in a Schottky barrier height of less than 0.1 eV. Lambrecht calculated the Schottky barrier height for copper on diamond (111) surfaces. A value of less than 0.1 eV for a clean surface and greater than 1.0 eV for a surface terminated with hydrogen were found [29]. These results indicate that the Schottky barrier height depends on the interface termination. Lower values for the Schottky barrier height and a greater likelihood of inducing a NEA are expected for metals deposited on clean surfaces than on non adsorbate free surfaces. The Schottky barrier heights reported in this study for Zr on diamond are in agreement with this. It is significant that a metal induced NEA was observed for deposition of Zr on both clean

and oxygen terminated surfaces. Previously a positive electron affinity was found for Ti on a oxygen terminated diamond (100) surface [7]. Ti has a workfunction only 0.3 eV higher than that of Zr. So far only metal diamond interfaces with low workfunction metals like Cs have been reported to exhibit a NEA for non adsorbate free diamond surfaces [30].

Field emission measurements were performed on diamond samples and on Zr films deposited on oxygen terminated and clean diamond surfaces. The emission threshold field was defined for a current of 0.1 μA . Thresholds between 20 and 79 V/ μm were measured. For a summary see Table I. Values of the same magnitude have been reported previously for diamond samples [31, 32]. As an example I-V curves for the diamond surface are shown in Fig. 3. The results from the field emission measurements have been compared to the Fowler-Nordheim equation [33]:

$$I = k \left(\frac{V}{d} \right)^2 \exp \left(\frac{-6530 d \phi^{3/2}}{V} \right) \quad (2)$$

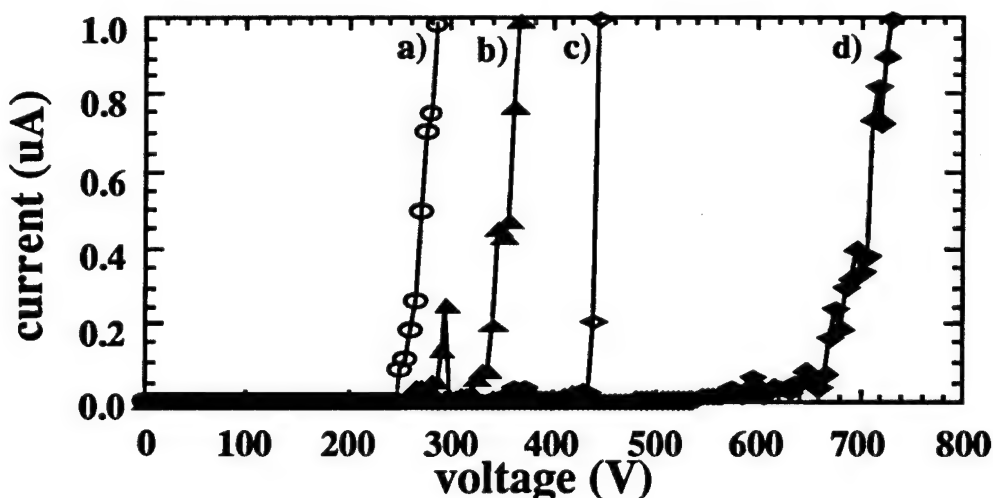


Figure 3. Field emission current - voltage curves for a type IIb single crystal diamond (100) sample. Distances between the sample and the anode: a) 3.3 μm , b) 4.3 μm , c) 5.6 μm , d) 8.5 μm .

I is the current in amps, V is the bias in volts, d is the distance between the sample and the anode in microns, k is a constant and ϕ is the effective barrier height in eV. The field enhancement factor has been neglected since the surfaces have been found to be essentially flat by means of AFM. By fitting the field emission data to equation (2) the effective barrier heights ϕ were obtained as shown in Table I. Depositing Zr onto both oxygen terminated and clean diamond (100) surfaces improves the emission properties. The best results were obtained for Zr on the clean surface. Both UPS and field emission measurements show these trends consistently.

D. Conclusions

Thin films of Zr were grown on diamond (100) surfaces annealed to 500°C or 1150°C. Using UPS the diamond samples were found to exhibit a positive electron affinity after either one of the heat treatments. Metal induced NEA's were observed for Zr deposition on either one of these surfaces. For Zr on clean surfaces emission even below E_C was detected. Depositing Zr on diamond reduced both the field emission threshold and the effective barrier height in a manner consistent with the UPS results.

E. Future Research Plans and Goals

The fabrication and characterization of metal contacts to diamond needs to be studied. The goal is to inject electrons into diamond. Future research will focus towards obtaining a better understanding of the field emission properties. We also plan to incorporate the NEA surfaces into emission devices.

F. References

1. F. J. Himpsel, D. E. Eastman, P. Heimann and J. F. van der Veen, *Phys. Rev. B* **24**, 7270 (1981).
2. B. B. Pate, M.H. Hecht, C. Binns, I. Lindau and W. E. Spicer, *J. Vac. Sci. Technol.* **21**, 364 (1982).
3. P. K. Baumann, T. P. Humphreys and R. J. Nemanich, in *Diamond, SiC and Nitride Wide Bandgap Semiconductors*, edited by C.H. Carter, G. Gildenblat, S. Nakamura, R.J. Nemanich, (Mater. Res. Soc. Proc. **339**, Pittsburgh, PA, 1994) 69-74.
4. J. van der Weide and R. J. Nemanich, *Appl. Phys. Lett.* **62** (1993) 1878.
5. J. van der Weide, Z. Zhang, P. K. Baumann, M. G. Wensell, J. Bernholc and R. J. Nemanich, *Phys. Rev. B* **50** (1994) 5803.
6. P. K. Baumann and R. J. Nemanich, *Proc. of the 5th European Conference on Diamond, Diamond-like and Related Materials*, edited by P. K. Bachmann, I. M. Buckley-Golder, J. T. Glass, M. Kamo: *J. Diamond Rel. Mat.*, **4** (1995) 802.
7. J. van der Weide and R. J. Nemanich, *J. Vac. Sci. Technol. B* **10** (1992) 1940.
8. J. van der Weide and R. J. Nemanich, *Phys. Rev. B*, **49** (1994) 13629.
9. P. K. Baumann and R. J. Nemanich, *Appl. Surf. Sci.*, accepted for publication.
10. P. K. Baumann and R. J. Nemanich, in *Diamond for Electronic Applications*, edited by C. Beetz, A. Collins, K. Das, D. Dreifus, T. Humphreys, P. Pehrsson, (Mater. Res. Symp. Soc. Proc. MRS, Pittsburgh, PA 1996), accepted for publication.
11. P. K. Baumann, T. P. Humphreys, R. J. Nemanich, K. Ishibashi, N. R. Parikh, L. M. Porter and R. F. Davis, *Proc. of the 4th European Conference on Diamond, Diamond-like and Related Materials*, edited by P.K. Bachmann, I. M. Buckley-Golder, J. T. Glass, M. Kamo: *J. Diamond Rel. Mat.* **3** (1994) 883.
12. C. A. Mead and T. C. McGill, *Phys. Lett.* **58A** (1976) 149.
13. F. J. Himpsel, D. E. Eastman and J. F. van der Veen, *J. Vac. Sci. Technol.* **17** (1980) 1085.
14. F. J. Himpsel, P. Heimann and D. E. Eastman, *Sol. State Commun.* **36**, 631 (1980).
15. J. W. Glesener, A. A. Morrish and K. A. Snail, *J. Appl. Phys.* **70** (1991) 5144.
16. M. W. Geis, D. D. Rathman, D. J. Ehrlich, R. A. Murphy and W. T. Lindley, *IEEE Electron Device Lett.* **8** (1987) 341.
17. H. Shiomi, H. Nakahata, T. Imai, Y. Nishibayashi and N. Fujimori, *Jpn. J. Appl. Phys.* **28** (1989) 758.
18. T. Tachibachi, B. E. Williams and J. T. Glass, *Phys. Rev. B* **45** (1992) 11975.

19. M. C. Hicks, C. R. Wronski, S. A. Grot, G. S. Gildenblat, A. R. Badzian, T. Badzian and R. Messier, *J. Appl. Phys.* **65** (1989) 2139.
20. S. A. Grot, S. Lee, G. S. Gildenblat, C. W. Hatfield, C. R. Wronski, A. R. Badzian, T. Badzian and R. Messier, *J. Mater. Res.* **5** (1990) 2497.
21. B. B. Pate, W. E. Spicer, T. Ohta and I. Lindau, *J. Vac. Sci. Technol.* **17** (1980) 1087.
22. M. Marchywka, P. E. Pehrsson, S. C. Binari and D. Moses, *J. Electrochem. Soc.*, **140**, No. 2 (1993) L19.
23. E. H. Rhoderick and R. H. Williams, *Metal-Semiconductor Contacts*, Clarendon, Oxford, (1988).
24. S.C. Erwin and W. E. Pickett, *Surf. Coat. Technol.* **47** (1991) 487.
25. S.C. Erwin and W. E. Pickett, *Solid State Commun.* **81** (1992) 891.
26. W. E. Pickett and S. C. Erwin, *Phys. Rev. B* **41** (1990) 9756.
27. W. E. Pickett and S. C. Erwin, *Superlatt. Microstruct.* **7** (1990) 335.
28. W. E. Pickett, M.R. Pederson and S. C. Erwin, *Mater. Sci. Eng. B* **14** (1992) 87.
29. W. R. L. Lambrecht, *Physica B* **185** (1993) 512.
30. M. W. Geis, J.C. Twichell, J. Macaulay, K. Okano, *Appl. Phys. Lett.* **67** (1995) 1.
31. W. Zhu, G.P Kockanski, S. Jin and L. Siebels, *J. of Appl. Phys.*, in press
32. S. P. Bozeman, P. K. Baumann, B. L. Ward, M. J. Powers, J. J Cuomo, R. J. Nemanich and D. L. Dreifus, *Proc. of the 6th European Conference on Diamond, Diamond-like and Related Materials*, edited by P.K. Bachmann, I. M. Buckley-Golder, J. T. Glass, M. Kamo: *J. Diamond Rel. Mat.* (1996), accepted for publication.
33. R. Gomer, *Field Emission and Field Ionization*, Cambridge, MA, (1961).

Nitrogen-based Materials

VII. Solvent Systems for Solution Growth of Single Crystal Aluminum Nitride

A. Introduction

Aluminum nitride (AlN) in single crystalline form has received considerable interest from many scientists due to its exceptional electronic, optical and piezoelectric properties. In conjunction with its superior bulk properties, single crystal AlN, as a substrate is an important constituent in the ongoing research concerning high-temperature and high-frequency semiconductor devices. In the past three decades, crystal growers have attempted to achieve bulk growth of single crystals of numerous semiconductor compounds via different techniques. Among these methods, the solution growth technique offers a number of advantages over the other techniques for those materials that have extreme melting temperatures and decompose before melting, such as AlN. The solution growth technique enables one to grow crystals at a very low temperature compared to the temperature required for growth from the pure melt. Also, the solution growth is considered the fastest and cleanest way of producing dislocation-free, bulk single crystals.

Solution growth of AlN [1, 2] has been limited by the lack of a solvent that could both dissolve AlN at appreciable rates *and* remain inert to reaction with the container. An extensive experimental study of this method for growing unseeded AlN single crystals has been conducted by Dugger [1, 2] using AlN-Ca₃N₂ solutions contained in graphite crucibles. The solutions were cooled at 2°/hr for 26 hours from 1550°C. Small (1.1 mm long × 0.3 wide) AlN crystals were achieved via nucleation on the walls of the crucible. The most important aspect of this work is that Ca₃N₂ is an effective solvent for AlN with solubilities exceeding 10% at 1200°C. However, it is incompatible with graphite crucibles. Research reported here was performed towards proving the feasibility of this technique; thus, the experimental set-up used is not suitable for solution growth of large boules. To our knowledge, the information presented in this report, with the exception of Ca₃N₂-AlN system, has not been proposed or experimented by another researcher for the same purpose.

B. Experimental Procedure

For compounds with high melting points such as AlN, the flux growth technique can provide an opportunity to grow single crystals of these materials at relatively low temperatures. Solution growth of these materials is also considered the fastest and the cleanest way of producing dislocation-free bulk single crystals. In this technique, saturation of selected reactants is achieved in a solvent which is subsequently cooled to allow precipitation and growth of the desired single crystal phase. For boule growth, good solubility ($\geq 10\%$) of the desired phase in the solvent, inert containers and the ability to continuously supply the source

material to the solvent are necessary. In using the solution growth method, crystal growth can be achieved via three different approaches.

The first route is called the slow-cooling method and can be designated by the route from A to C in Fig. 1. Here the temperature of the solution is decreased from A to B and the crystal growth occurs from B to C. The second route is the temperature gradient transport method where the source is placed in a hot zone (D) and the seed in low temperature zone (E) and crystal growth is achieved at the cooler end. The third route, which is not shown on the phase diagram, is the solvent evaporation method where the solvent is slowly evaporated in order to decrease the solubility of the solute in the solution, thus precipitating out the dissolved material. This route, in reality, follows the pathway of B to C. Our attention of a possible solution growth system is directed towards utilizing the first two methods since in the latter method puts too many constraints on the solvent material.

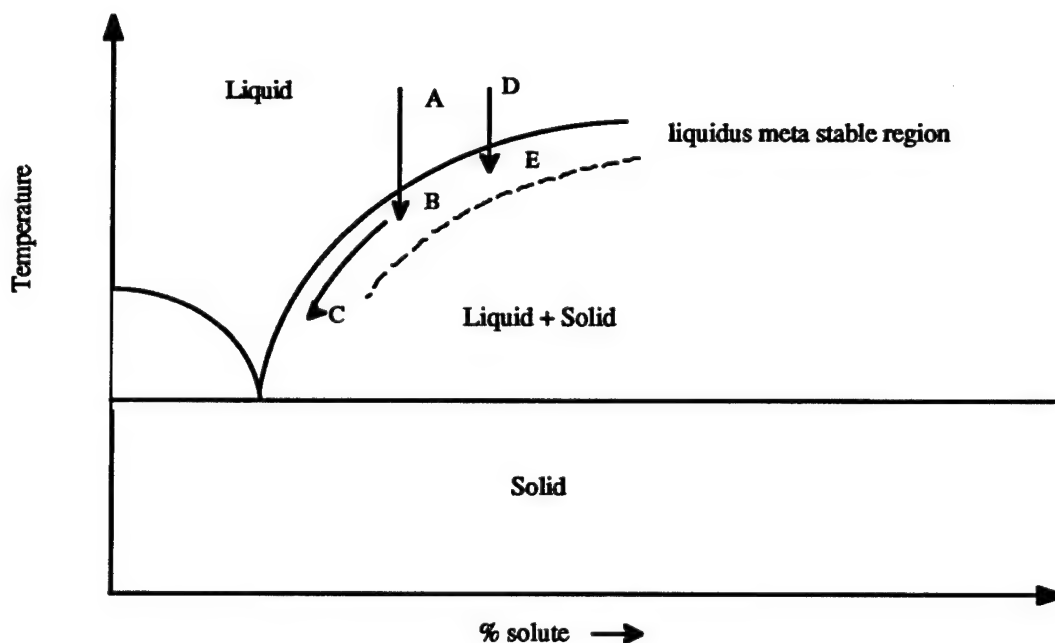


Figure 1. Sketch of crystal growth routes on a binary (or pseudo-binary) phase diagram.

When selecting a flux (solvent) for a high-temperature solution growth process, the following specific properties are desirable:

- the solute and the solvent must be completely miscible, but not form a solid solution;
- the solvent must have a relatively low melting temperature;
- high temperature dependence of solubility;
- a common ion is favorable to prevent contamination;
- low viscosity;
- low pressure;
- melting point must be lower than that of the solute;

- toxicity, expense and purity should also be considered;
- ease of separation after processing;
- compatibility with selected crucible materials; and
- specific to our purposes, a high solubility for aluminum and for nitrogen was also desired.

A basic sketch of a high-temperature solution growth system required for such a study is shown in Fig. 2. Such a configuration will allow studies at precisely-controlled temperatures, temperature gradients and pressures.

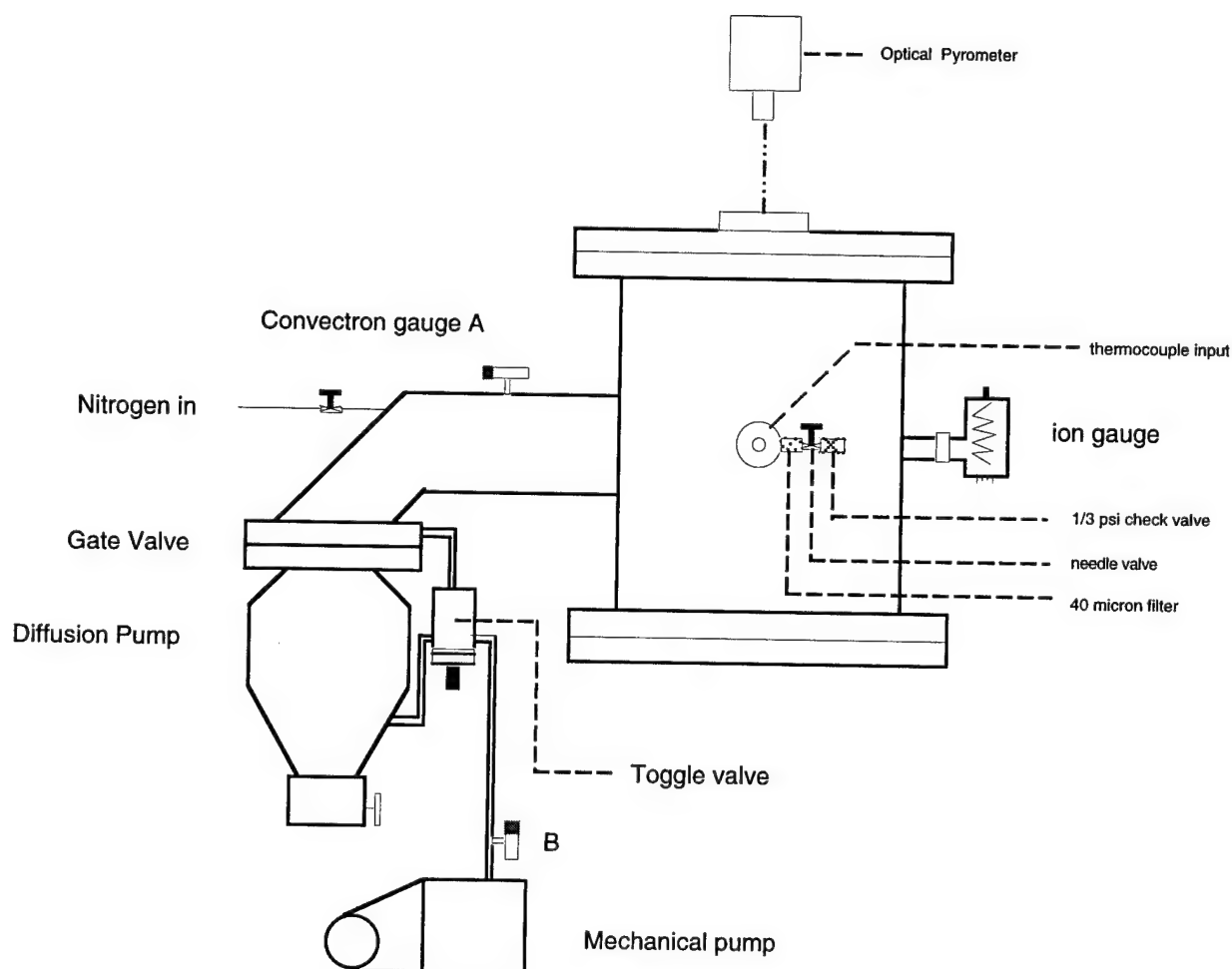


Figure 2. Solution growth system.

Solvents for AlN. We have considered four different categories of solvents that could be used to dissolve AlN: 1) metal solvent systems, 2) nitride systems, 3) binary or ternary oxide systems and, 4) reduction of a nitride in aluminum

Metal solvents have been used extensively in flux growth of many compounds. Metals are especially attractive candidates since most metals satisfy a large number of the requirements

listed earlier and can also be obtained in high purities. Our starting point in searching for a metal solvent was to look for high Al and N solubilities. For this purpose, a large database of ternary and binary phase diagrams [3, 4] was searched. After combining the noted criteria with the results of extensive thermodynamic calculations, as well as other relevant data and experimental studies, it was decided that cerium, yttrium and gadolinium metals have strong possibilities of being used as a solvent for AlN and should be experimented. During the literature search, it was also found that AlN did not have significant solubility in Li [5], Cr, Mo, Fe [6, 7], W, Mn or Re [8].

Instead of using a metal solvent, one can also consider using another nitride compound for the same purpose. The following criteria were considered for selecting nitrides to dissolve AlN: the nitride must be less stable than the nitride that is being grown, have a high solubility for the solute in question, and have relatively low vapor pressure, low viscosity and a low melting temperature. Also, using a nitride is advantageous due to the common nitrogen ion. Among the list of commercially available nitrides with the above factors considered, the following were selected: Ca_3N_2 , Li_3N , Cu_3N and Cr_2N . Revisiting the idea of using Ca_3N_2 by providing remedies to some of the problems noted by Dugger [2], using a seed crystal was also attempted. His studies demonstrated a sufficient solubility of Ca_3N_2 for AlN for boule growth. However, this solvent reacted with all the containers employed. Contact was made with Dr. Dugger and in-depth discussions occurred regarding his studies. Also, to be classified in the nitride solvents, a Li_3N - LiCl system was decided to be investigated. Gentaz *et al.*, have proven that AlN can be dissolved in a molten LiCl - Li_3N system. They observed that a mixture of $\text{Li}_3\text{N}:4\text{LiCl}$ can easily dissolve three moles of AlN.

As reported in several publications, it is possible to achieve a liquid phase in certain AlN-oxide or AlN-oxide-nitride systems when powders of these are mixed at compositions and temperatures in accordance with the phase diagrams [10-12]. A good example is the Al_2O_3 -AlN system [9]. This system was experimented prior to our literature search and formation of a solidified liquid consisting of Al-Si-O-N was observed. AlN and Al_2O_3 were mutually soluble in each other. However, when the pseudo-binary phase diagram [13] is reviewed, it can be seen that there is no phase region designated to L+AlN, which is the essential area for crystal growth. Although no success was made with this system, it reminded us that there could be oxide systems that could offer the liquid to liquid + AlN transition for growing crystals. After an extensive literature search on ternary and binary phase diagrams containing AlN as a constituent, we have distinguished the following system for experimentation.

The Li_2O - Si_3N_4 -AlN system was investigated by Yen and colleagues [15]. The ternary phase diagram determined in this study is presented in Fig. 3.

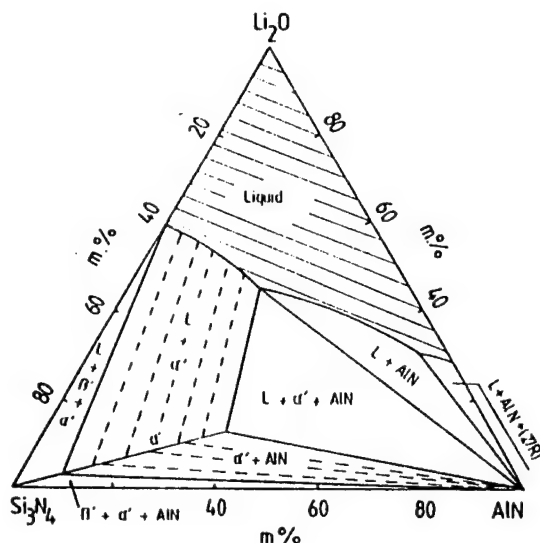


Figure 3. Isothermal section at 1750°C of the Li_2O - Si_3N_4 -AlN system [16].

Investigation of the Si_3N_4 -AlN-CaO system [16] showed a phase relationship at 1700°C as presented in the isothermal section shown in Fig. 4. The L+AlN region in this diagram could be very suitable to grow AlN crystals from a liquid consisting of Si_3N_4 , AlN and CaO.

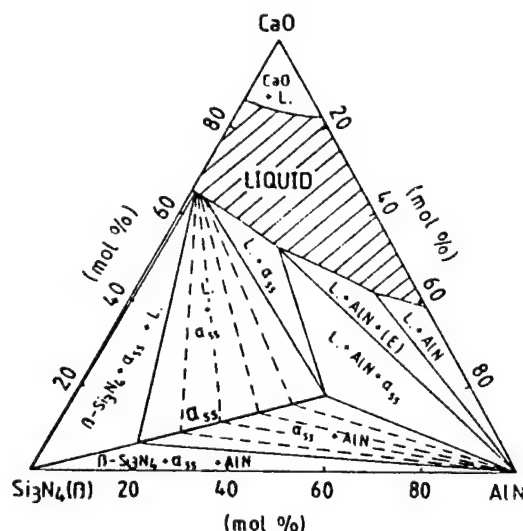


Fig. 4. Isothermal section of Si_3N_4 -AlN-CaO system at 1700°C [16].

SiO_2 -AlN is another system where constituents are soluble in each other and the phase diagram indicates a L+AlN region [17]. According to the quasi-binary phase diagram shown in Fig. 5, AlN and SiO_2 are fully miscible in each other at temperatures above the liquidus line.

Since the phase diagram shown is a calculated phase diagram, there is no sure way of knowing whether the designated phases will ppt in reality. Therefore, the initial step in investigating this system was to confirm the existence of the liquid phase consisting of AlN and SiO_2 .

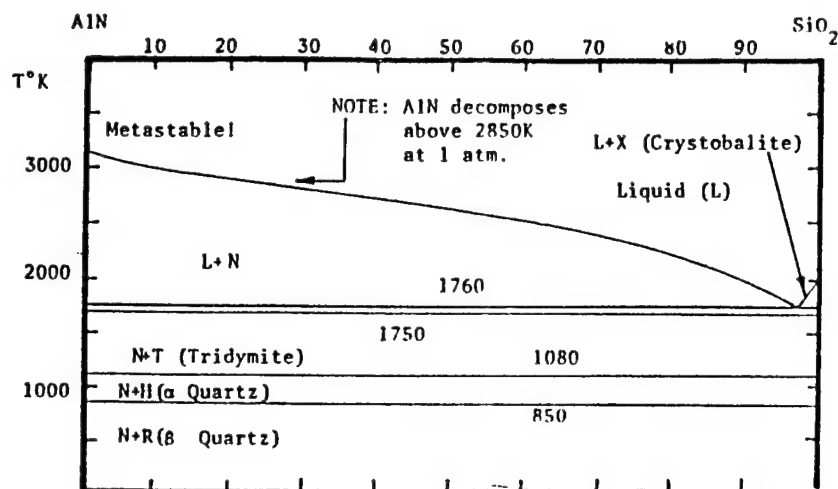


Figure 5. Calculated AlN-Si₂O phase diagram at 1 atm.

Y₂O₃-AlN phase diagram [18] is another calculated pseudo-binary phase diagram in which desired phase regions can be found. This diagram is presented in Fig. 6.

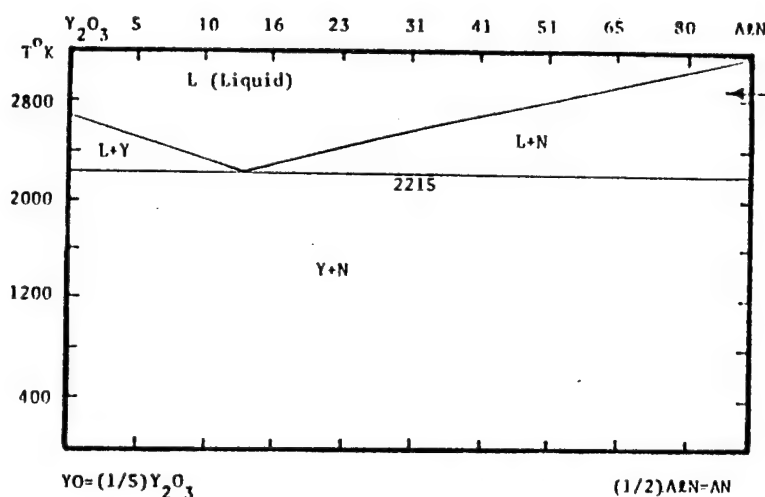


Figure 6. Calculated Y₂O₃-AlN phase diagram at 1 atm.

Crucible Selection. A very important issue in solution growth is the availability of a durable and chemically inert crucible. It has been mentioned by Dugger [2] that lack of having such crucibles caused noticeable problems in his studies. To date, no one has reported a crucible material that is compatible with AlN and the solvent that is experimented. A considerable amount of time was spent on solving this problem for each solution route that is explained above. Free-energy calculations were made for each system in question to select a suitable crucible. Calcium oxide (CaO) crucibles were purchased in the desired shape for this purpose. In the process of determining suitable crucibles for our experiments, the following two graphs (see Figs. 7 and 8) were constructed from the available thermochemical data.

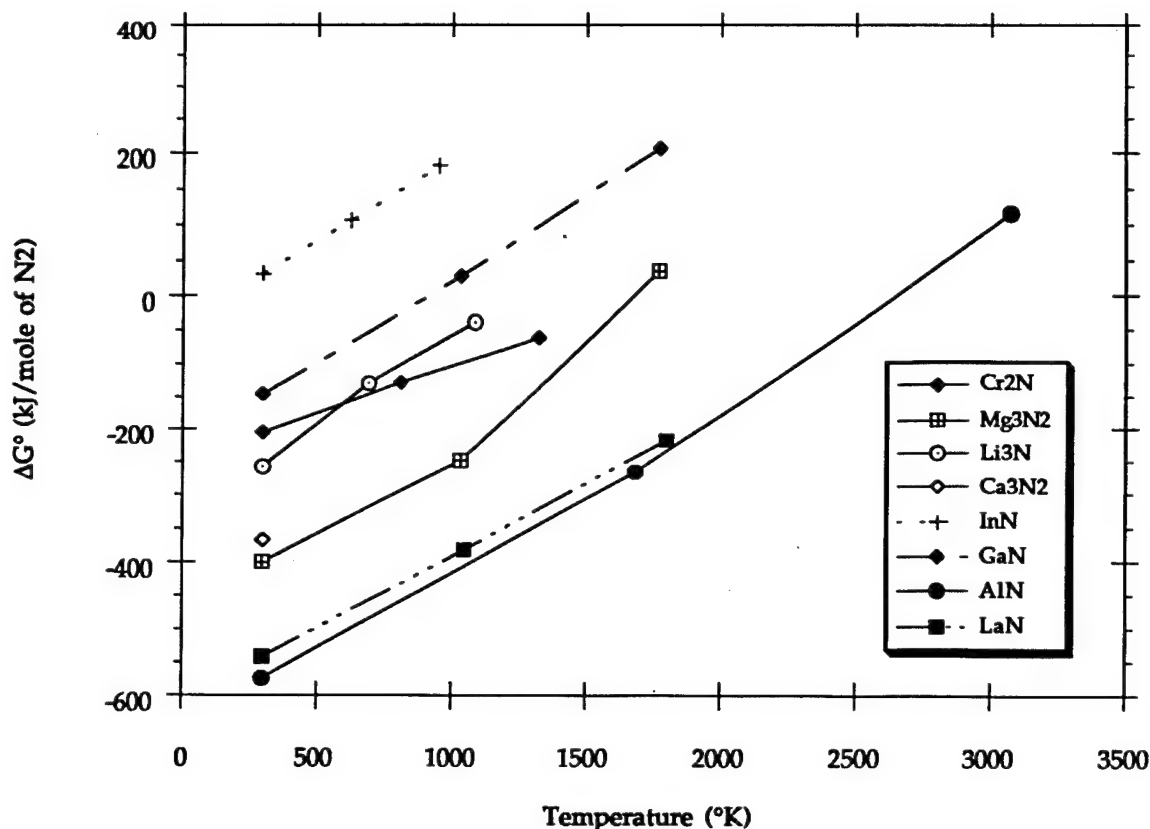


Figure 7. Free energy vs. temperature for various nitrides of interest.

Also, hot pressed AlN crucibles were purchased to be used in some of the solubility experiments. Since CaO crucibles are rather costly to obtain, Fig. 8 can be used to determine for which systems such crucibles are needed.

It is believed that using AlN crucibles would be advantageous in systems where the exact composition of the mixture is not known. If the solution can dissolve more AlN than was mixed in powder form, then it would be able reach saturation for a given temperature by dissolving the crucibles. By this course of thinking, any solvent considered can easily be tested by heating it in AlN crucibles. Since the surfaces of crucibles were relatively smooth prior to experiments, any attack can easily be seen.

C. Results and Discussion

Similar experimental procedures were used to investigate the following systems. Due to the hygroscopic nature of the powders used and to obtain good particle to particle contact, powders were cold pressed into pellet form in a glove box. After cold pressing, pellets were loaded into the solution system in which they were dried at 150°C under vacuum. Usually, samples were left under vacuum overnight until the system's base pressure was reached. After the system was backfilled with ultra high purity N₂, desired time-temperature recipes were implemented.

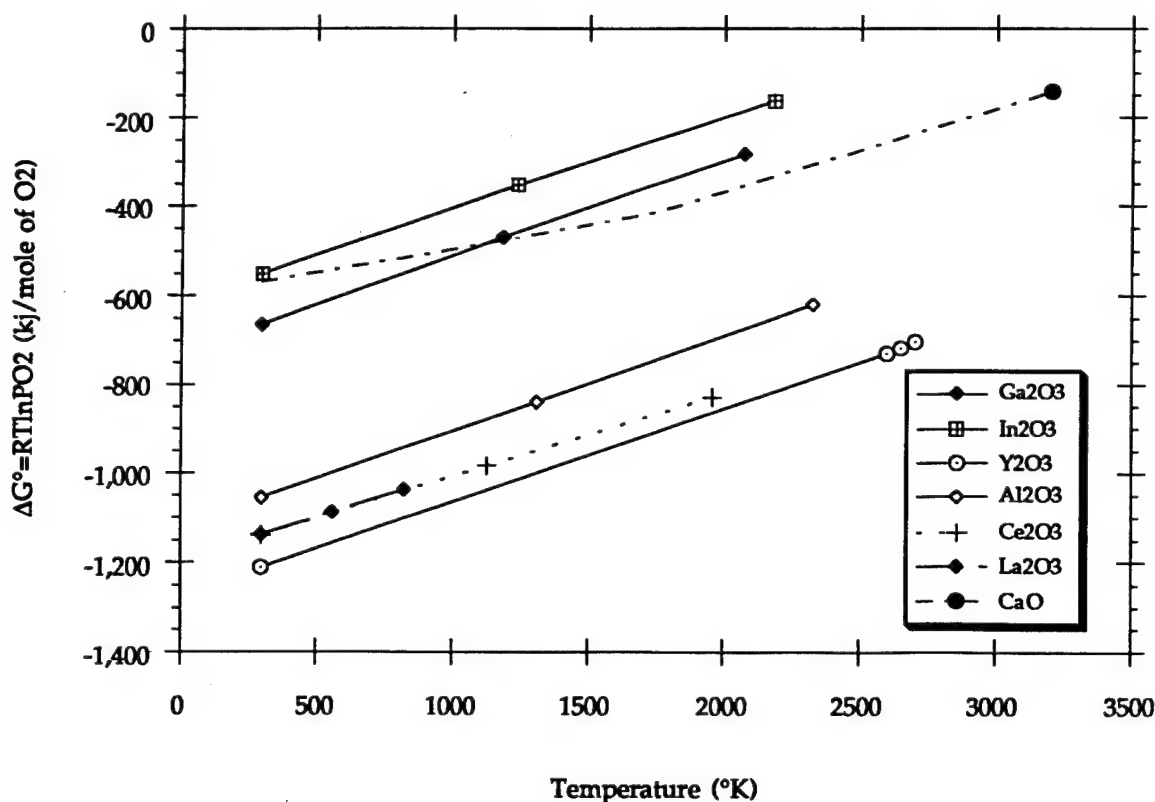


Figure 8. Free energy vs. temperature for various oxides of interest.

Metals. Yttrium, gadolinium and cerium rare earth metals were experimented as possible solvents. These metals were melted in AlN crucibles for prolonged periods of time. The melt was then slowly cooled to allow any AlN that might have been dissolved to precipitate out. Later the solidified melt was dissolved by an acid that only reacted with the metal. After this procedure, AlN crucibles were carefully examined under an optical microscope. No damage was observed on the crucibles, which indicates that AlN was not dissolved by any of the rare earth metals.

Nitrides. After extensive thermodynamical calculations, a suitable crucible material was found to be used. Due to Ca_3N_2 's high vapor pressure at the growth temperatures and its highly hygroscopic nature, our attempts to use Ca_3N_2 as a flux failed. Since the CaO crucibles used were not machinable into shapes that can be sealed, an essential amount of Ca_3N_2 was lost during experiments. The experimental procedure used was similar to that pursued in Dugger's work. For this compound to be used as a flux, excessive evaporation must be prevented.

As stated earlier, experiments involving the LiCl-Li₃N-AlN system were based on the initial work done by Gentaz *et al.*, [14]. A mixture of 55 %wt LiCl, 20 %wt Li₃N and 25 %wt of AlN was cold pressed into pellets. These pellets were then loaded into molybdenum (Mo) crucibles and heated up to 950°C. The melt was then cooled down to room temperature in three hours. The solidified melt was found to be fully soluble in water which suggested that no AlN

crystals had deposited. Also, the hot pressed piece of AlN placed in the crucible was not attacked by the melt. It is believed that these experiments should be repeated under much slower cooling rates.

Binary or Ternary Oxide Systems. To study the SiO₂-AlN system, pellets with 4:1 weight ratio of SiO₂ to AlN were prepared and cold pressed. After the drying step described above, the mixture was then heated up to 2000°C in boron nitride (BN) crucibles and soaked at this temperature for 1 hr. Rapidly-cooled samples were then analyzed by X-ray diffraction. Prior visual examination showed that the pellets had indeed melted and formed a liquid phase mixture. No weight loss was detected due to evaporation of either species. X-ray pattern obtained from the solidified mixture was believed to represent that of a Si-Al-O-N compound of unknown composition since it did not show any resemblance to AlN or SiO₂ diffraction patterns. This result was also confirmed by heating fully dense solid shapes of AlN and SiO₂. It was again observed that a melt mixture forms at temperatures above 1900°C.

The next step was to design and execute a crystal growth experiment in which the solution is slowly cooled across the L+N region. For this experiment, the mixture was solutionized at 2000°C for 2 hrs and then cooled down to 1400°C with a temperature gradient of 10°C/hr. Since the phase diagram taken as basis was theoretically drawn, hot pressed AlN crucibles were used in order to ensure saturation of the solution with respect to AlN. Small, needle-like, transparent crystals were grown on the outer face of the AlN crucible. These crystals are currently being analyzed to determine their composition.

To study Li₂O-Si₃N₄-AlN, Si₃N₄-AlN-CaO and Y₂O₃-AlN systems, cold pressed pellets at desired compositions have already been prepared and experiments will be performed in the near future.

D. Summary and Future Work

The results of the solution growth experiments and the future work that needs to be done are summarized in Table I.

It should be noted that due to time spent on alternative bulk growth techniques and the detailed nature of the experiments, not all of the suggested solvents were examined. However, all systems will be tested and reports will be upgraded accordingly.

E. References

1. C. O. Dugger, *Mat. Res. Bull.* **9**, 331 (1974).
2. C. O. Dugger, Air Force Report, AFORL-TR-75-0486, Hanscom AFB Massachusetts, (1975).
3. *The Handbook of Binary Phase Diagrams*, W.G. Moffatt, Genium Publishing Corp., (1990).
4. *Ternary Alloys, A Comprehensive Compendium of Evaluated Constitutional Data and Phase Diagrams*. New York, N.Y., USA: VCH, c1988.
5. H. Migge, *J. Nucl. Mat.* **105**, 655 (1982).

Table I.

	Solvent	Melting Point °C	Compatible Crucible	Remarks
Metals	Yttrium	1522	SiC	unsatisfactory
	Cerium	798	SiC(?)	unsatisfactory
	Gadolinium	1313	BN, SiC	unsatisfactory
Nitrides	Ca ₃ N ₂	1195	CaO, Pt	to be experimented
	Li ₃ N	850	Al ₂ O ₃ , MgO, CaO, Pt, ZrO ₂	to be experimented
	Cu ₃ N	300	" " " "	to be experimented
	Cr ₂ N	1700	Al ₂ O ₃ , Pt	to be experimented
	LiCl-Li ₃ N-AlN	950	Mo, BN, AlN	in progress
Oxide systems	Li ₂ O-Si ₃ N ₄ -AlN	1750<	BN, AlN	to be experimented
	Si ₃ N ₄ -AlN-CaO	1700<	BN, AlN	to be experimented
	AlN-Si ₂ O	1500<	BN, AlN	in progress
	Y ₂ O ₃ -AlN	2125<	BN, AlN	to be experimented
	Na ₃ AlF ₆	1200	Mo	unsatisfactory

6. H. Wada and R. Pehlke, Metall. Trans. B 9B, 441 (1978).
7. M. Hillert and S. Jonsson, Metall. Trans. A 23A, 3141 (1991).
8. J. C. Schuster and H. Nowotny, J. Mater. Sci. 20, 2787 (1985).
9. I. Adams, T. R. AuCoin, G. A. Wolff, J. Electrochem. Soc. 109 (11), 1050 (1962).
10. J. M. Lihrmann, J. Am. Ceram. Soc. 72 (9), 1704 (1989).
11. T. S. Yen, *et al.*, J. Mater. Sci. Lett. 9, 69 (1990).
12. T. S. Yen, *et al.*, J. Am. Ceram. Soc. 74 (11), 1704 (1991).
13. N.D. Corbin, J. Eur. Cer. Soc. 5, 143 (1989).
14. C. Gentaz, *et al.*, J. Electrochem. Soc. 120 (1), 102 (1982).
15. T. S. Yen, *et al.*, J. Mater. Sci. Lett. 9, 72 (1990).
16. D. S. Yan, *et al.*, J. Mater. Sci. Lett. 4, 255 (1985).
17. L. Kaufman, CALPHAD, 3 (4), 275 (1979).
18. L. Kaufman, CALPHAD, 5 (3), 163 (1981).

VIII. Growth, Doping and Characterization of $\text{Al}_x\text{Ga}_{1-x}\text{N}$ Thin Film Alloys on 6H-SiC(0001) Substrates

M. D. Bremser, W. G. Perry, T. Zheleva, N. V. Edwards, O. H. Nam, N. Parikh*, D. E. Aspnes**, and R. F. Davis

North Carolina State University, Department of Materials Science and Engineering,
Box 7909, Raleigh, NC 27695-7907

*University of North Carolina at Chapel Hill, Department of Physics and Astronomy,
Box 3255, Chapel Hill, NC, 27599-3255

**North Carolina State University, Department of Physics,
Box 8202, Raleigh, NC 27695-8202

ABSTRACT

Thin films of $\text{Al}_x\text{Ga}_{1-x}\text{N}$ ($0.05 < x < 0.96$) having smooth surfaces were deposited directly on both vicinal and on-axis 6H-SiC(0001) substrates. Cross-sectional TEM of $\text{Al}_{0.13}\text{Ga}_{0.87}\text{N}$ revealed stacking faults near the SiC/nitride alloy interface and numerous threading dislocations. EDX, AES and RBS were used to determine the compositions, which were paired with their respective CL near band-edge emission energies. A negative bowing parameter was determined. The CL emission energies were similar to the bandgap energies obtained by SE. FE-AES of the initial growth of $\text{Al}_{0.2}\text{Ga}_{0.8}\text{N}$ revealed an aluminum rich layer near the interface. N-type (silicon) and p-type (magnesium) doping was achieved for $\text{Al}_x\text{Ga}_{1-x}\text{N}$ for $0.12 \leq x \leq 0.52$ and $x \leq 0.13$, respectively. Superlattices of $\text{Al}_{0.2}\text{Ga}_{0.8}\text{N}/\text{GaN}$ were fabricated with coherent interfaces. Additionally, HEMT structures using an $\text{AlN}/\text{GaN}/\text{AlN}$ buffer structure were fabricated.

A. Introduction

The potential and employment of III-nitride materials for both optoelectronic and microelectronic applications has stimulated significant research [1]. The wurtzitic phase of GaN forms continuous solid solutions with InN and AlN such that bandgap engineering is possible from 1.95 eV to 6.2 eV. When alloyed solely with AlN, materials having bandgaps from 3.4 eV to 6.2 eV are possible. This makes $\text{Al}_x\text{Ga}_{1-x}\text{N}$ attractive for both ultraviolet emitters and detectors, as well as high-power and high-frequency microelectronic applications.

Single crystal GaN substrates are currently available in very limited quantities only via high-pressure, high-temperature processes [2]. As such, heteroepitaxy is the dominant growth process, and c-plane sapphire is the most commonly employed substrate. In order to accommodate the large lattice mismatch between GaN and sapphire, nitridation of the latter followed by the deposition of a low temperature amorphous GaN or AlN buffer layer is conducted prior to GaN film growth [3, 4]. This buffer layer is subsequently annealed to form a textured polycrystalline template upon which the GaN is deposited. Grain orientation competition in the GaN film occurs during the first 0.5 microns of growth which results in the formation of low angle grain boundaries which persist throughout the entire epitaxial layer [5, 6]. Substantial concentrations of threading dislocations exist near the film/buffer layer interface, some of which are annihilated by intersection within the film. As such, the growth of 3 to 4 microns of material is usually necessary to achieve "device quality" epitaxy.

In contrast, it has been shown that monocrystalline AlN can be deposited epitaxially on 6H-SiC(0001) at temperatures $>1050^\circ\text{C}$ [7, 8]. Use of a 1000Å AlN buffer layer deposited at 1100°C has been demonstrated to be an effective buffer layer [7, 8]. Subsequent GaN epitaxy also contains random threading dislocations but is free of low angle grain boundaries. Since conductive AlN has yet to be demonstrated, this buffer layer prohibits the effective use of the conductive SiC for the formation of backside contacts. Hence, the use of a conductive $\text{Al}_x\text{Ga}_{1-x}\text{N}$ as a buffer layer appears to hold more promise. In this research, the deposition, doping and characterization of $\text{Al}_x\text{Ga}_{1-x}\text{N}$ thin films growth directly on 6H-SiC(0001) wafers has been extensively studied and will be reported in the following sections.

B. Experimental Procedures

Thin films of $\text{Al}_x\text{Ga}_{1-x}\text{N}$ were deposited at $1050\text{--}1150^\circ\text{C}$ and 45 Torr in a cold-wall, vertical, pancake-style, RF inductively heated, OMVPE system using various ratios of triethylaluminum (TEA) and triethylgallium (TEG) in combination with 1.5 SLM of ammonia (NH_3) and 3 SLM of H_2 diluent. The total metalorganic precursor flow rate was $32.8\text{ }\mu\text{mol/min}$. Donor and acceptor type doping was accomplished by the addition of SiH_4 and Cp_2Mg , respectively. Additional experimental parameters are described elsewhere [7, 8].

The structural, microstructural, optical and electrical characteristics of the epitaxial $\text{Al}_x\text{Ga}_{1-x}\text{N}$ thin films were analyzed using several techniques. Scanning electron microscopy (SEM) was performed using a JEOL 6400FE operating at 5 kV and equipped with an Oxford Light Element Energy Dispersive X-ray (EDX) Microanalyzer. Conventional and high resolution transmission electron microscopies (TEM) were conducted using a Topcon EM-002B microscope operating at 200 kV. Double-crystal x-ray rocking curve (DCXRC) measurements were made on a Philips MR3 thin films diffractometer. Atomic Force Microscopy (AFM) was performed on a Digital Instruments Dimension 3000. The catholuminescence (CL) properties of the $\text{Al}_x\text{Ga}_{1-x}\text{N}$ films were determined at 4.2 K using a Kimball Physics EMG-14 electron gun as the excitation source. Spectroscopic ellipsometry (SE) was performed using a rotating analyzer ellipsometer with a xenon arc lamp (1.5 eV–5.75 eV). Capacitance-Voltage (CV) measurements were conducted using a MDC Model CSM/2-VF6 equipped with a mercury probe. Standard and field emission Auger electron spectroscopies (AES and FE-AES) were conducted using Perkin-Elmer Models 660 and 670, respectively, equipped with Zalar rotation. Rutherford backscattering analysis (RBS) was performed using 1.9 MeV He^+ ions with the detector at an angle of 165° .

C. Results and Discussion

Thin films of $\text{Al}_x\text{Ga}_{1-x}\text{N}$ ($0.05 < x < 0.96$) were deposited directly on both vicinal and on-axis 6H-SiC(0001) substrates. As shown in Figs. 1 and 2, films having $x < 0.5$ and deposited at 1100°C had smooth, featureless surfaces. SEM also revealed that, like GaN, smoother films were deposited on the on-axis substrates than on the vicinal ones. The surfaces of films with $x > 0.5$ were also very smooth but with occasional pits which increased in density with increasing Al composition. The occurrence of pits likely indicates the lack of surface mobility of the metal adatoms such that complete crystallographic coalescence of the two dimensional flat-top islands is inhibited [7, 8]. In order to eliminate this problem, deposition of the $\text{Al}_x\text{Ga}_{1-x}\text{N}$ for $x > 0.5$ was conducted at 1150°C . The resulting films possessed smooth surfaces which were free of pits; however, the growth rate decreased by more than a factor of three. Therefore, deposition in the range of $1120\text{--}1130^\circ\text{C}$ is likely optimum for our system for these higher AlN concentrations.

The compositions of the films grown under different conditions were determined using EDX, AES and RBS. Standards of AlN and GaN grown in the same reactor under similar conditions were used for the EDX and AES analyses. Compositions were assigned to each film after careful consideration of the errors (± 2 at.%) involved with each technique. The data from EDX and AES measurements showed excellent agreement. The RBS data did not agree as well with the other two techniques, due to small compositional variations through the thickness of

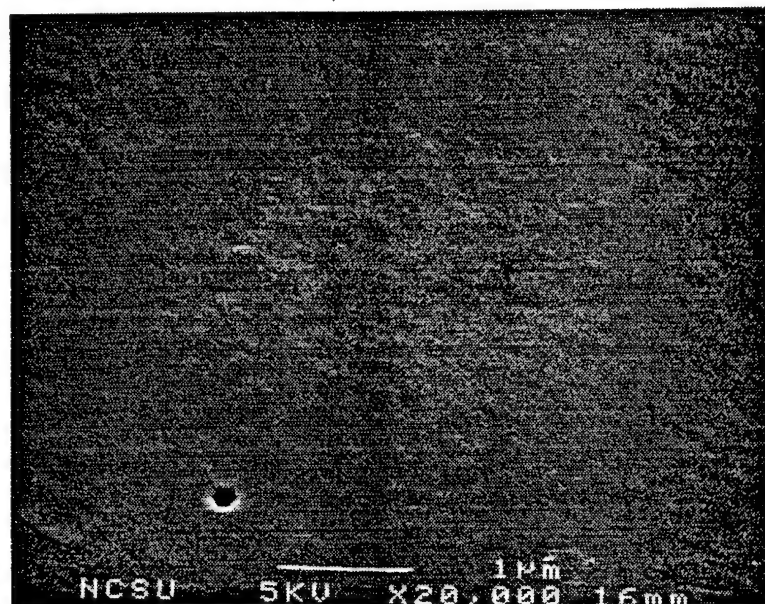


Figure 1. SEM micrograph of a 0.5 μm $\text{Al}_{0.41}\text{Ga}_{0.59}\text{N}$ film deposited directly on a vicinal 6H-SiC (0001) substrate.

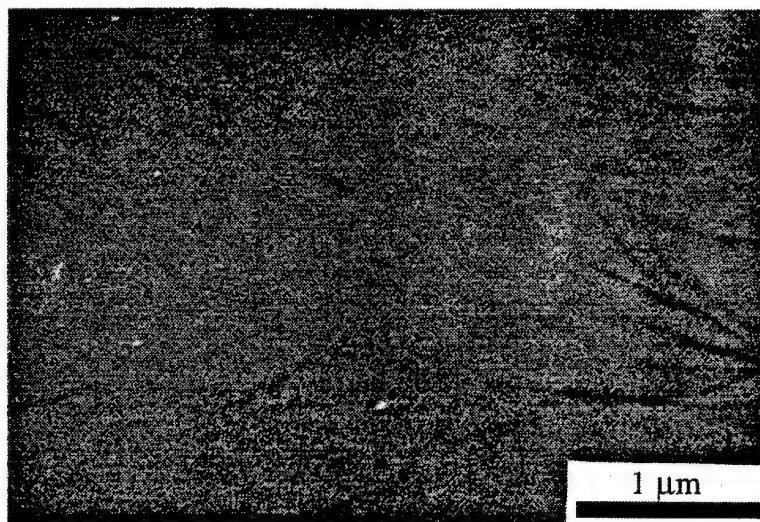


Figure 2. SEM micrograph of a 0.8 μm $\text{Al}_{0.13}\text{Ga}_{0.87}\text{N}$ film deposited directly on an on-axis 6H-SiC (0001) substrate.

the film. Simulation of the compositions determined by RBS was conducted only for the surface compositions. Analysis via EDX revealed that the $\text{Al}_x\text{Ga}_{1-x}\text{N}$ grown on the on-axis SiC substrates tended to be 1-2 atomic percent more Al rich than those grown off-axis SiC. It is thought that the presence of steps on the growth surface promotes the adhesion of the gallium adatoms.

In Fig. 3, these compositions are compared with their respective CL near band-edge emission energies. Additionally, in Fig. 4, the CL emission peaks are compared with bandgap values obtained by SE. Using a parabolic model, the following relationships describe the CL peak emission (I_2 -line emission) (Eq. 1) as a function aluminum mole fraction for $0 < x < 0.96$.

$$E_{I_2}(x) = 3.50 + 0.64x + 1.78x^2 \quad (1)$$

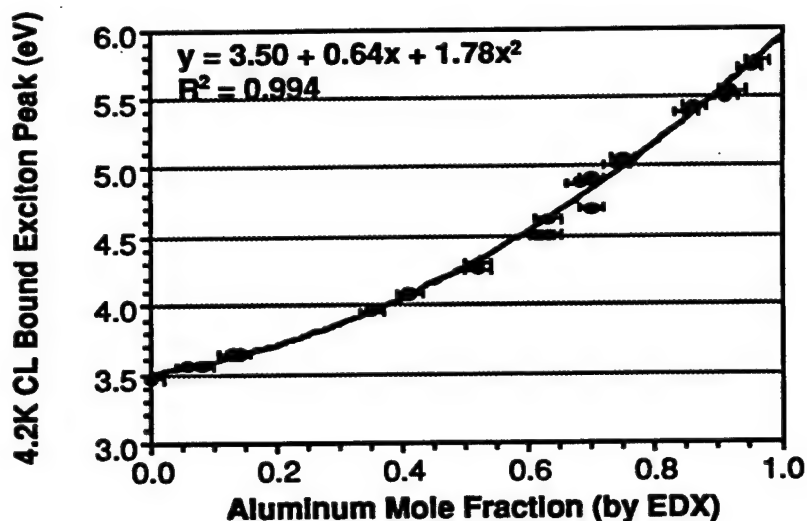


Figure 3. The relationship between aluminum mole fraction and 4.2K CL near band-edge emission from AlGaIn thin films deposited directly on vicinal and on-axis 6H-SiC (0001) substrates.

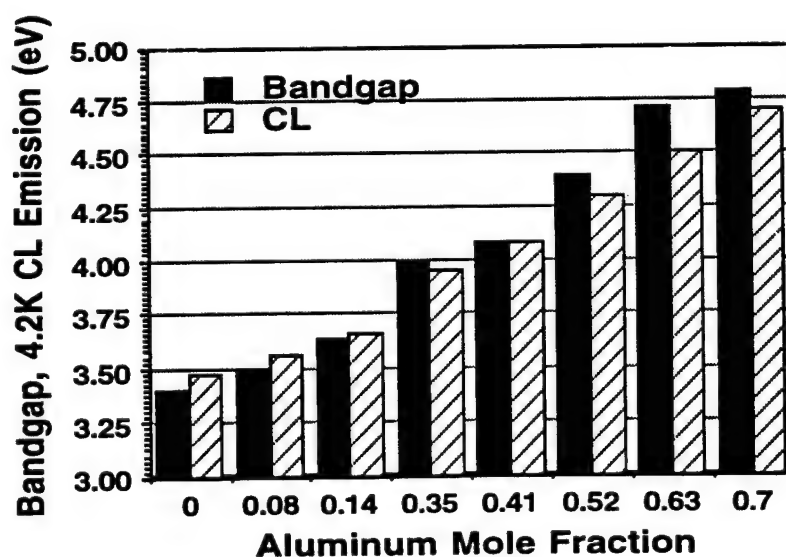


Figure 4. Comparison of 4.2K CL near band-edge emission and bandgap as determined by spectroscopic ellipsometry at room temperature.

Clearly, the model of the measurements shows a negative deviation from a linear fit. This is in agreement with earlier research by other investigators [9-11]. However, these films are highly strained due to incomplete relaxation of the tensile stresses generated by the differences in the coefficients of thermal expansion. The effect of strain has yet to be quantified. It should be noted that other researchers have seen a linear relationship between composition and absorption edge for thick or relaxed films on sapphire [12, 13]. Comparison of the CL spectra of $\text{Al}_{0.12}\text{Ga}_{0.88}\text{N}$ grown on a pre-deposited 1000\AA AlN buffer layer which is used for GaN deposition versus growth directly on 6H-SiC reveals a 75 meV red shift for the latter films (Fig. 5). This indicates that the films deposited directly on SiC are in greater tension than the ones deposited using an AlN buffer layer. Furthermore, there is a noticeable decrease in the defect peak centered around 3.2 eV. The reason for the reduction in this peak is unclear at this time and is under investigation.

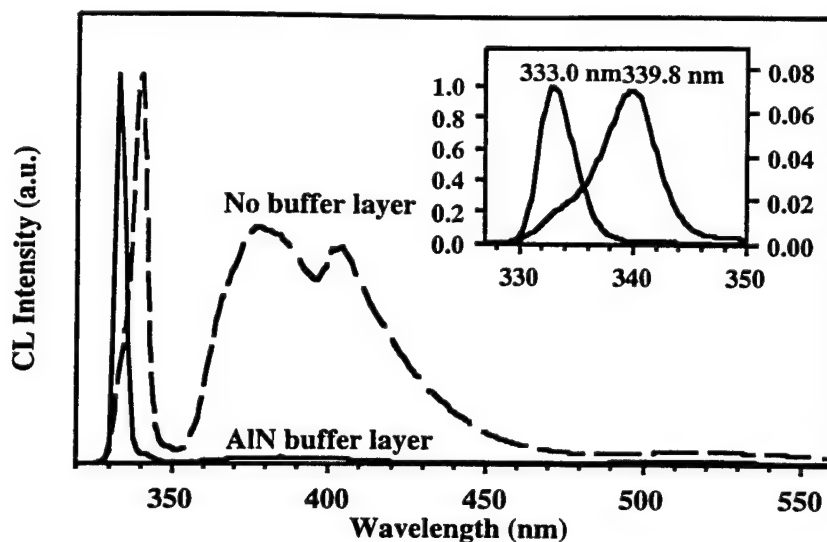


Figure 5. Comparison of 4.2K CL spectra of $\text{Al}_{0.12}\text{Ga}_{0.88}\text{N}$ deposited directly on 6H-SiC and using a 1000\AA AlN buffer layer.

The low temperature (4.2K) CL of undoped $\text{Al}_x\text{Ga}_{1-x}\text{N}$ films containing up to 0.96 mole fraction of aluminum exhibited near band-edge emission which has been attributed to an exciton bound to a neutral donor (I_2 -line emission) [14]. For increasing concentrations of aluminum, this emission became gradually weaker. No emission was observed for pure AlN other than a broad peak centered around 3.1 eV which previous researchers attribute to oxygen [15-17]. The most narrow near band-edge CL FWHM was 31 meV for $\text{Al}_{0.05}\text{Ga}_{0.95}\text{N}$. This value increased with aluminum concentration to a maximum of approximately 100 meV for $\text{Al}_{0.5}\text{Ga}_{0.5}\text{N}$. For higher aluminum compositions, this value did not increase. The broadening of the exciton features is likely due to both exciton scattering in the alloy, as well as small

variations in alloy compositions in the film. Additionally, two strong defect peaks were present at energies less than the band gap. Both of these features have been previously attributed to donor-acceptor transitions. The first peak is centered around 2.2 eV for GaN and is commonly associated with deep levels in the bandgap [18]. As shown in Fig. 6, these emissions changed sublinearly with changing composition. The nature of this behavior is under investigation. The second defect peak is centered around 3.27 eV which is attributed to a transition between a shallow donor and a shallow acceptor [19], and its position also changes sublinearly with increasing aluminum concentration, as shown in Fig. 7. This sublinear shift is attributed to the donor state moving deeper into the gap. For $\text{Al}_{0.05}\text{Ga}_{0.95}\text{N}$, the donor to acceptor pair (DAP) and its two LO-phonon replicas typically seen in GaN are still resolved, but for higher aluminum compositions, these peaks become one broad peak. Furthermore, for films deposited at 1150°C, this peak is no longer seen in the CL spectra. Increasing the growth temperature to eliminate this defect peak would indicate that it is impurity related. Attempts to determine this impurity are in progress.

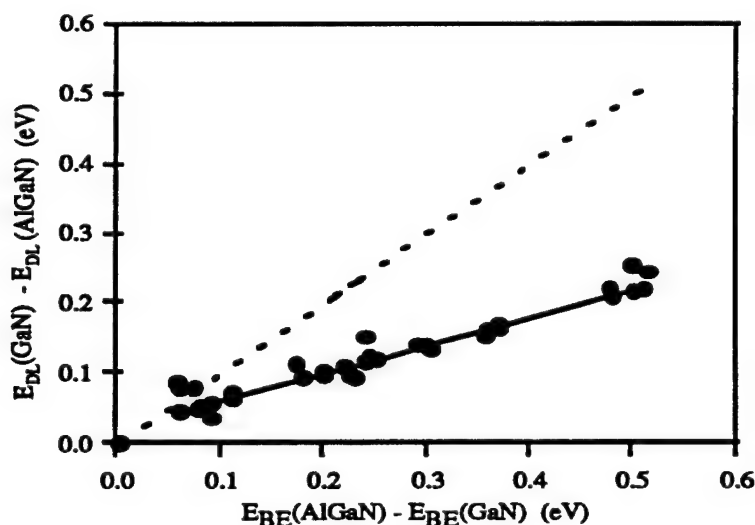


Figure 6. The sublinear shift in the deep level emission ("yellow luminescence") as a function of the increase in 4.2K CL near band-edge emission.

Initial studies of the initial growth of $\text{Al}_x\text{Ga}_{1-x}\text{N}$ directly on SiC give some insight into the strain relief mechanisms near the $\text{Al}_x\text{Ga}_{1-x}\text{N}/\text{SiC}$ interface. Despite the somewhat close lattice match between GaN and 6H-SiC(0001) (3.5%), previous research in our laboratories has shown that GaN epitaxy undergoes three dimensional island growth, since the critical thickness of GaN on 6H-SiC is $<10\text{\AA}$. By contrast, AlN films, with a critical thickness of 45\AA and a lattice mismatch of 0.9%, grow via coalescence of two dimensional flat-top islands which gradually roughens with increasing thickness [20]. At a thickness of 1000\AA , AFM measurements reveal a RMS roughness of 32\AA (Fig. 8) when deposited on vicinal SiC substrates.

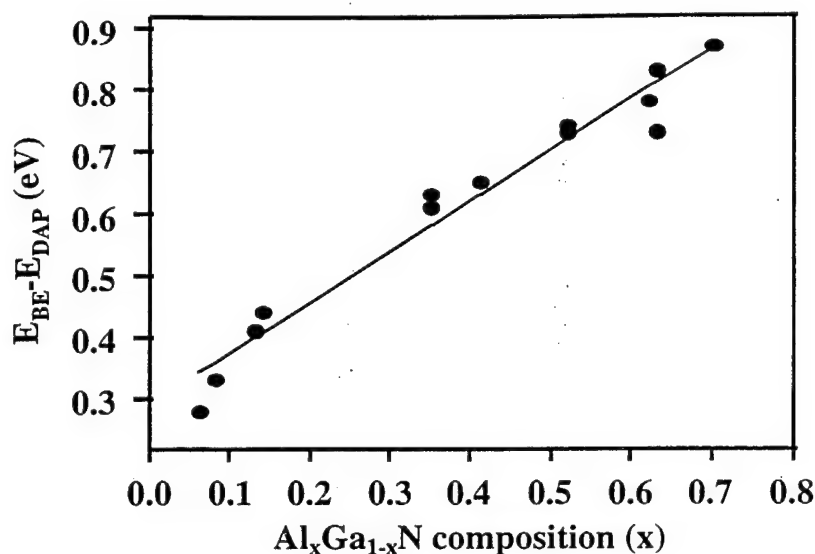


Figure 7. The difference in 4.2K CL near band-edge emission and the shallow donor to shallow acceptor (DAP) peak position as a function of aluminum mole fraction.

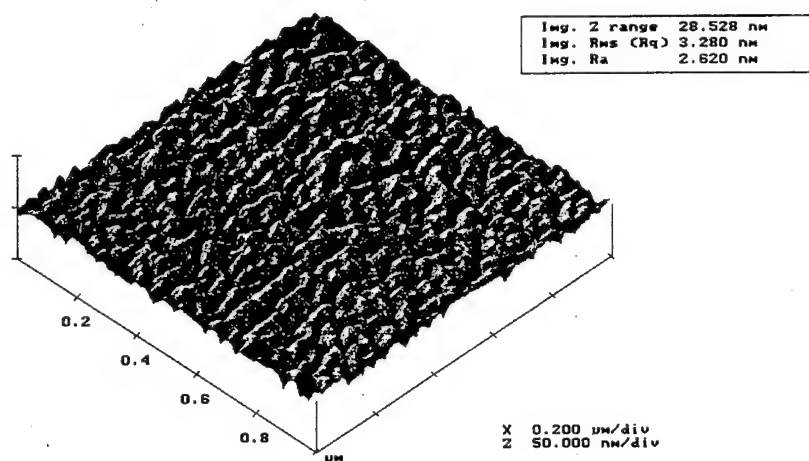


Figure 8. An AFM image of a 1000Å AlN buffer layer deposited on vicinal 6H-SiC.

In contrast, $\text{Al}_x\text{Ga}_{1-x}\text{N}$ films deposited at 1050°C undergo a considerably more complex growth mechanism. Figure 9 shows the results of five minutes of deposition with a gas phase mixture which results in a $\text{Al}_{0.2}\text{Ga}_{0.8}\text{N}$ thin film. It clearly shows two distinct regions of growth which are referred to as the “islands” and the “valleys.” The compositions of the islands and the valleys were determined using FE-AES (Fig. 10). Two important findings are evident from this graph. First, this data clearly shows that the interface region is aluminum rich and that the bulk film composition is achieved at approximately 100Å of film thickness. Secondly, the interface of the valley regions is significantly more aluminum rich than the islands. The valley regions appear to contain approximately 0.65 mole fraction of aluminum at the interface while the islands contains only 0.40 mole fraction of aluminum at the interface.

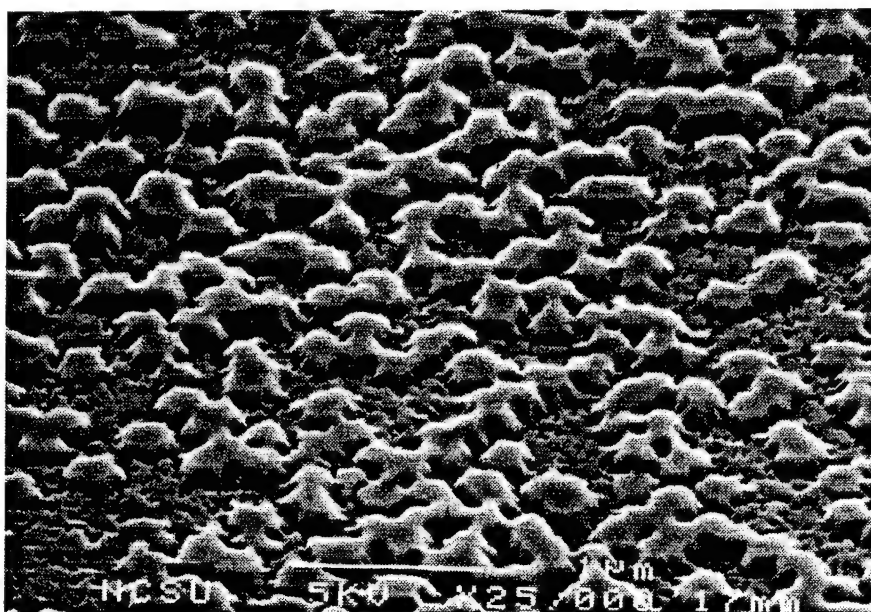


Figure 9. SEM of 5 minutes of growth of $\text{Al}_{0.2}\text{Ga}_{0.8}\text{N}$ at 1050°C directly on 6H-SiC.

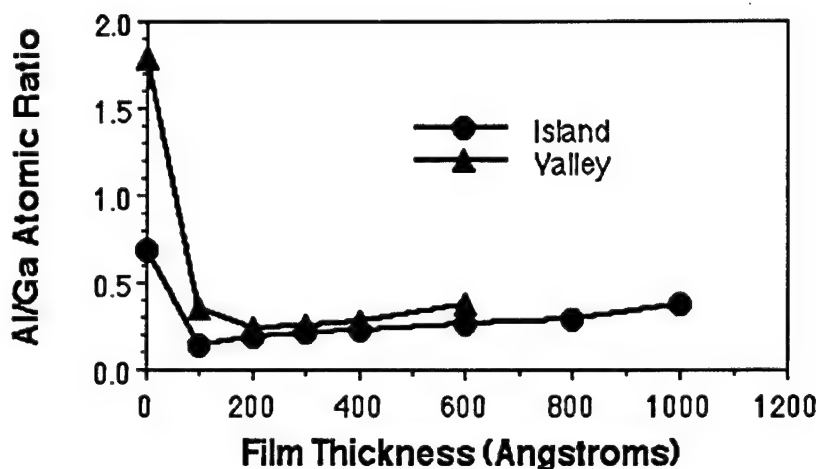


Figure 10. FE-AES of the various areas of the sample shown in Fig. 9.

Assuming Vegard's Law, this would imply an interfacial mismatch of only 1.9% for the valleys versus 2.5% for the islands. It should be noted that the mismatch of the islands is the same as that between AlN and GaN and, moreover, their morphology is similar to that observed for the first few hundred angstroms of GaN deposited on a high temperature AlN buffer layer [8]. The process of coalescence results in smooth $\text{Al}_x\text{Ga}_{1-x}\text{N}$ films similar to that shown in Figs. 1 and 2 after a few thousands angstroms of growth. It should be noted that profiling took place in 100\AA increments. Therefore, the possibility exists that an extremely thin AlN or aluminum rich $\text{Al}_x\text{Ga}_{1-x}\text{N}$ layer occurs within the first few angstroms of the interface;

thereby providing a graded buffer layer structure of less than 100Å in thickness. More notable, however, is the fact that low temperature CL revealed near band-edge emission at 3.53 eV. This indicates that a tremendous amount of tensial strain is present in this film since thicker films of the same composition have emission located at 3.83 eV. In summary, initial studies indicate that lattice strain is partial relieved at the interface during growth by the formation of an aluminum rich buffer layers which result in an island morphology. Subsequently, these islands coalesce into a smooth, coherent film containing tensial strain generated during cooling due to the differences in the thermal expansion coefficients, as well as numerous threading dislocations.

The TEM micrograph in Fig. 11 of a 1.8 micron thick $\text{Al}_{0.13}\text{Ga}_{0.87}\text{N}$ film deposited on an on-axis substrate revealed a microstructure dominated by threading dislocations, but free of low angle grain boundaries. Inspection of this and other micrographs reveals a progressive reduction in dislocation density as one moves away from the $\text{Al}_x\text{Ga}_{1-x}\text{N}/\text{SiC}$ interface. This is additionally supported by a narrowing of the full width at half maximum (FWHM) of the DCXRC of the $\text{Al}_{0.13}\text{Ga}_{0.87}\text{N}$ (0002) peak from 315 arcsec to 186 arcsec as the thickness of film increased from 0.9 microns to 1.8 microns. For films of similar thicknesses and compositions, films grown on vicinal SiC substrates exhibited higher FWHMs of the DCXRC

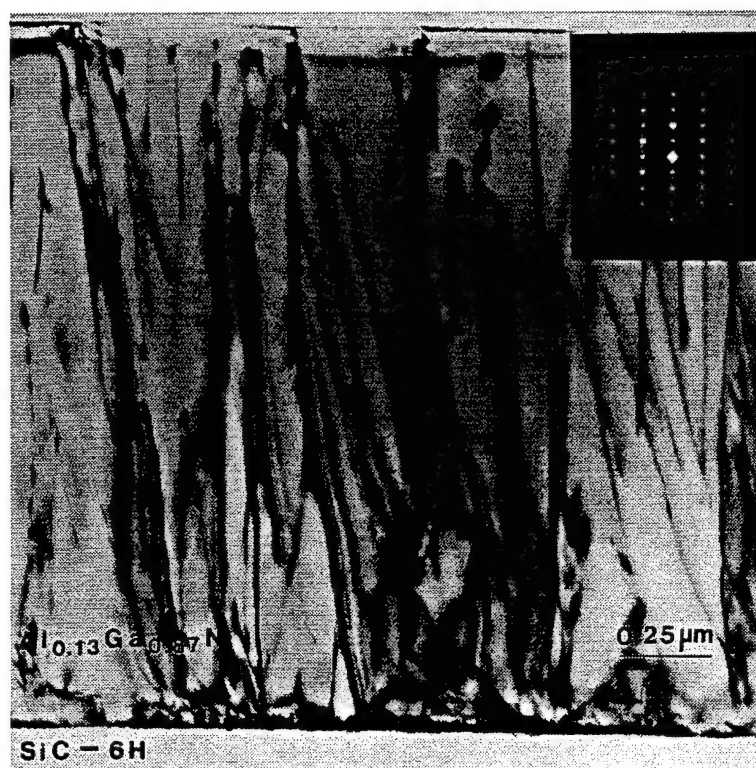


Figure 11. Cross-sectional TEM micrograph of 1.8μm AlGaIn (0001) film deposited at 1100°C and 45 Torr directly on 6H-SiC (0001) substrate. The inset shows the selected area diffraction.

of the AlGa_xN(0002). Furthermore, the growth rate on vicinal substrates was slightly higher due to increased density of steps on the surface; however, these steps probably act as formation sites for inversion domain boundaries [20]. Additionally, TEM revealed, as shown in Fig. 12, the presence of planar defects located parallel to the interface in the first few hundred angstroms of the Al_xGa_{1-x}N films.

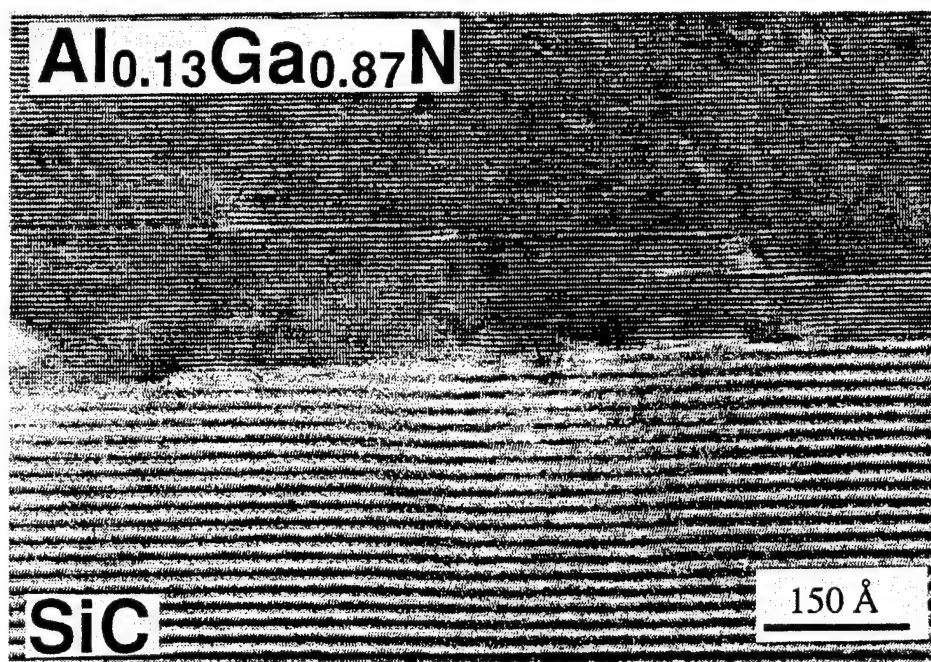
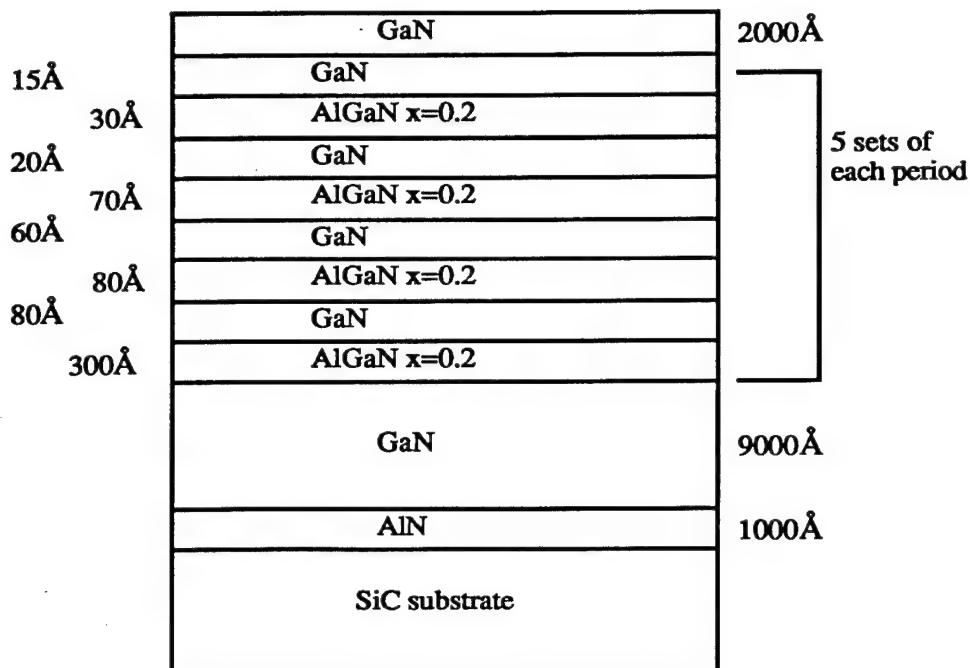
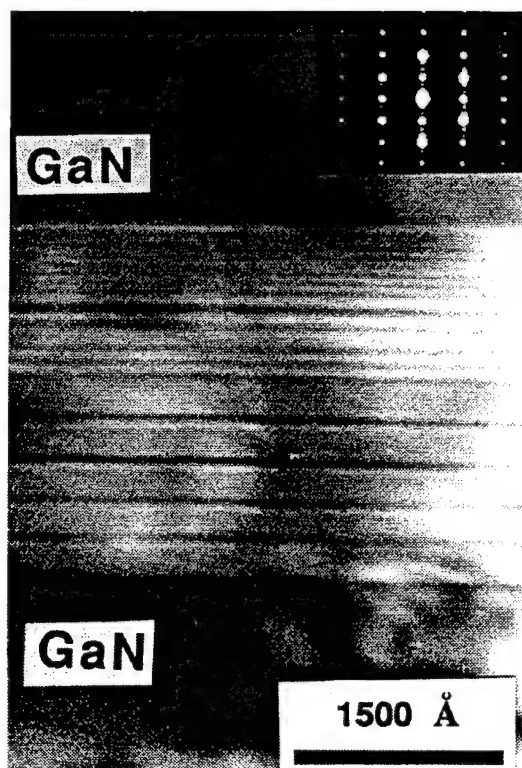


Figure 12. Cross-sectional TEM micrograph of interface region of 1.8 μm AlGa_{0.13}Ga_{0.87}N (0001) film deposited at 1100°C and 45 Torr directly on 6H-SiC (0001) substrate.

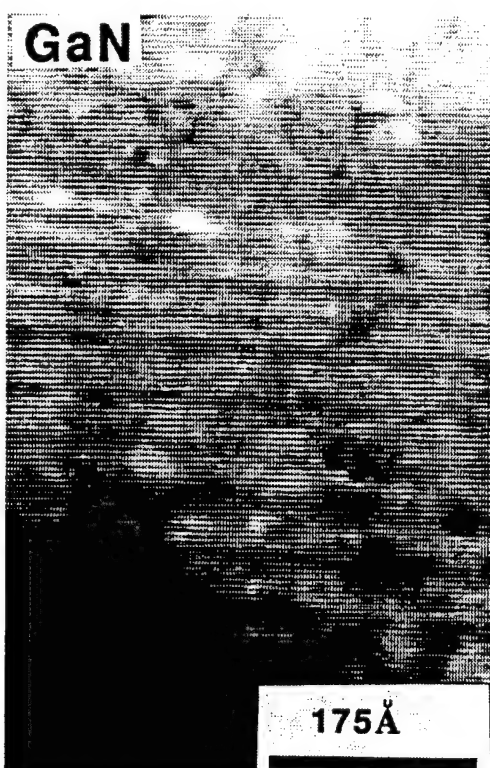
Several structures have been grown using GaN and Al_xGa_{1-x}N. A TEM micrograph of an Al_{0.2}Ga_{0.8}N/GaN superlattice with periods of various thicknesses is shown in Fig. 13. A schematic of the structure is shown in Fig. 13a. The superlattice structure was deposited on 0.6 microns GaN which was deposited on a 1000 Å, 1100°C AlN buffer layer. Each superlattice period was repeated 5 times and the structure was capped with 0.2 microns of GaN. Figures 13b and 13c shows coherent interfaces and the high quality of the superlattice structure. Observation of the structure in plan-view TEM did not indicate a reduction in dislocation density below that normally observed in single layer GaN films on a buffer layer. In Fig. 14, a TEM cross-section of a high electron mobility transistor (HEMT) device is shown. Growth was initiated similarly to the previous structure, but a second, 500 Å AlN layer was used both to allow pinch-off of the device, as well as to improve the quality of the GaN active layer. Results of device operation will be reported at a later date.



a



b



c

Figure 13. a) A schematic of a superlattice structure grown on 6H-SiC; b) a cross-section TEM micrograph showing the superlattice region of the structure; and c) a high resolution, cross-sectional TEM micrograph showing the 15Å GaN/30Å AlGaIn periods.

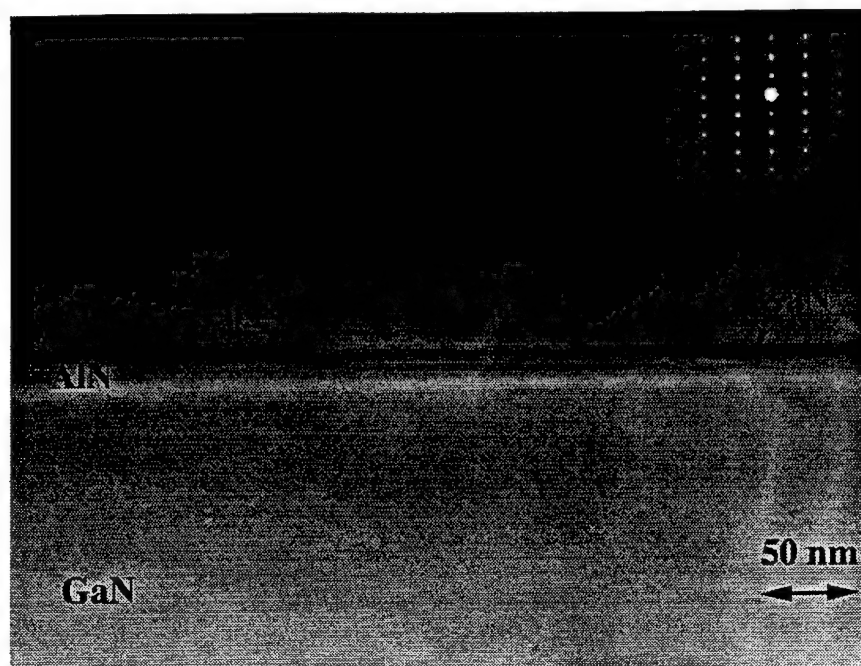


Figure 14. A cross-sectional TEM micrograph of a HEMT device.

Undoped, high-quality $\text{Al}_{0.05}\text{Ga}_{0.95}\text{N}$ films grown directly on vicinal 6H-SiC(0001) exhibited residual, ionized donor concentrations of $1 \times 10^{18} \text{ cm}^{-3}$. The ionized donor concentration decreased rapidly with increasing Al content and was $< 1 \times 10^{17} \text{ cm}^{-3}$ for $\text{Al}_{0.12}\text{Ga}_{0.88}\text{N}$ and $< 1 \times 10^{16} \text{ cm}^{-3}$ for $\text{Al}_{0.35}\text{Ga}_{0.65}\text{N}$, as determined by CV measurements. The origin of these donors is under investigation, since concentrations of $< 1 \times 10^{15} \text{ cm}^{-3}$ have been measured for GaN films grown on AlN buffer layers in the same reactor. Moreover, layers of undoped AlN having $N_D - N_A$ of $8 \times 10^{15} \text{ cm}^{-3}$ has also been deposited. However, the controlled introduction of SiH_4 allowed the reproducible achievement of ionized donor concentrations within the range of $2 \times 10^{17} \text{ cm}^{-3}$ to $2 \times 10^{19} \text{ cm}^{-3}$ in $\text{Al}_x\text{Ga}_{1-x}\text{N}$ films for $0.12 \leq x \leq 0.52$. For $x > 0.52$, additions of silicon resulted in films too resistive for CV measurements. The growth of p-type $\text{Al}_x\text{Ga}_{1-x}\text{N}$ films for $x \leq 0.13$ via the introduction of Mg has been successful.

D. Conclusions

Thin films of $\text{Al}_x\text{Ga}_{1-x}\text{N}$ ($0.05 < x < 0.96$) having smooth surfaces were deposited directly on vicinal and on-axis 6H-SiC(0001) substrates. Cross-sectional TEM of $\text{Al}_{0.13}\text{Ga}_{0.87}\text{N}$ revealed a microstructure similar to that of GaN grown on a high-temperature AlN buffer layer. EDX, AES and RBS were used to determine the compositions which were paired with their respective CL near bandedge emission energies. A negative bowing parameter was determined. The CL emission energies were similar to the bandgap values obtained by SE. FE-AES of the initial growth of $\text{Al}_{0.2}\text{Ga}_{0.8}\text{N}$ revealed an aluminum rich layer near the interface. $\text{Al}_{0.2}\text{Ga}_{0.8}\text{N}/\text{GaN}$ superlattices with coherent interfaces were fabricated. Additionally, HEMT

structures using AlN/GaN/AlN buffer structures were demonstrated. N-type (silicon) and p-type (magnesium) doping was achieved for $\text{Al}_x\text{Ga}_{1-x}\text{N}$ for $0.12 \leq x \leq 0.52$ and $x \leq 0.13$, respectively.

E. Acknowledgments

The authors express their appreciation to Cree Research, Inc. of Durham, North Carolina for providing the SiC wafers and Mr. T. Warren Weeks, Jr., Dr. A. D. Batchelor and Dr. K. Hiramatsu for their contributions and fruitful discussions. This research was supported by the Office of Naval Research under Contract N00014-092-J-1477.

F. References

1. S. Strite and H. Morkoc, *J. Vac. Sci. Technol. B* **10**, 1237 (1992).
2. T. Suski, P. Perlin, M. Leszczynski, H. Teisseyre, I. Grzegory, J. Jun, M. Bockowski, S. Porowski, K. Pakula, A. Wyszomolek and J. M. Baranowski, *Proceedings of the Materials Research Society*, **395** (1995).
3. S. Nakamura, *Jpn. J. Appl. Phys.* **30**, L1705 (1991).
4. H. Amano, I. Akasaki, K. Hiramatsu, N. Koide and N. Sawaki, *J. Cryst. Growth* **193**, 415 (1988).
5. A. A. Chernov, *Modern Crystallography III: Crystal Growth* (Springer, Berlin, 1984), p. 283.
6. W. Qian, M. Skowronski, M. DeGraef, K. Doverspike, L. B. Rowland and D. K. Gaskill, *Appl. Phys. Lett.* **66**, 1252 (1995).
7. T. W. Weeks, Jr., M. D. Bremser, K. S. Ailey, E. P. Carlson, W. G. Perry, and R. F. Davis, *Appl. Phys. Lett.* **67**, 401 (1995).
8. T. W. Weeks, Jr., M. D. Bremser, K. S. Ailey, W. G. Perry, E. P. Carlson, E. L. Piner, N. A. El-Masry, and R. F. Davis, *J. Mat. Res.* **11**, 1081 (1996).
9. S. Yosida, S. Misawa and S. Gonda, *J. Appl. Phys.* **53**, 6844 (1982).
10. Y. Koide, H. Itoh, M. R. H. Khan, K. Hiramatsu, N. Sawaki and I. Akasaki, *J. Appl. Phys.* **61**, 40 (1987).
11. M. R. H. Khan, Y. Koide, H. Itoh, N. Sawaki, I. Akasaki, *Solid State Commun.* **60**, 509 (1986).
12. D. K. Wickenden, C. B. Barger, W. A. Bryden, J. Miragliotta and T. J. Kistnermacher, *Appl. Phys. Lett.* **65**, 2024 (1994).
13. M. A. Khan, R. A. Skogman, R. G. Schulze, and M. Gershenson, *Appl. Phys. Lett.* **43**, 492 (1983).
14. R. Dingle, D. D. Sell, S. E. Stokowski and M. Ilegems, *Phys. Rev. B* **4**, 121 (1971).
15. A. Fischer, *Physik. Verhandl.* **7**, 204 (1957).
16. G. A. Wolff, I. Adams, J. W. Mellichamp, *Phys. Rev.* **114**, 1262 (1959).
17. I. Adams, T. R. Aucoin, G. A. Wolff, *J. Electrochem. Soc.* **109**, 1050 (1962).
18. W. Gotz, N. M. Johnson, R. A. Street, H. Amano and I. Akasaki, *Appl. Phys. Lett.* **66**, 1340 (1995).
19. R. Dingle and M. Ilegems, *Solid State Commun.* **9**, 175 (1971).
20. S. Tanaka, R. S. Kern, J. Bentley, and R. F. Davis, *Appl. Phys. Lett.* **66**, 37 (1995).

IX. Structural Characterization of Group III-Nitride Films and Their Interfaces by XRD and TEM

A. Introduction

To obtain the best performance from electronic and optoelectronic devices based on heterojunctions and superlattices, it is necessary to grow defect-free layers with morphologically and compositionally sharp interfaces [1]. TEM studies [2-6] have shown that the defects in epitaxial heterostructures such as GaN/AlN/6H-SiC or GaN on sapphire (α -Al₂O₃) could have different origins: (1) line or planar defects from the substrate extended during the growth into the epilayer, (2) defects introduced in the epilayer due to a loss of symmetry relative to the substrate, such as inversion domain boundaries, induced by the steps at the surface, (3) stress induced by the lattice and thermal mismatch across the interface, (4) growth errors leading to microtwins, stacking faults, impurities or polycrystalline or amorphous growth, and (5) clustering of excess point defects, such as vacancies, interstitials, or impurities. The last two origins of defect formation have been eliminated to a greater extent during OMVPE growth of GaN films on 6H-SiC [7-9]. The present study shows the defects due to a loss of symmetry induced by the surface morphology such as surface steps, can be eliminated as well. The use of AlN buffer layer with thickness ~ 100 nm helps to reduce the lattice mismatch from 3.5% if the GaN film is deposited directly on the 6H-SiC substrate to 2.4% between GaN and AlN when the AlN buffer layer is deposited first on the SiC substrate where the lattice mismatch between AlN and SiC is less than 1%. Thus, the lattice misfit strain is significantly reduced and up to a critical thickness the AlN and GaN films are expected to be coherently and compressively strained due to their lower in-plane lattice parameters with respect to these of the underlying films [10-12]. The thermal expansion coefficient mismatch is expected to strain compressively in-plane the GaN films, as well. This strain can either be stored as a strain energy in the film or can be accommodated by a network of misfit dislocations or other strain relieving defects at the interface. Another aspect of the strain accommodation is the change in the surface morphology which has already been shown for other systems, for example Si/Ge or GaAs/Si [13-15]. Thus, only the line defects such as threading and misfit dislocations are present in the OMVPE GaN/AlN/6H-SiC heterostructures and after the optimized growth conditions, GaN films reduced up to 10^7 - 10^8 /cm² are achieved.

B. Experimental Procedure

The structural properties of the GaN/AlN/6H-SiC heterostructures and Al_xGa_{1-x}N/GaN superlattices have been studied by transmission electron microscopy and x-ray diffraction. The samples were observed with a TOPCON EM-002B high-resolution transmission electron microscope, operated at 200 kV and point-to-point resolution 0.18 nm. Samples for TEM have

been prepared by conventional methods using mechanical grinding and polishing and Ar^+ ion-milling at a low angle in the final stages. Cross-sectional samples were prepared in $\langle 110 \rangle$ zone axis of the 6H-SiC substrate. High resolution x-ray rocking curves, ω -scans, have been performed using a triple crystal diffractometer-Philips Materials Research Diffractometer, using the Bartles monochromator: four-bounce Ge (220) incident beam optics (two-channel cut Ge crystals) and two-bounce Ge (220) diffracted beam optics (one-channel cut Ge crystal). The resolution limit with this optics is 12 arcsec. The rocking curve experiments have been performed with the receiving slit optics which is with lower resolution in comparison with the channel cut analyzer optics, but the AlN (002) signal is stronger.

C. Results

GaN/AlN/6H-SiC Grown at 1100°C (Off-axis 6H-SiC). The low magnification image of a thick GaN layer grown on (0001) surface of AlN/6H-SiC viewed in the $[11\bar{2}0]$ direction is shown in Fig. 1. The AlN and GaN layers are epitaxial with respect to the substrate, and have the wurtzite crystal structure as it is revealed from the superimposed SAED pattern inset. High density of low angle grain boundaries causing stacking mismatch defects are seen in the AlN film close to the 6H-SiC surface, as shown in Fig. 2. Careful inspection reveals that most often these defects are formed above surface steps as a consequence of the enhanced islands nucleation on a stepped surface. During the followed coalescence of such islands, stacking mismatch occurs as a result of inversion of the lattice sites of Al and N atoms, or the so-called inversion domain boundaries (IDB) are formed. The defect density in the GaN film is significantly reduced.

The GaN/AlN interface (lattice mismatch $\sim 2.4\%$) is of better epitaxial quality than AlN/6H-SiC interface, despite the smaller lattice mismatch between AlN and 6H-SiC (mismatch $\sim 1\%$). The predominant defects are threading dislocations with $\mathbf{b} = 1/3\langle 11\bar{2}0 \rangle$ and to a much lesser extent stacking faults along $\{0002\}$ planes and closer to the GaN/AlN interface (up to $\sim 0.3 \mu\text{m}$ thickness away from that interface) arising to compensate the AlN surface irregularities. Dislocation half loops originated from the interface with $\mathbf{b} = [0001]$ and laying on the $\{1\bar{1}00\}$ prism planes [16] are also readily observable close to the GaN/AlN interface. Very few cases of inversion domains as shown in Fig. 3 and originated from the GaN/AlN interface were also observed and they can be associated with nonstoichiometry or contaminations of the AlN surface [17]. Both interfaces reveal significant reduction of defect density with increasing distance away from the interface line. Plan view TEM image of the GaN film surface (Fig. 4) reveals the high density of dislocations $\sim 10^{10} - 10^{11} / \text{cm}^2$ for that heterostructure.

GaN/AlN/6H-SiC (AlN @ 1100°C, GaN @ 1050°C, on axis 6H-SiC, with 6H-SiC epilayer). Both GaN and AlN films exhibit epitaxial relationships with the 6H-SiC substrate.

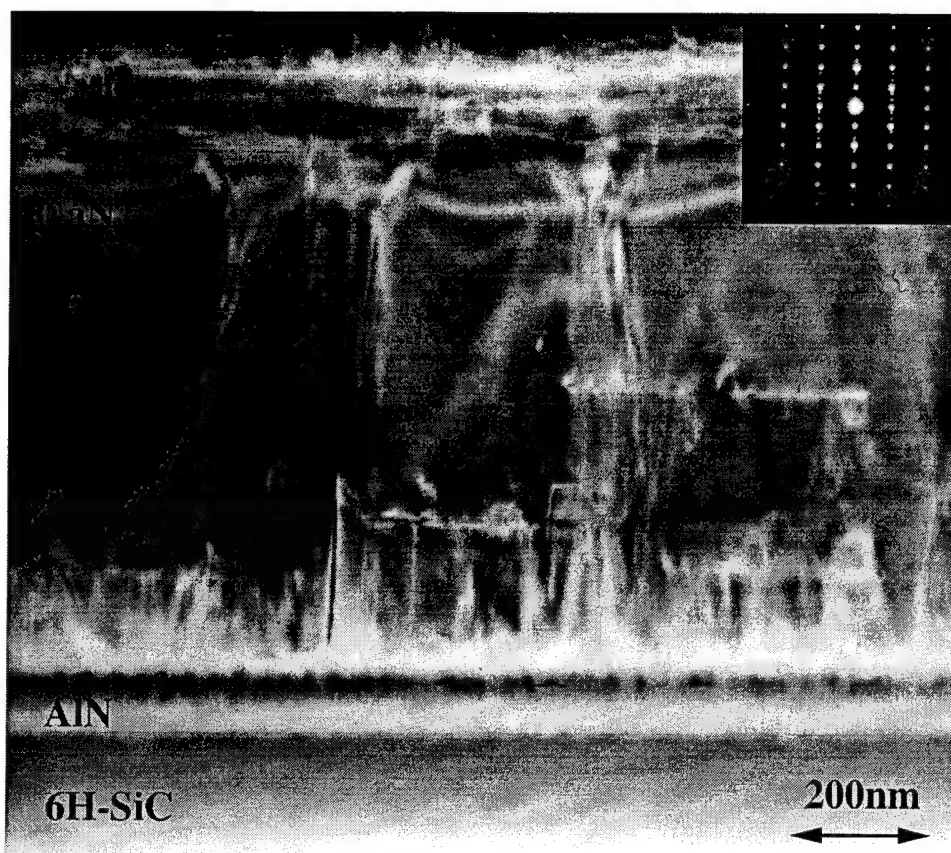


Figure 1. Cross-sectional micrograph of GaN/AlN/6H-SiC heterostructure grown on off-axis SiC substrate viewed in $[1\bar{1}20]$ direction.

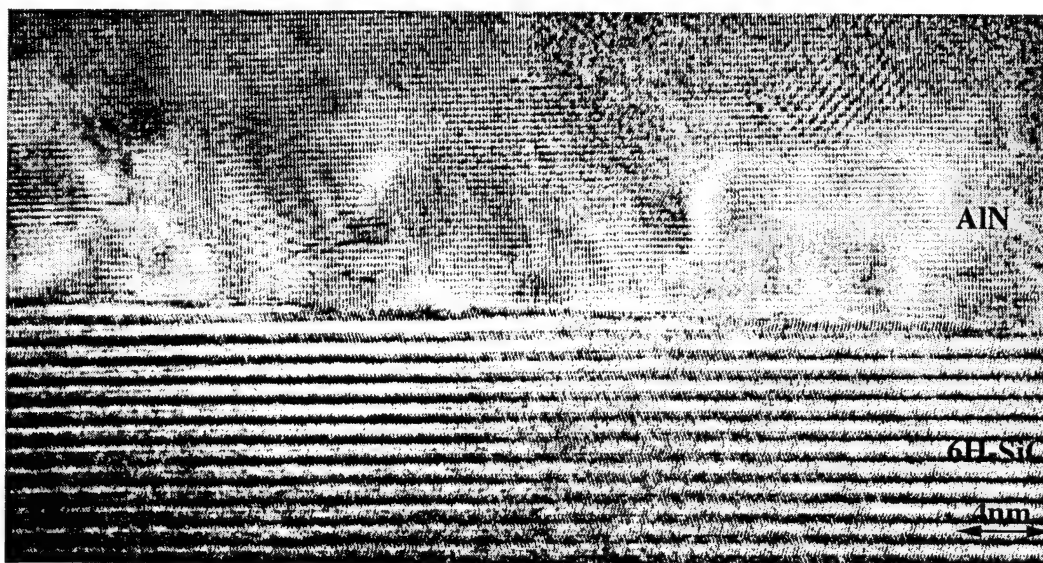


Figure 2. High-resolution micrograph from the AlN/6H-SiC interface of the same heterostructure shown in Fig. 1. Note the numerous low-angle grain boundaries typically originated above steps on the SiC surface.

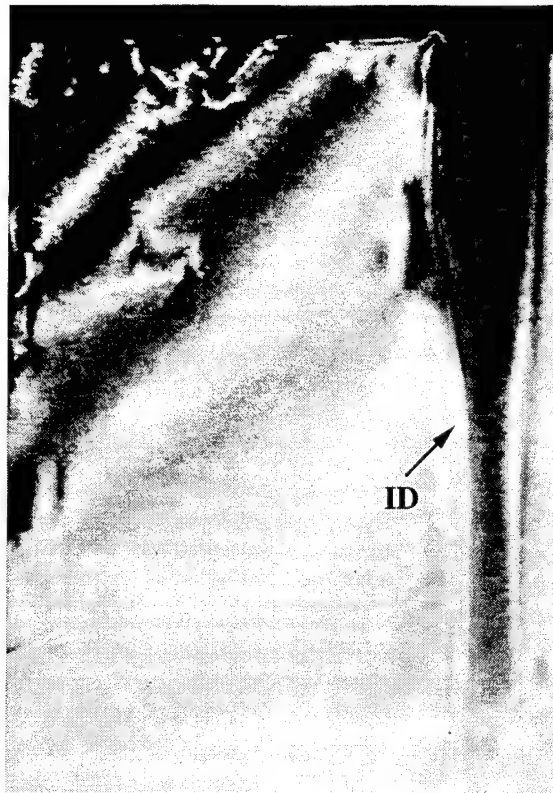


Figure 3. Cross-sectional TEM micrograph from a GaN film showing an inversion domain originated from the GaN/AlN interface as a consequence of a non-stoichiometry at that interface.

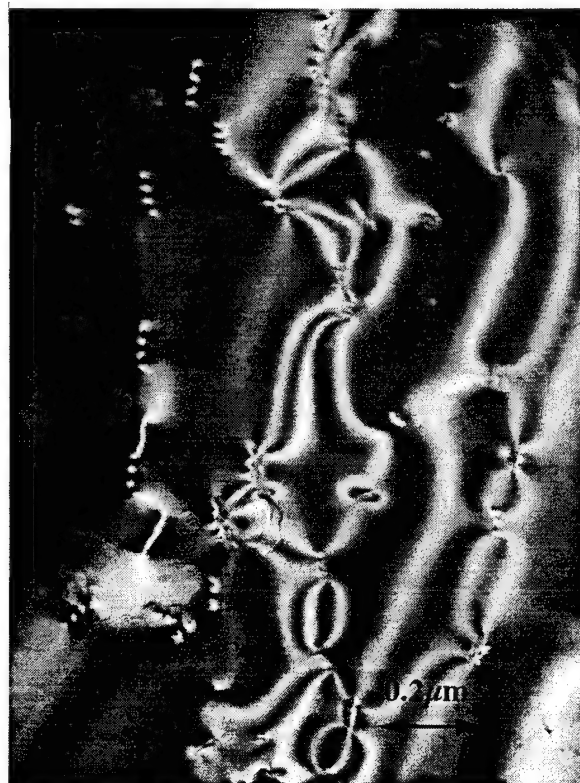


Figure 4. Plan view image of the GaN surface revealing high dislocation density in the film.

Typical low magnification TEM micrograph with the SADP inset is shown in Fig. 5. Compared to the previous growth system (3.1), the stacking fault density at the AlN/6H-SiC interface is much lower and the density of the threading dislocations in the AlN and GaN films is lower, as well. The predominant defects are mostly threading dislocations with $b=1/3\langle 11\bar{2}0 \rangle$. The reduced density of dislocation half loops and dislocation reactions [18], affect the defect density reduction in the GaN film grown at 50°C lower temperature than the growth temperature of AlN film. Figure 6 shows the quality of both AlN and GaN films is

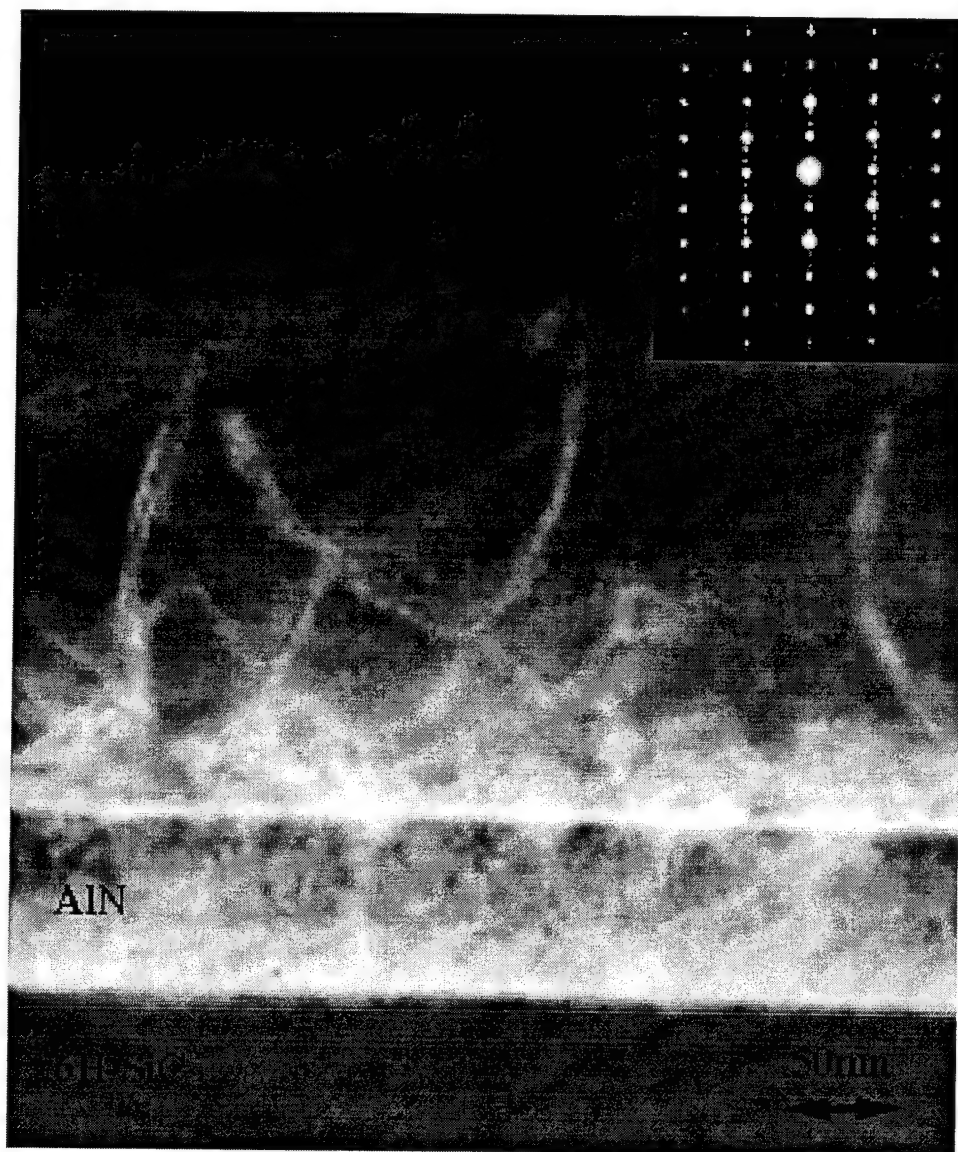


Figure 5. TEM micrograph showing cross-section view in $[11\bar{2}0]$ direction of the GaN/AlN/6H-SiC heterostructure grown on on-axis 6H-SiC substrate with SiC epilayer. Note the reduced defect density at the two interfaces compared to that for the off-axis grown layers.

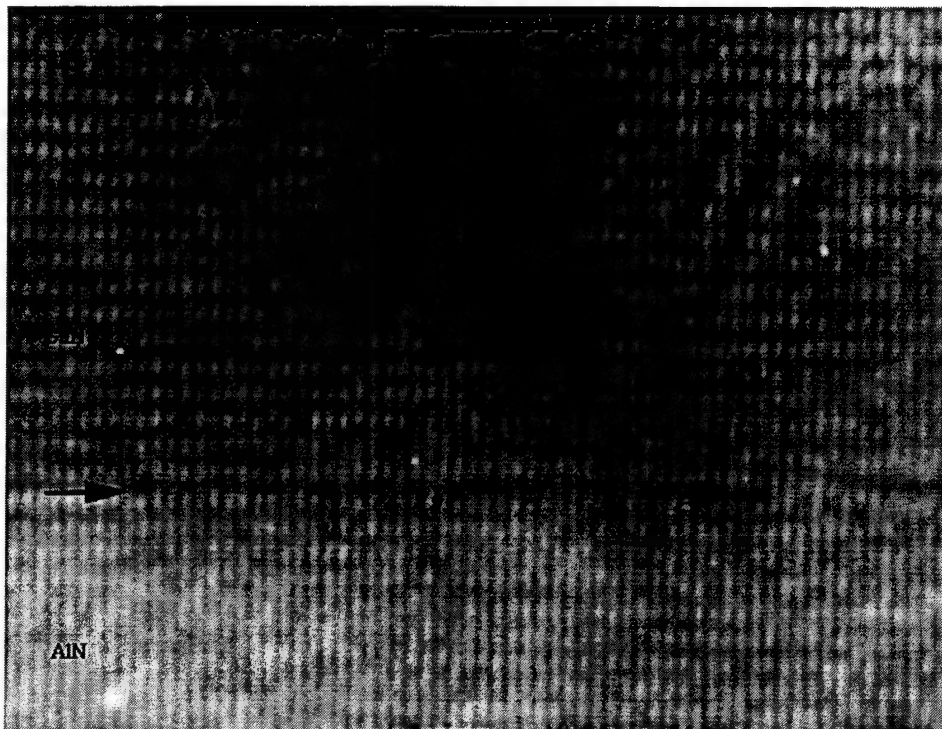


Figure 6. High-resolution TEM micrograph from the GaN/AlN interface of the above structure revealing the improved quality of that interface when the films are grown on on-axis 6H-SiC substrate.

higher ($\sim 10^9$ – 10^{10} /cm² dislocation density) suggesting that the significant reduction of the surface steps compared to the vicinal surface, as well as the thermal mismatch difference most probably play a role for the defect density reduction.

GaN/AlN/6H-SiC (AlN @ 1100°C, GaN @ 1050°C, On-axis 6H-SiC, without 6H-SiC Epilayer). The role of the quality of the 6H-SiC epilayer, usually deposited in advance on the 6H-SiC surface, on the GaN film perfection was investigated. AlN buffer layers and GaN films have been grown at exactly the same conditions as in the previous section with the only difference being that AlN film was deposited on the surface of a SiC substrate without the prior deposition of an epi SiC layer. These are the best quality AlN and GaN films grown to date by OMVPE as revealed from the cross-sectional TEM shown in Figs. 7 and 8, respectively. There are no planar defects like stacking faults or domain boundaries in the GaN film. The threading dislocation density is reduced and few threading segments are seen from the cross-sectional view in the $\langle 11\bar{2}0 \rangle$ direction as seen in Fig 7. The defect density in the top surface of the GaN film is reduced to 10^8 – 10^9 /cm². Close to the surface of GaN film, there are large areas a few microns, without a single dislocation, as it is seen from the plan view shown in Fig. 9.

Superlattice $\text{Al}_x\text{Ga}_{1-x}\text{N}/\text{GaN}$ ($x=0.2$) Interfaces. $\text{Al}_x\text{Ga}_{1-x}\text{N}/\text{GaN}$ ($x=0.2$) superlattice with periods of different thickness have been grown on 1.2 μm thick GaN film grown on 6H-SiC

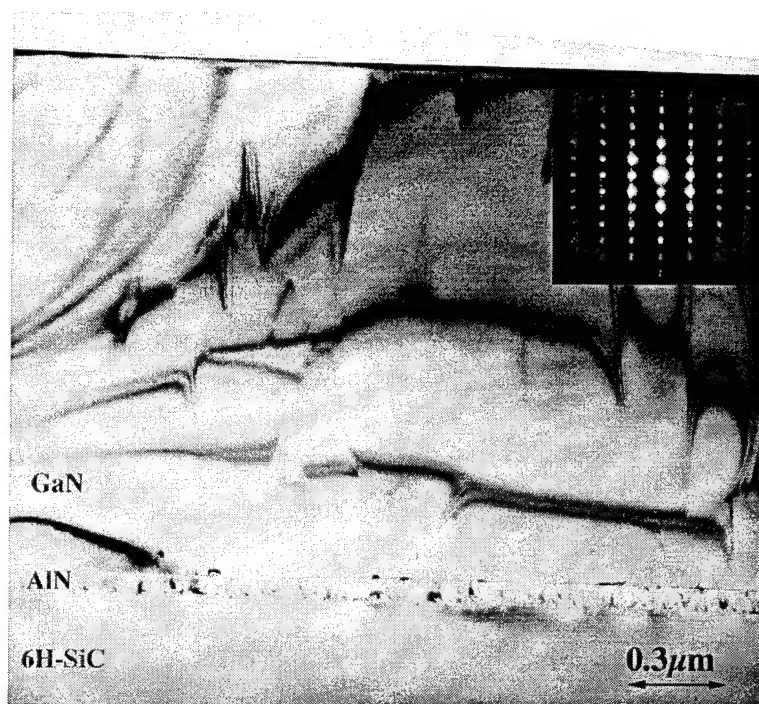


Figure 7. Low-magnification micrograph from GaN/AlN/6H-SiC heterostructure grown on on-axis SiC wafer without epi-SiC layer deposited in advance.

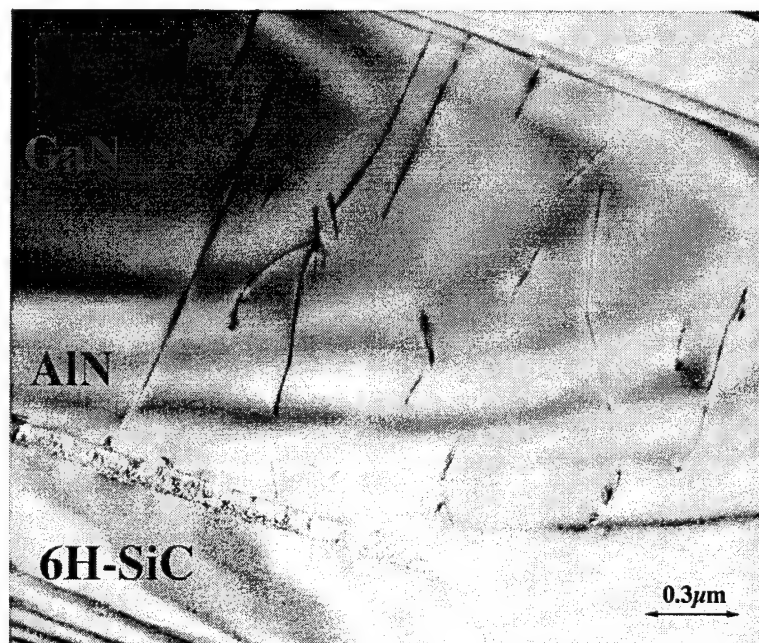


Figure 8. Low magnification TEM micrograph showing the significantly reduced dislocation density close to the top surface of the GaN film.

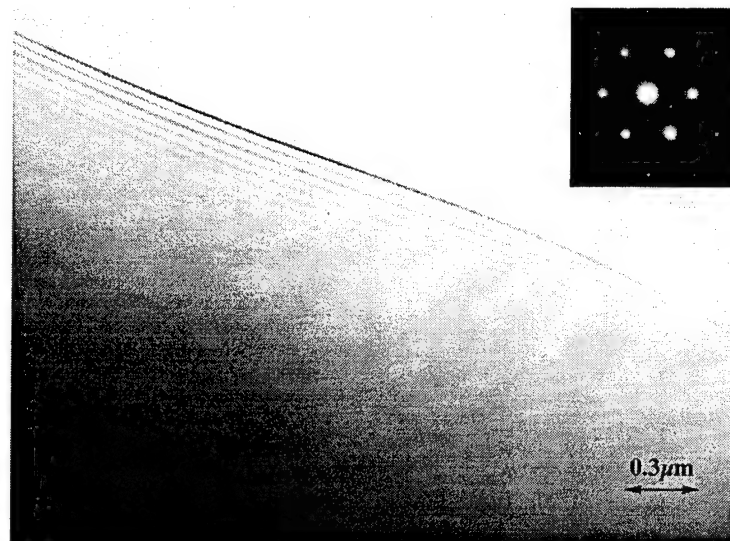


Figure 9. Plan-view TEM micrograph from the top surface of the GaN film shown in Fig. 7 and 8. Several microns size area is without a single dislocation.

with 0.1 μm thick AlN buffer layer. Low magnification and high resolution images of the superlattice are shown in Fig. 10 and 11, respectively. Despite the threading dislocations in the GaN film the superlattice is of very high quality due to the reduced dislocation density at the top of the underlying thick GaN film. In addition, the high quality of the superlattice is due to the lower mismatch (0.5%) between $\text{Al}_x\text{Ga}_{1-x}\text{N}$ and GaN.

GaN/AlGa N ($x=0.2$)/GaN/AlN/GaN/AlN/6H-SiC (HEMT). Low magnification TEM micrograph in cross-sectional view from the above heterostructure is shown in Fig. 12. The 0.1 μm thick AlN buffer layer and the thick GaN film exhibit the usual reduction of the defect

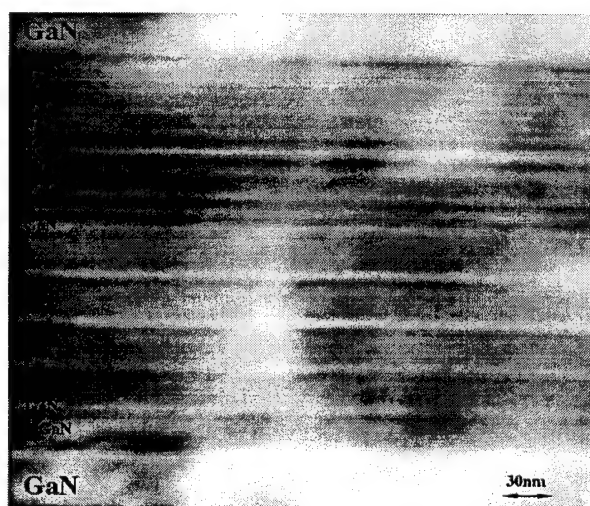


Figure 10. Cross-sectional TEM micrograph from the AlGa N /GaN ($x=0.2$) superlattice structure grown on a thick GaN film on a 6H-SiC substrate with an AlN buffer layer. The lower part of the picture is the top part of the thick GaN underlying layer.

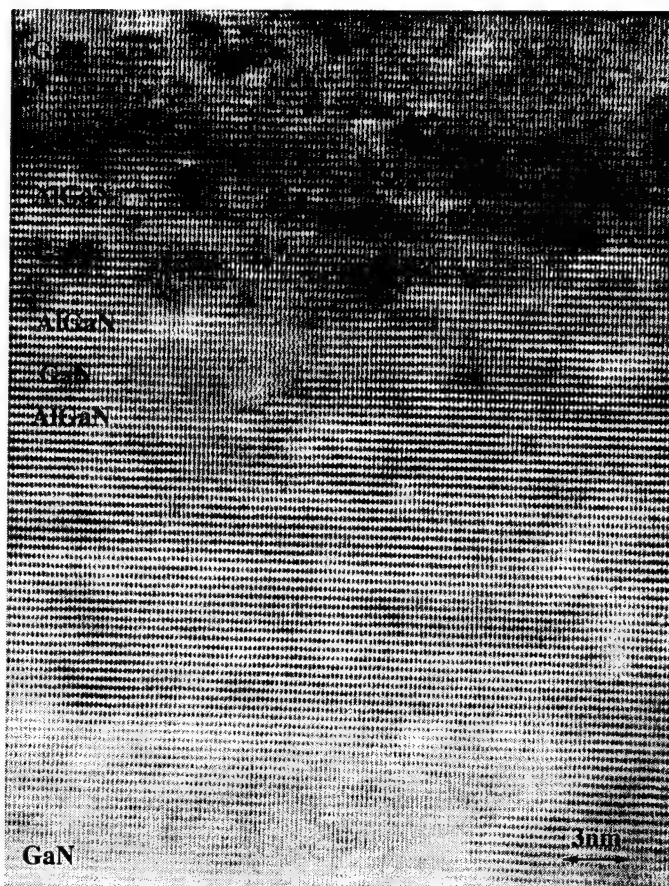
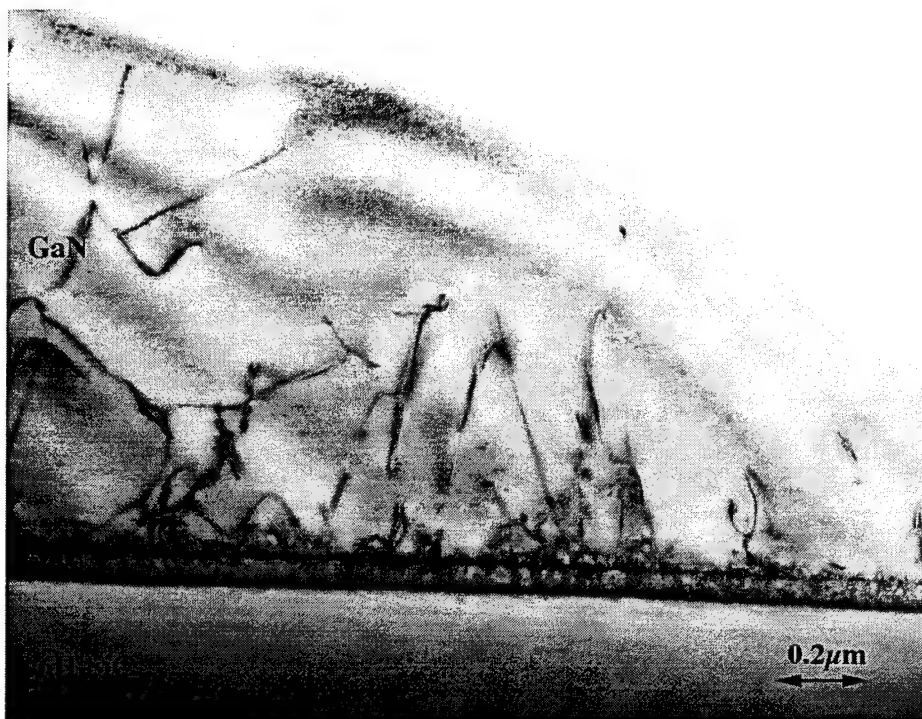


Figure 11. High resolution image from the superlattice structure showing the 15\AA GaN/ 30\AA AlGaIn periods.

density away from the AlN/6H-SiC and GaN/AlN interfaces, respectively. The numerous half-loops originated from the interface and the dislocation reactions have taken place for the defect density reduction. The predominant defects away from the GaN/AlN interface are the threading segments of dislocations. The SAD pattern in Fig. 13 (a) shows the common epitaxial relationships in the two films closest to the SiC substrate. Figure 13 (b) shows the SAD from the films above the thick GaN film (from top down): GaN/AlGaIn ($x=0.2$)/GaN/AlN that reveals that the above structure is coherently strained and, hence, the defect density is lessened in extent as it is seen from the TEM micrograph in Fig. 12(b).

GaN/AlN/GaN/AlN/GaN/AlN/6H-SiC. A TEM micrograph showing the above structure can be seen in Fig. 14. The AlN buffer layer exhibits the usual contrast due to the stress field across the AlN/6H-SiC interface. The 4500\AA thick GaN film deposited on the top of the AlN buffer reveals low defect density mostly threading dislocations running from the bottom to the interface with the next AlN film. In order to reduce the strain in the structure, two 400\AA thick AlN films have been grown sandwiching a 1500\AA thick GaN film. Thus the strain fields of

(a)



(b)

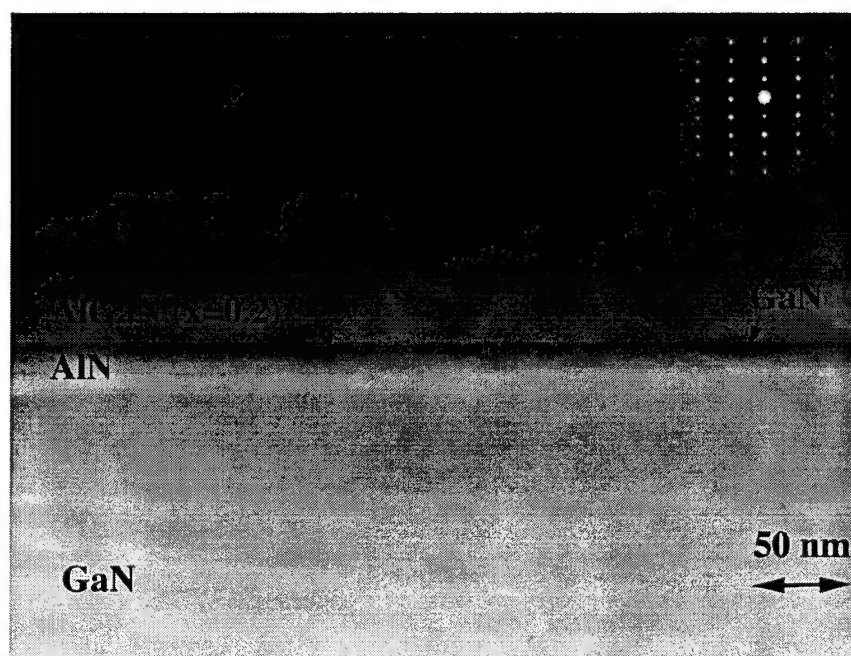


Figure 12. TEM micrograph from the HEMT heterostructure showing the high quality of the thick GaN film close to the substrate. Note the reduction of the dislocation density away from the GaN/AlN interface. (b). TEM micrograph from the top-most layers of the HEMT structure with the SAD inset revealing smooth epitaxial interfaces and low dislocation density.

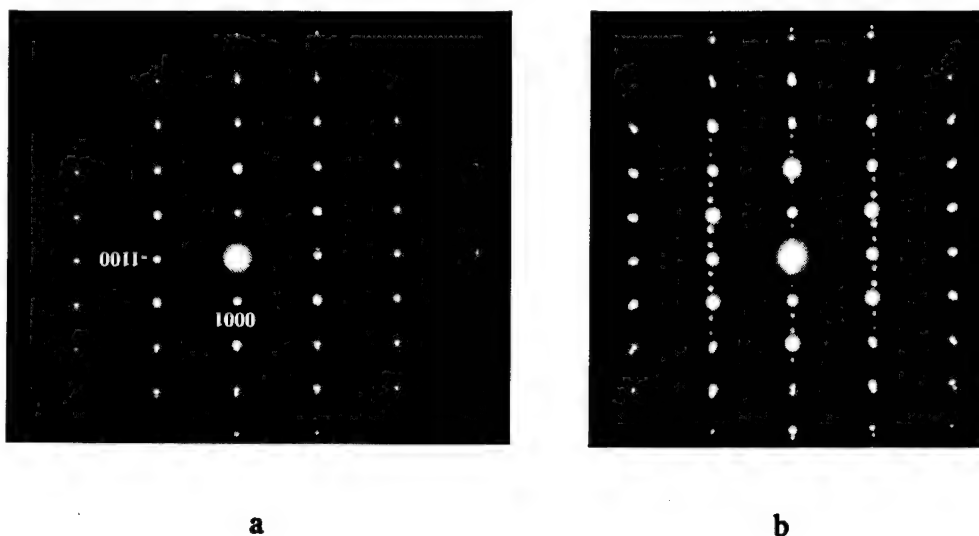


Figure 13. a) SADP from the GaN/AlN/6H-SiC interfaces of the HEMT structure revealing the epitaxial relationship of the films and substrate. (b) SADP from the top films of HEMT structure shown in Fig. 12 (b). The alignment of the weaker $[-1100]$ reflections belonging to the AlGaIn film with the same type reflections from the GaN films - the stronger spots indicates that the films are coherently strained and, hence, reduced defect density is expected.

opposite signs which cancel each other are “locked” at the GaN/AlN and AlN/GaN interfaces effectively reducing the overall strain in the structure. The top-most $1\mu\text{m}$ thick GaN film reveals notable reduction of the dislocation density.

D. Discussion

The analysis of the interfaces and defects in the as described group III-nitride heterostructures grown by MOCVD reveals that the best epitaxial and single crystalline quality of the GaN films and AlN buffer layers can be achieved if the layers are grown on on-axis 6H-SiC substrates. While the defect density in the GaN films grown on off-axis SiC substrate is on the order of $\sim 10^{10}$ – 10^{11} / cm^2 , for GaN films grown on on-axis 6H-SiC material the defect density is on the order of $\sim 10^8$ – 10^9 / cm^2 as shown from TEM studies.

The quality of the films has been studied by X-ray diffraction, as well. The FWHM from ω -2 θ scans is a direct measure of average length of a perfect crystal or particle size broadening (crystal coherence length). Typical values for the FWHM from ω -2 θ scans for different reflections from GaN/AlN/6H-SiC films grown by MOVPE are given in Table I. The narrower FWHM for GaN peaks reveal that the crystalline quality of GaN film is higher than that for the AlN buffer layer.

The epitaxial quality of the films have been studied by selected area diffraction in TEM. The typical epitaxial relationships for these heterostructures are: $(0001)\text{GaN} \parallel (0001)\text{AlN} \parallel (0001)$ 6H-SiC, and $[11\bar{2}0]\text{GaN} \parallel [11\bar{2}0]\text{AlN} \parallel [11\bar{2}0]$ 6H-SiC. Despite the epitaxiality, the

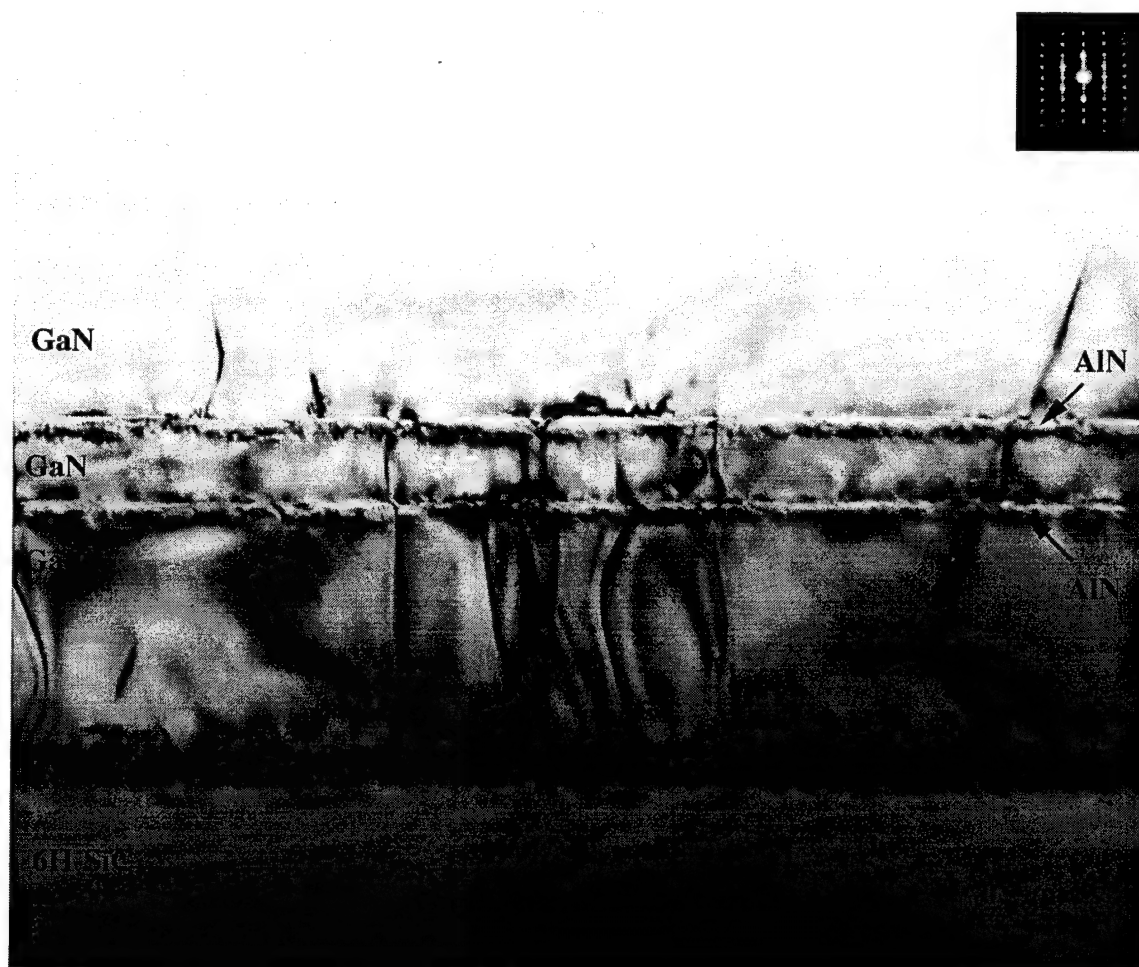


Figure 14. TEM micrograph from GaN/AlN/GaN/AlN/GaN/AlN/6H-SiC heterostructure. The AlN/GaN/AlN “sandwich” layers in the middle of the structure prove to be effective sink for the stresses in the films and thus very high quality of the top GaN film is achieved.

Table I. Typical FWHM (in arcsec) Taken at Different Points of the Sample for Different GaN/AlN/6H-SiC Heterostructures

	FWHM 6H-SiC (006)	FWHM AlN (002)	FWHM GaN (002)
GaN/AlN/SiC on-axis (with SiC epilayer)	54 - 72	304-342	249-260
GaN/AlN/SiC on-axis (without SiC epilayer)	41- 62	210-254	130-144

films reveal numerous types of defects. Typical defects in III-N films grown on 6H-SiC are misfit dislocations, threading dislocations, stacking faults, and inversion domain boundaries. The types of dislocations in GaN films are similar to that in hexagonal metals: (1) the edge type threading dislocations with $\mathbf{b} = 1/3\langle 11\bar{2}0 \rangle$, slip system $1/3\langle 11\bar{2}0 \rangle \{0001\}$; (2) the threading dislocations with $\mathbf{b} = [0001]$, slip system $\langle 10\bar{1}0 \rangle \{10\bar{1}0\}$, or $\{10\bar{1}1\}$; $\mathbf{b} = 1/3\langle 11\bar{2}3 \rangle$, slip system $\langle 1/3\langle 11\bar{2}3 \rangle \{11\bar{2}2\}$. Most of the dislocations originate from the AlN/SiC and GaN/6H-SiC interface [19].

AlN Films. Most of the defects in the 1000Å thick AlN films grown on off-axis SiC substrate are the domain boundaries which can be seen in Fig. 15 and 16. Such domains can be either inversion domains related by operation of inversion of atoms on their lattice sites, or double positioning domains, involving a 60° rotation along the c-axis [20, 21]. Recent studies show [22] that the steps on the vicinal surface provide sites for the growth of inversion domains. Such domains grow side-by-side and coalesce having a different stacking order, thus giving rise to the inversion domain boundaries observed in the HRTEM micrographs, as shown in Fig. 17. It should be noted that to the contrary, AlN films grown on on-axis 6H-SiC substrate do not exhibit the domain type of growth and the associated inversion domain boundaries, as shown in Fig. 19. Stacking faults parallel to the interface surface and the associated partial dislocations, are observed within ~200Å distance from the AlN/SiC interface.

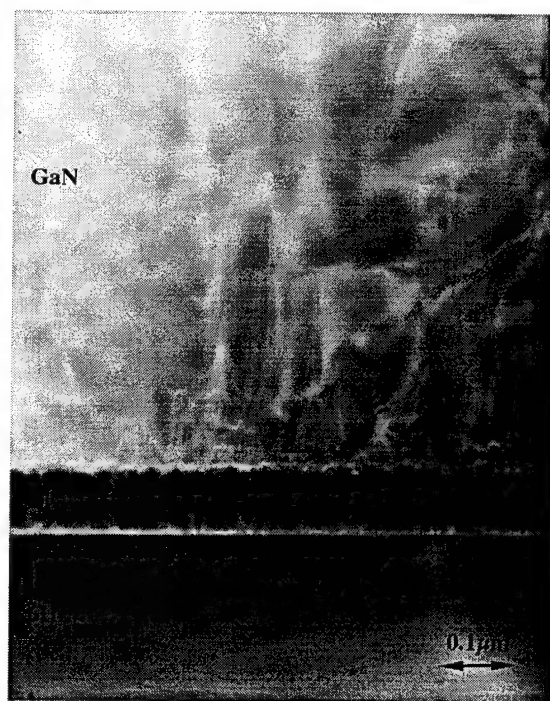


Figure 15. Low-magnification TEM micrograph from GaN/AlN/6H-SiC (off axis) heterostructure. The AlN film exhibits domain type of growth with the characteristic domain boundaries. GaN film reveals the high dislocation density ($\sim 10^{11}$ from plan view TEM), mostly threading dislocations and segments.



Figure 16. TEM micrograph from GaN/AlN/6H-SiC (off axis). The non-uniform contrast in the AlN film is due to the overlapping stress fields at the AlN/6H-SiC and GaN/AlN interfaces resulted from the lattice and thermal mismatch.

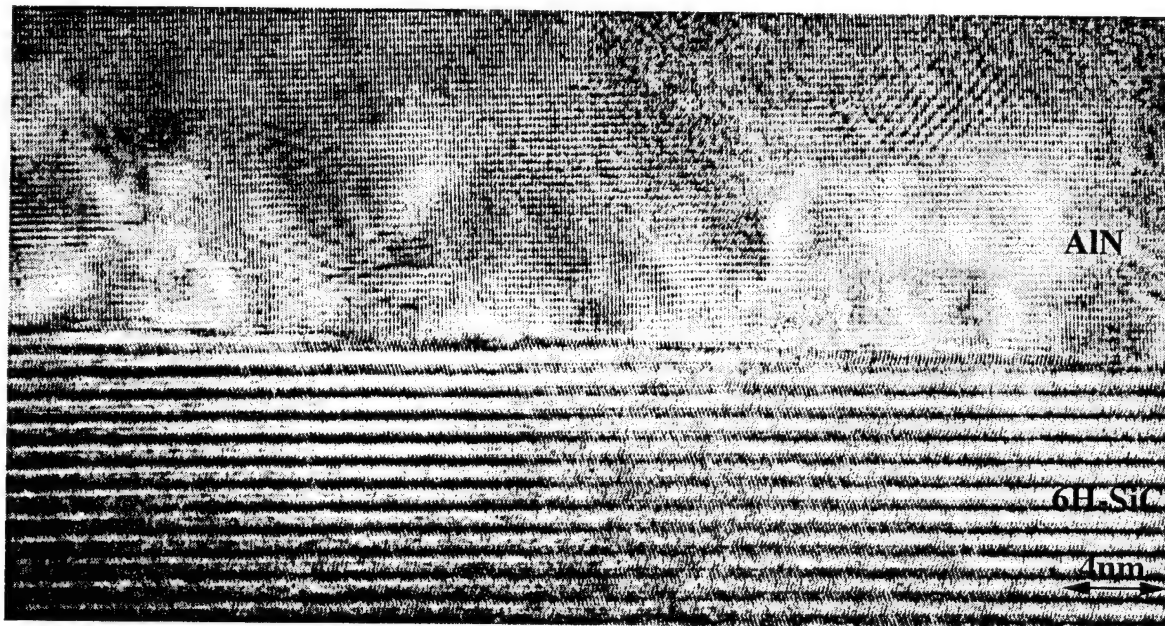


Figure 17. HR micrograph from AlN/6H-SiC-off axis interface revealing the strain due to the numerous domain boundaries formed when neighbor grains coalesce during the growth process.

It is well known [22] that stacking faults are equivalent to a local transitions of polytype which causes a difference in symmetry, and hence a difference in the physical properties of the film. Other defects in the AlN films grown on on-axis SiC substrate are the threading dislocations running from top to the bottom of the film, as can be seen from Fig. 19.

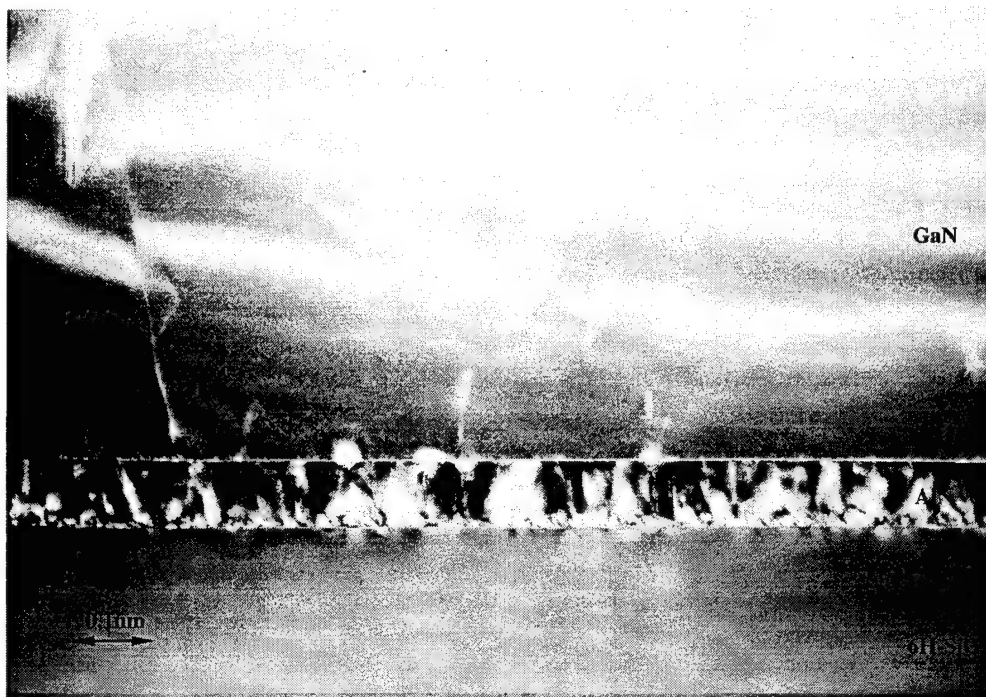


Figure 18. HR TEM micrograph from AlN/SiC on-axis substrate. There are no domains associated with the domain boundaries at that interface.

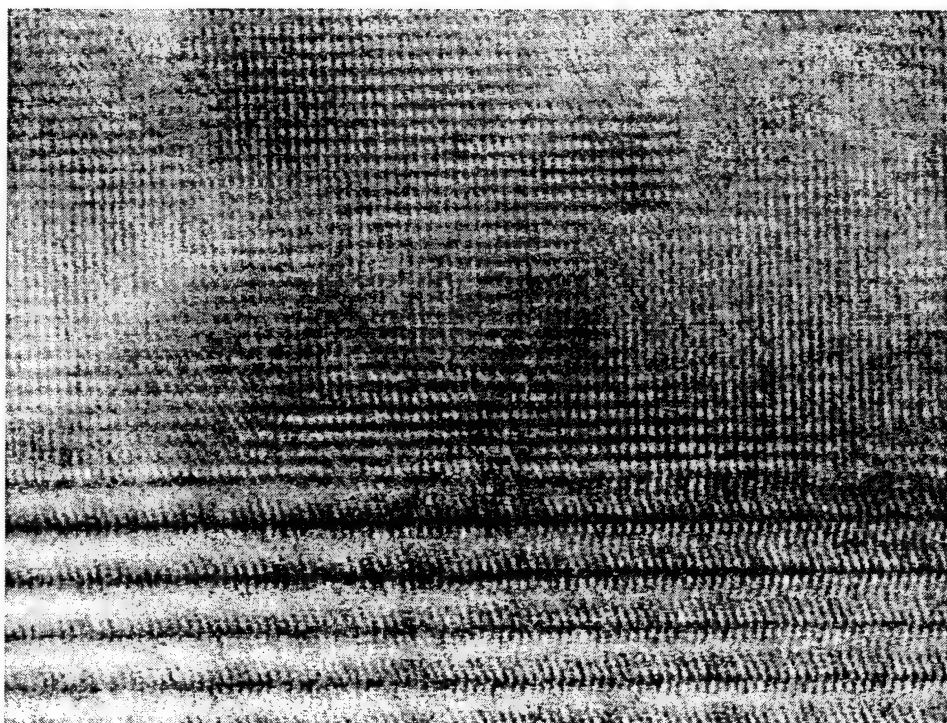


Figure 19. TEM micrograph from GaN/AlN/6H-SiC on-axis heterostructure showing the excellent quality of GaN/AlN and AlN/6H-SiC interfaces. Note the reduction of the defect density in comparison with the structure grown on off-axis SiC substrate.

GaN Films. The quality of the GaN films is influenced by the quality of the AlN buffer layer which "inherits" the crystal surface properties of the SiC substrate. GaN films grown on the cusp-like surface of AlN films grown on vicinal SiC surface reveal a high density of threading dislocations and threading segments throughout the film thickness, as well as dislocation loops and stacking faults close to the interface, as shown in Fig. 16. Our observations, as well as other studies [23] reveal that most of the dislocations are the edge type dislocations with Burgers vector $b=1/3\langle 11\bar{2}0 \rangle$ and $b=1/3\langle 1\bar{1}00 \rangle$ which are at the same time the misfit dislocations at the GaN/AlN interface. This means that most of the misfit strain at this interface is accommodated by the misfit dislocations.

It is well known that the stress generation factors in epitaxial systems are (i) the lattice mismatch, (ii) the thermal mismatch, and (iii) the difference in the chemical bonding across the interface. TEM studies supported by x-ray data reveal that the stress in group III-N films on 6H-SiC substrate is accommodated via (i) generation of misfit dislocations and stacking faults to compensate the atomic mismatch in the two contacted phases (GaN/AlN or AlN/6H-SiC), usually localized at or near the interface, respectively, (ii) propagation of threading dislocations through the entire bulk of the films, more strongly leading to degradation of semiconductor devices and dislocation reactions, and (iii) bending of the heterostructure in response to the stresses introduced by the lattice and thermal mismatch. The parameters pertinent to epitaxy and stress relief in Group III nitrides are given in Table II.

Table II. Parameters Relevant to Epitaxy in Group III Nitrides

Property		6H-SiC	AlN	GaN
Lattice parameter (Å)	a	3.081	3.1114	3.186
	c	15.092	4.9792	5.178
TEC $\times 10^6$ (K ⁻¹)	a	4.2	4.2	5.59
	c	4.68	5.3	3.17
Interplanar distances (Å)	Basal	2.516	2.49	2.59
	(11 $\bar{0}0$)	2.669	2.695	2.760
	(11 $\bar{2}0$)	1.541	1.556	1.591
Lattice mismatch w.r. SiC			0.01	0.035
	w.r. AlN			0.025

In order to assess the mismatch at the GaN/AlN and AlN/6H-SiC interfaces, HRTEM studies have been performed for the GaN/AlN/6H-SiC-on axis heterostructure in $[11\bar{2}0]$ orientation, as is seen from Figs. 18 and 20. Both interfaces are epitaxial, flat and free of low-angle grain boundaries. The average lattice mismatch calculated from the HRTEM image at the GaN/AlN interface was found to be 1.6% which is 0.8% lower than the theoretical value of 2.5% for that interface. This means there is a residual strain in the GaN film and that the GaN film is under compression. It is interesting to note that another piece of evidence for compression strain in GaN films is the contrast exhibited by the GaN films at distances of 50-80Å from the interface with the AlN. That contrast often reveals traces of rounded peaks and grooves which can be seen in Fig. 20. This type of morphology is typical for films that are under compression [24-26]. Such surface undulations are formed during heteroepitaxial growth by migration of surface deposited atoms under the strain-induced chemical potential gradients [27]. From the same figure, it can be seen that at the grooves, the interplanar distances are smaller than at areas close to the peaks. This shows there is a complimentary compression of the lattice plane at the locations of the surface grooves. The compressive strain in the GaN films is confirmed by PL and XRD studies performed on the same system [28].

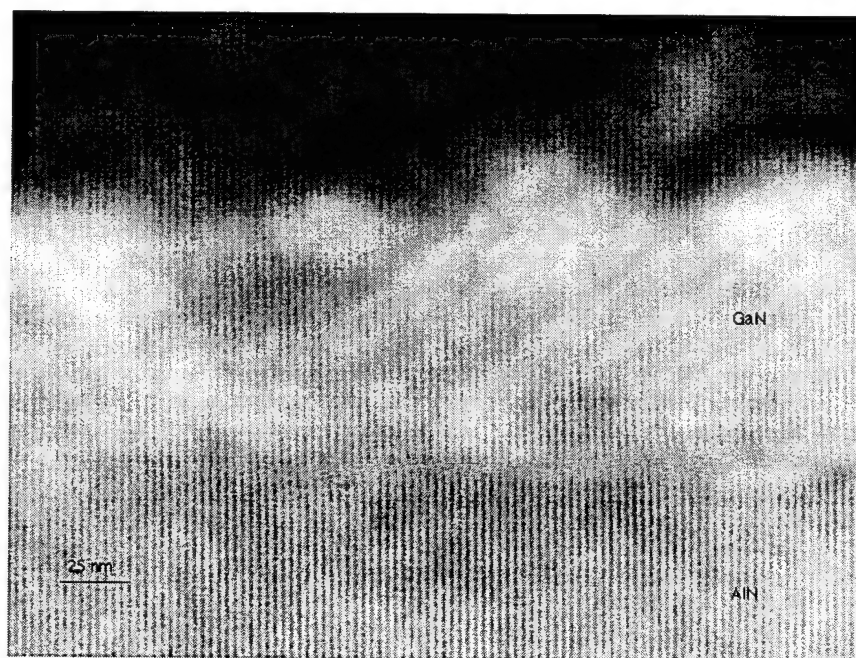


Figure 20. HRTEM micrograph from GaN/AlN interface of GaN/AlN/6H-SiC on-axis heterostructure. Note the extra-half plains in GaN film which are the misfit dislocations generated to relieve the misfit strain at that interface.

It is expected that when the thickness of the epilayer is very small the film is coherently strained to match the substrate interplanar distances. However, when the film thickness

increases the homogeneous misfit strain energy increases and at a critical thickness the nucleation of dislocations becomes favorable. For interfaces with large lattice mismatch (>2%) such as GaN/AlN with lattice mismatch of 2.5%, the term "critical thickness" can be defined as that thickness of the film beyond which misfit dislocations with $\mathbf{b} = 1/3 \langle 1 \bar{1} 00 \rangle$ are generated at the interface. The critical thickness of the wurtzite GaN film on the wurtzite AlN(0001) film is assessed by using the force balance method of Matthews and Blakeslee [29]. This method uses the consideration that there is a balance between (i) the force that drives the extension of the misfit dislocation along the interfacial plane which is due to the misfit stress in the structure and (ii) the force due to the line tension of the misfit dislocation. Employing this method the critical thickness for misfit dislocation generation in GaN film grown on AlN film (the latter considered with its bulk value lattice parameter) is assessed to be 12Å. This is considered reasonable if comparing the critical thickness of 46Å for misfit dislocation generation in AlN film grown on a 6H-SiC substrate, where the mismatch is much smaller and, hence, the misfit dislocation nucleation is expected at a higher thickness [30].

E. Conclusions

The TEM and XRD studies of GaN and AlN films and interfaces and their alloys grown on 6H-SiC substrates reveal the following:

- (i) The GaN films deposited on 6H-SiC substrates with an AlN buffer layer are epitaxial and single crystalline with a wurtzite type structure and have the following epitaxial relationships:

$$(0001)\text{GaN} \parallel (0001)\text{AlN} \parallel (0001) \text{ 6H-SiC},$$

$$[11\bar{2}0]\text{GaN} \parallel [11\bar{2}0]\text{AlN} \parallel [11\bar{2}0] \text{ 6H-SiC}.$$

- (ii) The dislocation density of GaN films grown on on-axis 6H-SiC substrate is 10^8 - 10^9 /cm² which is two orders of magnitude lower than the dislocation density of 10^{10} - 10^{11} /cm² for films grown on off-axis 6H-SiC substrate.
- (iii) The predominant type of defects in the GaN films grown on off-axis substrates are the threading dislocations with $\mathbf{b} = 1/3[11\bar{2}0]$. The predominant defects in GaN films grown on on-axis SiC substrate are the short threading segments of dislocations and short dislocation half-loops originated from the interface.
- (iv) Engineering of the AlN/GaN heterostructures utilizing "sandwich" AlN/GaN/AlN layers under the thick GaN film proves to be useful for significant reduction of the dislocation density in the GaN films due to strain field compensation within the "sandwich."
- (v) From HRTEM studies it is found that the GaN films are under residual biaxial compression. There is ~0.8% residual compressive strain in the GaN films. The

presence of the compressive strain in these films is additionally confirmed by the typical contrast morphology of GaN films in the near-interface region between GaN and AlN.

- (vi) Using the force balance method of Matthews and Blakeslee, the critical thickness for misfit dislocation generation in GaN films grown on AlN films is found to be 12Å.

F. References

1. J. Washburn, E. Kvam, and Z. Liliental-Weber, *J. Electron. Mater.*, **155** (1991).
2. X. Ning, F. Chien, P. Pirouz, J. Yang, and M. Khan, *J. Mat. Res.*, **11**, 580 (1995).
3. Meng W., Sell J., Eesley G., and Perry T., *J. Appl. Phys.*, **74**, 2411-2414 (1993).
4. Z. Liliental-Weber, H. Sohn, N. Newman and J. Washburn, *J. Vac. Sci. & Technol. B* **134** (1995).
5. D. Smith, D. Chandrasekhar, B. Sverdlov, A. Botchkarev, A. Salvador, and H. Morcoc, *Appl. Phys. Lett.* **67**, 13 (1995).
6. F. Ponce, B. Krusor, J. Major, Jr., W. Plano, and D. Welch, *Appl. Phys. Lett.* **67** 410 (1995).
7. W. Weeks, Jr., M. Bremser, K. Ailey, E. Carlson, W. Perry, and R. F. Davis, *Appl. Phys. Lett.* **67**, 401 (1995).
8. M. Bremser, W. Perry, N. Edwards, T. Zheleva, O. Nam, N. Parikh, D. Aspnes, and R. F. Davis, submitted in *J. Appl. Physics* (1996).
9. M. Bremser, W. Perry, N. Edwards, T. Zheleva, N. Parikh, D. Aspnes, and R. F. Davis, *MRS Symposium on Group III-Nitrides*, (1995).
10. F. Chien, X. Ning, S. Stemmer, P. Pirouz, Bremser M., and Davis R.F., *MRS Symposium on Group III-Nitrides*, (1995).
11. D. Smith, S. Tsen, B. Sverdlov, G. Martin and H. Morcoc, *Proceedings TWN* (1995).
12. J. Matthews, A. Mader, and T. Light, *J. Appl. Physics* **41**, 3800 (1970).
13. A. Cullis, D. Robbins, S. Barnett, and A. Pidduk, *J. Vac. Sci. and Technology A* **12**, 1924 (1994).
14. D. Jesson, S. Pennycook, J. Baribeau, and D. Houghton D., *ibid.* **71**, 1744 (1993).
15. D. Eaglesham and M. Cerullo, *Phys. Rev. Lett.* **64**, 690 (1990).
16. S. Liliental-Weber *et al.*, *MRS Symposium on Group III-Nitrides*, (1995).
17. A. Westwood, R. Youngman, M. McCartney, A. Cormack, M. Notic, *J. Mater. Res.* **10**, 1270 (1995).
18. F. Chien, X. Ning, S. Stemmer, P. Pirouz, M. Bremser and R. F. Davis, Submitted to *J. Mater. Res.*
19. S. Tanaka, S. Kern, J. Bentley, and R. F. Davis, submitted in *Japn. J. Appl. Phys.* Nov. (1995).
20. A. Westwood and M. Notic, *J. Amer. Ceram. Soc.* **74**, 1226 (1991).
21. P. Pirouz P. *et al.*, *Nitride Workshop on Wide Bandgap Nitrides*, S. Louis, (1996).
22. S. Liliental-Weber *et al.*, submitted *J. Mater. Res* (1996).
23. J. Tersoff and R. Tromp, *Phys. Rev. Lett.* **70**, 2783 (1993).
24. W. Yang and D. Srolovitz, *ibid.* **71**, 1593 (1993).
25. C. Roland, *MRS Bulletin* **21**, 27 (1996).
26. A. Cullis, *MRS Bulletin* **21**, 21 (1996).
27. B. Perry, *ONR report* (1996).
28. J. Matthews and A. Blakeslee, *J. Cryst. Growth* **27**, 118 (1974).
29. R. Hull and J. Bean, in *Strained-Layer Superlattices: Materials Science and Technology* Ed. T. Pearsal, Acad. Press 1991.

X. Luminescence and XRD Studies of Stresses in GaN Films Grown on 6H-SiC(0001) Substrates via MOVPE

A. Introduction

Gallium nitride is one of the most promising semiconductor materials for optical devices in the blue to ultraviolet region due to its direct energy band-gap of 3.39 eV at room temperature. Single crystals of GaN are not commercially available, and therefore, heteroepitaxial growth must be employed. Two sources of stress are prevalent for heteroepitaxial films: lattice mismatch and thermal expansion mismatch. The total stress results in a biaxial strain of the film where the change in the lattice parameters c and a are given by Poisson's ration, $\nu = (\Delta a/a_0)/(\Delta c/c_0)$.

Currently, the most common substrates are sapphire (0001), although a large difference in lattice constants and thermal expansion coefficients exists between GaN and sapphire. Buffer layers of AlN have been used to improve film quality, although a significant difference in lattice parameters between AlN and sapphire ($\Delta a/a_0 \approx 13\%$) still exists [1]. The stress due to lattice mismatch, which is compressive for GaN on sapphire, is presumed to be relieved after several nanometers of growth according to critical thickness theory [2]. The primary relief mechanism is the formation of dislocations at the film/substrate interface during film growth. Upon cooling, the difference in thermal expansion coefficients ($\alpha_{\text{sapphire}} > \alpha_{\text{GaN}}$) results in a compressive stress.

Recent work though suggests the lattice mismatch stress is not fully relieved [3]. Unfortunately, it is difficult to substantiate this due to each stress being compressive, along with the variances in published lattice constants and thermal expansion coefficients used in calculations. The resulting residual strain in the film alters the lattice constants a and c of the GaN wurtzite structure from their relaxed values. Previous work [2, 4] measured the change in lattice constants with film thickness. The compressive stress in GaN was strongest for very thin films and decreased as the thickness increased. As a result c decreased and a increased, which is expected for a reduction in biaxial compressive strain.

Recent work [1] has used SiC as a substrate, with AlN as a buffer layer. The lattice mismatch between AlN and SiC is much smaller ($\approx 1\%$), but the critical thickness is still very small (47 Å for hexagonal structures) [5], and misfit dislocations readily form at the interface. Any residual stress that remains would be compressive ($a_{\text{GaN}} > a_{\text{SiC}}$). The difference in thermal expansion coefficients is opposite in sign to that of GaN and sapphire ($\alpha_{\text{GaN}} > \alpha_{\text{SiC}}$), resulting in a tensile stress contribution. Thus, the two main stresses in this heteroepitaxial system are opposite in sign, offering the potential to confirm if residual stress exists in the films.

One consequence of film strain is a variation in the band-gap energy (E_g) [6]. Variations in E_g may be detected by low temperature photoluminescence (PL). At $T \leq 4.2$ K, the PL of

high-quality GaN reveals intense near-band edge emission attributed to free excitons (both A and B) and/or excitons bound to shallow neutral donors (BX) [1,7-9]. These structures are sensitive to variations in E_g due to their shallow nature. Amano, *et al.* [10] observed a shift in bound exciton energy (E_{BX}) with film strain. Reported E_{BX} values for GaN on sapphire vary widely from 3.467 to 3.494 eV [7-9, 11]. This variation may be due to differences in the state of strain of the materials tested.

In this report the relationship between E_{BX} and lattice parameters (and hence, strain) will be examined for 18 GaN films grown on SiC. These results will be compared and contrasted to results for GaN on sapphire. Also discussed will be the role of the AlN buffer layer and the degree of off-axis tilt of the SiC substrate.

B. Experimental Procedure

Absolute lattice constants values were measured using a Philips X'Pert MRD diffractometer in the triple-axis mode. The method used was originally proposed by Fewster, and is comparable to, and in many ways more accurate than, the commonly used "Bond" method [12]. The high resolution of the triple-bounce analyzer crystal and the steps taken to eliminate inaccuracies due to the 2θ zero error and sample centering account for this. The data were collected using 2θ - ω scans, with corrections made for refraction. The accuracy of lattice parameters measured using this system is predicted to be better than 0.0005 Å. In this study the lattice parameter c is measured using the (002) reflection and a is measured using both the (002) and (015) reflections.

Photoluminescence measurements of the GaN films on SiC were made at 4.2 K using a He-Cd laser ($\lambda=325$ nm) as the excitation source, unless otherwise noted. Further details of the PL system are described in a previous report [13]. The films were grown in an OMVPE system described previously[1]. All of the films were unintentionally doped, with n-type carrier concentrations ranging from 1×10^{17} to below 1×10^{16} /cm³. Both on-axis and vicinal (off-axis) 6-H SiC(0001) wafers were used as substrates. A 1000 Å AlN buffer layer was grown on each substrate at 1100°C before the GaN layer was deposited.

C. Results

The GaN films on SiC exhibited strong near-band-edge emission due to both free and donor-bound excitons. Photoluminescence (PL) from a 3.7 μ m GaN film on SiC at various temperatures is shown in Fig. 1. The emission labeled BX decreases much faster than that labeled FX as temperature increases from 10 to 100 K. This behavior is indicative of excitons bound to neutral donors. The emission labeled FX is due to the recombination of the A free excitons. The high energy shoulder resolved at 100 K is the B free exciton. The GaN films in this study are dominated by the bound exciton emission, and its dependence on lattice parameter values will be discussed in this study.

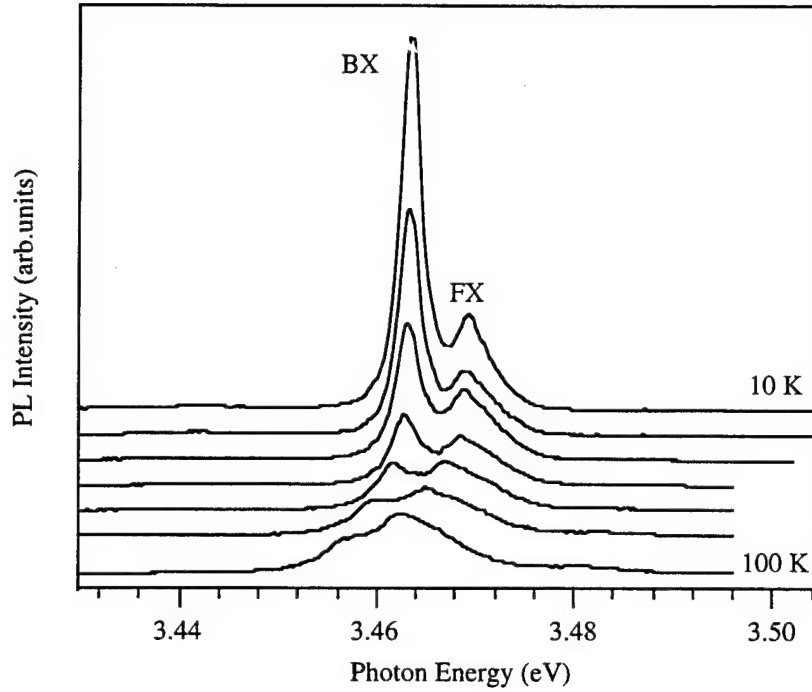


Figure 1. PL of a 3.7 μm GaN layer on SiC at 10, 20, 30, 40, 60, 80 and 100 K.

The bound exciton energy (E_{BX}) determined at 4.2 K as a function of the lattice constant c is displayed in Fig. 2 for a number of GaN films on SiC. These samples were grown at various temperatures and film thicknesses, the effects of which will be discussed later in this report. As c decreases the bound exciton emission shifts to lower energies. The strain along the c -axis, $\Delta c/c_0$, is in response to a strain along the a -axis, $\Delta a/a_0$, due to biaxial stress applied in the plane of the film by thermal mismatch. This relationship is given by Poisson's ratio, where $\nu = (\Delta c/c_0)/(\Delta a/a_0)$. For GaN, values between 0.372 and 0.38 are generally accepted for ν [4,14]. Thus a decrease in the lattice parameter c indicates the tension in the film is increasing, which causes E_g to decrease and E_{BX} to shift to lower energies.

The lattice parameter c for relaxed GaN is 5.1855 Å [15]. As shown in Fig. 2, it falls in the middle of the data, an indication that GaN on SiC can either be in compression or tension, depending on the growth conditions. This is contrary to what is expected, indicating the stress in the film is not entirely due to the differences in thermal expansion coefficients.

From the slope of the data, E_{BX} can be estimated using $E_{\text{BX}} = (-14.76 + 3.561 \cdot c) \text{ eV}$, where c is in angstroms. The relaxed value for E_{BX} is predicted to be 3.469 eV. This compares favorably to values of 3.467 and 3.469 reported for thick relaxed GaN layers on sapphire [7]. The linear dependence between E_{BX} and c indicates that the wide variety of energy values reported for the donor-bound exciton in the literature are due to different amounts of strain. For GaN on sapphire, typical E_{BX} values are between 3.467-3.494 eV, which are in the energy range indicated for films under compression in this report. Included in Fig. 2 is a data point for

a 4.7 μm GaN film grown on sapphire provided by Barbara Goldenberg. This indicates the model in this work can be used to predict E_{BX} using c values for GaN grown on any substrate.

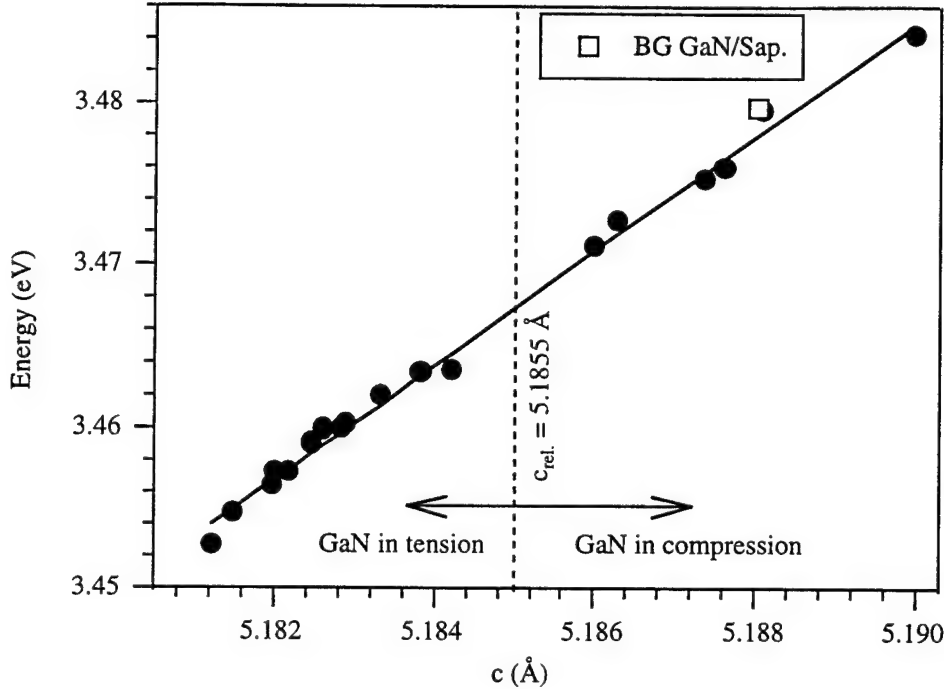


Figure 2. Lattice constant c vs. bound exciton energy (E_{BX}), determined at 4.2 K for GaN on SiC.

The shift of E_{BX} due to biaxial film stress (σ_a) can be estimated using Hooke's law, $\sigma_a = [(c-c_0)/c_0]E/\nu$, where E is the bulk modulus (195 GPa), and ν is Poisson's ratio (.372) [16]. Using the data in Fig. 2, a value of $dE_{\text{BX}}/d\sigma_a = 36.0$ meV/GPa is calculated. This result is higher than that found previously for GaN on sapphire (27 meV/GPa) [17], but it compares favorably to results from hydrostatic pressure experiments (39 and 40 meV/GPa) [18,19].

The dependence of growth temperature on film strain was measured using two films grown at 1050 and 1100°C on both on- and off-axis SiC. The results are shown in Fig. 3. The film thickness is 0.6 μm for each film. For both sets of films E_{BX} is lower for those grown at 1100°C compared to 1050°C, an indication these films are in more tension. This result is expected, as the higher growth temperature increases the thermal gradient for cooling to room temperature. This increases the strain due to thermal mismatch that is given by $\epsilon_{\text{Thermal}} = \Delta T(\alpha_{\text{GaN}} - \alpha_{\text{SiC}})$, where ΔT is the difference between the growth and room temperature and α_{GaN} and α_{SiC} are the thermal expansion coefficients for GaN and SiC, respectively.

A similar energy shift due to strain was seen for the donor-acceptor pair (DAP₁) emission at 3.26-3.27 eV in Fig. 3. This emission is accompanied by two longitudinal optical (LO) phonon

replicas that are 92 and 184 meV lower in energy. This data is displayed more clearly in the insets for both substrates. DAP emission is stronger for thinner films ($<0.7 \mu\text{m}$) due to compensation by shallow acceptors, which reportedly result from carbon impurities trapped at dislocations [20]. The origin of the second set of peaks for the off-axis SiC (DAP₂) is unknown, although recent work suggest that oxygen is acting as a deep donor [21]. This emission shows a similar energy shift.

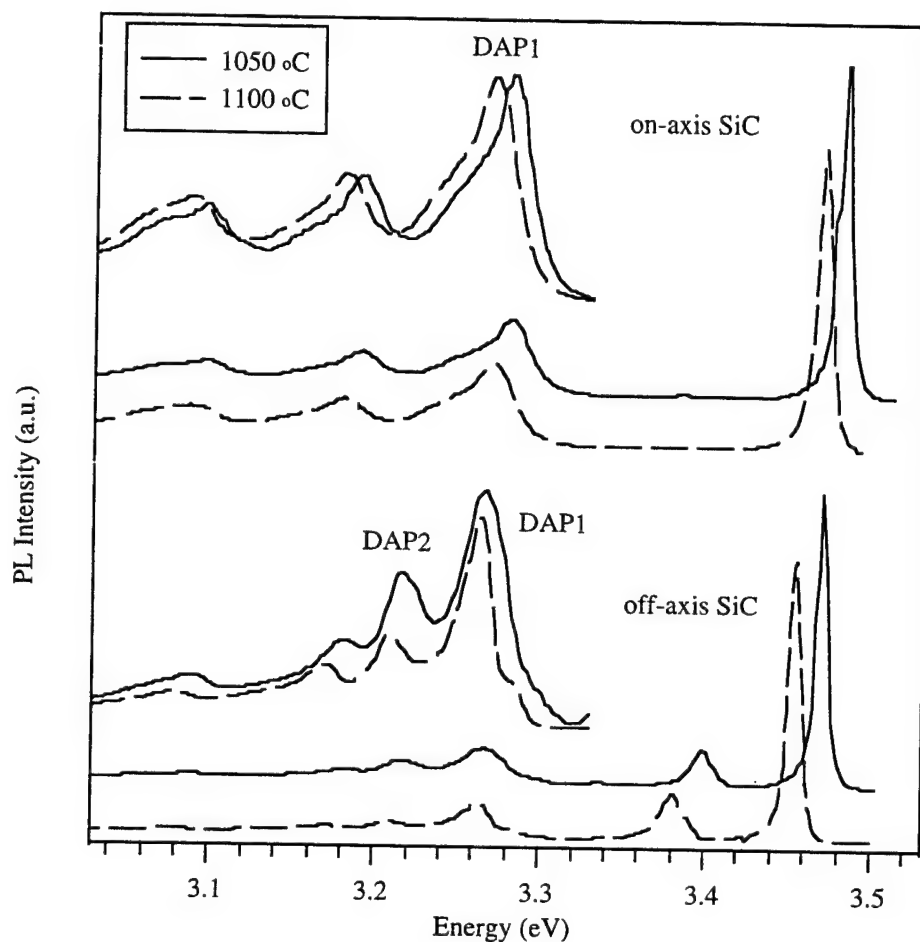


Figure 3. PL from GaN films of equal thickness at $T_g = 1050$ and 1100°C .

A GaN film with a thickness variation of $0.5 \mu\text{m}$ grown on a SiC wafer (30 mm diameter) was used to further study the relationship between lattice constants and E_{BX} . The film thickness was roughly $1.5 \mu\text{m}$ at the center of the wafer to $1.0 \mu\text{m}$ at the edge, as verified by spectroscopic ellipsometry. The variation in the lattice constants c and a across the radius of the wafer are shown in Fig. 9. As thickness decreased a also decreased, indicating that the compressive stresses in the film increased (a was near its relaxed value of 3.1892 \AA at the

wafer center). At the edge of the wafer a increased slightly, indicating the film thickness may have increased slightly. This variation was also seen in spectroscopic ellipsometry.

E_{BX} across the wafer surface, as determined by PL measurements at 4.2 K, is displayed in the inset of Fig. 9. Temperature-dependent PL confirmed this peak is due to the recombination of excitons at neutral donors. E_{BX} increased as the film thickness decreased. At the edge of the wafer E_{BX} increased slightly, similar to the trend seen in the x-ray data.

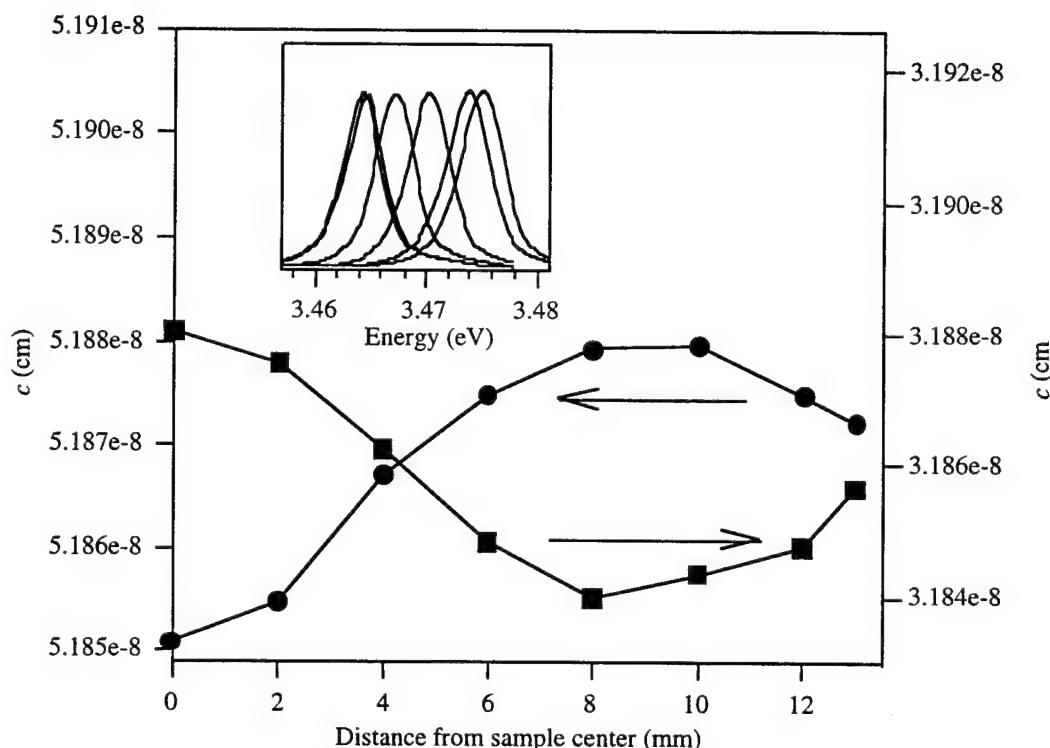


Figure 4. Change in lattice parameters c and a for a GaN film with thickness varying from 1.5 to 1.0 μm across the wafer. Displayed in the inset is the shift in bound-exciton peak across the sample.

The lattice constant c of the AlN buffer layer was also measured using the absolute lattice measurements, and the results are shown in Fig. 10. The 1000 \AA thickness of the buffer layer led to very low x-ray signals, but long count rates were used to improve the accuracy of these measurements to better than .001 \AA . The lattice parameter c for relaxed AlN is 4.982×10^{-8} cm, indicating the buffer layer is in tension across the wafer. However, the accuracy of this value has not been exhaustively studied as in the case of GaN.

Further measurements were made on the AlN buffer layer of selected films. The data is presented in Table I. All of the films listed were grown on off-axis SiC. The stress in each layer was calculated using Hooke's law (tensile stress is positive), where the bulk modulus (E) for GaN and AlN are 195 and 308 GPa, respectively, and ν is Poisson's ratio (0.372) for both

layers [12,14]. The results show that for the GaN films under the strongest tensile stress (152 and 164) the buffer layer is also under tension, with the stress in the AlN buffer layer 9 times that in the GaN layer. Two films have a buffer layer under compression (97 and 110), while the GaN is in tension.

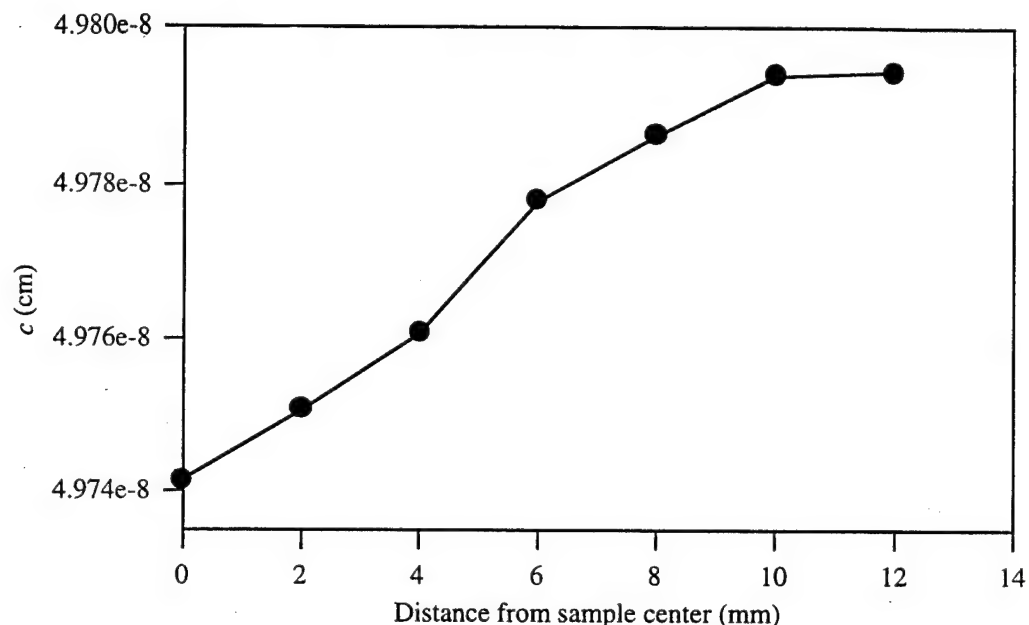


Figure 5. Change in c for AlN buffer layer on SiC, using the (002) reflection with an absolute lattice parameter method.

Table I. Lattice Parameters for GaN Film and Accompanying AlN Buffer Layer

Sample #	c AlN	σ_{AlN}	c GaN	σ_{GaN}
96	4.975E-08	1.142	5.186E-08	-0.100
97	4.982E-08	-0.033	5.183E-08	0.214
152	4.965E-08	2.748	5.182E-08	0.299
110	4.986E-08	-0.693	5.184E-08	0.116
126	4.971E-08	1.730	5.183E-08	0.236
154	4.969E-08	2.124	5.183E-08	0.165
164	4.965E-08	2.735	5.182E-08	0.297

One explanation for these results is that the mismatch between the GaN and AlN layers (4%) are not fully relieved like they are for GaN/AlN/Sapphire, where the AlN buffer layer is polycrystalline. This residual stress may account for the GaN being in compression for some samples, as $a_{\text{AlN}} < a_{\text{GaN}}$. As the GaN film thickness increases the layer would overpower the AlN layer, and the tensile stress due to the thermal mismatch would dominate.

As the tension in the GaN layer increases the AlN layer may try to match it, resulting in the high values of σ_{AlN} for some of the films. Eventually the stress in the AlN layer exceeds a critical stress, resulting in cracking of the AlN buffer layer. TEM of our materials show the AlN buffer layer is very poor structurally, which could provide a number of locations for cracking to begin. Due to the brittle nature of these layers this cracking may act to partially relax the GaN layer as well, similar to the phenomena seen for GaN on sapphire [4].

The dependence of E_{BX} and strain in GaN due to SiC substrate orientation was also investigated. Fourteen of the films in this study were grown concurrently on on-axis and vicinal (off-axis) 6-H SiC(0001) wafers, using a 1000 Å buffer layer, where the off-axis tilt is normally between 3-4°. The results off these runs are displayed in Table II. Film sets 151-154 were part of a growth temperature study. Although their thicknesses are unknown they should all be over 1 µm thick, with the films grown at 950°C the thickest. It should also be noted that the vicinal substrate for film set #192 appears is only 2° off-axis, compared to 3-4° for the other films.

The results show that the thinner (≤ 0.6 µm) films on on-axis SiC are in compression, as indicated by E_{BX} and lattice parameter c values, relative to films grown on vicinal SiC, with an energy difference of up to 15.6 meV. As thickness increases this effect diminishes, with the GaN film grown at 950°C (#154) in tension relative to that grown on vicinal SiC. It is possible that these films are relaxed.

To understand these results it is necessary to examine the growth of GaN on SiC using an AlN buffer layer. During growth an inversion domain boundary readily forms at each SiC step that threads through the AlN buffer layer and possibly into the GaN film. These boundaries are thought to act as relief mechanisms for lattice strain in a manner similar to misfit dislocation/threading dislocation combinations. The density of these boundaries should increase as the number of steps on the SiC increases, i.e. as the off-axis tilt increases.

Initial TEM studies have verified these boundaries are much more prevalent in GaN films grown on vicinal SiC compared to on-axis SiC. Thus it is possible that the stress due to lattice mismatch is not fully relieved for the films on on-axis SiC, which is contrary to what is predicted by critical thickness theory. This would result in a residual compressive stress applied to the GaN film due to the lattice parameter $a_{\text{SiC}} < a_{\text{GaN}}$. Some or all of the residual stress in this scenario may originate from the lattice mismatch between the GaN film and AlN layer, as discussed previously. If this compressive stress is larger than the tensile stress due to thermal expansion mismatch then the GaN films should be in compression.

This hypothesis may explain why the thinner GaN films grown on on-axis SiC are in compression, while films grown concurrently on off-axis SiC for sample sets 181 and 164 are in tension. The compressive strain for GaN film # 192 on off-axis SiC may due to the off-axis tilt only being 2°. The compressive stress for the on-axis films decreases as film thickness

increases. One possible explanation is that as thickness increases the inversion domain boundaries present are long enough to relieve the stress due to lattice mismatch, allowing thermal mismatch effects to dominate the state of stress in the films.

Table II. Comparison of GaN Films on Vicinal (off-axis) and On-axis SiC Substrates

Sample #	on/ off	Growth Temp. (°C)	film thick. (μm)	Energy (eV)	$E_{\text{on}}-E_{\text{off}}$ meV	c (Å)	$C_{\text{on}}-C_{\text{off}}$
164	on	1100	.6	3.473		5.186E-08	
164	off	1100	.6	3.457	15.5	5.182E-08	4.26E-11
181	on	1050	.6	3.483		5.190E-08	
181	off	1050	.6	3.467	15.6	5.183E-08	7.20E-11
192	on	1050	.3	3.479		5.188E-08	
192	off	1050	.3	3.475	4.29	5.187E-08	7.15E-12
110	on	1050	1.4	3.466			
110	off	1050	1.4	3.463	2.52		
151	on	1000	>1	3.455		5.182E-08	
151	off	1000	>1	3.453	2.02	5.181E-08	2.76E-12
152	on	1050	>1	3.457		5.182E-08	
152	off	1050	>1	3.456	.77	5.182E-08	1.86E-12
154	on	950	>1	3.460		5.183E-08	
154	off	950	>1	3.462	-1.64	5.183E-08	-4.21E-12

D. Conclusions

We have presented photoluminescence and x-ray results for GaN films on SiC substrates. A linear dependence was seen between the bound exciton peak energy (E_{BX}) and the lattice constant c . From this data E_{BX} for relaxed GaN ($c=5.1855$ Å) is 3.469 eV, which agrees favorably with results for relaxed GaN on sapphire. From the slope of the data it is possible to estimate E_{BX} from x-ray data and vice-versa.

The results also show that GaN on SiC can either be in compression or tension, depending on the growth conditions. This indicates that the stresses are not entirely due to the mismatch in thermal expansion coefficients. One possibility is that there is some residual stress due to lattice mismatch, which would add compressive stresses to the film. This compressive stress appears to decrease with thickness, as the tension in the film increased with thickness (until cracking occurs to relieve stress).

Two possible sources for this residual stress were discussed. One is that residual stress may exist between the GaN film and the AlN buffer layer. This residual stress, however small, would act to counterbalance the tensile stress due to thermal mismatch.

The other possibility is that the on-axis SiC substrate does not offer enough steps for inversion domain boundary to form and fully relieve stress in the GaN film during growth. The result is that residual stress would exist due to lattice mismatch between GaN and SiC, and quite possibly GaN and AlN. This explanation is supported by the difference in the state of strain between thin GaN films grown concurrently on vicinal and on-axis SiC.

One possible source of GaN film relaxation is the cracking of the AlN buffer layer. Calculations show that the tensile stress in the AlN buffer layer is nine times higher than those in GaN films under the most tension in this study. If the stress in the AlN exceeds a critical stress then cracking would result. This cracking may act to relieve stress in the whole structure.

E. References

1. T. W. Weeks, M. D. Bremser, K. S. Ailey, E. Carlson, W. G. Perry, and R. F. Davis, *Appl. Phys. Lett.* **67** (3), 401 (1995).
2. K. Hiramatsu, T. Detchprohm, and I. Akasaki, *Jpn. J. Appl. Phys.* **32** (4), 1528 (1993).
3. X. J. Ning, F. R. Cein, P. Pirouz, J. W. Yang, and M. A. Khan, *J. Mater. Res.* **11**, 580 (1996).
4. T. Detchprohm, K. Hiramatsu, K. Itoh, and I. Akasaki, *Jpn. J. Appl. Phys.* **31** (10B), L1454 (1992).
5. S. Tanaka, PhD thesis, NCSU.
6. Krishnankutty, R. M. Kolbas, M. A. Khan, J. N. Kunzia, J. M. Van Hove and D. T. Olson, *J. of Electron. Mat.* **21** (6), 609 (1992).
7. C. Merz, M. Kunzer, and U. Kaufmann, submitted to *Phys. Rev. B.*, 1995.
8. B. Monemar, J. P. Bergman, I. A. Buyanova, H. Amano, I. Akasaki, K. Hiramatsu, N. Sawaki, and T. Detchprohm, presented at the Topical Workshop on III-V Nitrides, Nagoya, Japan (1995).
9. D. Volm, K. Oettinger, T. Streibl, D. Kovalev, M. Ben-Chorin, J. Diener, B. K. Meyer, J. Majewski, L. Eckey, A. Hoffman, H. Amano, I. Akasaki, K. Hiramatsu, and T. Detchprohm, submitted to *Phys. Rev. B.*, 1995.
10. H. Amano, K. Hiramatsu, and I. Akasaki, *Jpn. J. Appl. Phys.* **27** (8), L1484 (1988).
11. W. J. Choyke and I. Linkov, *Inst. Phys. Conf. Ser.* **137** (3), 141 (1994).
12. P. F. Fewster and N. L. Andrew, *J. Appl. Cryst.* **28**, 451 (1995).
13. Nitride Semiconductors for Ultraviolet Detection, Semiannual Report, 1995.
14. V. A. Savastenko and A. U. Sheleg, *Phys. Status Solidi A* **48**, 135 (1978).
15. C. M. Balkas, C. Basceri, and R. F. Davis, *Powder Diffraction* **10**, 266 (1995).
16. D. Gerlich, S. L. Dole and G. Slack, *J. Phys. Chem. Solids* **47**, 437 (1986).
17. W. Rieger, T. Metzger, H. Angerer, R. Dimitrov, O. Ambacher, M. Stutzmann, *Appl. Phys. Lett.* **68** (7), 970 (1995).
18. W. Shan, T. J. Schmidt, R. J. Hauenstien, J. J. Song and B. Goldenberg, *Appl. Phys. Lett.* **66** (25), 3492 (1995).
19. P. Perlin, I. Gorczyca, N. E. Christensen, I. Grzegory, H. Teisseyre, and T. Suski, *Phys. Rev. B* **45** (13), 307 (1992).
20. E. R. Glaser, T. A. Kennedy, S. W. Brown, J. A. Freitas, Jr., W. G. Perry, M. D. Bremser, T. W. Weeks, and R. F. Davis, *Gallium Nitride and Related Materials*, edited by Russell D. Dupuis, Fernando A. Ponce, John A. Edmond, and Shuji Nakamura (Materials Research Society, Pittsburgh, 1996), in press.
21. G. D. Chen, M. Smith, J. Y. Lin, H. X. Jiang, A. Salvador, B. N. Sverdlov, A. Botchkary, and H. Morkoc, *J. Appl. Phys.* **79**, 2675 (1996).

XI. UV Photoemission Study of Heteroepitaxial AlN Films Grown on 6H-SiC Non-Polar Surfaces

A. Introduction

There is increasing interest in electronic devices composed of III-nitride materials for optoelectronic applications in the blue and UV region [1]. An alternative application of these semiconductors is in electron emission devices. Recent studies have demonstrated that diamond surfaces can exhibit a negative electron affinity (NEA). NEA surfaces may prove to be critical elements for cold cathode devices, vacuum microelectronics, and photodetectors [2,3]. In addition to diamond, thin films of AlN grown on 6H SiC have been shown to exhibit a negative electron affinity (NEA) [4,5]. Some AlN NEA surfaces were obtained from air exposed surfaces and do not appear to be readily poisoned. In contrast to diamond, AlN and GaN materials exhibit the wurtzite crystal structure. One of the most significant limitations in the application of diamond is that reliable n-type doping has not been achieved. In contrast, n-type doping has been obtained for GaN and some AlGa_N alloys. This study explores further the electron affinity of epitaxial AlN films on 6H-SiC of different orientations. Specifically, we study the electronic properties of AlN grown on the non-polar surfaces of SiC.

The wurtzite AlN and GaN form a continuous solid solution of Al_xGa_{1-x}N for $0 \leq x \leq 1$ with bandgaps that range from 3.4 eV (GaN) to 6.2 eV (AlN). Figure 1 displays the bandgap of several materials as a function of the equivalent hexagonal lattice constant. The alloys are also miscible with In, hence the inclusion of InN could extend the range to 1.9 eV. The electron affinity of a semiconductor is related to the surface dipole and to the fundamental energy levels of the materials. Because the valence and conduction bands of the semiconductors have origin in the sp^3 bonding and antibonding levels, it may be suggested that the larger bandgap materials will exhibit a smaller or negative electron affinity. In comparison with diamond, it might be assumed that AlGa_N alloys with a bandgap greater than 5.4 eV could exhibit an NEA. In this paper, studies are reported of AlN grown on alternative substrate orientations.

The AlN films used in this study were grown on 6H-SiC substrates. The n-type SiC substrates used have a small lattice mismatch with AlN (3.08 Å vs. 3.11 Å) and GaN ($a = 3.19$ Å). The small lattice mismatch enables heteroepitaxial growth of the wurtzite (2H) structure. Furthermore, the fact that the substrates are conducting avoids charging problems associated with photoemission from large bandgap and insulating materials.

The electron affinity of a semiconductor or the presence of an NEA can be determined by ultraviolet photoemission spectroscopy (UPS) [6-8]. The experiments described here involve directing 21.2 eV light (the He I resonance line) to the surface of the sample and detecting the spectrum of the emitted photo excited electrons as a function of electron kinetic energy.

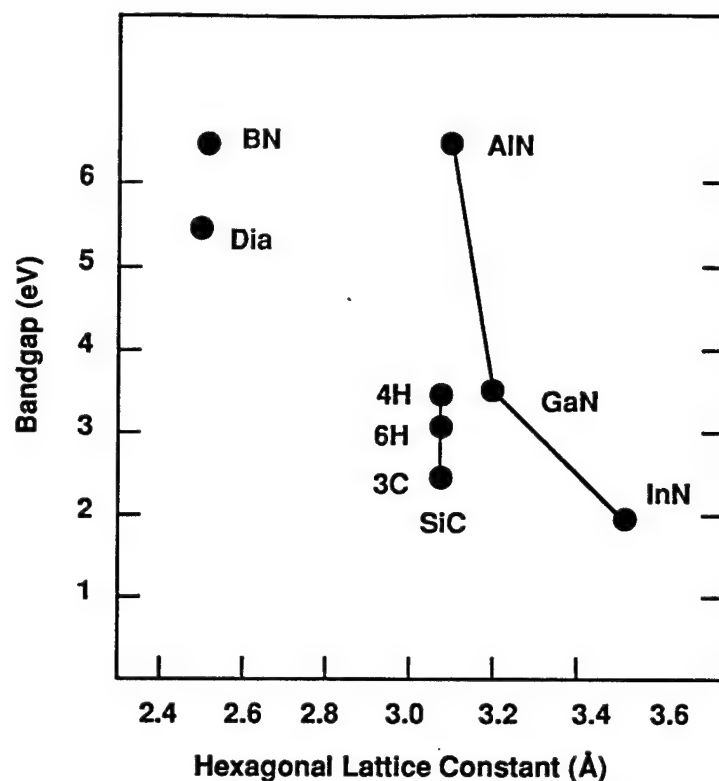


Figure 1. The bandgap vs. hexagonal lattice constant (a) for a variety of wide bandgap semiconductors. The lattice constant for the cubic materials has been determined from the (111) plane.

Typically, UPS is used to obtain a profile of the valence band (VB) electronic states. As such, most studies of UPS of semiconductors present data of the most energetic electrons emitted from the surface. Electrons scattered to lower energy and secondary electrons will be displayed in the spectrum at lower kinetic energies. In addition, for a semiconductor which exhibits an NEA surface, a distinctive peak may be observed at the low kinetic energy (highest binding energy) end of the photoemission spectra. Figure 2 depicts a schematic representation of the photoemission spectra from a semiconductor with a negative or positive electron affinity. The low kinetic energy feature is due to secondary electrons which (quasi) thermalize to the conduction band minimum. Note that the solid line indicates a material with a positive electron affinity while the dashed line is a feature indicative of an NEA. In this paper, samples with both positive and negative affinity surfaces are discussed.

The sharp features typical of an NEA have been observed from spectra of (111) and (100) diamond surfaces [6-10]. In the studies of diamond, a correlation was made between the presence of hydrogen and the NEA peak [9,10]. In addition, it was also shown that thin metal layers such as Ti or other moderate work function metals could induce an NEA on the diamond surface [10,11]. These measurements verify that the surface dipole can be influenced by surface processing and that the effects contribute to the observation of an NEA.

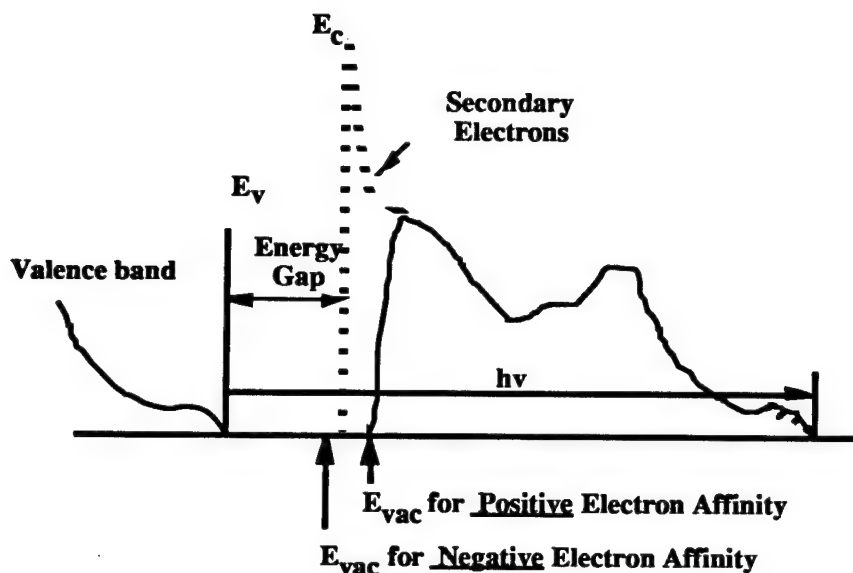


Figure 2. A schematic of the difference in the photoemission spectra of a semiconductor with a positive or negative electron affinity.

B. Experimental Procedure

The 6H-SiC substrates used in this study were supplied by Cree Research, Inc. The samples were n-type with doping concentrations of 10^{16} to $10^{18}/\text{cm}^3$. To avoid surface contamination the AlN samples were grown in the integrated UHV transfer system by gas source molecular beam epitaxy (GSMBE). This system includes the UPS system, LEED, Auger, hydrogen and argon plasma processing chamber, and XPS as well as the GSMBE. The system is described elsewhere [9,11]. Recently added is the capability of gas source MBE (GSMBE) to grow undoped AlN and GaN films.

Nitride thin films were previously grown on n-type, Si-face $\alpha(6\text{H})\text{-SiC}(0001)$ substrates at $1000\text{-}1050^\circ\text{C}$. The other substrate wafers were SiC $\langle 1010 \rangle$ and $\langle 1120 \rangle$ surfaces. The as-received SiC pieces were degreased, dipped into a 10% HF solution for 10 minutes to remove the thermally grown oxide layer and blown dry with N_2 before being loaded onto the transfer system. We examine AlN layers on (1010) and (1120) SiC as well as reporting, for the first time, AlN on C face (0001) SiC.

The growth took place in a GSMBE. The cleaning procedure is described above, once in vacuum the substrate is annealed in a silane flux [12]. The samples were not intentionally doped, but since very thin films were employed, charging problems were avoided. Al and Ga are solid sources in K cells while ammonia (NH_3) provides the N source.

The UPS measurements were excited with 21.21 eV radiation (He I resonance line), and emitted electrons are collected with a hemispherical energy analyzer. The base pressure of the UPS system is 2×10^{-10} Torr, and operating conditions involve pressures up to 1×10^{-9} Torr,

but the higher pressure is due to the helium inflow and does not contaminate the sample. The 50 mm mean radius hemispherical electron analyzer was operated at a 0.15 eV energy resolution and a 2° angular resolution. The analyzer (VSW HA50) is mounted on a double goniometer and can be tilted with respect to the sample in two independent directions. The samples were fastened with tantalum wire to a molybdenum sample holder. The sample holder is biased by up to 3 V to allow low energy electrons to overcome the work function of the analyzer. The Fermi level of the system (sample and analyzer) is determined by UPS measurement of the sample holder with no sample bias (i.e., grounded). The sample holder can be heated to 1150°C, and the temperature is measured by a thermocouple.

C. Results and Discussion

The UV photoemission spectra of the (1010) and (1120) samples are shown in Fig. 3. The AlN films were prepared in by GSMBE and transferred under UHV to the photoemission system. Samples were biased with 2-3 V to overcome the work function of the analyzer, and all spectra were shifted to be aligned at the valence band maximum. The spectra were scaled such that the strongest emission was the same for all curves.

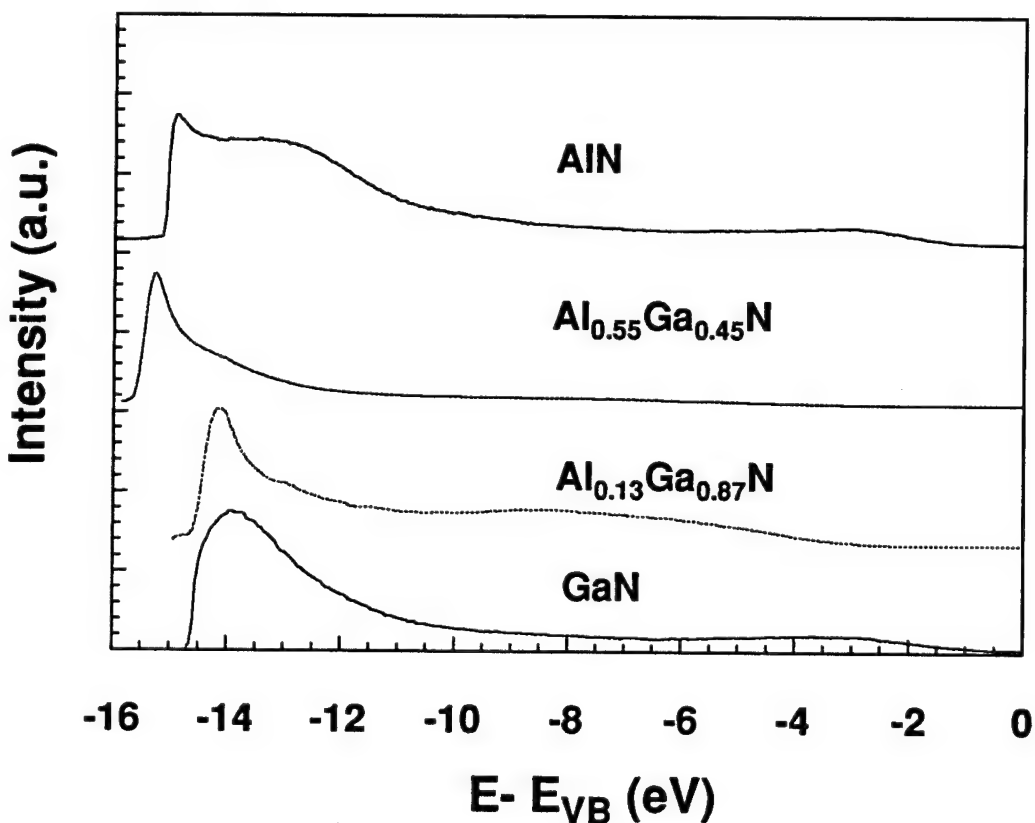


Figure 3. The UV photoemission spectra of AlN grown on the (1010) and (1120) surface. Spectra were aligned at the valence band maximum.

A more precise description of the relation of the NEA is obtained from the spectral width. The spectral width is obtained from a linear extrapolation of the emission onset edge to zero intensity at both the low kinetic energy cutoff and at the high kinetic energy end (reflecting the valence band maximum). For a material with a positive electron affinity, Fig. 2 shows that $\chi = h\nu - E_g - W$, and for a material with a negative electron affinity Fig. 2 indicates that $0 = h\nu - E_g - W$, or rewriting, $h\nu = E_g + W$. Note that the photoemission measurements cannot be used to determine the energy position of the electron affinity for the NEA case.

To determine the energy position of the valence band maximum, the spectral gain was increased, and the intensity was extrapolated to 0 emission. The spectra for the two oriented surfaces are aligned in Fig. 3 at the deduced valence band maximum. In applying the relations noted above, the bandgap of the bulk AlN must also be known. The literature value of the AlN bandgap is 6.2 eV.

Another aspect that is evident from the photoemission spectra is the position of the surface Fermi level relative to the valence band maximum. Features are seen indicative of Fermi level pinning which might be due to impurities. In particular, the strong affinity of Al with oxygen often results in increased oxygen incorporation for these films.

The AlN grown on C face SiC has a positive affinity which is in agreement with theory [13]. It is expected that growth on Si face (0001) gives Al terminated AlN while growth on the C face gives N terminated AlN. It is expected that H termination will induce a negative electron affinity on N terminated AlN. This surface was terminated with hydrogen and while this reduced the affinity, it was still positive.

AlN grown on silicon surfaces were studied also. Samples grown in the integrated system showed no LEED pattern and exhibited positive affinity. Also observed is that AlN grown on (0001) SiC will exhibit positive affinity if no LEED pattern is evident. These two observations lead to the conclusion that surface disorder tends to produce positive affinity surfaces.

While previous results have shown that hydrogen can induce a negative electron affinity surface on diamond [7,10], less clear is the effect of H termination on AlN. Additionally, no effort was made to control the surface termination for these samples. For diamond, it was found that the observation of an NEA is critically dependent on the surface termination. It is evident that further studies are necessary to characterize the surfaces more completely.

D. Conclusions

In summary, we have observed features in the UPS spectra indicative of an NEA surface for AlN grown on (0001) Si face SiC and (1010) SiC while growth on the C face of (0001) and the (1120) surface have positive affinities. The AlN NEA surfaces spectra exhibited both the sharp features at low kinetic energy that have been found to be characteristic of an NEA, and the width of the spectra was also consistent with the observed effect. Furthermore, surface

disorder was found to lead to positive affinity surfaces. The surface Fermi level was found to be pinned towards the middle of the band gap for the samples, and this may indicate oxygen impurities.

E. Acknowledgments

This work was supported in part by the Office of Naval Research through grants N0014-92-J-1477 and N0014-92-J-1604. The SiC substrates used were supplied by Cree Research .

F. References

1. S. Strite and H. Morkoç, J. Vac. Sci. Technol. B **10**, 1237 (1992).
2. J. H. Edgar, J. Mater. Res. **7**, 235 (1992).
3. M. D. Williams, M. D. Feuer, S. C. Shunk, N. J. Sauer, and T. Y. Chang, J. Appl. Phys. **71**, 3042 (1992).
4. M. C. Benjamin, C. Wang, R. Davis, and R. J. Nemanich, Appl. Phys. Lett. **64**, (1994).
5. M. C. Benjamin, C. Wang, R. S. Kern, R. F. Davis, and R. J. Nemanich, Mat. Res. Soc. Symp. **339**, 81 (1994).
6. F. J. Himpsel, J. A. Knapp, J. A. van Vechten and D. E. Eastman, Phys. Rev. B **20**, 624 (1979).
7. B. B. Pate, Surf. Sci. **165**, 83 (1986).
8. B. B. Pate, M. H. Hecht, C. Binns, I. Lindau and W. E. Spicer, J. Vac. Sci. Technol. **21**, 364 (1982).
9. J. van der Weide and R. J. Nemanich, J. Vac. Sci. Technol. B **10**, 1940 (1992).
10. J. van der Weide and R. J. Nemanich, Appl. Phys. Lett. **62**, 1878 (1993).
11. J. van der Weide and R. J. Nemanich, Phys. Rev. B **50**, 13629 (1994).
12. R. Kaplan, Surface Science **215**, 111 (1989).
13. J. Bernholc, Private Communication (1996).

XII. New Buffer Layers for GaN on Sapphire by Atomic Layer and Molecular Stream Epitaxy

A. Introduction

Good quality GaN has been grown by conventional MOCVD and ECR-assisted MBE. For GaN/InGaN grown on sapphire using an AlN/GaN buffer, the large lattice mismatch and thermal mismatch between GaN and sapphire is known to enhance three-dimensional nucleation that may lead to low angle grain boundaries. The most common buffer layer growth method involves depositing a low temperature AlN or GaN film then anneal at 1000°C or higher to recrystallize before depositing the GaN film [1-3].

This approach has worked well and several device structures including a blue LED based on the AlGaIn/InGaIn/AlGaIn double heterostructure was produced in Japan based on this buffer layer growth method. However, this method has several problems. First, the electrical properties of the GaN critically depend on the thickness of this buffer layer. Second, the recrystallization of this buffer layer produces low angle grain boundaries that form a source of dislocation nucleation and propagation to the epilayer surface with a density of $\sim 10^{10} \text{ cm}^{-2}$. And third, these dislocations can be perpendicular to the GaN/buffer layer interface and thread to the growing surface making their reduction by dislocation interaction and annihilation less probable.

In an attempt to reduce the defect density of GaN grown on sapphire, we report on two different approaches for the buffer layer growth; Atomic Layer Epitaxy (ALE) and Molecular Stream Epitaxy (MSE). These techniques can enhance two-dimensional growth of the buffer layer opposed to the three-dimensional growth of the low temperature then annealed AlN buffer. Both techniques were developed by our group in the epitaxial growth of GaAs and their related compounds [4-7].

In ALE, the substrate rotates between two streams; one containing metalorganics (MO) and the second, NH_3 , as shown in Fig. 1a. ALE offers the advantage of reactant gas separation, thereby eliminating gas-phase reactions which can hinder high-quality material growth. The MSE process is shown in Fig. 1b where the substrate rotates crossing one stream containing both MO and NH_3 thus depositing a few monolayers per rotation. The deposited layer is being annealed during the rest of the cycle and, for example, for a 30 rpm rotational speed growing by MSE, the growth time is 0.2 seconds followed by an annealing time of 1.8 seconds. For conventional MOCVD, the susceptor is stationary and both reactant gases flow over the substrate simultaneously. Typical rotation rates are 30 to 60 rpm. The design of our reactor allows the growth of III-nitride thin films by either conventional MOCVD, MSE, or ALE or any combination of the three.

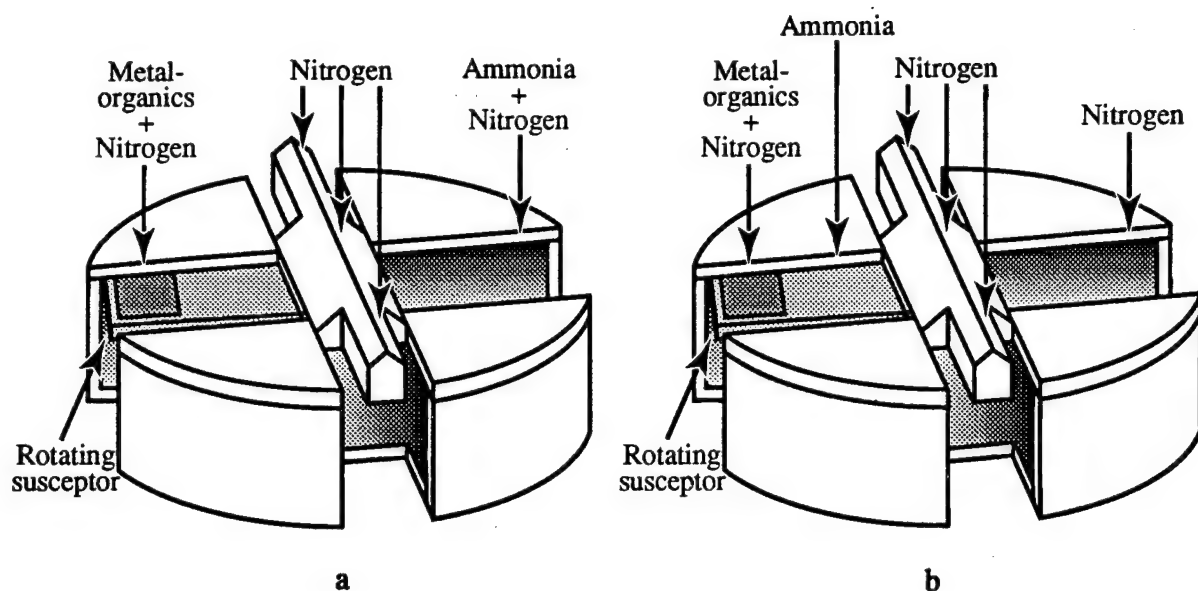


Figure 1 a) Schematic drawing of the susceptor and gas flow locations for the ALE growth method; b) schematic drawing of the susceptor and gas flow locations for MSE and MOCVD growth methods.

B. Experimental Procedure

The nitride films are grown on on-axis (0001) sapphire. Prior to growth, the substrate is cleaned and etched in $\text{H}_2\text{SO}_4:\text{H}_2\text{O}_2$ (1:1) for 45 minutes at 120°C . It is then annealed at 1050°C for 15 minutes inside the reactor and then passivated with ammonia for 1 minute. The layers are grown at temperatures ranging from 550 to 900°C . Column III reactants are TMAI ($+18^\circ\text{C}$), TMGa (-10°C), and EDMIn ($+10^\circ\text{C}$) with flows varying from 3-15, 1-8, and 15-120 sccm, respectively. The column V reactant is NH_3 with flows in the range of 0.5-2 slm. The carrier and purge gases are purified nitrogen. The pressure in the growth chamber can also be varied from less than 100 torr to atmospheric. All samples grown are characterized by double crystal x-ray diffraction (DCXRD) and transmission electron microscopy (TEM) will also be used for interface and microstructural analysis. Photoluminescence (PL) will be used to assess the optical properties.

C. Results

It is well known that a strained layer superlattice (SLS) can be used to suppress threading dislocations in zinc-blende semiconductor epilayers. However, the threading dislocations in GaN films are mostly perfect edge type that have slip planes of $\{1100\}$ type, which require larger resolved shear stress to initiate glide. Furthermore, since the strain field introduced by the SLS is parallel to the (0001) growth plane, the resolved shear stress on the $\{1100\}$ plane is zero. Therefore, it can be expected that, to suppress or eventually eliminate this type of threading dislocation with a SLS could be difficult. The nature of these threading dislocations suggests that it is important to carefully select the thickness, deposition parameters and growth

mode of the buffer layer to minimize or avoid formation of the edge type dislocation in the III-nitride films.

In this work we have studied the effect of the buffer layers grown by MSE and ALE on the crystalline quality and defect densities of the grown GaN films. The objective is to enhance two dimensional growth of a single crystal buffer layer at lower growth temperatures. Lower growth temperatures reduce the effect of the thermal mismatch between the grown layers and the substrate. The two dimensional growth will enhance the lattice mismatch relief by forming misfit dislocations that are parallel to the interface between the buffer layer and the substrate. We studied the effect of the growth parameters of the buffer layer such as the gas flows, growth temperature and the reactor pressure on the crystalline quality of the grown films.

To compare the effect that the buffer layer has on the GaN film, buffer layers grown by MSE and ALE were observed in cross-sectional TEM (XTEM). For all samples, the substrate was (0001) sapphire and the GaN on the buffer was grown by conventional MOCVD at 900°C. The GaN films are single crystalline as determined by x-ray diffraction and selected area diffraction in the TEM.

ALE Grown Buffer Layer. GaN films on ALE grown buffer layers show a significant reduction in the density of threading dislocations; in the low 10^9 range. Figure 2 shows the microstructure of a thin GaN film ($\sim 0.3 \mu\text{m}$) grown at 750°C on a 3.5 nm AlN buffer layer deposited at 700°C and 100 Torr by ALE. The quality of this film is reflected in the FWHM of 130 arc seconds obtained by DCXRD and shown in Fig. 3. (The absence of the (0002) AlN peak is due to the thinness of the film.) It should be noted that this 130 arcsec FWHM is for a film which is less than the thickness required ($0.4 \mu\text{m}$) for obtaining significant dislocation interaction and reduction. An even lower FWHM would be observed for the same film grown thicker ($1.0 \mu\text{m}$ or greater). PL analysis indicates a sharp GaN band edge peak at 368 nm with no deep level peaks observed.

There are several features observed in films grown on ALE buffer layers. First, the layers grow by two dimensional growth modes as single crystals at lower temperatures with thicknesses as small as 2 nm. Second, the lattice mismatch between the buffer layer and the sapphire substrate is mainly relieved by forming misfit dislocations at the buffer/substrate interface. Figure 4 illustrates these interfacial misfit dislocations. These misfit dislocations are in contrast under two beam diffraction conditions where the operating g-vector is a basal plane vector and are not observed under $g = [0002]$. This indicates that these misfit dislocations are perfect dislocations of the $1/3\langle 1120 \rangle$ type. From the diffraction contrast in the figure, these dislocations are parallel to the interface which is the favorable conditions for relieving lattice mismatch in these materials.

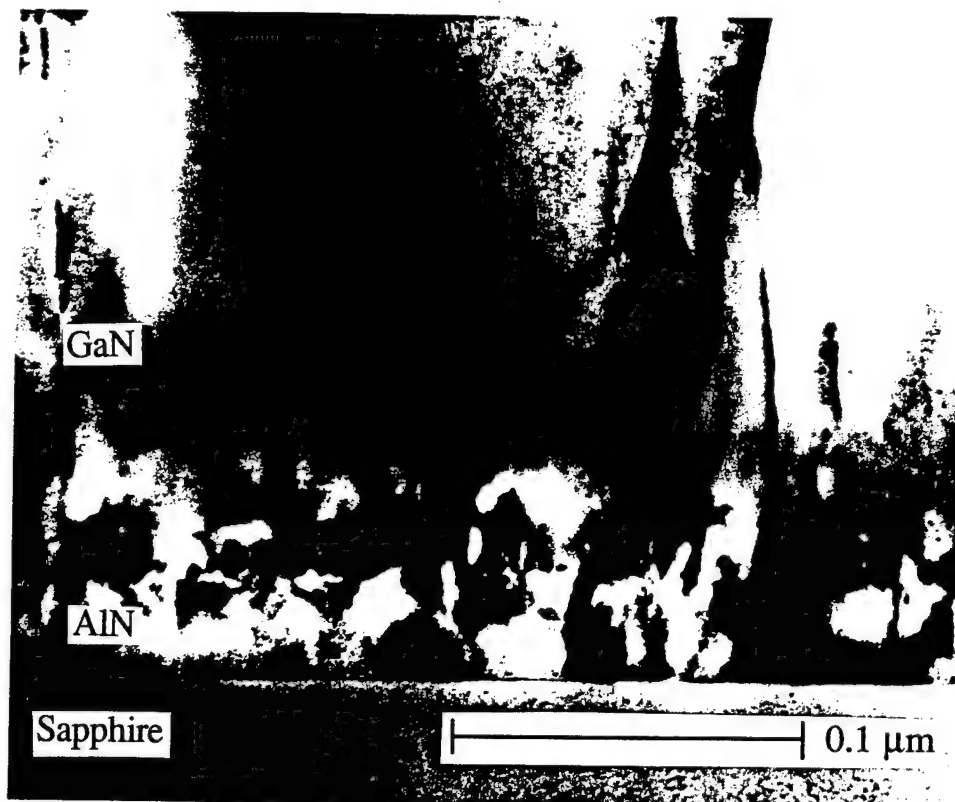


Figure 2. XTEM micrograph of GaN grown on (0001) sapphire at 900°C by MOCVD buffered by an AlN layer grown at 700°C and 100 torr by ALE.

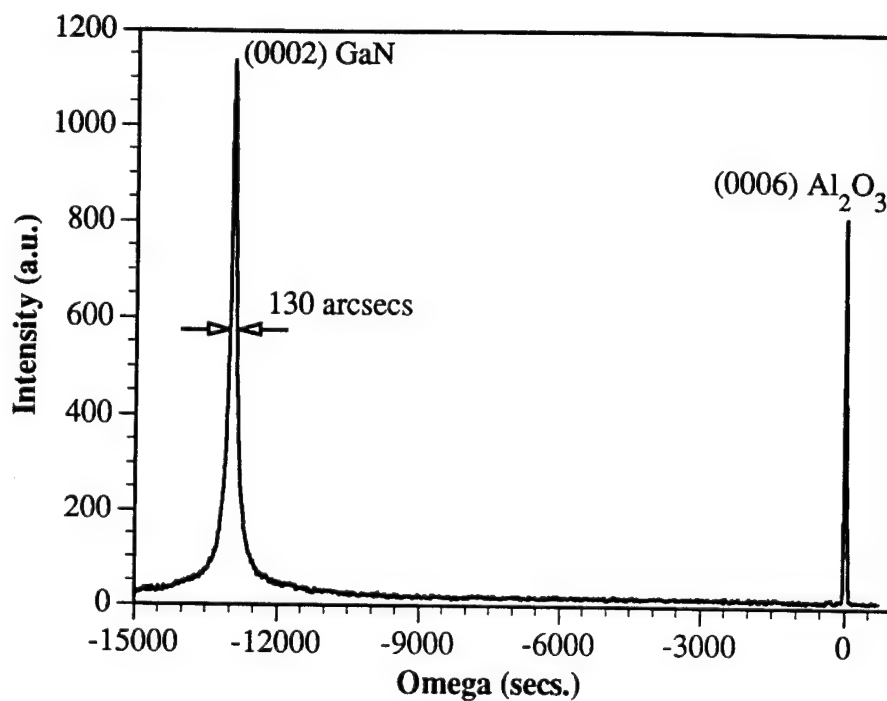


Figure 3. DCXRD of MOCVD GaN epilayer on a 700°C/100 torr ALE AlN buffer with (0001) sapphire as the substrate.

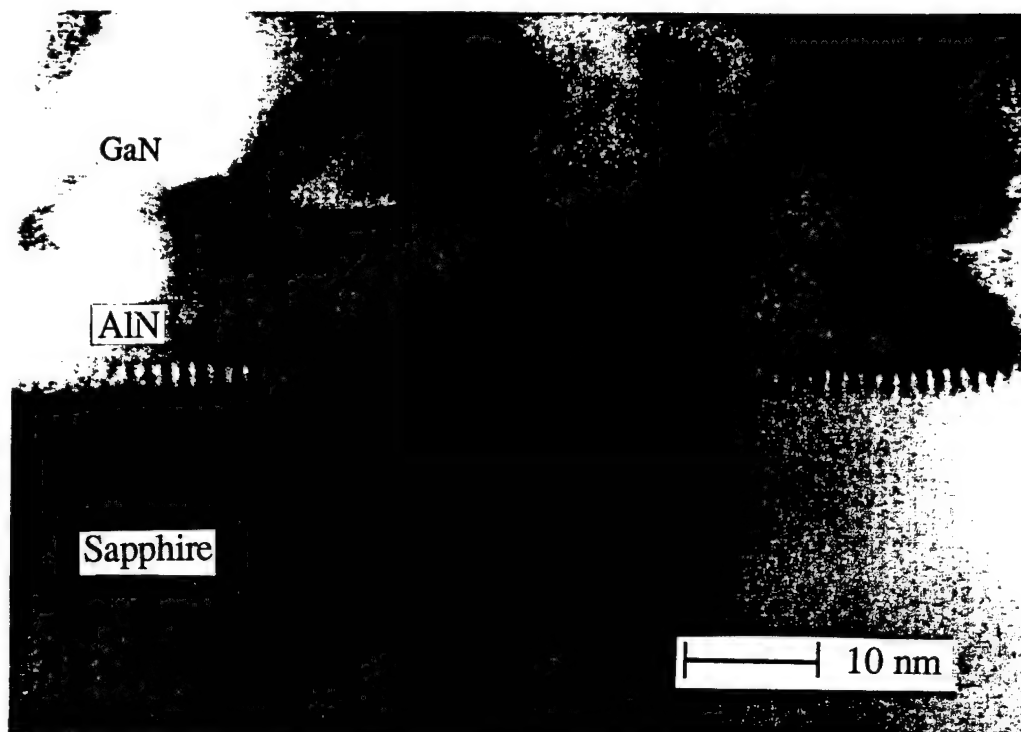


Figure 4. XTEM micrograph of MOCVD GaN grown on an ALE AlN buffer all on a sapphire substrate showing strain contrast fringes at the buffer/substrate interface indicating misfit strain relief by the formation of interfacial misfit dislocations.

MSE Grown Buffer Layer. Figure 5 shows a XTEM brightfield micrograph of GaN grown on an AlN buffer layer deposited at 900°C/100 Torr by MSE. Threading dislocations of the same order of magnitude seen in conventional buffer layer growth methods are observed as a result of the misfit strain caused by the mismatch between the epilayer and substrate lattices, and low angle grain boundaries. The defect density is highest at the GaN/buffer layer interface and decreases with increasing thickness of the GaN layer as observed by others [8]. The DCXRD FWHM for films grown on these buffer layers are as low as 510 arc seconds as shown in Fig. 6. However, this mode of growth has not been fully optimized.

D. Conclusions

The results of several studies into the effect the buffer layer has on the quality of GaN films has been presented. The ALE buffer layer growth technique offers a promising alternative to the commonly used low temperature/annealed technique. The MSE buffer layer growth technique has comparable crystal quality to the more commonly used technique. Optimization of the growth conditions help in obtaining good quality buffer layers, as well as studying the optimum thickness and its effect on the dislocation density, microstructure, electrical and optical properties of device quality GaN and InGaN films.

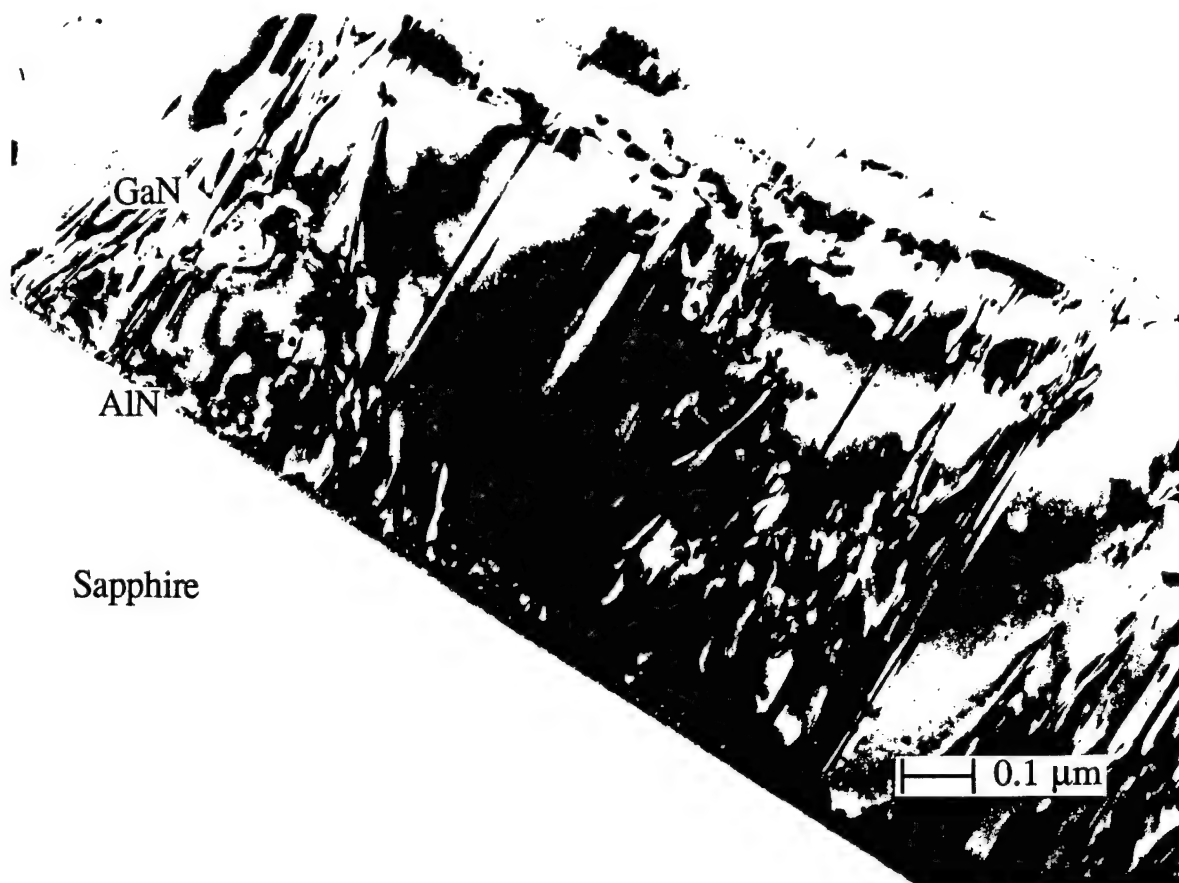


Figure 5. XTEM micrograph of MOCVD GaN on (0001) sapphire buffered by an AlN layer grown at 900°C and 700 Torr by MSE.

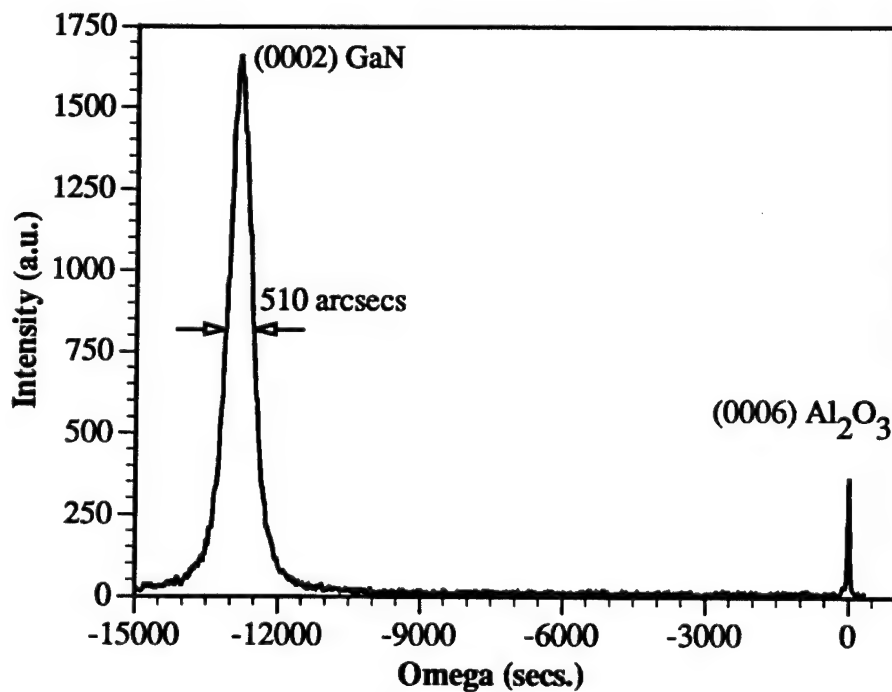


Figure 6. DCXRD of MOCVD GaN/MSE AlN buffer on a (0001) sapphire substrate.

E. References

1. H. Amano, T. Asahi, and I. Akasaki, *Jpn. J. Appl. Phys.* **29**, L205 (1990).
2. S. Nakamura, Y. Harada, and M. Seno, *Appl. Phys. Lett.* **58**, 2021 (1991).
3. J. N. Kuznia, M. Asif Khan, D. T. Olson, R. Kaplan, and J. Freitas, *J. Appl. Phys.* **73**, 4700 (1993).
4. S. M. Bedair, M. A. Tischler, N. Katsuyama, and N. A. El-Masry, *Appl. Phys. Lett.* **47**, 51 (1985).
5. N. Katsuyama, M. A. Tischler, N. Karam, N. A. El-Masry, and S. M. Bedair, *Appl. Phys. Lett.* **51**, 529 (1987).
6. S. M. Bedair, B. T. McDermott, Y. Ide, M. A. Tischler, and N. A. El-Masry, *J. Cryst. Growth* **93**, 182 (1988).
7. S. M. Bedair, and N. A. El-Masry, *Appl. Surf. Sci.* **82**, 7 (1994).
8. W. Qian, M. Skowronski, M. De Graef, K. Doverspike, L. B. Rowland, and D. K. Gaskill, *Appl. Phys. Lett.* **66**, 1252 (1995).

XIII. Growth of High Quality InGaN Films by Metalorganic Chemical Vapor Deposition

A. Introduction

Blue, green, and yellow emission from nitride compounds can rely on impurity transitions in the GaN or $\text{In}_x\text{Ga}_{1-x}\text{N}$ active layers [1-3]. This approach works fairly well in LED's with a low current injection, however band to band transitions and broad emissions are also observed when a high injection level is used, such as might be expected in semiconductor lasers [4]. Rather than moving the emission wavelength through deep impurity levels, the more efficient band edge transition, that necessitates an $\text{In}_x\text{Ga}_{1-x}\text{N}$ ($x > 0.2$) active layer may be a better alternative to achieve light emitting devices that emit from the blue through orange region of the visible spectrum. While there have been many reports on the growth of high quality GaN films by MOCVD in recent years, fewer reports have been published on the growth of high-quality $\text{In}_x\text{Ga}_{1-x}\text{N}$, having structural and optical properties that are approaching device quality.

In addition to the usual problems facing MOCVD III-nitride growth such as the lack of suitable substrates, the growth of InGaN alloys by MOCVD can suffer from several other difficulties. These difficulties include: 1) The high equilibrium vapor pressure of nitrogen that is required during growth to prevent the dissociation of the In-N bond. The equilibrium vapor pressure of nitrogen over InN, for example, is several orders of magnitude greater than that of AlN and GaN [5]. 2) In based compounds suffer from parasitic gas phase reactions between organometallic sources and hydride precursors. It seems that these parasitic reactions are more severe when NH_3 is used relative to the AsH_3 [6] and the PH_3 [7] cases, especially when In based organometallics (OMs) are used. 3) AlGaN/InGaN heterostructures can suffer from the fairly high lattice mismatch between these ternary alloys. The quaternary alloy AlInGaN can offer a lattice matched platform for InGaN growth, but this quaternary alloy has barely been studied. 4) High quality interfaces between the InGaN wells and the AlGaN or AlInGaN barrier layers can be difficult to achieve. Poor interfaces can result from poor nucleation (3D vs 2D), lattice mismatch, surface reconstruction, segregation and reaction of In at the interfaces and incompatible growth temperatures. In this paper we report on the growth of $\text{In}_x\text{Ga}_{1-x}\text{N}$ ($0 < x < 0.40$) epitaxial films and AlGaN/InGaN double heterostructures (DHs). These MOCVD grown films were deposited on buffer layers grown by Atomic Layer Epitaxy (ALE) in a specially designed hybrid growth system.

B. Experiment

A versatile growth system, capable of operating in several growth modes, has been designed for the growth of III-N compounds. The versatility of the system arises from its unique susceptor design, shown in Fig. 1. For this work, the system was operated in two growth modes, *ALE mode*, for the growth of buffer layers, and *conventional MOCVD mode*,

for the growth of the InGaN alloys. Either growth mode could be selected on demand at any time during a growth experiment. For the conventional MOCVD mode (Fig. 1), the substrate is kept stationary under a mixed flow of column III and V precursors. To improve the quality of the deposited films, a novel configuration of quartz tubes minimizes parasitic gas phase mixing of the NH_3 and metalorganic precursors until the gases near the substrate surface. For ALE style growth, the reactants are physically kept separated by injecting them through windows on opposite sides of the stationary susceptor, while the moving part of the susceptor sequentially rotates the substrate under the physically separated gas streams. The exposure time of the substrate to each reactant, as well as the time per growth cycle, is controlled by the rotational speed and pause times under the reactant gas stream. This hybrid growth system has been used to grow GaN [8] and $\text{In}_{0.27}\text{Ga}_{0.73}\text{N}$ [9] by ALE at 550 and 650°C, respectively.

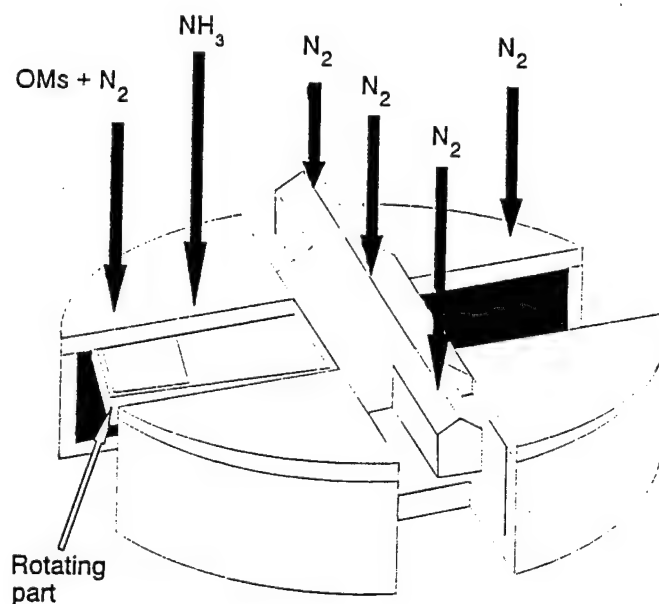


Figure 1. Susceptor design: Conventional MOCVD growth mode.

Source gases used were, trimethylgallium (TMG, -10°C), trimethylaluminum (TMA, $+18^\circ\text{C}$), ethyldimethylindium (EdMIn, $+10^\circ\text{C}$) and NH_3 ; N_2 was used as the carrier gas. Basal plane sapphire, cleaved into $\sim 1.5\text{ cm} \times 1.5\text{ cm}$ squares, was used as substrate material. After solvent cleaning, substrates were loaded and annealed in N_2 and NH_3 for 15 minutes and 1 minute respectively. ALE growth of AlN/GaN buffer layers [10] was performed at 700°C , while InGaN films were grown by MOCVD between $750\text{--}800^\circ\text{C}$. The InGaN alloys were typically grown on GaN that was deposited by MOCVD at higher temperatures ($900\text{--}950^\circ\text{C}$). MOCVD grown AlGaIn cladding layers for DHs were also grown by MOCVD between 900 and 950°C . In/Ga vapor phase ratios were ≤ 2 for the growth conditions used in this work.

C. Results

$\text{In}_x\text{Ga}_{1-x}\text{N}$ epitaxial layers have been grown with values of InN up to 40% in the ternary alloy. The full width at half maximum (FWHM) of the double crystal X-ray diffraction (DCXRD) data is broad for high values of x , but is comparable to that of GaN grown at higher temperatures for low values of InN% in the ternary, as shown in Fig. 2. Figure 2 shows DCXRD data for an $\text{In}_{0.06}\text{Ga}_{0.94}\text{N}$ alloy grown at 780 °C on GaN. The X-ray line width has a FWHM of ~250 arc seconds, the lowest reported to date for InGaN. The X-ray peak of the underlying GaN layer is also relatively sharp. Figure 3 shows Q - 2Q X-ray data for an $\text{In}_{0.40}\text{Ga}_{0.60}\text{N}$ film grown at 750 °C on GaN. The X-ray line width has broadened, due at least in part to the increased lattice mismatch between the underlying GaN layer and the InGaN alloy. This composition of 40% InN was achieved by MOCVD with a In/Ga gas phase ratio of only ~2, a relatively low ratio as compared to other published results on InGaN having even lower InN% [11].

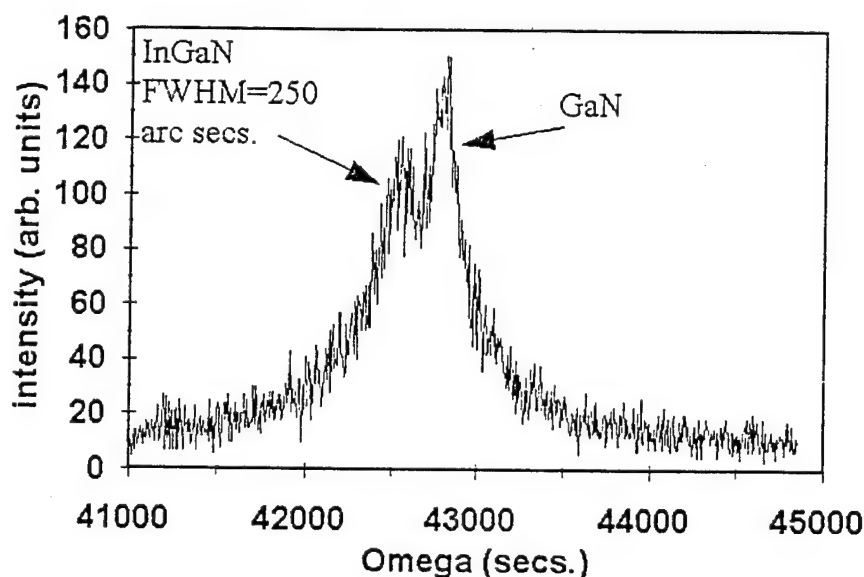


Figure 2. DCXRD data for $\text{In}_{0.06}\text{Ga}_{0.94}\text{N}$ grown by MOCVD at 780°C on GaN.

The optical properties of InGaN films grown in our hybrid MOCVD reactor show intense band edge (BE) emission that is sometimes accompanied by emission from deep levels. Room temperature photoluminescence (PL) data of several $\text{In}_x\text{Ga}_{1-x}\text{N}$ films is presented in Figs. 4 and 5. Figure 4 shows PL data of an $\text{In}_{0.15}\text{Ga}_{0.85}\text{N}$ alloy that was grown at 750 °C. Strong BE emission near 410 nm, having a FWHM of ~190 Å is observed for this film. The peak is fairly sharp and almost free of deep level emission. Room temperature PL data for an $\text{In}_{0.35}\text{Ga}_{0.65}\text{N}$ alloy, also grown at 750°C, is shown in Fig. 5. The PL spectrum shows BE emission at ~470 nm accompanied by a tail which may be attributed to emission from deep levels. This

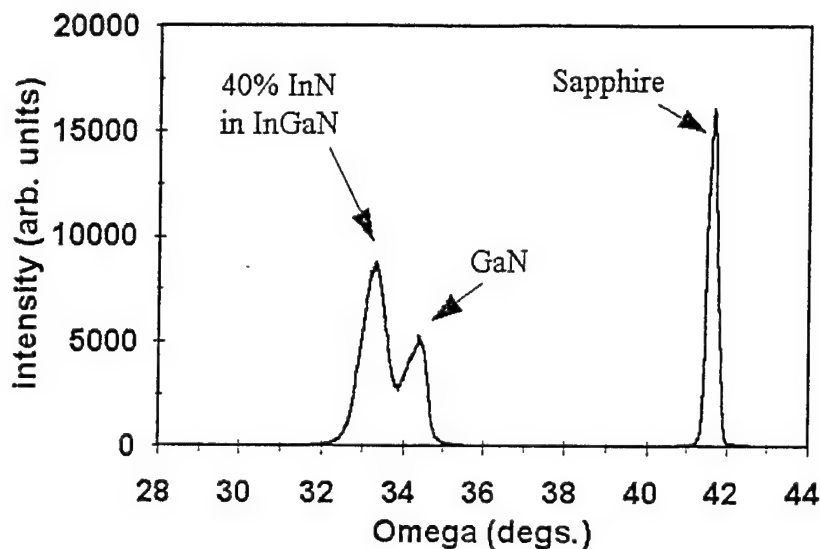


Figure 3. X-ray data for $\text{In}_{0.40}\text{Ga}_{0.60}\text{N}$ grown by MOCVD at 750°C on GaN.

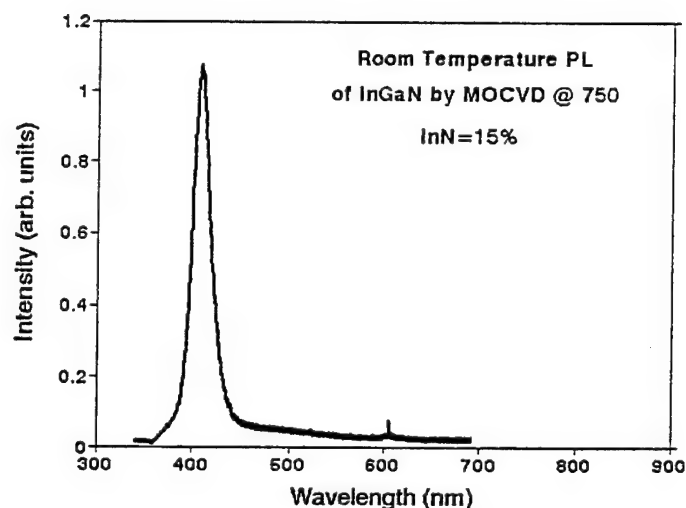


Figure 4. Room temp. PL of $\text{In}_{0.15}\text{Ga}_{0.85}\text{N}$ grown at 750°C by MOCVD.

observed PL of Fig. 5, with 35% InN, represents one of the highest reported values of x , to date. The good-to-excellent optical properties of these MOCVD grown InGaN alloys, with room temperature PL spectra dominated by BE emission, offer the potential of a basis for light emitting structures.

Preliminary investigations have been conducted into the growth of AlGaN/InGaN/AlGaN DHs by MOCVD. AlGaN was used as the cladding layer for these structures to offer increased carrier confinement, and was grown with AlN composition between 10 - 30%. Figure 6 shows room temperature PL spectra of $\text{Al}_{0.3}\text{Ga}_{0.7}\text{N}/\text{In}_x\text{Ga}_{1-x}\text{N}/\text{Al}_{0.3}\text{Ga}_{0.7}\text{N}$ DH with $0.1 < x < 0.15$ grown by MOCVD on a GaN buffer layer. The AlGaN was grown at 900 °C, while the InGaN film was grown at 780 °C. The PL spectrum, which includes BE emission from the GaN

buffer layer, shows BE emission from the InGaN active layer with a FWHM of about 15 nm. This value is comparable with that reported by Nichia obtained from their EL studies.

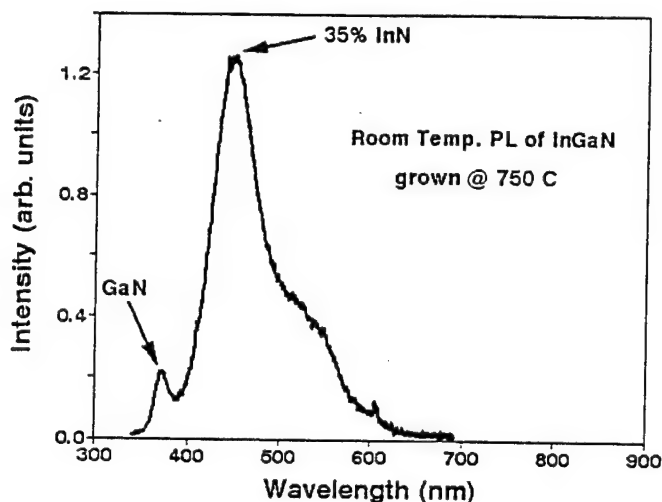


Figure 5. Room temp. PL of $\text{In}_{0.35}\text{Ga}_{0.65}\text{N}$ grown at 750°C by MOCVD.

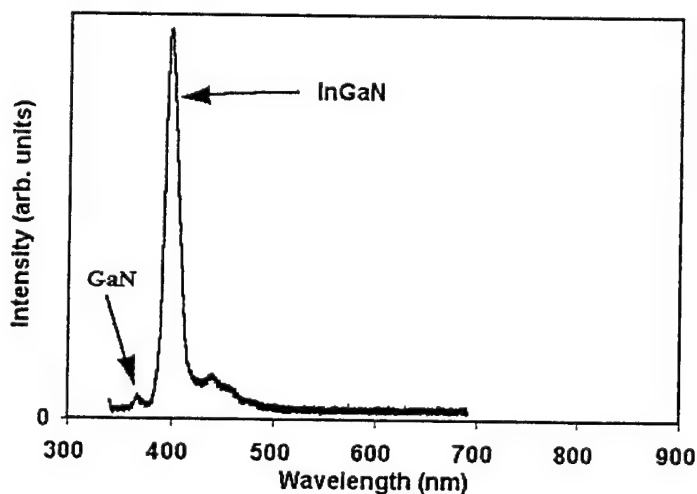


Figure 6. Room temp. PL of a $\text{AlGaIn}/\text{InGaIn}/\text{AlGaIn}$ DH grown by MOCVD on GaN.

D. Conclusions

High quality InGaIn alloys have been grown by MOCVD having an InN composition as high as 40 %. For low values of x , the $\text{In}_x\text{Ga}_{1-x}\text{N}$ epilayers have a sharp X-ray FWHM, with values as low as 250 arcsec observed, and sharp room temperature PL spectra that are dominated by BE emission. For higher values of x , the X-ray line widths broaden and room temperature PL spectra, while still showing BE emission, also exhibit some emission from deep levels. An $\text{AlGaIn}/\text{InGaIn}/\text{AlGaIn}$ DH has been grown that shows very sharp (FWHM = 15nm) BE emission corresponding to an InN composition of $\sim 10\%$ in the active layer.

E. References

1. S. Strite and H. Morkoç, J. Vac. Sci. Tech. **B10**, 1237 (1992).
2. M. Asif Khan, S. Krishnankutty, R. A. Skogan, J. N. Kunznia, D. T. Olsen and T. George, Appl. Phys. Lett. **65**, 520 (1994).
3. K. G. Fertitta, A. L. Holmes, J. G. Neff, F. J. Ciuba and R. D. Dupuis, Appl. Phys. Lett. **65**, 1823 (1994).
4. S. D. Lester, F. A. Ponce, M. G. Craford, and D. A. Steigerwald, Appl. Phys. Lett. **66**, 1249 (1995).
5. T. Matsuoka, H. Tanaka, T. Sasaki, and A. Datsui, Inst. Phys. Conf. **106**, 141 (1989).
6. H. Amano, N. Sawaki, I. Akasaki, and Y. Toyada, Appl. Phys. Lett. **48**, 353 (1986).
7. B. M^cDermott, et. al., Appl. Phys. Lett. **56**, 1172 (1990).
8. N. Karam, T. Parados, W. Rowland, J. Schetzina, N. El-Masry and S. M. Bedair, Appl. Phys. Lett. **67**, 94 (1995).
9. K. S. Boutros, F. G. McIntosh, J. C. Roberts, S. N. Bedair, E. L. Piner and N. A. El-Masry, Appl. Phys. Lett., accepted.
10. E. L. Piner, *et al.*, presented at MRS 1995 Fall Meeting
11. S. Nakamura, T. Mukai, Jpn. J. Appl. Phys. **31**, 1457 (1992).

XIV. AlGaInN Quaternary Alloys by MOCVD

A. Introduction

Current approaches in achieving $\text{In}_x\text{Ga}_{1-x}\text{N}$ based heterostructures rely on the AlGaIn ternary alloys as the high bandgap barrier/confinement layers [1, 2]. The large lattice mismatch between these two ternary alloys will limit either the value of x or the thickness of the InGaIn well. For example, the critical layer thicknesses for the $\text{Al}_{0.1}\text{Ga}_{0.9}\text{N}/\text{InGaIn}$ system with 40% and 60% InN are approximately 20\AA and 15\AA , respectively. This will limit the applications of InGaIn in the green and yellow regions. Such limitations can be avoided if AlGaIn is replaced by a more versatile $\text{Al}_x\text{Ga}_{1-x-y}\text{In}_y\text{N}$ quaternary compound. As shown in Fig. 1, by varying the value of x and y , the bandgap and the lattice constants can each be independently adjusted to achieve AlGaInN/InGaIn lattice matched structures. In Fig. 2, a potential LED structure with a lattice matched quantum well is shown.

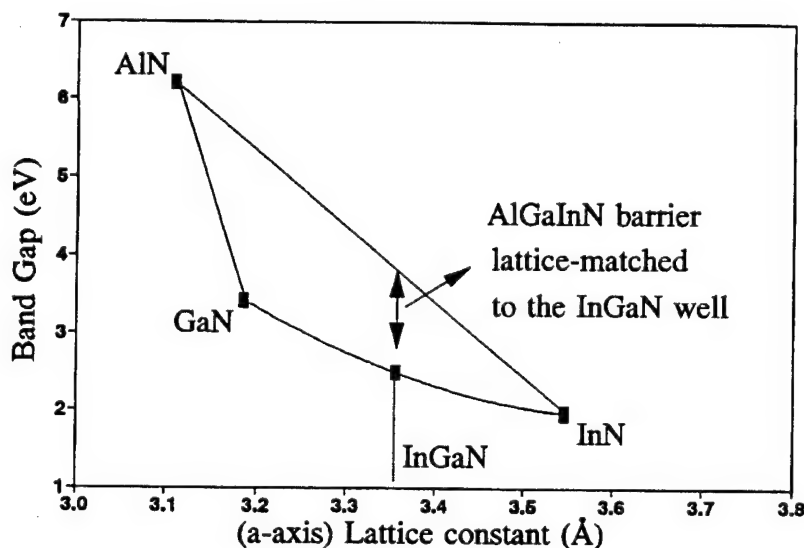


Figure 1. Bandgap versus lattice constants for the AlGaInN quaternary system showing how an InGaIn well can be lattice matched to wider bandgap AlGaInN barrier layers.

One of the major obstacles in the development of the quaternary is the determination of the optimal growth temperature. Aluminum based compounds generally require higher growth temperatures. Any residual background oxygen impurities in the deposition system or source gases will result in the incorporation of oxygen in the growing films. Therefore, higher temperatures are required in order to desorb these oxides and prevent their incorporation into the epitaxial film. Lower temperatures, however, are required for indium-based compounds. Indium compounds have relatively high vapor pressures and the growth temperature must be lowered in order to increase the indium incorporation and to reduce the dissociation of the In-N

bond. The growth temperature will therefore govern the limits to which both In and Al can be incorporated into the AlGaInN quaternary alloy.

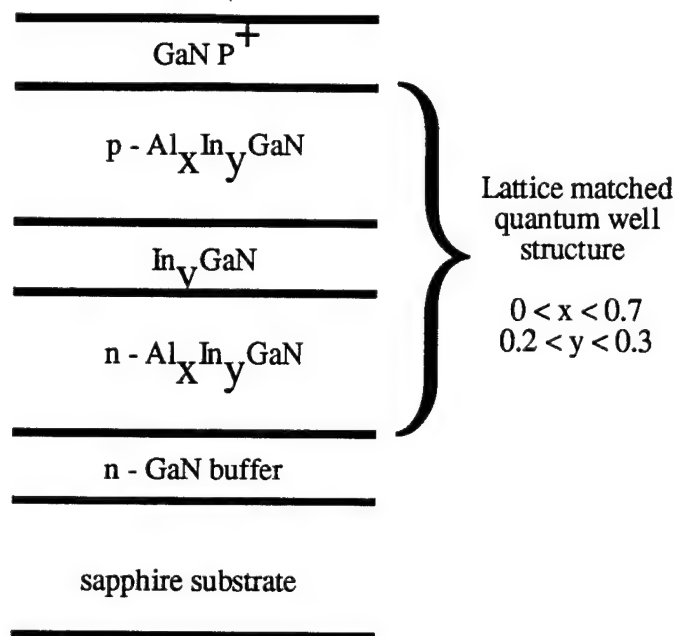


Figure 2. Potential heterostructure design with AlGaInN barrier layers lattice matched to the InGaN well.

Reported here is the growth of $\text{Al}_x\text{Ga}_{1-x-y}\text{In}_y\text{N}$ with the composition range ($0 < x < 0.2$) and ($0 < y < 0.15$) using a modified MOCVD reactor. Band edge transition has been observed of this quaternary alloy by room temperature photoluminescence. These results were achieved by first investigating the MOCVD growth of InGaN and AlGaN in the 750-800°C temperature range. This growth temperature seems to be a good compromise for the contradicting requirements for both the aluminum and indium containing compounds. The growth parameters and temperatures used for these ternary alloys were used to determine the favorable conditions for the deposition of high quality AlGaInN.

B. Experiment

The reactor design is based on the rotating susceptor and has been previously described [1, 2]. This design allows for three modes of crystal growth: MOCVD, molecular stream epitaxy (MSE), and atomic layer epitaxy (ALE). The organometallics and the ammonia are injected through separate tubes above one of the windows in the graphite susceptor. This configuration is designed to minimize gas phase reactions between the ammonia and the organometallics prior to reaching the surface of the substrate. For MOCVD, the substrate is positioned directly under this window during the entire growth process.

The growth was conducted at 750 Torr on a sapphire substrate. The substrate was first annealed and ammonia passivated at 1050°C. Next an AlN buffer layer was grown by ALE at 700°C, followed by a GaN film grown at 900°C using the MOCVD technique. For the results presented here, the growth temperature was then lowered to the 750-800°C temperature range for the AlGaInN layer deposition. Trimethylaluminum (TMA), trimethylgallium (TMG), ethyldimethylindium (EDMIn) and ammonia were used as precursors. The ammonia flow used was 50,000: mol/min., and the TMA and EDMIn were varied to control the quaternary composition. Quaternary films with thicknesses of about 0.5 μm were grown and characterized by energy dispersive spectroscopy (EDS), double crystal X-ray diffraction (DCXRD) and room temperature photoluminescence (PL).

C. Results

The chemical compositions of the AlGaInN quaternary films were obtained by EDS. First EDS was calibrated for In, Al and Ga using standards made from InGaN and AlGaIn ternary films of known compositions determined from DCXRD and using Vegard's law for determination of these ternary compositions. Figure 3 shows the X-ray diffractions pattern of a quaternary film, indicating a lattice constant (c-axis) of 5.185Å. The lattice constants can be also predicted from the following formula [1]:

$$a[\text{Al}_x\text{Ga}_{1-x-y}\text{In}_y\text{N}] = x a_{\text{AlN}} + (1 - x - y) a_{\text{GaN}} + y a_{\text{InN}} \quad (1)$$

This formula is based on the assumption that a solid solution of the binary constituents is present in the quaternary alloy. There is a reasonable agreement between the lattice constants measured from Fig. 3 and the value deduced from the above relation using EDS results in obtaining the chemical composition x and y [1]. Thus at least in the composition range studied, a solid solution does exist between the binary constituents.

The ultimate use of AlGaInN is reducing the lattice mismatch at AlGaInN/InGaIn interfaces. Figure 4 shows the DCXRD results of an AlGaInN/InGaIn/AlGaInN heterostructure. From this figure it is difficult to resolve the ternary and quaternary peaks due to the fairly close lattice constants. The arrows labeled T and Q in this figure show the lattice constants, determined by X-ray diffraction, of the ternary and quaternary films, respectively, when grown separately, but using the same flows as in this heterostructure. From this figure and the corresponding lattice constants of the ternary and quaternary alloys it can be shown that the lattice mismatch at the InGaIn/AlGaInN heterointerface is about 0.3%. The corresponding lattice mismatch of this InGaIn film in an AlGaIn/InGaIn heterostructure is 1.5%. Figure 5 shows the room temperature photoluminescence for this quaternary film, indicating band edge emission from the active InGaIn layer.

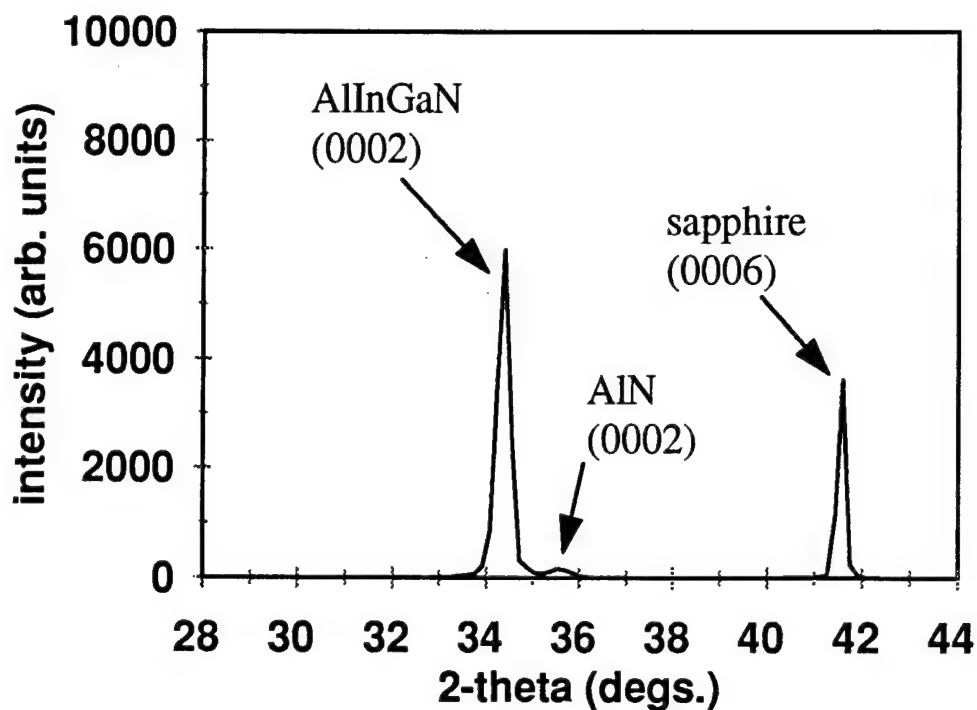


Figure 3. X-ray results for a quaternary film grown by MOCVD at 780°C.

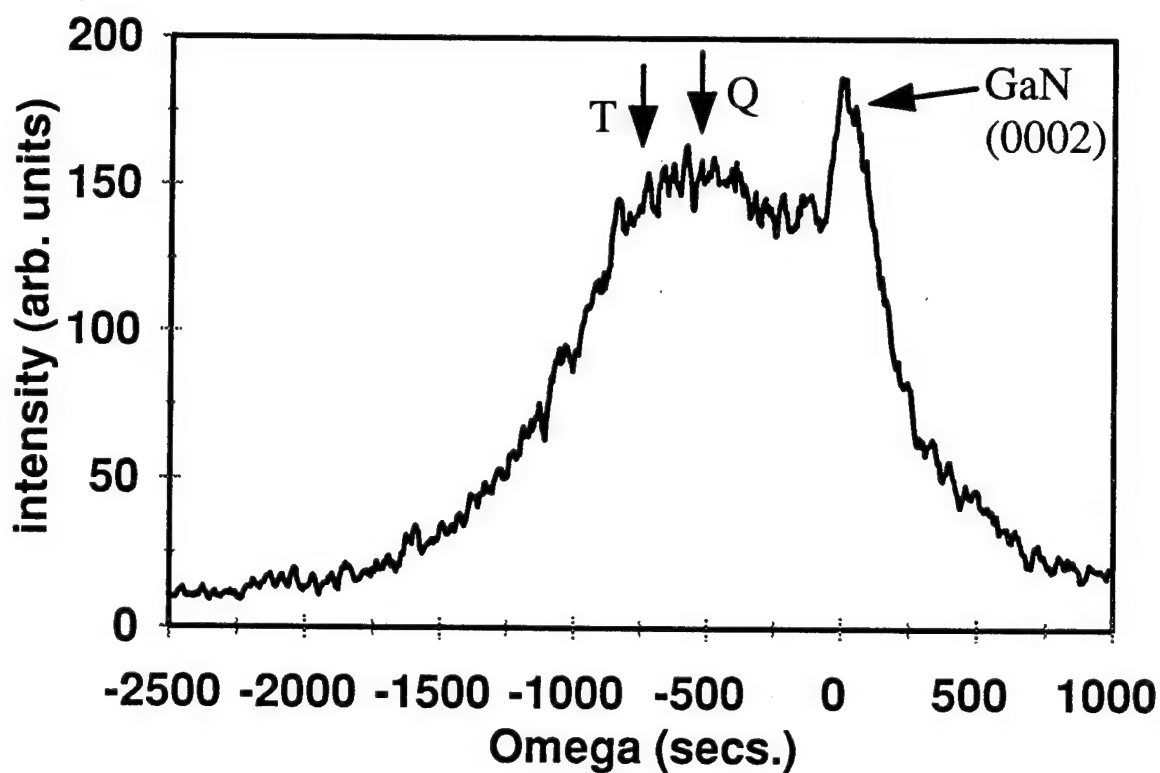


Figure 4. DCXRD results for an AlGaInN/InGaN/AlGaInN heterostructure grown by MOCVD at 780°C.

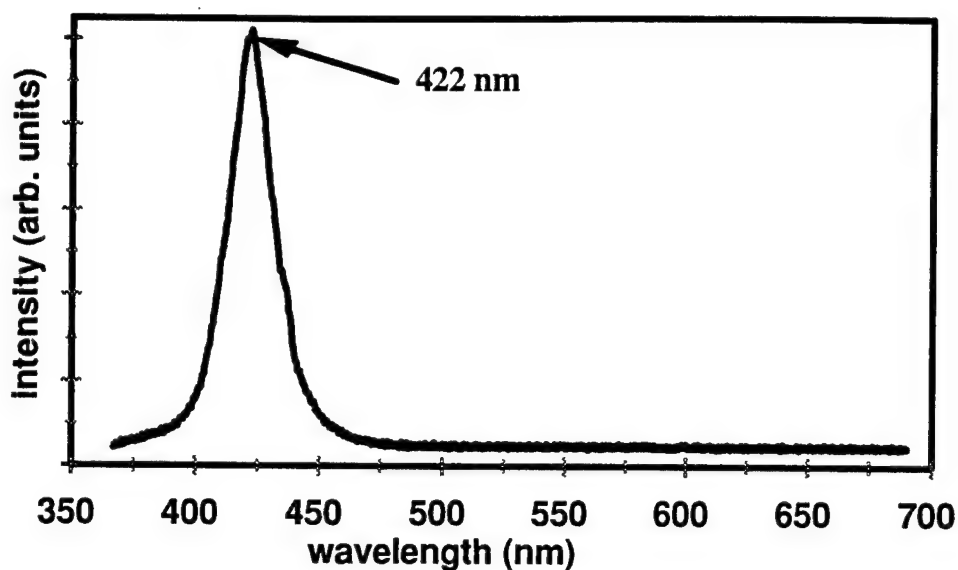


Figure 5. Room temperature PL for the AlGaInN/InGaN/AlGaInN heterostructure shown in Fig. 4.

D. Conclusions

In conclusion, $\text{Al}_x\text{Ga}_{1-x}\text{In}_y\text{N}$ films were epitaxially grown on GaN by MOCVD in the composition range $0 < x < 0.2$, $0 < y < 0.15$. AlGaInN/InGaN nearly lattice matched heterostructures were grown, allowing the potential for new optoelectronic device structures with the generation of misfit dislocations at critical interfaces.

E. References

1. S. Nakamura, T. Mukai and M. Senoh, Appl. Phys. Lett. **64**, 1687 (1994).
2. Nakamura, T. Mukai and M. Senoh, J. Appl. Phys. **76**, 8189 (1994).
3. K. S. Boutros, F. G. McIntosh, J. C. Roberts, S. M. Bedair, E. L. Piner and N. A. El-Masry, Appl. Phys. Lett. **67**, 1797 (1995).
4. N. Karam, T. Parados, W. Rowland, J. Schetzina, N. El-Masry, and S. M. Bedair, Appl. Phys. Lett. **67**, 94 (1995).
5. C. K. Williams, T. H. Glisson, J. R. Hauser, and M. A. Littlejohn, J. Elect. Mat. **7**, 639 (1978).
6. F. G. McIntosh, K. S. Boutros, J. C. Roberts, S. M. Bedair, E. L. Piner and N. A. El-Masry, to be published in Applied Phys. Lett. Jan., 1996.

XV. Theory of Surfaces and Interfaces in the Wide-Gap Nitrides

Krzysztof Rapcewicz, Marco Buongiorno Nardelli, Bin Chen,
Ze Zhang and J. Bernholc

Department of Physics,
North Carolina State University,
Raleigh, NC 27695-8202

ABSTRACT

A selection of the results of an ongoing theoretical investigation of the properties of the wide-gap III-V nitride semiconductors are presented. The energetics of the 2×2 reconstructions of GaN surfaces have been studied. The nitrogen-adatom reconstruction on the gallium-terminated face has the lowest energy of the reconstructions considered; on the nitrogen-terminated face, the nitrogen-vacancy has the lowest energy. The electron affinity at selected AlN surfaces has been calculated. Negative electron affinity (NEA) is found for the 2×2 aluminium-vacancy reconstruction on the aluminium terminated face, while the 1×1 hydrogen-passivated nitrogen-terminated surface has a very small electron affinity. A detailed study of (001) zinc-blende interfaces of AlN/GaN/InN is described. The band offsets show that the interfaces are of type I.

INTRODUCTION AND SUMMARY

Semiconductor heterojunctions find wide applications in microelectronics. These include lasers, photodetectors, high-efficiency solar cells and radiation-resistant integrated circuits [1]. The III-V nitrides with their wide band-gaps, high thermal stability and conductivity and radiation resistance have long been viewed as attractive candidates for use in microelectronic devices [2]. The recent demonstration of stimulated emission in the blue region has served to further increase awareness of the potential of nitride-based devices [3] and elicited the interest of a number of theoretical groups [4].

We have studied the energetics of selected 2×2 reconstructions of GaN surfaces and find that on the gallium-terminated face, the surface with an adsorbed nitrogen adatom is of lowest energy, while on the nitrogen-terminated face, the nitrogen

vacancy reconstruction has the lowest energy. Motivated by the experimental discovery of negative electron affinity at AlN surfaces [5], we have investigated the electron affinity [6]. We find that the 2×2 aluminium-vacancy reconstruction on the aluminium-terminated face has a negative electron affinity and that the 1×1 hydrogen-passivated nitrogen-terminated surface has a very small electron affinity. The electronegativity difference between the adatom and the atomic species comprising the surface is found to be a guide for anticipating the presence of NEA. In particular, NEA may occur when the adatom is much more electropositive than the surface atoms.

We investigated the zinc-blende (001) interfaces of AlN/GaN/InN [7]. The elastic energy of GaN grown on AlN is lower than AlN grown on GaN, indicating that the quality of pseudomorphic growth should be higher when AlN is used as the substrate. Further, the effects of strain on the valence-band offset are significant, as is illustrated by the calculated values of the valence-band offset for AlN/GaN (-0.58 eV) and GaN/AlN (-0.70 eV). The band offsets of AlN/GaN/InN were computed, using the AlN in-plane lattice constant and including strain effects. They are all of type I and the transitivity rule is satisfied. No interface states were found in the gap. The $\text{Al}_{0.2}\text{Ga}_{0.8}\text{N}/\text{In}_{0.1}\text{Ga}_{0.9}\text{N}$ interface was studied using the virtual crystal approximation. It is of type I and there are no interface states in the gap.

CALCULATIONS

In all of the calculations, the standard *ab initio* plane-wave pseudopotential method was employed [8, 9, 10]. For the exchange-correlation energy, the Perdew-Zunger parametrization [11, 12] was chosen. Non-local potentials were included using the Kleinman-Bylander approach [13].

The calculations of the surface reconstructions and the electron affinity used Γ -point sampling and a plane-wave energy cut-off of 30 Ry. Norm-conserving, pseudopotentials [14, 15, 16] were used for aluminium (p-local) and gallium (d-local), while for nitrogen a soft-core p-local pseudopotential was used [17].

The plane-wave energy cut-off for the interface calculations was 50 Ry. The equivalent of 10 k-points for bulk and superlattice calculations in the zinc-blende structure [18] were chosen. For all species, d-local norm-conserving pseudopotentials [14, 15, 16] were used. Further, the nonlinear core correction was included for the cation species [19]. The calculated bulk properties of the zinc-blende nitrides obtained using these pseudopotentials are shown in Table 1. The agreement with experiment is excellent. For interface calculations, we studied 4×4 superlattices (16 atoms in the supercell) along (001).

2×2 RECONSTRUCTIONS OF GaN SURFACES

The surface energy is an important consideration in growth, where the relationship between the surface energies of faces and the interface energy determines the

Table 1: Calculated bulk properties of zinc-blende nitride semiconductors. The values of the gap at the Γ -point (E_Γ) and of the valence-band width (ΔE_{vbw}) are the LDA results. Experimental values are in brackets and follow Ref. [20].

	AlN	GaN	InN
a_0 (Å)	4.37 (4.38)	4.52 (4.5)	5.01 (4.98)
B_0 (MBar)	2.02 (2.02)	1.70 (1.90)	1.58 (1.37)
E_Γ (eV)	4.09	2.24 (3.45)	0.16
ΔE_{vbw} (eV)	14.86	15.48	14.01
c_{11} (10^{11} dyne/cm ²)	24.85	23.74	20.24
c_{12} (10^{11} dyne/cm ²)	13.37	11.23	12.96

mode of growth. The standard approaches to the calculation of the surface energy from total energy calculations are invariably slab calculations. In certain favorable instances, for example the zinc-blende (001) surfaces, a slab geometry can be found in which both faces of the slab are the same. In most cases, however, this is not possible and the surface energies can only be determined relative to some reference surface, usually the 1×1 unreconstructed, unrelaxed surface, even if the surface energy is absolutely defined.

The surface energy, σ , which is defined as an excess quantity, is

$$E_{slab} = E_{bulk} + \sigma, \quad (1)$$

where E_{slab} is the energy of the system with the surface and E_{bulk} is the energy of the equivalent bulk, i.e. the energy of the equivalent amount of material considered to be part of an infinite bulk. It has been shown that the surface energy is only absolutely defined for crystal systems with sufficiently high symmetry, for example in zinc-blende crystals [21]. Nonetheless, in crystals of lower symmetry, e.g. wurtzite, where the surface energy is no longer absolutely defined, combinations of surface energies that occur in physically meaningful situations remain well-defined.

Chetty and Martin [22] developed an approach using symmetry-adapted unit cells that made possible the calculation of the surface energy in certain cases. In doing so they introduced the energy-density which is defined through the relation

$$E = \int_V d^3r \epsilon(\mathbf{r}), \quad (2)$$

where E and V are the total energy and volume of the system, respectively and $\epsilon(\mathbf{r})$ is the energy density.

In the present approach we use the energy-density formalism but not the symmetry-adapted cells, which cannot be appropriately defined for the wurtzite structure. Instead we devised a formalism based upon a subdivision of the total energy

into atomic "blocks", rigorously defined [23] in terms of generalized Wigner-Seitz volumes (see below). The slab and the bulk are considered to be composed of such blocks. The cost of the i^{th} block in the bulk is ϵ_i^{bulk} , while the cost of the equivalent block in the slab is ϵ_i^{slab} . The surface energy is then the excess or deficit cost of building the slab instead of the bulk. The shape and volume of a block in the bulk, V_i , is defined using the symmetry of the lattice and the charge-sum rule

$$Z_i = \int_{V_i} d^3r \rho_{bulk}(\mathbf{r}), \quad (3)$$

where Z_i is the valence of the i^{th} atom, $\rho_{bulk}(\mathbf{r})$ is the charge density in the bulk. This volume, which can be viewed as a generalization of the Wigner-Seitz cell, we denote as the charge-neutral atomic Wigner-Seitz volume for the i^{th} atom. This permits the definition of the "bulk-atom" energy, ϵ_i , for the i^{th} atom, which is the integral of the energy density in the bulk over the atomic Wigner-Seitz volume, i.e.

$$\epsilon_i^{bulk} = \int_{V_i} d^3r \epsilon_{bulk}(\mathbf{r}). \quad (4)$$

In this way the surface energy is

$$\sigma = \sum_{halfslab} \left[\int_{\tilde{V}_i} d^3r \epsilon_{slab}(\mathbf{r}) - \epsilon_i \right], \quad (5)$$

where the summation is over those volumes (and, hence, atoms) in the half-slab under consideration (\tilde{V}_i is the relaxed atomic volume in the slab). This approach provides a consistent methodology for calculating surface energies that reproduces the standard calculations along high-symmetry directions, for example for the (001) zinc-blende surface.

This methodology has been used in conjunction with the Car-Parrinello method to determine the energy of 2×2 reconstructions of wurtzite (0001) GaN. Three reconstructions on each surface were studied, namely the gallium- and nitrogen-adatom, and vacancy reconstructions. The adatoms were placed on the hollow site.

For the gallium-terminated surface, the nitrogen adatom structure has the lowest energy while the gallium-vacancy structure is of somewhat higher energy. In the nitrogen-adatom reconstruction, the three gallium atoms bonded to the nitrogen adatom move towards the adatom. The remaining gallium atom relaxes inwards towards the nitrogen layer. The subsurface N atom, which has three bonds with the surface gallium atoms bonded to the N-adatom, moves outwards towards the Ga atoms, becoming almost coplanar with them. In the vacancy reconstruction, the three gallium atoms relax inwards towards the subsurface nitrogen layer. On the nitrogen-terminated surface, the nitrogen vacancy has the lowest energy while the gallium-adatom has a somewhat higher energy. The results are shown in Figs. 1 and 2. The sum of the surface energies of the Ga- and N-terminated faces is an absolutely defined quantity.

NEGATIVE ELECTRON AFFINITY AT AlN SURFACES

The electron affinity is defined as the difference between the bottom of the conduction band and the vacuum level. Negative electron affinity occurs when the conduction band bottom is below the vacuum level. It has potential use in electron emitters, cold cathodes and other optoelectronic devices. The recent experimental observation of negative electron affinity at AlN surfaces [5] provides the motivation to study the electron affinity at AlN surfaces.

The value of the electron affinity is modified by the surface dipole moment and the space charge due to the occupation of surface states by free carriers from the bulk. The presence of free carriers leads to band bending near the surface; however, this effect is significant only in doped materials and need not be considered at present. Rather it is the effect of chemisorption and surface reconstructions on the the surface dipole that constitutes our present interest.

The electron affinity of a semiconductor is defined as

$$\chi = D - (E_c - V_{bulk}) \quad (6)$$

where D , the surface dipole strength, determines the relative positions of the bulk electron states and the vacuum level [24], while $(E_c - V_{bulk})$ is the position of the conduction band minimum relative to the bulk-averaged electrostatic potential. The latter is purely a bulk property and can be obtained in a calculation of the AlN bulk. It is well-known that the local density functional theory consistently underestimates the size of semiconductor band-gaps. For this reason, the conduction-band minimum was rigidly shifted to the experimental value of 6.2 eV using the so-called scissors operator. The surface dipole strength was obtained from the difference of the electrostatic potential across the surface.

The 1×1 (0001) Al- and N-terminated surfaces (with neither adatoms nor vacancies) were studied. Both surfaces exhibit some inward relaxation, while the geometries in the surface plane did not significantly change. The electron affinities are 0.85 eV and 0.30 eV for the Al- and N-terminated surfaces, respectively. These 1×1 structures are expected to have higher surface energies than the 2×2 reconstructed structures. As the 2×2 vacancy reconstructions were among the lower energy 2×2 reconstructions of (0001) GaN, the 2×2 vacancy reconstructions of the (0001) surfaces of AlN were next investigated. With one-quarter of a monolayer of the Al surface atoms removed, the surface can accommodate a much larger inward relaxation than the 1×1 structure. In this case, the electron affinity is -0.70 eV. For the same reconstruction on the N-terminated face, the electron affinity is 1.40 eV. The effect of hydrogen chemisorption on the electron affinity of the 1×1 (0001) Al- and N-terminated surfaces was also examined. Hydrogen adsorption reduced the electron affinity of the N-terminated surface to 0.05 eV; however, the electron affinity of Al-terminated surface increased to 1.60 eV.

The changes in the electron affinity reflect modification of the net surface dipole. During chemisorption, the adsorbates saturate the dangling bonds of the surface

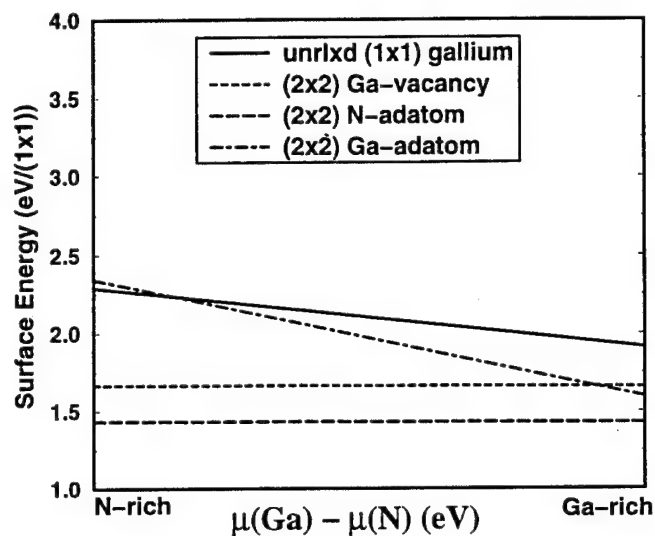


Figure 1: Surface energies of the 2x2 reconstructions on the gallium-terminated face.

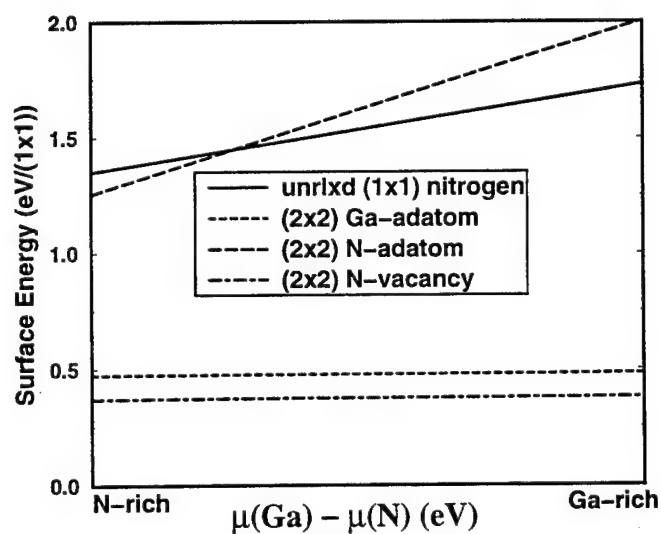


Figure 2: Surface energies of the 2x2 reconstructions on the nitrogen-terminated face.

atoms resulting in charge transfer between the adsorbates and surface atoms. This transfer manifests itself as an additional dipole field, the strength and direction of which determines the change of the electron affinity. The diamond (111) surface provides another example of this effect. The bare surface has a positive electron affinity; however it has a negative electron affinity when it has been passivated by hydrogen. Since carbon is more electronegative than hydrogen, charge transfers from the hydrogen adatom to the surface carbon atom. This induces an additional dipole which points outwards and reduces the electron affinity to a negative value [25]. As nitrogen is more electronegative than hydrogen, this also occurs when hydrogen is chemisorbed on the N-terminated AlN surface. In contrast, aluminium has a smaller electronegativity than hydrogen and consequently we expect the opposite to occur when hydrogen adatoms are chemisorbed on the Al-terminated surface. This is indeed the case. The electronegativity difference between the surface species and the adsorbed species provides insight into manner in which the adatoms modify the surface charge density and hence the electron affinity. Of course, bonding properties will be affected by the detailed nature of the surface, but nonetheless strongly electropositive elements, such as Li and Be, may result in negative electron affinity when adsorbed on the surface.

INTERFACES OF WIDE-GAP NITRIDES

Because of the lattice-mismatch between AlN and GaN (2.5%) and between InN and AlN (12.1%), superlattices of these materials will be strained. We have studied the energetics of two different interfaces, namely the strained GaN/AlN (with AlN in-plane lattice constant) and the strained AlN/GaN (with GaN in-plane lattice constant). The elastic energy for these interfaces, which is the difference of the strained and unstrained energy per pair, is 46 meV/pair for the GaN/AlN interface, while it is 63 meV/pair for AlN/GaN. The interface energy, defined as the excess or deficit energy due to the presence of the interface, is extremely small, namely ~ 1 meV/atom, which is of the order of the precision of the calculations. Thus the interfaces show similar bonding characteristics. These results suggest that the critical thickness for pseudomorphic AlN/GaN is significantly smaller than for GaN/AlN, in agreement with the observation that epitaxially grown GaN/AlN results in higher quality samples [26].

The band offsets of the strained heterojunctions have also been studied. Following the conclusions of the previous paragraph, AlN is taken to be the substrate in all of the cases presented below. The valence-band offsets are -0.70 eV for GaN/AlN and -0.44 eV for AlN/GaN (001) strained interfaces, indicating that the effect of strain on the value of the valence-band offset is significant. The interfaces are all of type I and there are no interface states in the gap. We then investigated the band offsets of the (001) GaN/AlN, InN/AlN and InN/GaN strained heterojunctions. The band offsets are shown in Fig. 3. In determining the conduction-band offsets, the conduction band minima were shifted to their experimental values using the

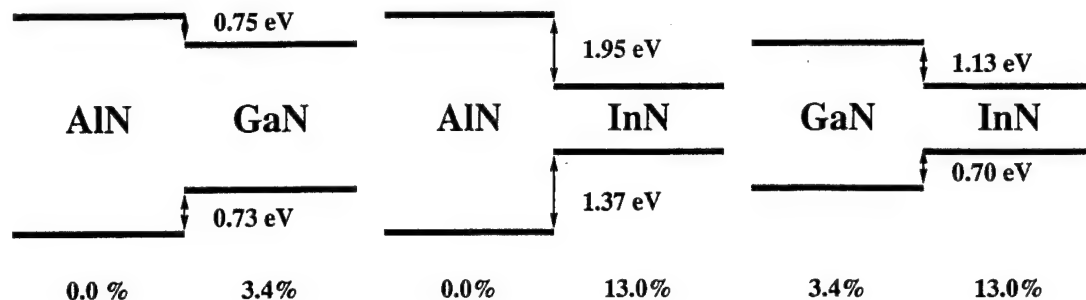


Figure 3: Calculated band offsets for the three interfaces described in the text (an AlN substrate is assumed). The lattice mismatch shown is with respect to AlN.

so-called scissors operator. Each of the interfaces is of type I and the transitivity rule is satisfied. Further, states at the top of the valence band are mostly confined to the epilayer with the smaller gap and there are no interface states in the gap of the superlattice.

The possible sources of systematic error of the calculation of the band offsets include the neglect of the anion p - and cation d -state repulsion [27] and the well-known neglect of many-body effects in the local density approximation. In GaN/AlN interfaces, the inclusion of the $3d$ -electrons as valence electrons results in a constant shift of 0.2 eV which is less than the experimental error [28] and does not change the character of the interface. Incorporating this shift gives results in agreement with previous estimates using a d -valence pseudopotential [29] and an all-electron calculation [30]. The importance of many-body effects on the band offsets is not known and awaits a future GW calculation.

We also studied an alloy interface based upon the nitride-based multi-quantum-well structure that Nakumura et al. [3] used to demonstrate stimulated emission in the blue region of the spectrum. The bulk properties of the two zinc-blende alloys comprising the epilayers of the multi-quantum-well, calculated using the virtual crystal approximation, are shown in Table 2. In the virtual crystal approximation, the pseudopotentials of the constituent species are averaged by their fractional composition [31]. Vegard's rule is seen to be satisfied.

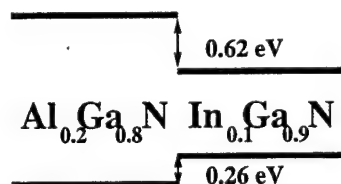


Figure 4: Calculated band offsets for the zinc-blende (001) $\text{Al}_{0.2}\text{Ga}_{0.8}\text{N}/\text{In}_{0.1}\text{Ga}_{0.9}\text{N}$ interface described in the text assuming an AlN substrate.

Table 2: Calculated bulk properties of zinc-blende $\text{Al}_{0.2}\text{Ga}_{0.8}\text{N}$ and $\text{In}_{0.1}\text{Ga}_{0.9}\text{N}$ semiconductors within the virtual crystal approximation. The values of the gap at the Γ -point (E_{Γ}) and of the valence-band width (ΔE_{vbw}) are the LDA results. The AlN in-plane lattice constant is used (the mismatch is with respect to the AlN lattice constant).

	$\text{Al}_{0.2}\text{Ga}_{0.8}\text{N}$	$\text{In}_{0.1}\text{Ga}_{0.9}\text{N}$
a_0 (Å)	4.51	4.61
B_0 (MBar)	1.67	1.78
E_{Γ} (eV)	2.56	1.68
ΔE_{vbw} (eV)	15.10	15.31
c_{11} (10^{11} dyne/cm ²)	23.46	20.75
c_{12} (10^{11} dyne/cm ²)	10.88	12.02
Vegard's Rule (Å)	4.49	4.57
Lattice Mismatch	3.1	5.2

The zinc-blende (001) interface of these alloys was investigated. Strain effects were explicitly included using macroscopic elasticity theory (using the theoretically determined elastic constants shown in Table 2) and a total energy minimization. The values for scissors corrections of the band gap of the alloys were estimated using a Vegard-type rule, namely the gap of the alloy was taken to be the average of the band gap of the pure phase weighted by its fractional composition. The band offsets are shown in Fig. 4. The interface is of type I and there are no interface states in the gap.

REFERENCES

- [1] R. Bauer and G. Margaritondo, *Physics Today*, **40**, 27 (1987).
- [2] M.-E. Lin, B. N. Sverdlov, S. Strite, H. Morkoç and A.E. Drakin, *Electron. Lett.* **29**, 1759 (1993).
- [3] S. Nakamura et al., *Jpn. J. Appl. Phys.* **35**, L74 (1996).
- [4] See, e.g., B. Min, C. Chan and K. Ho, *Phys. Rev. B* **45**, 1159 (1992), V. Fiorentini, M. Methfessel and M. Scheffler, *Phys. Rev. B* **47**, 13353 (1993), E. Albanesi, W. Lambrecht and B. Segall, *J. Vac. Sci. Technol. B* **12**, 2470 (1994), A. Rubio, J. Corkill and M. L. Cohen, *Phys. Rev. B* **49**, 1952 (1994), C. Yeh, S. Wei and Z. Zunger, *Phys. Rev. B* **50**, 2715 (1994), A. F. Wright and J. S. Nelson, *Phys. Rev. B* **51**, 7866 (1995) and M. Palummo, L. Reining, R.W. Godby,

C.M. Bertoni and N. Bornsen, *Europhys. Lett.* **26**, 607 (1995). For a general reference, see W. Lambrecht and B. Segall, in *Properties of Group III Nitrides*, edited by J. Edgar, EMIS Data Series (IEE, London, 1994), chapt. 5.

- [5] M. C. Benjamin, C. Wang, R. F. Davis and R. J. Nemanich, *Appl. Phys. Lett.* **64**, 3288 (1994).
- [6] B. Chen, K. Rapcewicz, Z. Zhang and J. Bernholc, to be published (1996).
- [7] M. Buongiorno Nardelli, K. Rapcewicz and J. Bernholc, to be published (1996).
- [8] M. C. Payne, M. P. Teter, D. C. Allan, T. A. Arias and J. D. Joannopoulos, *Rev. Mod. Phys.* **64**, 1045 (1992).
- [9] W. Pickett, *Comp. Phys. Rep.* **9**, 115 (1989).
- [10] D. Remler and P. Madden, *Mol. Phys.* **70**, 921 (1990).
- [11] J. Perdew and A. Zunger, *Phys. Rev. B* **23**, 5048 (1981).
- [12] D. Ceperley and B. Alder, *Phys. Rev. Lett.* **45** 566 (1980).
- [13] L. Kleinman and D. Bylander, *Phys. Rev. Lett.* **48**, 1425 (1982).
- [14] G. Bachelet, D. R. Hamann and M. Schlüter, *Phys. Rev. B* **26**, 4199 (1982).
- [15] D. R. Hamann, M. Schlüter and C. Chiang, *Phys. Rev. Lett.* **43**, 1494 (1979).
- [16] D. R. Hamann, *Phys. Rev. B* **40**, 2980 (1989).
- [17] G. Li, and S. Rabii, unpublished (1992).
- [18] S. Froyen, *Phys. Rev. B*, **39**, 3168 (1989).
- [19] S. Louie, S. Froyen and M.L. Cohen, *Phys. Rev. B* **26**, 1738 (1982).
- [20] A. F. Wright and J. S. Nelson, *Phys. Rev. B* **50**, 2159 (1994).
- [21] J. Lee, H. Aaronson and K. Russel, *Surf. Sci.* **51** 302 (1975) and E. Arbel and J. Cahn, *Surf. Sci.* **51**, 305 (1975).
- [22] N. Chetty and R.M. Martin, *Phys. Rev. B* **45**, 6074 (1992), *ibid.* **45**, 6089 (1992) and *ibid.* **44**, 5568 (1991).
- [23] K. Rapcewicz, B. Chen, B. Yakobson and J. Bernholc, to be published (1996).
- [24] A. Zangwill, *Physics at Surfaces*, (Cambridge University Press, Cambridge, England, 1988).

- [25] Z. Zhang, M. Wensell, and J. Bernholc, Phys. Rev. B. **51**, 5291 (1995).
- [26] See, for instance, H. Morkoç et al., J. Appl. Phys. **76**, 1363 (1994), M. Paisley and R.F Davis, J. Cryst. Growth **127**, 136 (1992).
- [27] S. Wei and A. Zunger, Phys. Rev. Lett. **59**, 144 (1987).
- [28] G. Martin et al., Appl. Phys. Lett. **65**, 610 (1994).
- [29] V. Fiorentini, M. Methfessel and M. Scheffler, Phys. Rev. B **47**, 13353 (1993).
- [30] E. Albanesi, W. Lambrecht and B. Segall, J. Vac. Sci. Technol. B **12**, 2470 (1994).
- [31] M. Peressi, S. Baroni, A. Baldereschi and R. Resta, Phys. Rev. B **41**, 12106 (1990).

XVI. Theory of Defects, Doping, Surfaces and Interfaces in Wide Gap Nitrides

J. BERNHOLC, P. BOGUSLAWSKI,¹ E. L. BRIGGS, M. BUONGIORNO NARDELLI, B. CHEN, K. RAPCEWICZ, Z. ZHANG

Department of Physics, North Carolina State University
Raleigh, NC 27695, Bernholc@ncsu.edu

ABSTRACT

The results of extensive theoretical studies of group IV impurities and surface and interface properties of nitrides are presented and compared with available experimental data. Among the impurities, we have considered substitutional C, Si, and Ge. C_N is a very shallow acceptor, and thus a promising p -type dopant. Both Si and Ge are excellent donors in GaN. However, in AlGa_N alloys the DX configurations are stable for a sufficiently high Al content, which quenches the doping efficiency. At high concentrations, it is energetically favorable for group IV impurities to form nearest-neighbor $X_{cation}-X_N$ pairs. Turning to surfaces, AlN is known to exhibit NEA. We find that the NEA property depends sensitively on surface reconstruction and termination. At interfaces, the strain effects on the band offsets range from 20% to 40%, depending on the substrate. The AlN/GaN/InN interfaces are all of type I, while the Al_{0.5}Ga_{0.5}N/AlN zinc-blende (001) interface may be of type II. Further, the calculated bulk polarizations in wurtzite AlN and GaN are -1.2 and -0.45 $\mu\text{C}/\text{cm}^2$, respectively, and the interface contribution to the polarization in the GaN/AlN wurtzite multi-quantum-well is small.

INTRODUCTION AND SUMMARY

Current interest in wide band-gap nitrides is due to possible applications in blue/UV light-emitting diodes and lasers, and in high-temperature electronics [1, 2]. The recent demonstration of stimulated emission in the blue region has served to further increase awareness of the potential of nitride-based devices [3] and elicited the interest of a number of theoretical groups [4].

In this paper we describe several of our recent results [5, 6, 7, 8, 9, 10] concerning substitutional group-IV impurities in wurtzite GaN and AlN, electron affinity of AlN surfaces in the wurtzite structure, and the zinc-blende (001) interfaces of AlN/GaN/InN.

The group IV impurities are potentially important dopants (*e.g.*, Si is frequently used as a n -type dopant of epitaxial GaN). Both C and Si may also be unintentionally incorporated as contaminants during growth. In general, a group-IV atom is likely to become a donor when incorporated on the cation site, and an acceptor on the anion site. This possibility of the amphoteric behavior critically depends on the conditions of growth. We have recently shown [7] that C is preferentially incorporated on the N site under Ga-rich conditions of growth, while both Si and Ge occupy cation sites under N-rich conditions. However, at high concentrations self-compensation, *i.e.*, a simultaneous incorporation of the dopant on both cation and anion sublattice, is expected, which would limit the doping efficiency. We therefore also discuss the electronic structure of X_{cation} , X_N , and $X_{cation}-X_N$ nearest-neighbor pairs. We further consider a possible transition of X_{cation} from the substitutional

¹also at Institute of Physics, PAN, 02-668 Warsaw, Poland.

to the DX-like configuration. Such a transition is commonly accompanied by a capture of electron on a stable (or metastable) state, which quenches the doping efficiency. Some of the results for C were published in [6].

Motivated by the experimental discovery of negative electron affinity at AlN surfaces [11], we have investigated the electron affinity [8]. We find that the 2×2 aluminium-vacancy reconstruction on the aluminium-terminated face has a negative electron affinity and that the 1×1 hydrogen-passivated nitrogen-terminated surface has a very small electron affinity. The electronegativity difference between the adatom and the atomic species comprising the surface is found to be a guide for anticipating the presence of NEA. In particular, NEA may occur when the adatom is much more electropositive than the surface atoms.

We have also investigated the zinc-blende (001) interfaces of AlN/GaN/InN [9]. The elastic energy of GaN grown on AlN is lower than AlN grown on GaN, indicating that the quality of pseudomorphic growth should be higher when AlN is used as the substrate. Further, the effects of strain on the valence-band offset are significant, as is illustrated by the calculated values of the valence-band offset for AlN/GaN (-0.58 eV) and GaN/AlN (-0.70 eV). The band offsets of AlN/GaN/InN were computed using the AlN in-plane lattice constant and including strain effects. They are all of type I and the transitivity rule is satisfied. No interface states were found in the gap. The $\text{Al}_{0.2}\text{Ga}_{0.8}\text{N}/\text{In}_{0.1}\text{Ga}_{0.9}\text{N}$ interface was studied using the virtual crystal approximation. It is of type I and there are no interface states in the gap.

CALCULATIONS

The calculations were performed using either quantum molecular dynamics [12], or standard plane wave codes. Technical details for the defect and impurity calculations were given in [5]. Soft pseudopotentials for N and C were used [13], while the pseudopotential of Ge was generated according to Ref. [14].

The calculations of the electron affinity used Γ -point sampling and a plane-wave energy cut-off of 30 Ry. Norm-conserving pseudopotentials [15, 16, 17] were used for aluminium (p-local), while for nitrogen a soft-core p-local pseudopotential was used [18].

The plane-wave energy cut-off for the interface calculations was 50 Ry. The equivalent of 10 k-points for bulk and superlattice calculations in the zinc-blende structure [19] were chosen while 6-kpts were used for calculations in the wurtzite structure. For all species, d-local norm-conserving pseudopotentials [15, 16, 17] were used. Further, the nonlinear core correction was included for the cation species [20]. The calculated bulk properties of the zinc-blende nitrides obtained using these pseudopotentials are shown in Table 1. The agreement with experiment is excellent. For interface calculations, we studied 4+4 superlattices (16 atoms in the supercell) along (001).

GROUP IV IMPURITIES

We first briefly discuss configurations of substitutional impurities and strain effects. A substitutional impurity in a wurtzite crystal has four nearest neighbors. One of them, located along the c -axis relative to the impurity (called here type-1 neighbor), is non-equivalent to the remaining three neighbors (called here type-2 neighbors). For the group-IV atoms considered here, this non-equivalence is small, since the bond lengths with type-1 and type-2 neighbors are equal to within 1 per cent. In all cases, we find that breathing mode distortions preserve the local hexagonal symmetry. The calculated changes in bond lengths are given in Table 2, together with the energy gain E_{rel} due to the relaxation

Table 1: Calculated bulk properties of zinc-blende nitride semiconductors. The values of the gap at the Γ -point (E_{Γ}) and of the valence-band width (ΔE_{vbw}) are the LDA results. Experimental values are in brackets and follow Ref. [25].

	AlN	GaN	InN
a_0 (Å)	4.37 (4.38)	4.52 (4.5)	5.01 (4.98)
B_0 (MBar)	2.02 (2.02)	1.70 (1.90)	1.58 (1.37)
E_{Γ} (eV)	4.09	2.24 (3.45)	0.16
ΔE_{vbw} (eV)	14.86	15.48	14.01
c_{11} (10^{11} dyne/cm ²)	24.85	23.74	20.24
c_{12} (10^{11} dyne/cm ²)	13.37	11.23	12.96

from the ideal substitutional configuration to the final one. As follows from Table 2, the inclusion of relaxation effects is necessary for a proper description of C_{cation} , Si_N , and Ge_N , due to the large differences between the atomic radii of the impurity and host atoms. The calculated ΔE_{rel} are systematically greater for AlN than for GaN, reflecting the higher stiffness of AlN.

As follows from Table 2, C, Si, and Ge occupying the cation site in both GaN and AlN are effective-mass donors. The only exception is C_{Al} in AlN, where the C-induced level is at about 0.4 eV below the bottom of the conduction band. In GaN, because of its lower band gap, the C-derived level is a resonance situated at 0.9 eV above the bottom of the conduction band.

In addition to the substitutional configuration of X_{cation} donors, we have investigated the stability of the DX-like configuration [21]. In this configuration one bond between the impurity and its first neighbor is broken, and one of these atoms (or both) are shifted to an interstitial site. We have analyzed only one possible DX state, namely that with the broken bond between the impurity and the type-1 neighbor; the configuration with the broken bond to the type-2 N atom should have very similar properties.

We first consider GaN. We find that C_{Ga}^* is metastable not only in the negative but also in the neutral charge state. The energy of C_{Ga}^* is higher than that of the substitutional C_{Ga} by 0.54 and 0.35 eV for the neutral and the negative charge state, respectively. In the DX state both the host N atom and the impurity are significantly displaced along the c -axis (see Ref. [6] for details). In contrast, Si is unstable in the DX state, since there is no energy barrier for the transition from the initial DX configuration to the substitutional one. This holds for both the neutral and the negatively charged Si. Finally, a DX state is metastable for the negatively charged Ge, and its energy is higher by 0.3 eV than that of Ge_{Ga}^- . Unlike for C_{Ga}^* , Ge atom is located at the lattice site, and the nearest-neighbor N atom is displaced along the c -axis. The Ge-N distance is 2.61 Å, to be compared with 1.93 Å for the substitutional configuration. $Ge_{Ga}^*(-)$ introduces a singlet at about 0.4 eV below the bottom of the conduction band. For the neutral charge state, the DX configuration is unstable.

Turning to AlN, we find that in the negative charge state C_{Al}^* is more stable than C_{Al}^- by 0.2 eV. In the neutral charge state C_{Al}^* is metastable, as its energy is higher by 0.48 eV than that of the ground state. Unlike in GaN, the DX configurations are *stable* for both Si and Ge in the negative charge state. Their energies are lower by 0.15 and 1.2 eV than those of the respective substitutional cases. In both cases the impurity remains on

Table 2: Effects of atomic relaxations around impurities: Δb is the change of the bond length, ΔE_{rel} is the relaxation energy, E_{imp} is the position of the impurity level, with e.m. denoting the effective-mass state, and ΔE_{imp} is the relaxation-induced shift of the impurity level.

	Δb (%)	ΔE_{rel} (eV)	E_{imp} (eV)	ΔE_{imp} (eV)
GaN				
C:Ga	-18.1	1.65	e.m.	-
Si:Ga	- 5.6	0.65	e.m.	-
Ge:Ga	- 1.4	0.25	e.m.	-
C:N	-2.0	0.1	$E_v+0.2$	-
Si:N	13.6	3.9	$E_v+1.2$	0.8
Ge:N	13.5	4.1	$E_v+1.35$	0.8
AlN				
C:Al	-17.2	2.6	$E_c-0.4$	1.2
Si:Al	- 7.0	0.7	e.m.	-
Ge:Al	- 2.9	0.3	e.m.	-
C:N	2.0	0.4	$E_v+0.4$	0.1
Si:N	16.5	6.75	$E_v+1.7$	1.0
Ge:N	16.7	6.95	$E_v+1.75$	1.05

the substitutional site, and the N atom is strongly displaced. For Si_{Al}^* the distance to the N atom is 2.95 Å compared to 1.78 Å for Si_{Al} , and for Ge the respective values are 2.83 and 1.86 Å. $Si_{Al}^*(-)$ introduces a level at -1.5 eV below the bottom of the conduction band. For Ge, the gap state is even deeper, at -2.0 eV below the bottom of the conduction band. Finally, the DX configurations are unstable for both Si and Ge in the neutral charge state.

The different DX configurations found for C, as opposed to Si and Ge, are in part due to atomic size effects. For example, when C substitutes for the much bigger Ga atom, the C-N bonds are highly stretched, because they are shorter than the equilibrium Ga-N bonds by about 15 %. In the DX state one C-N bond is broken, and C is free to relax and to shorten the three remaining C-N bonds. Consequently, the C_{Ga}^* -N bonds are shorter by about 7 % than C_{Ga} -N bonds in the substitutional case. At equilibrium, C* forms a nearly planar configuration with the type-2 neighbors. Such a geometry is additionally stabilized by the tendency of C to form planar sp^2 bonds. Both factors may contribute to the stabilization of C_{Ga}^* in the neutral charge state. In contrast, these factors are not operative for Si and Ge impurities, which remain on the substitutional site.

The predicted stability of DX^- states for C, Si, and Ge in AlN implies that the reaction $2d^0 \rightarrow d^+ + DX^-$ is exothermic, and the electrons are captured by the deep DX-derived levels. Consequently, the doping efficiency is quenched. In $Al_{1-x}Ga_xN$ alloys the doping efficiency with C, Si, and Ge should thus strongly depend on the alloy composition. These dopants should be efficient donors up to a crossover composition given by the stability of the DX state.

We will now consider the acceptors X_N . In zinc-blende crystals, acceptor levels of group-IV atoms are three-fold degenerate. Due to the wurtzite symmetry of GaN and AlN, the triplets are split into doublets and singlets by the energy E_{split} . In all cases considered

here, the energies of doublets (given in Table 2), E_D , are higher than those of singlets, E_S . Both the acceptor energies and the splittings strongly depend on the impurity. We find that C is a shallow acceptor with $E_D=0.2$ eV in GaN, which is in an excellent agreement with the recent experimental data [22]. Thus, C is a promising *p*-type dopant, since it is a shallower acceptor than the commonly used Mg [2]. In AlN, C is deeper ($E_D=0.4$ eV) and more localized. The doublet-singlet splitting E_{split} is about 0.2 eV in both materials. In contrast, both Si and Ge are deep acceptors. For GaN:Si $E_D=1.2$ eV and $E_{split}=0.6$ eV, and for GaN:Ge $E_D=1.35$ eV and $E_{split}=0.6$ eV. In AlN the binding energies and the splittings are even higher, and we find $E_D=1.7$ (1.75) eV and $E_{split}=0.7$ (0.7) eV for Si_N and Ge_N, respectively).

Finally, we turn to the electronic structure of the nearest-neighbor $X_{cation}^+-X_N^-$ pairs. Compared to the case of distant X_{cation} and X_N impurities, the main modification is a substantial increase of the doublet-singlet splittings. In the case of GaN, E_{split} rises from 0.6 to 1.0 eV for Si-Si pairs, and from 0.6 to 1.05 eV for Ge-Ge pairs. For AlN, the increase is from 0.7 to 1.4 eV for Si-Si pairs, and from 0.7 to 1.35 eV for Ge-Ge pairs. This effect is due to the close proximity of the X_{cation} donor, located along the *c*-axis, relative to the acceptor X_N .

NEGATIVE ELECTRON AFFINITY AT AlN SURFACES

The electron affinity is defined as the difference between the bottom of the conduction band and the vacuum level. Negative electron affinity occurs when the conduction band bottom is below the vacuum level. It has potential use in electron emitters, cold cathodes and other optoelectronic devices. The recent experimental observation of negative electron affinity at AlN surfaces [11] provides the motivation to study the electron affinity at AlN surfaces.

The value of the electron affinity is modified by the surface dipole moment and the space charge due to the occupation of surface states by free carriers from the bulk. The presence of free carriers leads to band bending near the surface; however, this effect is significant only in doped materials and need not be considered at present. Rather, it is the effect of chemisorption and surface reconstructions on the the surface dipole that constitutes our present interest.

The electron affinity of a semiconductor is defined as

$$\chi = D - (E_c - V_{bulk}) \quad (1)$$

where D , the surface dipole strength, determines the relative positions of the bulk electron states and the vacuum level [28], while $(E_c - V_{bulk})$ is the position of the conduction band minimum relative to the bulk-averaged electrostatic potential. The latter is purely a bulk property and can be obtained in a calculation of the AlN bulk. It is well-known that the local density functional theory consistently underestimates the size of semiconductor band-gaps. For this reason, the conduction-band minimum was rigidly shifted to the experimental value of 6.2 eV using the so-called scissors operator. The surface dipole strength was obtained from the difference of the electrostatic potential across the surface.

The 1×1 (0001) Al- and N-terminated surfaces (with neither adatoms nor vacancies) were studied. Both surfaces exhibit some inward relaxation, while the geometries in the surface plane did not significantly change. The electron affinities are 0.85 eV and 0.30 eV for the Al- and N-terminated surfaces, respectively. These 1×1 structures are expected to have higher surface energies than the 2×2 reconstructed structures. As the 2×2 vacancy

reconstructions were among the lower energy 2×2 reconstructions of (0001) GaN, the 2×2 vacancy reconstructions of the (0001) surfaces of AlN were next investigated. With one-quarter of a monolayer of the Al surface atoms removed, the surface can accommodate a much larger inward relaxation than the 1×1 structure. In this case, the electron affinity is -0.70 eV. For the same reconstruction on the N-terminated face, the electron affinity is 1.40 eV. The effect of hydrogen chemisorption on the electron affinity of the 1×1 (0001) Al- and N-terminated surfaces was also examined. Hydrogen adsorption reduced the electron affinity of the N-terminated surface to 0.05 eV; however, the electron affinity of Al-terminated surface increased to 1.60 eV.

The changes in the electron affinity reflect modification of the net surface dipole. During chemisorption, the adsorbates saturate the dangling bonds of the surface atoms resulting in charge transfer between the adsorbates and surface atoms. This transfer manifests itself as an additional dipole field, the strength and direction of which determines the change of the electron affinity. The diamond (111) surface provides another example of this effect. The bare surface has a positive electron affinity; however, it has a negative electron affinity when it has been passivated by hydrogen. Since carbon is more electronegative than hydrogen, charge transfers from the hydrogen adatom to the surface carbon atom. This induces an additional dipole which points outwards and reduces the electron affinity to a negative value [29]. As nitrogen is more electronegative than hydrogen, this also occurs when hydrogen is chemisorbed on the N-terminated AlN surface. In contrast, aluminium has a smaller electronegativity than hydrogen and consequently we expect the opposite to occur when hydrogen adatoms are chemisorbed on the Al-terminated surface. This is indeed the case. The electronegativity difference between the surface species and the adsorbed species provides insight into manner in which the adatoms modify the surface charge density and hence the electron affinity. Of course, bonding properties will be affected by the detailed nature of the surface, but nonetheless strongly electropositive elements, such as Li and Be, may result in negative electron affinity when adsorbed on the surface.

INTERFACES OF WIDE-GAP NITRIDES

Because of the lattice-mismatch between AlN and GaN (2.5%) and between InN and AlN (12.1%), superlattices of these materials will be strained. We have studied the energetics of two different interfaces, namely the strained GaN/AlN (with AlN in-plane lattice constant) and the strained AlN/GaN (with GaN in-plane lattice constant). The elastic energy for these interfaces, which is the difference of the strained and unstrained energy per pair, is 46 meV/pair for the GaN/AlN interface, while it is 63 meV/pair for AlN/GaN. The interface energy, defined as the excess or deficit energy due to the presence of the interface, is extremely small, namely ~ 1 meV/atom, which is of the order of the precision of the calculations. Thus the interfaces show similar bonding characteristics. These results suggest that the critical thickness for pseudomorphic AlN/GaN is significantly smaller than for GaN/AlN, in agreement with the observation that epitaxially grown GaN/AlN results in higher quality samples [30].

The band offsets of the strained heterojunctions have also been studied. Following the conclusions of the previous paragraph, AlN is taken to be the substrate in all of the cases presented below. The valence-band offsets are -0.70 eV for GaN/AlN and -0.44 eV for AlN/GaN (001) strained interfaces, indicating that the effect of strain on the value of the valence-band offset is significant. The interfaces are all of type I and there are no interface states in the gap. We then investigated the band offsets of the (001) GaN/AlN, InN/AlN and InN/GaN strained heterojunctions. The band offsets are shown in Fig. 1.

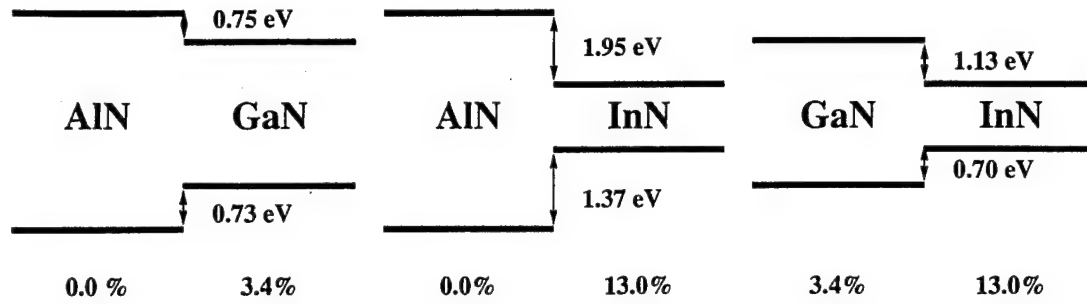


Figure 1: Calculated band offsets for the three interfaces described in the text (an AlN substrate is assumed). The lattice mismatch shown is with respect to AlN.

Table 3: Calculated bulk properties of zinc-blende $\text{Al}_{0.2}\text{Ga}_{0.8}\text{N}$ and $\text{In}_{0.1}\text{Ga}_{0.9}\text{N}$ semiconductors within the virtual crystal approximation. The values of the gap at the Γ -point (E_{Γ}) and of the valence-band width (ΔE_{vbw}) are the LDA results. The AlN in-plane lattice constant is used (the mismatch is with respect to the AlN lattice constant).

	$\text{Al}_{0.2}\text{Ga}_{0.8}\text{N}$	$\text{In}_{0.1}\text{Ga}_{0.9}\text{N}$
a_0 (Å)	4.51	4.61
B_0 (MBar)	1.67	1.78
E_{Γ} (eV)	2.56	1.68
ΔE_{vbw} (eV)	15.10	15.31
c_{11} (10^{11} dyne/cm ²)	23.46	20.75
c_{12} (10^{11} dyne/cm ²)	10.88	12.02
Vegard's Rule (Å)	4.49	4.57
Lattice Mismatch	3.1	5.2

In determining the conduction-band offsets, the conduction band minima were shifted to their experimental values using the so-called scissors operator. Each of the interfaces is of type I and the transitivity rule is satisfied. Further, states at the top of the valence band are mostly confined to the epilayer with the smaller gap and there are no interface states in the gap of the superlattice.

The possible sources of systematic error of the calculation of the band offsets include the neglect of the anion p - and cation d -state repulsion [31] and the well-known neglect of many-body effects in the local density approximation. In GaN/AlN interfaces, the inclusion of the $3d$ -electrons as valence electrons results in a constant shift of 0.2 eV which is less than the experimental error [32] and does not change the character of the interface. Incorporating this shift gives results in agreement with previous estimates using a d -valence pseudopotential [33] and an all-electron calculation [34]. The importance of many-body effects on the band offsets is not known and awaits a future GW calculation.

We also studied an alloy interface based upon the nitride-based multi-quantum-well structure that Nakamura et al. [3] used to demonstrate stimulated emission in the blue region of the spectrum. The bulk properties of the two zinc-blende alloys comprising the

epilayers of the multi-quantum-well, calculated using the virtual crystal approximation, are shown in Table 3. In the virtual crystal approximation, the pseudopotentials of the constituent species are averaged by their fractional composition [35]. Vegard's rule is seen to be satisfied.

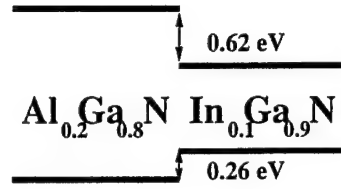


Figure 2: Calculated band offsets for the zinc-blende (001) $\text{Al}_{0.2}\text{Ga}_{0.8}\text{N}/\text{In}_{0.1}\text{Ga}_{0.9}\text{N}$ interface described in the text assuming an AlN substrate.

The zinc-blende (001) interface of these alloys was investigated. Strain effects were explicitly included using macroscopic elasticity theory (using the theoretically determined elastic constants shown in Table 2) and a total energy minimization. The values for scissors corrections of the band gap of the alloys were estimated using a Vegard-type rule, namely the gap of the alloy was taken to be the average of the band gap of the pure phase weighted by its fractional composition. The band offsets are shown in Fig. 2. The interface is of type I and there are no interface states in the gap.

Because of its low symmetry, the wurtzite system may display pyroelectric and piezoelectric behavior [36]. These effects, if present, will manifest themselves macroscopically in multi-quantum-wells along those directions that do not have a perpendicular mirror-plane [37, 38]. Thus, for instance, macroscopic fields are not observed in the strained (001) interfaces in zinc-blende structure, while they are observed in strained (111) interfaces [37]. Indeed, a polarization will be induced only if off-diagonal components of the strain are present. In (0001) strained GaN/AlN, we observe a substantial electric field as has been previously noted by Satta and coworkers [39]. In order to distinguish the bulk pyroelectric and piezoelectric contributions to this field from that induced by the interface, we have calculated the spontaneous bulk polarization of unstrained AlN and the strain induced polarization for the GaN epilayer [40]. The spontaneous polarization (P_3) of AlN and GaN in equilibrium are $-1.227 \mu\text{C}/\text{cm}^2$ and $-0.448 \mu\text{C}/\text{cm}^2$ respectively; the polarization of the strained GaN is $-0.454 \mu\text{C}/\text{cm}^2$. These values are comparable to the computed bulk polarization in BeO [40]. The effect of the interface dipole is small; the polarization in the GaN/AlN multi-quantum-well is well described by the superposition of the polarizations of the constituent epilayers of the multi-quantum-well. The estimated contribution of the interface dipole (which includes the response of one epilayer to the field of the other) is $0.057 \mu\text{C}/\text{cm}^2$, which is of opposite sign and an order of magnitude smaller than the bulk polarizations. The computed value of the polarization in the superlattice agrees with that estimated from experiment by Martin *et al.* [32].

This work was supported in part by grants NSF DMR 9408437, ONR N00014-92-J-1477, and KBN 2-P03B-178-10.

REFERENCES

- [1] R. F. Davis, *Physica B* **185**, 1 (1993).
- [2] H. Morkoc, S. Strite, G. B. Gao, M. E. Lin, B. Sverdlov, and M. Burns, *J. Appl. Phys.* **76**, 1363 (1994).

- [3] S. Nakamura et al., Jpn. J. Appl. Phys. **35**, L74 (1996).
- [4] See, e.g., B. Min, C. Chan and K. Ho, Phys. Rev. B **45**, 1159 (1992), V. Fiorentini, M. Methfessel and M. Scheffler, Phys. Rev. B **47**, 13353 (1993), E. Albanesi, W. Lambrecht and B. Segall, J. Vac. Sci. Technol. B **12**, 2470 (1994), A. Rubio, J. Corkill and M. L. Cohen, Phys. Rev. B **49**, 1952 (1994), C. Yeh, S. Wei and Z. Zunger, Phys. Rev. B **50**, 2715 (1994), A. F. Wright and J. S. Nelson, Phys. Rev. B **51**, 7866 (1995) and M. Palummo, L. Reining, R.W. Godby, C.M. Bertoni and N. Bornsen, Europhys. Lett. **26**, 607 (1995). For a general reference, see W. Lambrecht and B. Segall, in *Properties of Group III Nitrides*, edited by J. Edgar, EMIS Data Series (IEE, London, 1994), chapt. 5.
- [5] P. Bogusławski, E. M. Briggs, and J. Bernholc, Phys. Rev. B **51**, 17255 (1995).
- [6] P. Bogusławski, E. M. Briggs, and J. Bernholc, Appl. Phys. Lett., July (1996).
- [7] P. Bogusławski and J. Bernholc, to be published.
- [8] B. Chen, K. Rapcewicz, Z. Zhang and J. Bernholc, to be published (1996).
- [9] M. Buongiorno Nardelli, K. Rapcewicz and J. Bernholc, to be published (1996).
- [10] K. Rapcewicz, B. Chen, B. Yakobson and J. Bernholc, to be published (1996).
- [11] M. C. Benjamin, C. Wang, R. F. Davis and R. J. Nemanich, Appl. Phys. Lett. **64**, 3288 (1994).
- [12] R. Car and M. Parrinello, Phys. Rev. Lett. **55**, 2471 (1985).
- [13] G. Li and S. Rabii, unpublished (1992).
- [14] X. Gonze, R. Stumpf, and M. Scheffler, Phys. Rev. B **44**, 8503 (1991).
- [15] G. Bachelet, D. R. Hamann and M. Schlüter, Phys. Rev. B **26**, 4199 (1982).
- [16] D. R. Hamann, M. Schlüter and C. Chiang, Phys. Rev. Lett. **43**, 1494 (1979).
- [17] D. R. Hamann, Phys. Rev. B **40**, 2980 (1989).
- [18] G. Li, and S. Rabii, unpublished (1992).
- [19] S. Froyen, Phys. Rev. B, **39**, 3168 (1989).
- [20] S. Louie, S. Froyen and M.L. Cohen, Phys. Rev. B **26**, 1738 (1982).
- [21] D. J. Chadi and K. J. Chang, Phys. Rev. Lett. **61**, 873 (1988).
- [22] S. Fisher, C. Wetzel, E. E. Haller, and B. K. Meyer, Appl. Phys. Lett. **67**, 1298 (1995).
- [23] R. Bauer and G. Margaritondo, Physics Today, **40**, 27 (1987).
- [24] M.-E. Lin, B. N. Sverdlov, S. Strite, H. Morkoç and A.E. Drakin, Electron. Lett. **29**, 1759 (1993).
- [25] A. F. Wright and J. S. Nelson, Phys. Rev. B **50**, 2159 (1994).

- [26] J. Lee, H. Aaronson and K. Russel, *Surf. Sci.* **51** 302 (1975) and E. Arbel and J. Cahn, *Surf. Sci.* **51**, 305 (1975).
- [27] N. Chetty and R.M. Martin, *Phys. Rev. B* **45**, 6074 (1992), *ibid.* **45**, 6089 (1992) and *ibid.* **44**, 5568 (1991).
- [28] A. Zangwill, *Physics at Surfaces*, (Cambridge University Press, Cambridge, England, 1988).
- [29] Z. Zhang, M. Wensell, and J. Bernholc, *Phys. Rev. B.* **51**, 5291 (1995).
- [30] See, for instance, H. Morkoç et al., *J. Appl. Phys.* **76**, 1363 (1994), M. Paisley and R.F Davis, *J. Cryst. Growth* **127**, 136 (1992).
- [31] S. Wei and A. Zunger, *Phys. Rev. Lett.* **59**, 144 (1987).
- [32] G. Martin et al., *Appl. Phys. Lett.* **65**, 610 (1994).
- [33] V. Fiorentini, M. Methfessel and M. Scheffler, *Phys. Rev. B* **47**, 13353 (1993).
- [34] E. Albanesi, W. Lambrecht and B. Segall, *J. Vac. Sci. Technol. B* **12**, 2470 (1994).
- [35] M. Peressi, S. Baroni, A. Baldereschi and R. Resta, *Phys. Rev. B* **41**, 12106 (1990).
- [36] N. W. Ashcroft and N. D. Mermin, *Solid State Physics* (Saunders College, Philadelphia 1976). Ch. 27.
- [37] D. Smith, *Solid State Commun.* **57**, 919 (1986).
- [38] A. Bykhovski, B. Gelmont and M. Shur, *Appl. Phys. Lett.* **63**, 2243 (1993); *J. Appl. Phys.* **74**, 6734 (1993).
- [39] A. Satta, V. Fiorentini, A. Bosin, F. Meloni and D. Vanderbilt, preprint (1996).
- [40] M. Posternak, A. Baldereschi, A. Catellani and R. Resta, *Phys. Rev. Lett.* **64**, 1777 (1990).

XVII. Strain Effects on the Interface Properties of Nitride Semiconductors

Marco Buongiorno Nardelli, Krzysztof Rapcewicz and J. Bernholc

Department of Physics, North Carolina State University, Raleigh, NC 27695-8202

Abstract

An *ab initio* study of nitride-based heteroepitaxial interfaces that explicitly treats the strain due to lattice-mismatch is presented. AlN is the preferred substrate and strain effects on the band offsets range from 20% to 40%. The AlN/GaN/InN interfaces are all of type I, while the $\text{Al}_{0.5}\text{Ga}_{0.5}\text{N}/\text{AlN}$ zinc-blende (001) interface may be of type II. Further, the calculated bulk polarizations in wurtzite AlN and GaN are -1.2 and $-0.45 \mu\text{C}/\text{cm}^2$, respectively, and the interface contribution to the polarization in the GaN/AlN wurtzite multi-quantum-well is small.

71.15.Hx, 71.15.Nc, 81.05.Ea, 73.40.Kp

With the recent demonstration of stimulated emission in the blue region of the spectrum from a nitride-based multi-quantum-well structure [1], interest in the nitride-based semiconductors has burgeoned. This discovery has served to underscore the very attractive properties of the nitride-based materials, which include a wide band-gap and the ability to form a continuous range of solutions of GaN, AlN and InN, materials which have very different band gaps. This latter property makes possible the engineering of band gaps which span the range from the deep ultra-violet to the visible [2].

Not surprisingly the potential technological importance of these materials has elicited the interest of a number of theoretical groups [3-7]. In spite of this, the strained interfaces of these lattice-mismatched materials have not been studied. We find that strain effects are significant and AlN lattice-matched substrates are clearly preferred for pseudomorphic heteroepitaxial growth. Further, the strain induces changes of 20% to 40% in the value of the band offset and these changes increase with decreasing in-plane lattice parameter. The AlN/GaN/InN interfaces are all of type I, while the $\text{Al}_{0.5}\text{Ga}_{0.5}\text{N}/\text{AlN}$ zinc-blende (001) interface is found to be of type II. Finally, we studied the GaN/AlN wurtzite interface, where qualitatively new features, namely pyro- and piezoelectric effects, appear due to the low symmetry of the wurtzite lattice.

The standard *ab initio* plane-wave pseudopotential method [8-10] was employed in the calculations. The energy cut-off for the plane-wave expansion was 50 Ry to ensure convergence of the nitrogen pseudopotential. We used the equivalent of 10 k-points for bulk and superlattice calculations in the zinc-blende structure [11] and 6 k-points for calculations of the wurtzite structure [12]. Convergence both in the size of the plane-wave basis and in the number of special points has been carefully checked. The Perdew-Zunger parametrization [13] of the Ceperley-Alder form [14] of the exchange-correlation energy was used. For interface calculations, we employed 4+4 superlattices (16 atoms) along the (001) and (0001) directions. The non-local, norm-conserving pseudopotentials [15-17] were included using the Kleinman-Bylander approach [18]. For nitrogen, we used a neutral configuration as the atomic reference for all states.

In pseudopotentials where d -electrons are treated as core electrons, experience with II-VI semiconductors [19] has shown that the inclusion of the nonlinear core correction [20] results in a substantial improvement of the bulk properties. As an early work demonstrated [5], the reference atomic state plays a critical role in the generation of the pseudopotential. In order that the pseudopotential be consistently descreened, it is necessary, when using the nonlinear core correction, that the reference atomic state be the same for all angular-momentum channels. This is in contrast with standard Bachelet, Hamann and Schlüter prescription [15] in which the atomic ground state is used as a reference for each angular-momentum channel present in the ground state, while, to improve transferability, an appropriately ionized, excited-atom configuration is used as the reference state for the angular-momentum channels present only in the excited states. Dal Corso et al. [21] have dealt with the inconsistency between the restriction imposed by the use of the nonlinear core correction and the importance of different atomic reference configurations for different angular-momentum channels by simultaneously fitting the pseudopotential and the core charge to more than one configuration.

The approach used here resolves this inconsistency while maintaining the improved transferability obtained through the choice of different, atomic reference configurations. This is achieved by choosing as the initial reference configuration the neutral ground state and generating the angular momenta channels for it together with the core charge. For angular momenta present only in the excited states, we use the appropriately ionized, excited-atom configuration of the frozen-core atom (with the core from the neutral ground state). We generated pseudopotentials for aluminium, gallium and indium with this procedure using the standard reference configurations for the empty d -channel [16,22], namely $3s^{0.75} 3p^0 3d^{0.25}$ for aluminium, $4s^{0.75} 4p^0 4d^{0.25}$ for gallium and $5s^1 5p^{0.75} 5d^{0.25}$ for indium.

The calculated bulk properties are presented in Table I. In general, agreement with experiment is excellent [23,24]. The theoretical lattice parameters of both the zinc-blende and wurtzite forms agree very well with experiment; a similar level of accuracy is expected for the interface calculations described below. We have also calculated the bulk properties of

GaN treating the 3d-electrons of gallium as valence electrons following Ref. [7]. With a cut-off of 240 Ry, we find $a_0 = 4.46 \text{ \AA}$ and $B_0 = 2.14 \text{ Mbar}$, which reproduces the experimental values to the same degree as our calculations employing the present pseudopotentials with the d -electrons in core.

The properties of nitride-based semiconductor devices are critically dependent upon their interface properties. Due to the lattice-mismatch between AlN and GaN (3.5%) and between InN and AlN (12.8%), superlattices of these materials are expected to be strained [25]. We investigate first the (001) zinc-blende interface. The supercell for the strained superlattice was determined using macroscopic elasticity theory [26]. In this theory, each half of the heterojunction is treated as a strained bulk with a fixed in-plane lattice constant $a_{||}$. The perpendicular lattice constant of the epilayer c is obtained by minimizing the strain energy of the system subject to the fixed in-plane constant. For AlN, GaN and InN, the calculated elastic constants used to determine the strains are given in Table II. Using total energy calculations, we find that macroscopic elasticity theory predicts well the perpendicular lattice constant for the epilayer. The residual relaxation of the atoms at the interface is negligible ($< 0.05 \text{ \AA}$) and does not affect the band offset of the interface.

The interface energy for the (001) direction can be calculated in a straightforward manner because the supercell contains two identical interfaces. The interface energy of the interface AC/BC is

$$E_{\text{interface}} = \frac{1}{2}(E_{\text{supercell}} - N_{AC}E_{AC} - N_{BC}E_{BC}), \quad (1)$$

where E_{AC} (E_{BC}) is the energy of the AC (BC) pair in the appropriately strained bulk and N_{AC} (N_{BC}) is the number of AC (BC) pairs in the supercell. We considered three different interfaces, namely the strained GaN/AlN (with AlN in-plane lattice constant), the strained AlN/GaN (with GaN in-plane lattice constant) and the "unstrained" GaN/AlN (with average lattice parameter) interfaces. In each case, the interface energy was found to be extremely small, $\sim 1 \text{ meV/interface atom}$, which is of the order of the precision of the calculations. Therefore, all of the interfaces show similar bonding characteristics. This is not

the case, however, with the elastic energies of the interfaces. The elastic energy, which is the difference of the strained energy and the unstrained energy per pair, manifests itself as an extrinsic volume effect governing the thickness of the pseudomorphic layer. We find that the elastic energy is 46 meV/pair for GaN/AlN and is 63 meV/pair for AlN/GaN. The elastic energy in the "unstrained" case is comparable to that in AlN/GaN. Thus the critical thickness for pseudomorphic AlN/GaN is significantly smaller than GaN/AlN, an observation which is consonant with the fact that epitaxially grown GaN/AlN results in higher quality samples [2]. In the light of these conclusions, we restrict further considerations to interfaces grown on an AlN substrate, i.e. the in-plane lattice constant for all the superlattices is the AlN value.

We have investigated the band offsets of the (001) GaN/AlN, InN/AlN and InN/GaN strained heterojunctions following the procedure of Ref. [27]. In each case AlN is taken to be the substrate. The results are shown in Fig. 1 [28]. We find that each interface is of type I, with the InN band edges sandwiched by the band-edges of the other materials, since the band gap in InN is the smallest. The transitivity rule is satisfied. We do not observe any interface states in the gap of the superlattice. As might be expected, states at the top of the valence band are mostly localized to the epilayer with the smaller gap. Similar behavior is observed for the conduction-band minimum; the degree of localization of the states at the conduction-band minimum increases with increasing band offset. Strain effects on the valence-band offsets have been investigated for the interfaces formed by AlN and GaN. They vary between 20% and 40%. In particular, the valence-band offsets are -0.75 eV for GaN/AlN, -0.44 eV for AlN/GaN and -0.58 eV for "unstrained" GaN/AlN.

The case of the wurtzite (0001) GaN/AlN interface was also investigated. Strain effects were explicitly included using macroscopic elasticity theory [29] and a total energy optimization. The calculated valence-band offset is estimated to be -0.57 eV, a value smaller than the result for the strained non-polar (001) GaN/AlN interface. The ratio of the conduction-band to valence-band offset is 65:20. Our results agree very well with the experimental measurements of the (0001) wurtzite interface [30].

The possible sources of systematic error of the calculation include the neglect of the anion p - and cation d -state repulsion [31] and the well-known neglect of many-body effects in the LDA. In GaN/AlN interfaces, the inclusion of the $3d$ -electrons as valence electrons results in a constant shift of 0.2 eV, which is less than the experimental error [30], and does not change the character of the interface. Incorporating this shift gives results in agreement with previous estimates using a d -valence pseudopotential [6] and an all-electron calculation [4]. The importance of many-body effects on the band offsets is not known and awaits a future GW calculation.

Because of its low symmetry, the wurtzite system may display pyroelectric and piezoelectric behavior [32]. These effects, if present, will manifest themselves macroscopically in multi-quantum-wells along those directions that do not have a perpendicular mirror-plane [33,34]. Thus, for instance, macroscopic fields are not observed in the strained (001) interfaces in zinc-blende structure, while they are observed in strained (111) interfaces [33]. Indeed, a polarization will be induced only if off-diagonal components of the strain are present. In (0001) strained GaN/AlN, we observe a substantial electric field as has been previously noted by Satta and coworkers [35]. In order to distinguish the bulk pyroelectric and piezoelectric contributions to this field from that induced by the interface, we have calculated the spontaneous bulk polarization of unstrained AlN and the strain induced polarization for the GaN epilayer [36]. The spontaneous polarization (P_3) of AlN and GaN in equilibrium are $-1.227 \mu\text{C}/\text{cm}^2$ and $-0.448 \mu\text{C}/\text{cm}^2$ respectively; the polarization of the strained GaN is $-0.454 \mu\text{C}/\text{cm}^2$. These values are comparable to the computed bulk polarization in BeO [36]. The effect of the interface dipole is small; the polarization in the GaN/AlN multi-quantum-well is well described by the superposition of the polarizations of the constituent epilayers of the multi-quantum-well. The estimated contribution of the interface dipole (which includes the response of one epilayer to the field of the other) is $0.057 \mu\text{C}/\text{cm}^2$, which is of opposite sign and an order of magnitude smaller than the bulk polarizations. The computed value of the polarization in the superlattice agrees with that estimated from experiment by Martin *et al.* [30].

Alloying provides another way to tune band offsets through changes to the strain in the system and changes to the electronic structure. The virtual crystal approximation in which the pseudopotentials of the constituent species are averaged by their fractional composition has been shown to adequately describe band offsets in certain alloy interfaces [37]. We have studied the zinc-blende (001) $\text{Al}_{0.5}\text{Ga}_{0.5}\text{N}/\text{AlN}$ interface in the virtual crystal approximation. First, we used the virtual crystal approximation to calculate the elastic properties of the zinc-blende alloy (with theoretical lattice constant of 4.44 \AA), finding $c_{11} = 23.55 \times 10^{11} \text{ dyne/cm}^2$ and $c_{12} = 11.84 \times 10^{11} \text{ dyne/cm}^2$, and used macroscopic elasticity theory to predict the strains. In contrast to the pure nitride interfaces, we found that this particular alloy interface is a staggered type II interface. The valence-band offset is -0.39 eV and the conduction-band offset -0.17 eV . In order to verify the accuracy of the approach, we compared the lineup of the virtual crystal approximation with a fully relaxed $(\text{GaN})_1(\text{AlN})_1/\text{AlN}$ interface; the alloy was replaced by the 1×1 superlattice, an extreme example of an ordered alloy. The results are -0.37 eV and -0.09 eV for the valence- and conduction-band offsets, respectively. Further, the character of the interface remains unchanged. Therefore, the virtual crystal approximation well describes the band offsets of this alloy superlattice and, within the present theoretical scheme, the interface will change its character as the gallium composition of the alloy is increased.

In summary, we have investigated the influence of strain on the interface properties of nitride-based heterostructures. In these lattice-mismatched heterojunctions, the in-plane lattice constant can be varied by changing the characteristics of the substrate and so tune the band offset. The elastic energy of the AlN/GaN interface is appreciably larger than that of the GaN/AlN interface, making AlN the preferred substrate for pseudomorphic growth. Strain effects on the band offsets in GaN/AlN range from 20% to 40%. The bulk spontaneous polarization of the constituent materials, which range from -1.227 to $-0.448 \times 10^{-2} \text{ C/m}^2$ for AlN and GaN , respectively, constitutes the preponderant contribution to the polarization present in the low symmetry wurtzite GaN/AlN interface, i.e. the interface contribution to the polarization is small. Finally, the pure interfaces are all of type I, while

the $\text{Al}_{0.5}\text{Ga}_{0.5}\text{N}/\text{AlN}$ interface may be of type II, suggesting that a change of character will occur as the gallium composition of the alloy is increased.

We acknowledge helpful conversations with Drs. D. J. Sullivan and E. L. Briggs.

REFERENCES

- [1] S. Nakamura et al., Jpn. J. Appl. Phys. **35**, L74 (1996).
- [2] See, for instance, H. Morkoç et al., J. Appl. Phys. **76**, 1363 (1994), M. Paisley and R. Davis, J. Cryst. Growth **127**, 136 (1992).
- [3] These include: A. Rubio, J. Corkill and M.L. Cohen, Phys. Rev. B **49**, 1952 (1994), C. Yeh, S. Wei and Z. Zunger, Phys. Rev. B **50**, 2715 (1994) and M. Palummo, L. Rein- ing, R.W. Godby, C.M. Bertoni and N. Bornsen, Europhys. Lett. **26**, 607 (1995). For a general reference, W. Lambrecht and B. Segall, in *Properties of Group III Nitrides*, edited by J. Edgar, EMIS Data Series (IEE, London, 1994), chapt. 5.
- [4] E. Albanesi, W. Lambrecht and B. Segall, J. Vac. Sci. Technol. B **12**, 2470 (1994).
- [5] B. Min, C. Chan and K. Ho, Phys. Rev. B **45**, 1159 (1992).
- [6] V. Fiorentini, M. Methfessel and M. Scheffler, Phys. Rev. B **47**, 13353 (1993).
- [7] A. Wright and J. Nelson, Phys. Rev. B **50**, 2159 (1994); Phys. Rev. B **51**, 7866 (1995).
- [8] M. Payne, M. Teter, D. Allan, T. Arias and J. Joannopoulos, Rev. Mod. Phys. **64**, 1045 (1992).
- [9] W. Pickett, Comp. Phys. Rep. **9**, 115 (1989).
- [10] D. Remler and P. Madden, Mol. Phys. **70**, 921 (1990).
- [11] S. Froyen, Phys. Rev. B, **39**, 3168 (1989).
- [12] D.J. Chadi and M.L. Cohen, Phys. Rev. B **8**, 5747 (1973).
- [13] J. Perdew and A. Zunger, Phys. Rev. B **23**, 5048 (1981).
- [14] D. Ceperley and B. Alder, Phys. Rev. Lett. **45** 566 (1980).
- [15] G. Bachelet, D. Hamann and M. Schlüter, Phys. Rev. B **26**, 4199 (1982).

- [16] D. Hamann, M. Schlüter and C. Chiang, Phys. Rev. Lett. **43**, 1494 (1979).
- [17] D. Hamann, Phys. Rev. B **40**, 2980 (1989).
- [18] L. Kleinman and D. Bylander, Phys. Rev. Lett. **48**, 1425 (1982).
- [19] G. Engel and R. Needs, Phys. Rev. B **41**, 7876 (1990) and A. Qteish and R. Needs, Phys. Rev. B **43**, 4229 (1991).
- [20] S. Louie, S. Froyen and M.L. Cohen, Phys. Rev. B **26**, 1738 (1982).
- [21] A. Dal Corso, R. Resta, S. Baroni and S. de Gironcoli, Phys. Rev. B **47**, 3588 (1994) and A. Dal Corso, Ph.D. Thesis, Trieste, (1993).
- [22] X. Gonze, P. Käckell and M. Scheffler, Phys. Rev. B **17**, 12264 (1990).
- [23] Transferability was also verified by calculating the bulk properties of AlAs, GaAs and InAs; we find the same degree of accuracy as commonly used pseudopotentials.
- [24] Calculations for aluminium metal show excellent agreement with experiment and prior calculations, E. Briggs, (private communication, 1996).
- [25] The percentages given refer to the computed mismatch in the zinc-blende structure and the computed mismatch of the in-plane lattice constant in wurtzite, which are the same for both structures. Further, the experimental lattice-mismatch between AlN and GaN is 2.5% while between AlN and InN it is 12.1%.
- [26] C. Van de Walle and R.M. Martin, Phys. Rev. B **34**, 5621 (1986).
- [27] A. Baldereschi, S. Baroni and R. Resta, Phys. Rev. Lett. **61**, 734 (1988).
- [28] In order to correct for the well-known underestimation of the band gaps by the LDA, the conduction-band offsets were corrected by shifting the conduction-band minima to recover the experimental band-gaps.
- [29] The experimental ratio [38], $c_{13}/c_{33} = 0.59$, was used to determine the starting point

of the total energy minimization.

- [30] G. Martin et al., Appl. Phys. Lett. **65**, 610 (1994), *ibid.* **68**, 2541 (1996).
- [31] S. Wei and A. Zunger, Phys. Rev. Lett. **59**, 144 (1987).
- [32] N. W. Ashcroft and N. D. Mermin, *Solid State Physics* (Saunders College, Philadelphia 1976). Ch. 27.
- [33] D. Smith, Solid State Commun. **57**, 919 (1986).
- [34] A. Bykhovski, B. Gelmont and M. Shur, Appl. Phys. Lett. **63**, 2243 (1993);
J. Appl. Phys. **74**, 6734 (1993).
- [35] A. Satta, V. Fiorentini, A. Bosin, F. Meloni and D. Vanderbilt, preprint (1996)
- [36] M. Posternak, A. Baldereschi, A. Catellani and R. Resta, Phys. Rev. Lett. **64**, 1777 (1990).
- [37] M. Peressi, S. Baroni, A. Baldereschi and R. Resta, Phys. Rev. B **41**, 12106 (1990).
- [38] *Landolt-Börnstein: Numerical Data and Functional Relationships in Science and Technology*, ed. O. Madelung (Springer, New York, 1982), vol. 17.

TABLES

TABLE I. Calculated bulk properties of zinc-blende and wurtzite nitride semiconductors. The values of the gap at the Γ -pt (E_{Γ}) and of the valence-band width (ΔE_{vbw}) are the LDA results. Experimental values are in brackets and follow Ref. [7].

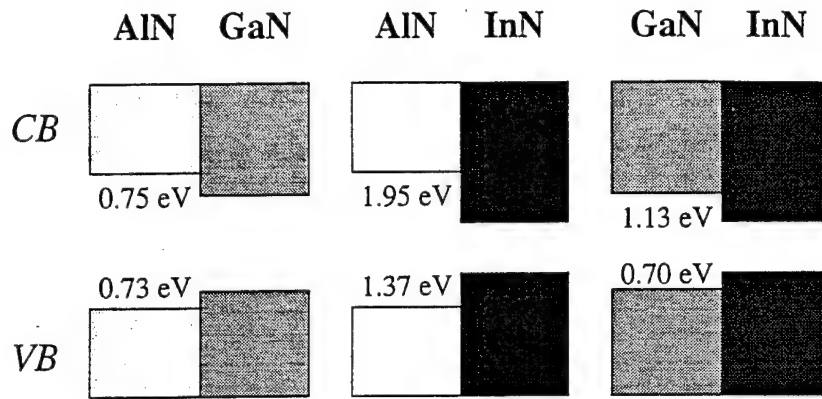
zinc-blende			
	AlN	GaN	InN
a_0 (Å)	4.37 (4.38)	4.52 (4.5)	5.01 (4.98)
B_0 (MBar)	2.02 (2.02)	1.70 (1.90)	1.58 (1.37)
E_{Γ} (eV)	4.09	2.24 (3.45)	0.16
ΔE_{vbw} (eV)	14.86	15.48	14.01
wurtzite			
a (Å)	3.09 (3.11)	3.20 (3.19)	3.55 (3.54)
c/a	1.62 (1.60)	1.63 (1.63)	1.63 (1.61)
u (units of c)	0.378 (0.382)	0.376 (0.377)	0.375
B_0 (MBar)	1.99 (2.02)	1.69 (1.95, 2.37)	1.62 (1.26, 1.39)
E_{Γ} (eV)	4.44 (6.28)	2.29 (3.50)	0.16 (1.89)
ΔE_{vbw} (eV)	14.89	15.60	14.00

TABLE II. Elastic constants calculated for zinc-blende AlN, GaN and InN (in units of 10^{11} dyne/cm²). The experimental values in brackets are from wurtzite [38].

	AlN	GaN	InN
c_{11}	24.85	23.74 (29.6 \pm 1.8)	20.24
c_{12}	13.37	11.23 (13.0 \pm 1.1)	12.96

FIGURES

FIG. 1. Calculated band offsets for the three interfaces described in the text assuming an AlN substrate.



Marco Buongiorno Nardelli et al.

Figure 1.

XVIII. Photothermally Assisted Dry Etching of GaN

A. Introduction

The ability to process devices from III-Nitride materials, especially GaN, depends heavily on the development of controlled etching and masking techniques for these materials. Removing material requires some type of etchant species (reactive or unreactive, as in Ar ion milling) and a means to provide kinetic energy for desorption of etch products and/or to enhance the etching reaction. Means to provide the necessary energy can be in the form of heat, biased ion beam, kinetic energy transfer, or photons. The masking selects where the material is removed, but the masking material must be compatible with the etching process. Since the ultimate goal is to uniformly etch only beyond the boundaries of the mask, the etching processes must also have a non-crystallographic anisotropic character to transfer the masked pattern.

Both dry and wet techniques can be used for device processing. Dry, plasma etching techniques in the form of reactive ion etching (RIE) [e.g. 1, 2], magnetron electron cyclotron resonance (ECR) etching [3, 4], and chemically assisted ion beam etching (CAIBE) [5, 6] have been very popular for etching the III-N materials. Although these techniques have high etch rates ranging between 200 to 3500 Å/min, they rely on bombardment of an electrically biased surface with ions that can produce damage, degrading the optical and electrical properties of devices, unless used at low ion energies [7, 8]. Wet etches are ineffective due to the III-N materials resistance to chemical attack, with low etch rates around 20 Å/min [9] for GaN. Conventional wet etches also have the drawback of isotropic etching, leading to undercutting of the mask; however, these etches can be effective for surface cleaning [10].

Photoassisted etching techniques using both wet and dry etchant species are being developed as alternatives to plasma etching III-N materials to potentially reduce the damage associated with ion beams. Photoassisted wet etching of undoped n-type GaN has also been shown effective in producing etch rates as high as 4000 Å/min using (1:3) 45% KOH and 400 Å/min using (1:10) HCl; H₂O coupled with a He-Cd (325 nm) laser [11]. The etch features were also reported to be smooth and distinct, with the etch mechanism suggested as photoelectrochemical in nature. Recently we have reported the photoassisted dry etching of GaN [12] using an ArF excimer laser (193 nm) and 100% HCl etchant gas at ~0.5 mTorr, producing distinct sidewalls and smooth etched features with an etch rate of ~80 Å/min. Results from so called dark etching, without laser interaction, have shown that no appreciable etching occurs. Also, no appreciable etching is observed with raising the sample temperature to ~400 °C under the same HCl conditions, again, without laser radiation. Both HCl and UV radiation were necessary to produce etching of GaN.

This report presents the effect of surface temperature, HCl pressure, and laser fluence on both etch rate and etched surface morphology.

B. Experiment

The system used in this study has been previously described [12], and consists of a load locked ultra high vacuum chamber (base pressure 3×10^{-9} Torr) equipped with an internal shower head doser for delivering HCl, with the gas flux coincident with laser radiation and the GaN material. GaN samples grown in-house [13] epitaxially on (0001) sapphire and purchased from Cree Research, Inc. (undoped n-type carrier concentrations $< 1 \times 10^{17} / \text{cm}^3$) were used in this study. The experiments were performed with no thermal bias to the substrate at ambient temperatures near 23°C , surface heating due to laser between ~ 200 - 300°C , and HCl (99.999% purity) pressures ~ 0.5 to 1 mTorr. An ArF (193 nm) excimer laser was used at 30 Hz and 26 kV to produce laser fluences which were attenuated using non-coated optic flats and all energy losses were measured by a pyroelectric Joule meter. The laser power was measured at the entrance to the chamber, taking into account the loss due to the laser port at the system. The laser beam was focused from the original 1×2 cm size at the laser exit to approximately 3×6 mm at the sample.

Samples were masked using a contact mask made of tungsten wire physically placed over the surface. After etching, the samples were characterized by optical microscopy with Nomarski differential interference contrast, stylus profilometry, and scanning electron microscopy (SEM) to determine the etch rate and the quality of surface/ sidewall morphology. The etch rate was determined by dividing the etch depth determined by profilometry by the time to pulse the laser (dependent on the repetition rate). Typical number of pulses/ sample was $\sim 25,000$ taking approximately 14 minutes.

C. Results and Discussion

A typical etch profile is shown in Fig. 1. Etching conditions for this sample were ~ 0.5 mTorr HCl with laser fluence of ~ 19 mJ/ pulse. The sidewalls are very distinct and the etch depth for this sample is between ~ 0.6 to $1 \mu\text{m}$ deep. Non-uniformity in the etch depths on both sides of the mask is due to the non-uniformity of the laser beam itself: the intensity profile of the beam is not a perfect "top hat" shape, but is more rounded in dimensions; thus, the intensity of the laser is not the same for all regions on the sample.

Typical surface morphology of etched regions produced by increasing laser fluences are seen in Fig. 2. Figure 2(a) shows a very slightly textured etched surface compared to the masked unetched surface under low laser fluences of ~ 10 mJ/pulse. Figure 2(b) reveals that at higher laser fluence, 12 mJ/ pulse, the surface becomes more heavily textured. Finally in Fig. 2(c), the surface is roughly textured corresponding to the highest laser fluence used in the

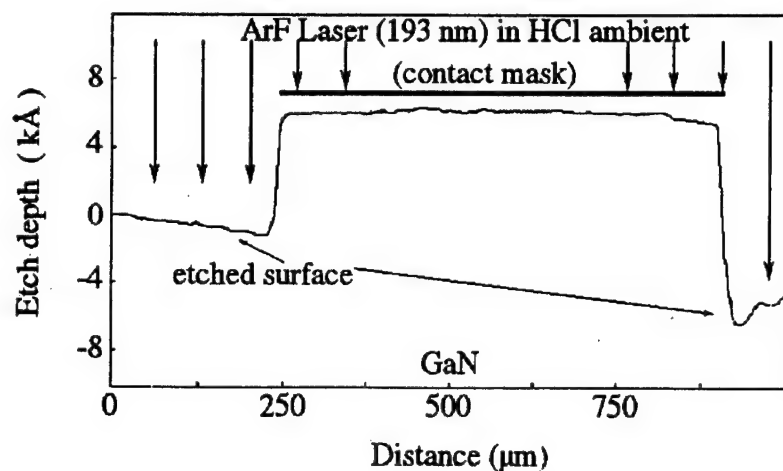


Figure 1. Typical etch profile measured by profilometry.

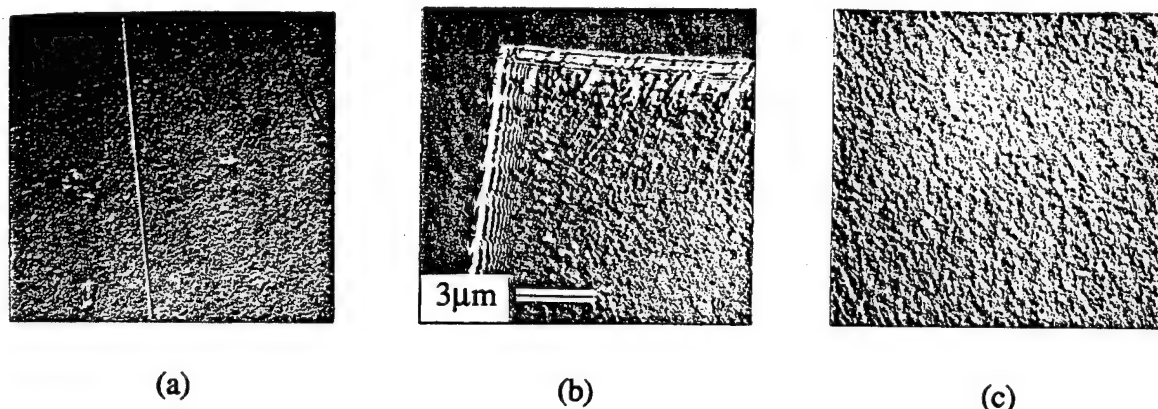


Figure 2. Nomarski optical microscopy, 400x observation of etched surface morphology with increasing laser fluence : (a) 10 mJ/ pulse; (b) 12 mJ/ pulse; (c) 19 mJ/ pulse.

study, 19 mJ/ pulse, and is the same sample as in Fig. 1. The edges between the etched and unetched regions of Fig. 2(b) show some diffraction effects due to the incomplete contact masking of the samples. Preliminary work using photolithographed Ni masks on these GaN samples indicate that with a well adhered mask, these specific diffraction effects can be reduced. SEM results have revealed cracks in the Ni mask possibly due to the differences in thermal expansion between GaN and Ni. Because of this, the sidewall morphology cannot be determined due to poor mask adhesion. A more suitable mask is being considered to reduce these effects.

The effect of laser fluence on etch rate is shown in Fig. 3(a). The temperature rise associated with laser—material interaction has been determined by many authors [e.g. 14] by solution of the heat equation and assumption of a beam shape. Using known thermal constants

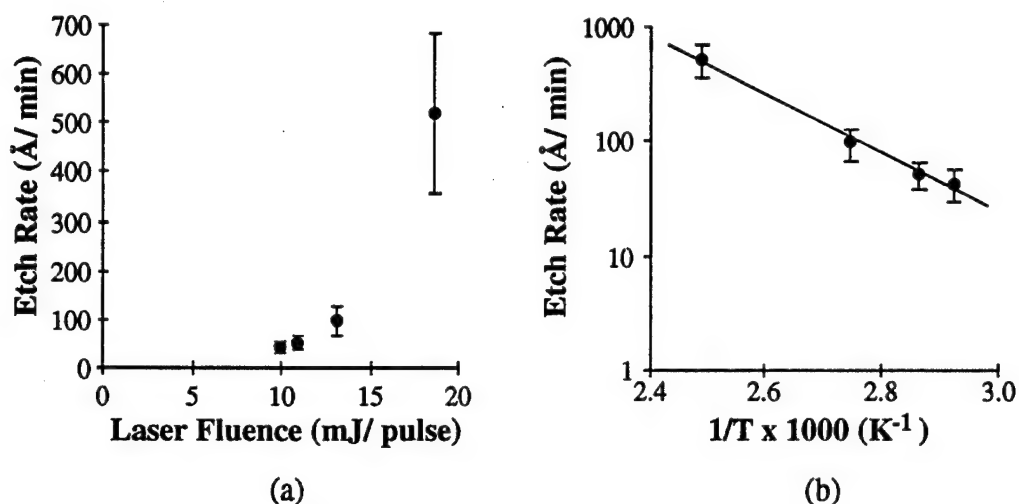


Figure 3. (a) Etch rate vs. laser fluence for photoassisted etching of GaN; (b) Arrhenius plot of the etch rate vs. the calculated surface temperature rise with increasing laser fluences.

for GaN, a temperature rise between 300 to 400 °C can be associated with the laser power density hitting the sample, assuming all of the laser fluence is transformed to heat. Fig. 3(b) relates the laser fluence to surface temperature, resulting in an Arrhenius plot of etch rate vs. the inverse temperature related to the intensity of the laser radiation. Note that the temperature rise is limited to the surface region only, with the heat dissipating between the 30 Hz, 18 nsec pulses. The error bars included in the graph reveal the effect of a non-uniform radiation source.

The results in Fig. 3(b) suggest that the photoassisted etching of GaN is thermally enhanced by the laser—material interaction in this HCl pressure range. Line fitting techniques through these points indicate a residuals squared value of ~ 0.99 , confirming the Arrhenius form of the etch rate vs. $1/T$. The activation energy calculated from these results is ~ 1.2 kcal/mol, higher than the activation energy of 0.65 kcal/mol for reactive fast atom beam etching (r-FABE) determined by Tanaka [15]. Possible differences in these two activation energies could be due to the different methods of removing the etch products, and considering the effect of the energetic beam in both cases. For the reactive FABE, no reason is given for the temperature dependence of the etch rate or mechanism. The energetic fast atom beam could be adding the necessary energy to further desorb the etch products, thus lowering the activation energy. In photothermally assisted etching, the laser energy is doing all of the work: both the surface is heated and the etch products desorb due to the laser irradiation.

The observations for photoassisted etching of GaN are similar to those for GaAs. Brewer [16] and Tejedor [17] both reported on the photoassisted etching of GaAs with $\text{CF}_3\text{Br}/193$ nm and $\text{Cl}_2/193$ nm, respectively, and showed that with increasing the laser fluence, the etch rate did increase, and the surface morphology roughened with laser fluences above 30 - 35 mJ/cm². They suggested the laser—material interaction produced physical ablation or at least laser

enhanced desorption of the GaAs. By comparing the results of Figs. 2 and 3 to that of the GaAs results, similar etching behavior (and possibly mechanism) is occurring.

Compared with the wet photoelectrochemical etching reaction described by Minsky [11], at this time there is no evidence supporting photoelectrochemical etching with the dry etching process conditions used here. This does not mean, however, that they do not exist, since the laser energy ($6.4 \text{ eV} \gg E_g^{\text{GaN}} \sim 3.4 \text{ eV}$) is more than sufficient for the production of the electron-hole pairs involved in the photoelectrochemical reaction.

The mechanism for photoassisted dry etching is not well understood. The surface roughness resulting with increasing laser fluence suggests that there is some non-uniform interaction of the material with the etching energy of the laser and reactivity of the process gas. Ablation has been suggested to explain the roughness in the photoassisted etching of GaAs, but for GaN, whether or not true ablation occurs, it is obvious that some reactive decomposition of the surface is occurring. The cause of the surface roughness could result from such etching decomposition if the etch products were agglomerating from incomplete desorption, creating local roughness that a uniform etching process could not preferentially remove. For this gas-material interaction, it is expected that the laser dissociates the HCl gas molecules into the etching species. In this case, increasing the amount of reactant species, and/ or increasing the surface temperature would be necessary to remove these agglomerated etch products.

D. Conclusion

We have shown that for the process conditions, the photoassisted etching reaction is thermal in nature, with the activation energy $\sim 1.2 \text{ kcal/mol}$. Increases in the laser fluence results in the increase of etch rate, however, the surface also becomes increasingly rougher. Distinct etch features can be produced with this technique with smooth surfaces at the expense of etch rate. With changes in the process conditions, we hope to improve the surface morphology. Extension of this research to different III-N materials is already underway to determine the effect of photoassisted etch damage and will be reported on in the future.

E. Acknowledgements

The authors would like to acknowledge the help of Professor N. A. El-Masry, F. G. McIntosh, J. C. Roberts, and the support of the Office of Naval Research University Research Initiative project.

F. References

1. S. J. Pearton, F. Ren, T. R. Fullowan, A. Katz, W. S. Hobson, U. K. Chakrabarti, and C. R. Abernathy, *Mater. Chem. Phys.* **32**, 215 (1992).
2. M. E. Lin, Z. F. Fan, Z. Ma, L. H. Allen, and H. Morkoç, *Appl. Phys. Lett.* **64**, 887 (1994).
3. S. J. Pearton, *Mater. Sci. Eng.* **B27**, 61 (1994).

4. S. J. Pearton, C. R. Abernathy, and F. Ren, *Appl. Phys. Lett.* **64**, 2294 (1994).
5. A. T. Ping, C. Youtsey, and I. Adesida, *J. Electron. Mater.* **24**, 229 (1995).
6. A. T. Ping, I. Adesida, and M. Asif Khan, *Appl. Phys. Lett.* **67**, 1250 (1995).
7. M. Heinbach, J. Kaindl, and G. Franz, *Appl. Phys. Lett.* **67**, 2034 (1995).
8. S. J. Pearton, J. W. Lee, J. D. MacKenzie, and C. R. Abernathy, *Appl. Phys. Lett.* **67**, 2329 (1995).
9. S. J. Pearton, C. B. Vartuli, R. J. Shul, and J. C. Zolper, *Mater. Sci. Eng.* **B31**, 309 (1995).
10. S. W. King, L. L. Smith, J. P. Barnack, J. H. Ku, J. A. Christman, M. C. Benjamin, M. D. Bremser, R. J. Nemanich, and R. F. Davis, to be published in Fall 1995 MRS Proceedings.
11. M. S. Minsky, M. White, and E. L. Hu, *Appl. Phys. Lett.* **68**, 1531 (1996).
12. R. T. Leonard and S. M. Bedair, *Appl. Phys. Lett.* **68**, 794 (1996).
13. K. S. Boutros, F. G. McIntosh, J. C. Roberts, S. M. Bedair, E. L. Piner, and N. A. El-Masry, *Appl. Phys. Lett.* **68**, 1856 (1996).
14. S. M. Bedair and H. P. Smith, Jr., *J. Appl. Phys.* **40**, 4776 (1969).
15. H. Tanaka, F. Shimokawa, T. Sasaki, and T. Matsuoka, *Optoelectronics—Devices and Technologies* **6**, 150 (1991).
16. P. Brewer, S. Halle, and R. M. Osgood, Jr., *Appl. Phys. Lett.* **45**, 475 (1984).
17. P. Tejedor and F. Briones, *Mat. Res. Soc. Symp. Proc.* **201**, (1991).

XIX. Ohmic Contact Formation to GaN

A. Introduction

The work described in this section is part of a systematic study of ohmic contact strategies for GaN. The majority of successful ohmic contact systems that have so far been implemented with the more conventional compound semiconductors have relied upon alloying (liquid-phase reaction) or sintering (solid-phase reaction) via post-deposition annealing treatments, and/or the presence of high carrier concentrations near the interface [1-4]. However, many otherwise successful ohmic contact systems have only limited thermal stability and are subject to degradation—usually in the form of extensive interdiffusion, interfacial reaction, and interphase growth, accompanied by increase in contact resistivity—under subsequent thermal processing steps.

One area of contacts development that has received a significant amount of attention is that of the metal silicide compounds. Silicide thin films have been extensively studied and applied as contacts and interconnects, mostly for silicon-based technology [5-10]. In comparison, the properties of the metal germanides are not well documented. As a general rule, germanides have been found to be more resistive than silicides and their chemistry with Si-based materials more complex. However, in a series of studies, M. O. Aboelfotoh *et al.* have shown that a particular phase of copper germanide, specifically the ordered monoclinic phase ϵ_1 -Cu₃Ge, is an exception to these rules [10-14]. Thin films of Cu₃Ge exhibit remarkably low resistivities, unlike Cu₃Si, and unlike both Cu and Cu₃Si, are surprisingly stable with respect to oxygen and air exposure. As such, Cu₃Ge presents itself as a potentially useful contact metal. Indeed, preliminary experimentation with Cu₃Ge contacts on GaAs and GaN, primarily on n-type and heavily-doped p-type material, has produced some favorable results in terms of ohmic contact formation. For these reasons copper-germanium contacts were investigated as part of this study as possible candidates for high-quality, low-resistivity ohmic contacts.

B. Experimental Procedure

The substrates used for III-nitride film growth were 6H-SiC wafers supplied by CREE Research, Inc. Two growth methods have been used for the deposition of III-N films for these contacts studies: ECR plasma-enhanced gas-source molecular beam epitaxy (MBE) and metal-organic vapor phase epitaxy (MOVPE). The dopants of Ge and Si were introduced via MBE and MOVPE respectively to achieve n-type material. Dopant levels and carrier concentrations for the n-GaN films varied. The nitride films were cleaned with a 50:50 HCl:H₂O dip and carefully pulled dry from the solution, prior to deposition of the metals. Any remaining cleaning solution was blown dry with N₂. Prior to metal deposition, the GaN samples were thermally desorbed in vacuum at 700C for 15 min. The Cu and Ge comprising this contact

system were deposited via electron beam evaporation as sequential layers, 800 Å of Cu followed by 1200 Å of Ge. The alloying of the layers was accomplished by heating at 400°C for 15 minutes, while in vacuum after the metal evaporation, as described by Aboelfotoh *et al.* [10-14]. Film thicknesses were monitored using a quartz crystal oscillator. Photolithography was used to define the TLM test patterns.

After deposition, I-V measurements were taken at room temperature between separate pads of the TLM patterns, using tungsten probe tips and an HP 4145C Semiconductor Parameter Analyzer. TLM measurements were taken by measuring the total resistance between identical contact pads as a function of separation distance l . The contact resistivity was obtained from the plot of $R(l)$ vs. l , as described by Reeves and Harrison [15]. Subsequent annealing treatments were performed under ultra high vacuum conditions, having a base pressure of 1×10^{-9} Torr.

C. Results

Preliminary measurements were made from Cu_3Ge contacts deposited on n-type GaN (MBE, Ge-doped) at IBM's Yorktown Heights research facility in a UHV e-beam evaporation system. Current-voltage measurements of these contacts on Ge-doped GaN revealed ohmic behavior with low overall resistance. In addition, the contacts retained a shiny, smooth surface, indicative of little or no roughening or reaction at the interface. At the present time the work function and electron affinity properties of CuGe compounds have not yet been measured, so it is not known how this contact system compares with the Schottky-Mott-Bardeen model. It is often observed, however, that even if a contact metal does not have a favorable work function relationship to a semiconductor for ohmic contact formation according to the Schottky model, the role of a barrier at the surface can be bypassed by means of other current transport mechanisms.

Current-voltage measurements of the Cu_3Ge contacts on MOVPE-grown GaN:Si ($n=7.4 \times 10^{18} \text{ cm}^{-3}$) revealed nearly-linear ohmic behavior with low overall resistance, as shown in Fig. 1. TLM measurements showed the ρ_c to be $4.9 \times 10^{-3} \Omega \text{ cm}^2$. The same contact system deposited on lower-doped GaN ($n=4.5 \times 10^{17} \text{ cm}^{-3}$) was much more resistive and showed more nonlinearity in the I-V measurements; a ρ_c of 18 cm^2 was obtained. In both cases, the as-alloyed contacts had a shiny, smooth surface, indicative of little or no roughening or reaction at the interface. Subsequent annealing of the samples under UHV conditions resulted in little change in ρ_c for both doping levels, until the samples were heated at 800°C. However, after the 600°C anneal, the I-V measurements of the contacts on the lightly-doped GaN ($n=4.5 \times 10^{17} \text{ cm}^{-3}$) became substantially more linear. After the 800°C annealing step, the Cu_3Ge ρ_c for both GaN doping levels increased sharply, as shown in Fig. 2. For the $n=7.4 \times 10^{18} \text{ cm}^{-3}$ contacts, the ρ_c rose to 1.0 cm^2 , and on the $n=4.5 \times 10^{17} \text{ cm}^{-3}$ contacts the

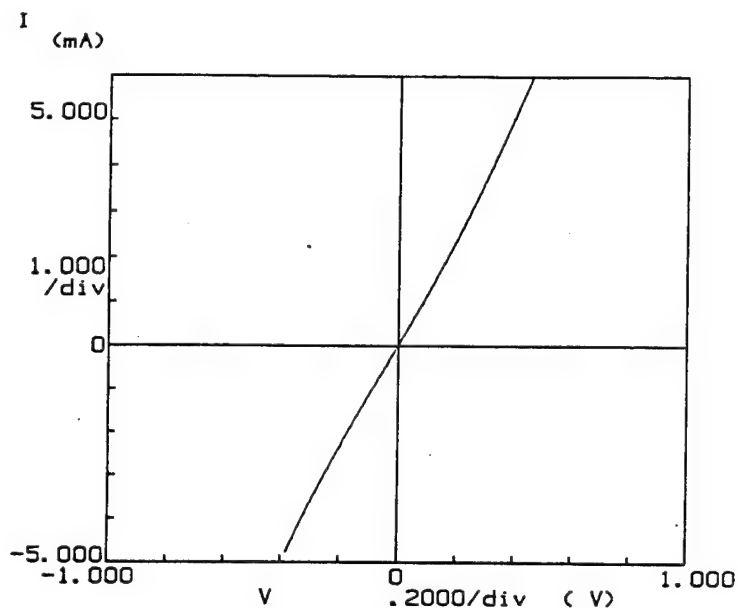


Figure 1. I-V data for as-alloyed Cu_3Ge contacts on n-GaN.

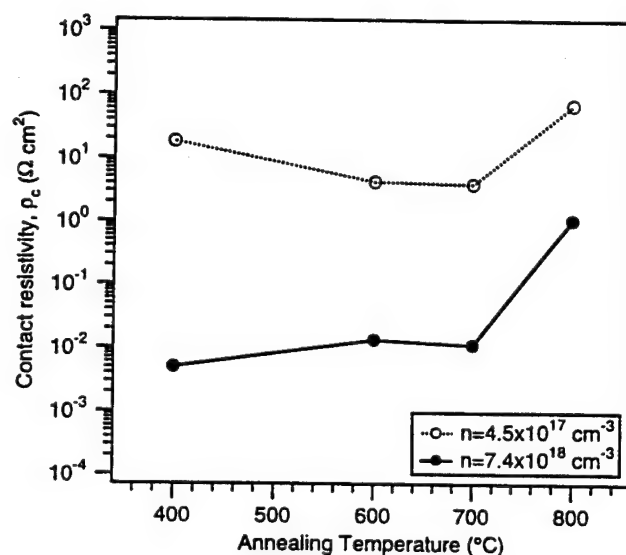


Figure 2. Specific contact resistivity for $\text{Cu}_3\text{Ge}/\text{n-GaN:Si}$ contacts as a function of annealing temperature.

ρ_c reached 69 cm^2 . In addition, the metal contact surfaces appeared somewhat dulled after the 800°C anneal, indicating that some roughening had taken place. Current-voltage measurements of the Cu_3Ge metal layers themselves revealed that the metal layers had become much more resistive as a result of the 800°C anneal. This increased series resistance in the measurement circuit was responsible for the increase in calculated ρ_c values.

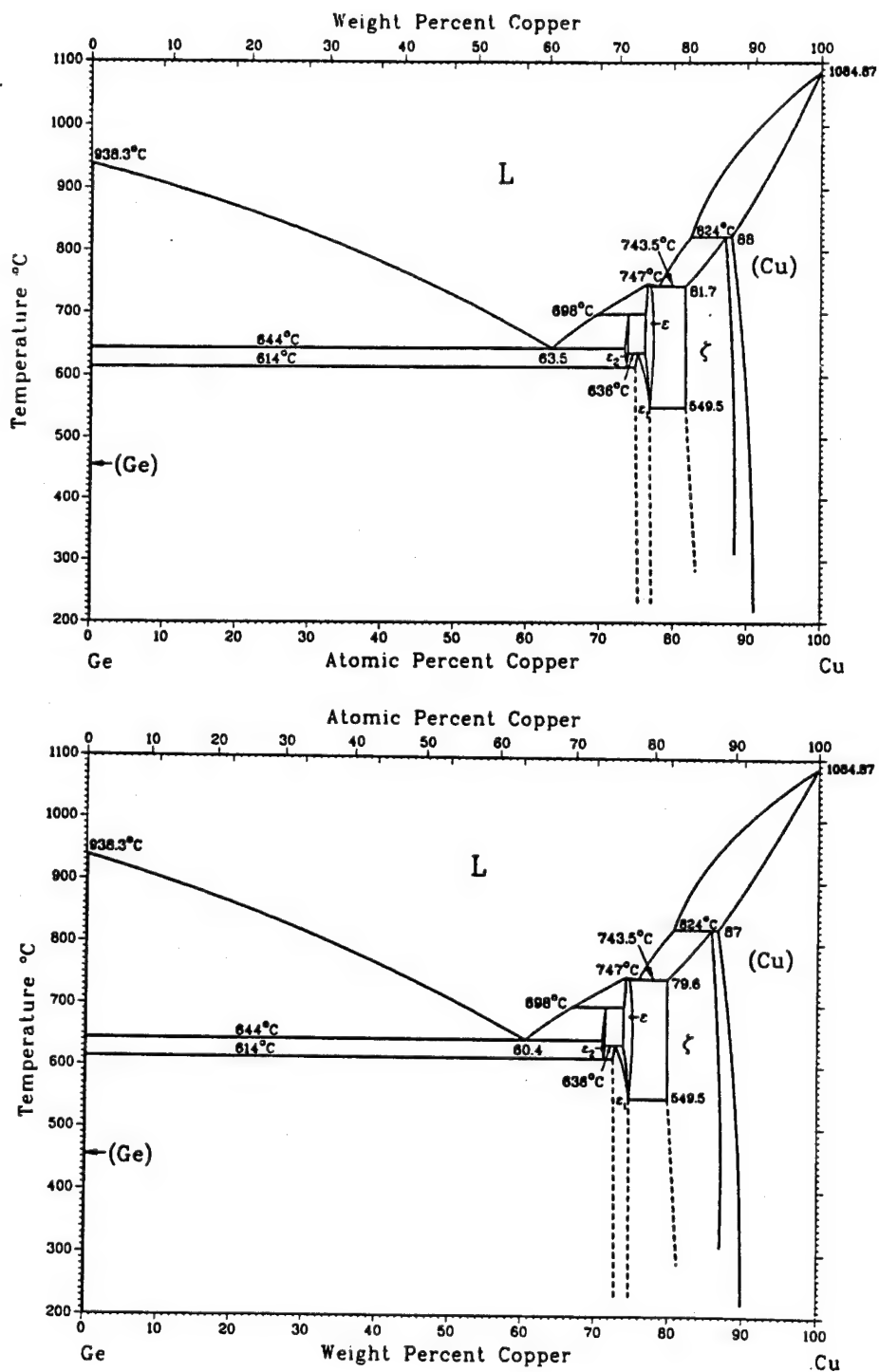
D. Discussion

As described above, the Cu_3Ge contacts on n-GaN:Si exhibited ohmic behavior on both moderately doped ($n=4.5\times 10^{17} \text{ cm}^{-3}$) and more heavily-doped ($n=7.4\times 10^{18} \text{ cm}^{-3}$) n-GaN films. This behavior was observed in both the as-alloyed contacts, alloyed in vacuum at 400°C , and contacts annealed in vacuum through 800°C for 30 min increments. The annealing treatments were intended to increase the donor concentration at the contact interface by means of Ge diffusion into the GaN. A reduction of ρ_c was not seen as a result of the annealing treatments up through 700°C , indicating that little transport of Ge into the GaN took place at these temperatures. The increase in ρ_c that occurred after the 800°C anneal was a result of degradation of the metal layer itself. In the as-alloyed state, the metal layer exhibited low-resistivity properties; after the 800°C anneal the probe-to-probe resistance of the metal layer had increased dramatically and overwhelmed all other electrical effects contributing to the I-V measurements used for TLM calculations. Since the Cu_3Ge compound undergoes liquid-phase peritectic decomposition at 743°C and melts completely at 748°C , as seen in the Cu-Ge phase diagram in Fig. 3 [16], the changes in metal properties are most likely due to its melting and cooling. The reason for heating the metal contact layer above its melting point was drawn from the industry's experience with the familiar Au-Ge ohmic contacts on n-GaAs , which are annealed at temperatures above the Au-Ge alloy melting point (425°C) to achieve ohmic behavior.

The tighter bonding of Ga and Al to N, in comparison to As, suggests that higher temperatures and possibly longer times are required for interfacial reactions to take place with GaN as compared with GaAs, and that some reactions may be inhibited or prevented. The behavior of the systems examined so far has been consistent with these suppositions. Having observed, however, that high-temperature annealing (above 750°C) causes degradation of the metal layer, a different processing scheme was also used as part of the effort to enhance the Cu_3Ge contact performance. Since heating the Cu_3Ge metal above its melting point resulted in degradation of the metal's low-resistivity properties, annealing was performed again at a lower temperature (600°C) for a longer period of time (6 hours). Again, two different doping levels were used for the GaN samples, $n=4.5\times 10^{17} \text{ cm}^{-3}$ and $n=4.5\times 10^{18} \text{ cm}^{-3}$. Specific contact resistivities for these samples were obtained via TLM measurements in the as-alloyed condition and after annealing at 600°C for 6 hrs, and are listed in Table I.

When the annealing temperature was held to 600°C , the Cu_3Ge metal did not undergo the degradation that it experienced when annealed at higher temperatures. Again, however, no improvement was seen in the ρ_c of the contacts. While the Cu_3Ge metal retained its own low-resistivity properties during this longer, lower-temperature anneal, there was no enhancement of the contact interface as a result of the heat treatment. Further improvements in the performance of this contact system may be inherently limited by the nature of the Cu_3Ge metal.

High temperatures (above 700°C) may be necessary to drive Ge diffusion into the GaN to provide increased donor concentrations at the contact interface, but the melting of the Cu₃Ge and consequent degradation of its properties make this difficult.



R.W. Olesinski and G.J. Abbaschian, 1986.

Figure 3. Phase diagram of the Cu-Ge binary system [16].

Table I. Specific Contact Resistivity Values (in $\Omega \text{ cm}^2$) for $\text{Cu}_3\text{Ge}/\text{n-GaN}$ Contacts

GaN Doping Level	$n=4.5 \times 10^{17} \text{ cm}^{-3}$	$n=4.5 \times 10^{18} \text{ cm}^{-3}$	$n=7.3 \times 10^{18} \text{ cm}^{-3}$
as-alloyed(400°C/30 min)	14-18	5.6×10^{-3}	4.9×10^{-3}
annealed 600°C/30 min	4.2	-	9.9×10^{-3}
annealed 700°C/30 min	3.9	-	1.1×10^{-2}
annealed 800°C/30 min	69	-	1.0
annealed 600°C/6 hrs	23.1	3.2×10^{-3}	-

E. Conclusions

An alloyed Cu_3Ge contact system was deposited on different doping levels of n-GaN:Ge and n-GaN:Si . The $\text{Cu}_3\text{Ge}/\text{n-GaN}$ contacts exhibited ohmic behavior, and the ρ_c varied substantially with the carrier concentration of the GaN studied. Transmission line measurements revealed as-alloyed ρ_c of 14-18 $\Omega \text{ cm}^2$ for $n=4.5 \times 10^{17} \text{ cm}^{-3}$, $5.6 \times 10^{-3} \Omega \text{ cm}^2$ for $n=4.5 \times 10^{18} \text{ cm}^{-3}$, and $4.9 \times 10^{-3} \Omega \text{ cm}^2$ for $n=7.4 \times 10^{18} \text{ cm}^{-3}$. However, these contacts deteriorated substantially after annealing at 800°C. There was no significant improvement in ρ_c as a result of post-deposition annealing, though in the case of Cu_3Ge contacts on the moderately-doped GaN the I-V behavior became substantially more linear after annealing at 600°C. The Cu_3Ge metal layers deteriorated as a result of annealing at temperatures above the metal's melting point. High temperatures (above 700°C) may be necessary to drive Ge diffusion into the GaN to provide increased donor concentrations at the contact interface, but the melting of the Cu_3Ge metal and consequent degradation of its properties make this difficult. It may be possible to preserve the integrity of the Cu_3Ge metal during higher-temperature annealing through the use of capping layers or other adjustments of processing parameters. Along with the development of improved contact systems for the III-nitrides, it is hoped that these studies will contribute to our understanding of crucial issues such as surface properties, band structure, and interface characteristics.

E. Future Research Plans and Goals

In addition to further chemical and structural characterization of the contact systems described in this report, other schemes for improving contact performance will be investigated. Combined with the search for improved contacts to the III-nitrides is the ongoing investigation of Fermi-level pinning and defect states, and the role played by work function and electron affinity differences in contact properties. The evidence examined to date indicates that GaN

does indeed experience much less Fermi-level pinning than its more covalently bonded relatives such as GaAs; further work will help to clarify this issue and assist the development of advanced microelectronic and optoelectronic devices.

For p-GaN, the challenges to contact improvement are formidable. By comparison, the advances that have been made with n-GaN contacts have been rather easily achieved. However, further improvement of p-GaN contacts must be made to reduce the high series resistance inherent in the LEDs and lasers now being fabricated. Despite the stronger need for progress in this area, very little detailed electrical characterization of p-GaN ohmic contacts has been reported to date. The only values for specific contact resistivity ρ_c that have been made available have come from the present work and announcements from CREE Research, Inc., which have reported ρ_c values on the order of $10^{-2} \Omega \text{ cm}^2$ for $p=10^{18} \text{ cm}^{-3}$ [13]. For proprietary reasons, the ohmic contact schemes used by Cree have not been described.

In order to take greater advantage of the valuable properties of GaN and to achieve the full range of superior device performance envisioned by the solid state community, it is necessary to reduce the ρ_c of p-GaN contacts at least three or four orders of magnitude below the levels already obtained. To accomplish this, it is almost certainly necessary to take full advantage of the two main avenues of contact improvement described above: to increase acceptor concentrations and to reduce the semiconductor band gap at the contact interface. With this in mind, the following approaches are recommended for further investigation, to identify the most efficient means of achieving superior contacts:

- Increase the doping level of acceptor impurities near the top surface of p-GaN films during growth. To improve the incorporation of acceptor impurities, it may be necessary to adjust the Ga-N ratio during growth to facilitate the addition of dopant atoms to the Ga sites. Activation of the dopant species must be optimized.
- Add acceptor impurities to the near-surface region of p-GaN films by means of ion implantation, prior to metallization. Again, activation of the dopant species must be optimized. Performing the implants at high temperature and/or post-implant annealing will be necessary to achieve this.
- Make use of metallurgical reactions of contact metal components with GaN, in order to draw Ga out of the GaN structure and leave behind Ga vacancies that can be filled with acceptor impurities. Nickel is suggested as a favorable candidate for this purpose. Contact studies by Trexler *et al.* [14], thermodynamic studies by Mohny *et al.* [15,16] and the surface analytical work of Bermudez *et al.* [17] have demonstrated that Ni reacts extensively with GaN, with some reaction occurring even at room temperature. At higher temperatures (~600C and above), Ga dissolves into Ni layers while the released N desorbs.

- Make use of InN or a gradation of InGaN as an interlayer to reduce the semiconductor band gap at the contact interface. To accomplish this for p-GaN contacts, it will be necessary to either (1) improve InN growth and achieve high-quality p-InGaN and p-InN films, or (2) incorporate In into contact metals such that In is able to substitute into the p-GaN lattice upon annealing of the contacts.

The issues of surface cleaning and sample preparation will continue to be important in the areas of device fabrication. The role of oxygen and other contaminants at the contact interface is important to understand, and will become even more critical for AlGaIn and AlN-based devices due to the strong affinity of Al for oxygen. For such cases the cleanliness of the contact deposition environment will probably be of greater importance, as well.

G. References

1. T. C. Shen, G. B. Gao, and H. Morkoç, *J. Vac. Sci. Technol. B* **10**(5), 2113 (1992).
2. R. Williams, *Modern GaAs Processing Techniques* (Artech House, Norwood, MA, 1990).
3. V. L. Rideout, *Solid-St. Electron.* **18**, 541 (1975).
4. E. D. Marshall and M. Murakami, in *Contacts to Semiconductors*, edited by L. J. Brillson (Noyes, Park Ridge NJ, 1993).
5. S. P. Murarka, *Silicides for VLSI Applications*, Academic Press, New York (1983).
6. L. Krusin-Elbaum, J. Y.-C. Sun, and C.-Y. Ting, *IEEE Trans. Electron Devices* **ED-34**, 58 (1987).
7. J. C. Hensel, R. T. Tung, J. M. Poate, and F. C. Unterwald, *Appl. Phys. Lett.* **44**, 913 (1984); *Phys. Rev. Lett.* **54**, 1840 (1985).
8. P. H. Woerlee, P. M. Th. M. van Attekum, A. A. M. Hoebe, G. A. M. Hurkx, and R. A. M. Wolters, *Appl. Phys. Lett.* **44**, 876 (1984).
9. M. T. Huang, T. L. Martin, V. Malhotra, and J. E. Mahan, *J. Vac. Sci. Technol. B* **3**, 836 (1985).
10. L. Krusin-Elbaum and M. O. Aboelfotoh, *Appl. Phys. Lett.* **58**(12), 1341 (1991).
11. M. O. Aboelfotoh, H. M. Tawancy, and L. Krusin-Elbaum, *Appl. Phys. Lett.* **63**(12), 1622 (1993).
12. M. O. Aboelfotoh, K. N. Tu, F. Nava, and M. Michelini, *J. Appl. Phys.* **75**(1), (1994).
13. M. O. Aboelfotoh, H. M. Tawancy, *J. Appl. Phys.* **75**(4) 1 (1994).
14. M. O. Aboelfotoh, C. L. Lin, and J. M. Woodall, *Appl. Phys. Lett.* **65**(25) 3245 (1994).
15. G. K. Reeves and H. B. Harrison, *IEEE Electron Device Lett.* **EDL-3** 111 (1982).
16. R. W. Olesinski and G. J. Abbaschian, in *Binary Alloy Phase Diagrams* 2nd Edition, Vol. 3, edited by T. B. Massalski, H. Okamoto, P. R. Subramanian, and L. Kacprzak (ASM International, Metals Park, Ohio, 1990) p. 1415.

XX. III-V Nitrides for Use in Semiconductor Microelectronic Device Applications

A. Introduction

With their distinct combination of physical and electronic properties, the III-V nitrides are promising materials for optoelectronic and microelectronic applications. AlN, GaN, and InN have direct band gaps of 6.2, 3.4, and 1.9 eV, respectively. In conjunction with their continuous solid solubility, one has the ability to engineer band gaps within the range of 1.9 to 6.2 eV, which can be used to construct blue LEDs and deep UV lasers.

Along with their wide bandgaps, the III-V nitrides have advantageous physical properties such as high thermal stability, high physical hardness, and high chemical stability. In combining these properties, the III-V nitrides lend themselves as excellent candidates for high power and high temperature devices [1].

At present, there is one significant drawback to the use of the III-V nitrides: the lack of a homoepitaxial substrate. In order to achieve monocrystalline thin films heteroepitaxy has been employed using a number of different substrates. This method has allowed the production of single crystal films, but the films have had poor crystal quality and high unintentional doping levels [2].

Recent developments have shown that good single crystal thin films of AlN and GaN can be grown using techniques such as Metal Organic Chemical Vapor Deposition (MOCVD) and Molecular Beam Epitaxy (MBE) [3-7]. The most successful of these films, which exhibit high resistivity and low unintentional doping, have been grown on Al_2O_3 (sapphire) and α -SiC. Conductive n and p-type GaN films have also been produced using the appropriate doping impurities.

With the production of device quality material successful attempts have been made to produce microelectronic devices using the III-V nitrides [8-15]. Khan *et al.* have made many strides in this area, including being the first to fabricate a MESFET device from the nitrides. Binari *et al.* have also fabricated MESFET devices along with MISFET structures. As shown in Fig. 1, Binari fabricated a depletion mode device using Si_3N_4 as the gate insulator. For a gate length of 0.9 μm the transconductance was 16 mS/mm at 30°C and 11 mS/mm at 200°C. The frequency response of these devices were measured resulting in a f_T and f_{max} of 5 and 9 GHz respectively [15].

Currently, much of the research concerning MISFET devices is directed towards depletion mode devices. This can be attributed to the inability to successfully process the material. Currently many strides have been made in the areas of implantation and etching [16-18]. Other areas of research which are beginning to be addressed include the investigation of insulator materials. Some initial work has been done by Casey *et al.* on SiO_2 -GaN MOS capacitors [19].

His results indicate that SiO₂ grown on GaN by a remote plasma method yielded a structure with low interface trap density.

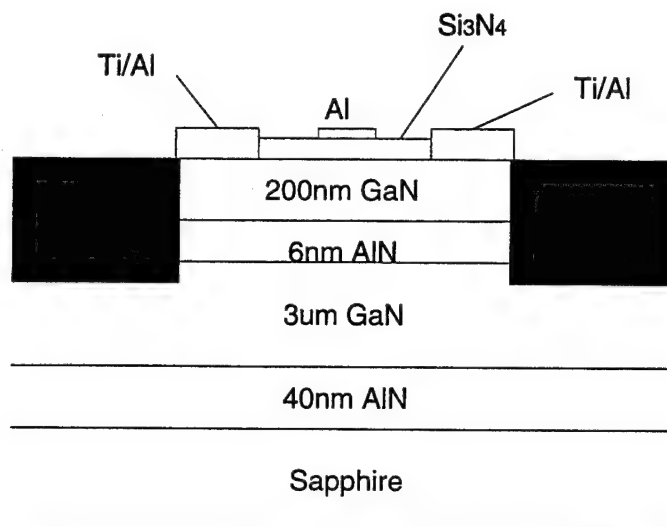


Figure 1. MISFET cross section.

It is the goal of this project to complete the steps needed to construct a MISFET structure. The steps will be discussed further in the following section.

B. Results

In order to produce a viable MISFET device a suitable insulating material must be found to use as the gate insulator. Three materials have been chosen to be investigated for this research. They include SiO₂, Si₃N₄, and AlN. To properly study the characteristics of the insulators on the MIS capacitors are used. From these two terminals, device information such as the charge in the insulator, number of traps, and the breakdown characteristics can be determined.

To theoretically model these devices modified versions of the equations derived for two terminal devices Si, from Tsividis [20] and Nicollian and Brews [21], are used. Due to GaN's long generation rate and short minority carrier lifetime, on the order of 10¹¹ years and 10⁻⁸s respectively (for a doping concentration of $\approx 1 \times 10^{17}/\text{cm}^3$), the inversion layer contribution to the capacitance can be ignored. This leaves only the accumulation and depletion modes to characterize. From this analysis an equation for the semiconductor capacitance is derived:

$$C_c(y) = \left[F \frac{\sqrt{N_d}}{2} \left(\phi_i e^{\left(\frac{\psi}{\phi_i} \right)} - \psi - \phi_i \right)^{-\frac{1}{2}} \left(e^{\left(\frac{\psi}{\phi_i} \right)} - 1 \right) \right] A \quad (1)$$

Where $F=(2qe_{\text{GaN}})^{1/2}$, N_d is the semiconductor doping concentration, f_t is the thermal voltage, and ψ is the surface potential. Substituting the results of the equation 1 into the following equation,

$$C_i(\psi) = \left(\frac{1}{C_{ox}} + \frac{1}{C_c(\psi)} \right)^{-1} \quad (2)$$

where C_{ox} is the capacitance of the insulator, the capacitance for the device can be calculated at various surface potentials. The equation for the gate voltage is derived from the potential drops across the capacitor:

$$V_{gb}(\psi) = V_{fb} - \frac{Q_{cs}(\psi)}{C_{ox}} - \psi \quad (3)$$

where V_{fb} is the flatband voltage and $Q_{cs}(\psi)$ is the charge at the semiconductor/insulator interface. From the above equations a theoretical C-V curve can be generated for n-type MIS capacitors. The next step is to fabricate a MIS capacitor.

This research group has demonstrated the ability to grow high-quality single crystal thin films of GaN and AlN with high resistivity and low levels of unintentional doping. These films have been grown by MBE and MOCVD on α -SiC, utilizing a high temperature monocrystalline AlN buffer layer. Through these methods both n and p type doping of the GaN films has been achieved.

Using the n-type GaN Grown by MOCVD a MIS capacitor has been fabricated. This device was fabricated in a lateral orientation rather than the typical vertical orientation used in silicon technology. This was done to avoid the insulating AlN buffer layer. Silicon oxide was grown via a low temperature chemical vapor deposition process. Aluminum was used as the gate metal and the ohmic contact for this device. The processing steps can be found in the appendix of this report (see Fig. 2).

Capacitance-voltage measurements were performed using a HP4284A precision LCR meter in conjunction with MDC software. The resulting curves showed that the device operated as expected in both the accumulation and depletion regions (see Fig. 3). To properly analyze C-V curves a good theoretical curve must be obtained. At this juncture a piece of information is missing that is needed to complete a proper curve. The value of the flatband voltage, which is the difference in the workfunctions of the gate metal and the semiconductor, is unknown because the workfunction of GaN has not been quantified. A solution to this problem has been devised and will be discussed further in the following section.

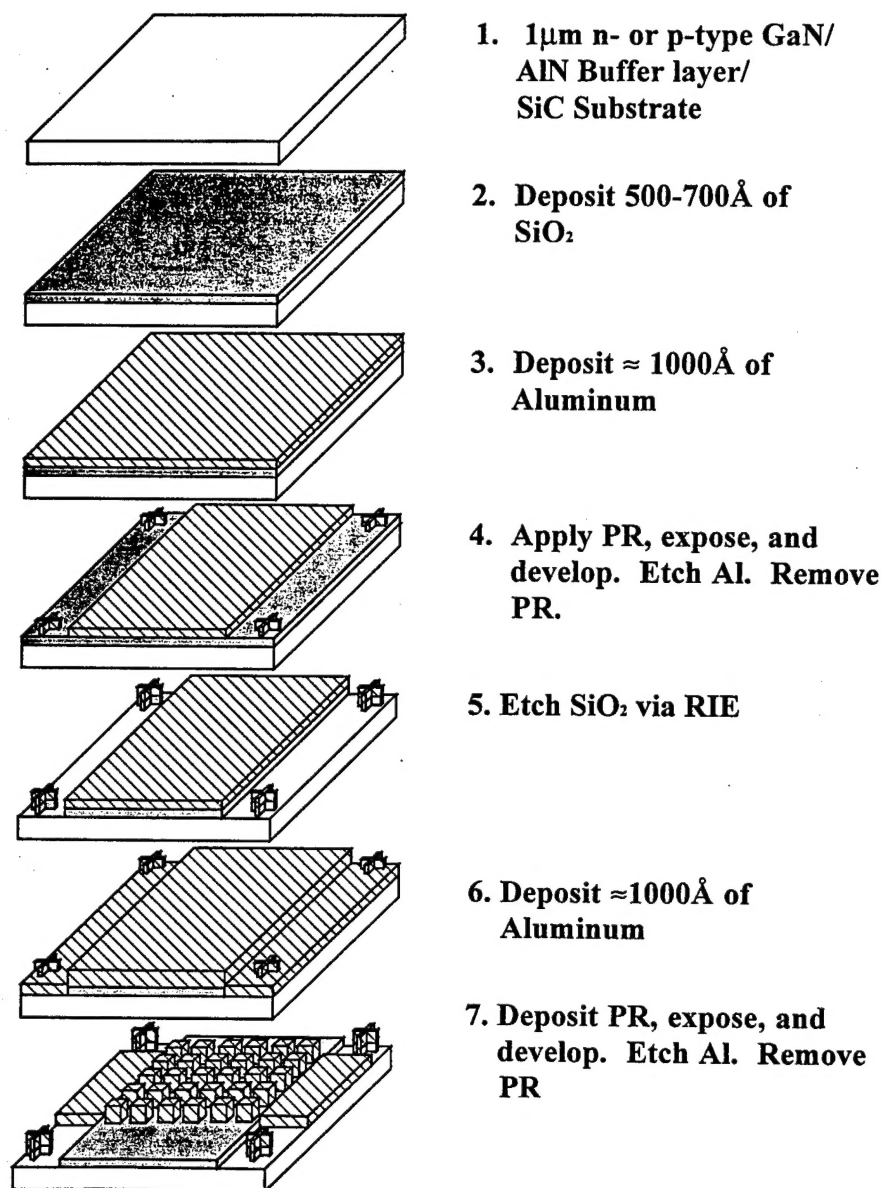


Figure 2. MIS capacitor processing procedure.

D. Discussion

Having demonstrated the ability to fabricate the two terminal devices, proper analysis must now be performed. To do this analysis material properties must be defined. Specifically the workfunction of GaN. To obtain this value an experimental procedure has been devised. Using one sample (i.e. a single piece of GaN with an insulator deposited upon it) three different gate metals with varying workfunctions will be deposited. By analyzing the shift in the C-V curve for each of these metals the value of the flatband voltage and thus the workfunction of GaN will be obtained.

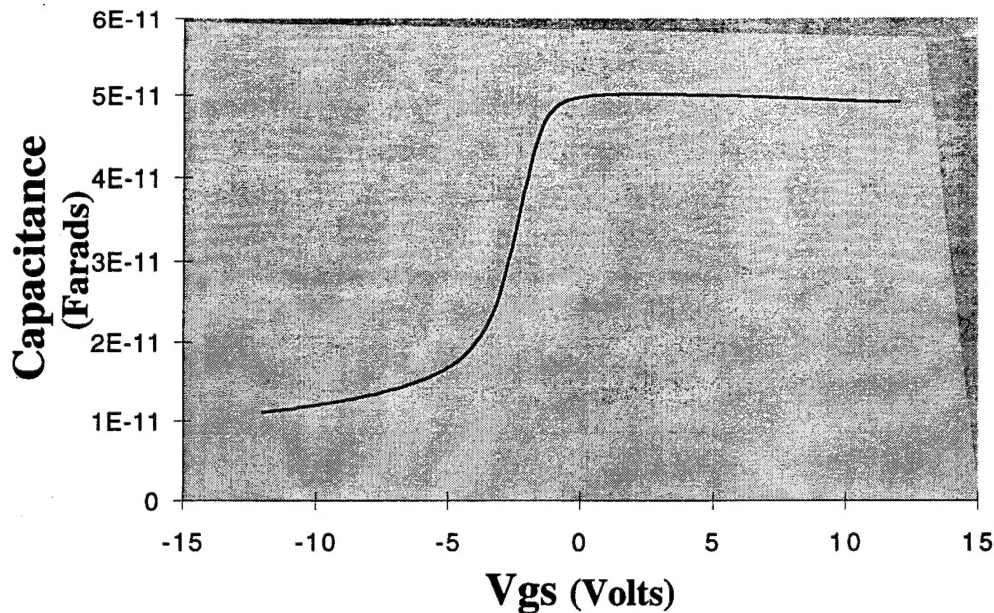


Figure 3. C-V curve for GaN/SiO₂ MIS capacitor.

Once this work has been completed and a true theoretical curve is made, measurements on the quantity of charge in the insulator will be performed. Through this work, the best insulator will be found to use in the MISFET device.

To reach the goal of an MISFET device, advances in material processing need to be made. Specifically in the areas of contacts, ion implantation, and etching. All of which are currently being addressed within this research group.

D. Conclusion

With their combination of thermal and electrical properties the III-V nitrides have the potential to be excellent materials for use in high power and high temperature applications. With the production of device quality material the time has arrived to develop these devices. There are a number of steps to be taken to fabricate devices which will perform well in the high power and frequency regimes. This project will take the necessary steps to achieve this goal.

E. References

1. R. F. Davis, Proc. IEEE **79**, 702 (1991).
2. S. Strite and H. Morkoç, J. Vacuum Sci. Technol. B **10**, 1237 (1992).
3. M. Asif Khan, J.N. Kuznia, J.M. Van Hove, D.T. Olson, S. Krishnankutty, and R.M. Kolbas, Appl. Phys. Lett. **58**, 526 (1991).
4. H Amano, T. Asahi, and I. Akasaki, Jpn J. Appl. Phys. **29**, L205 (1990).
5. S. Yoshida, S.Gonda, and S. Misawa, J. Appl. Phys. **53**, 6844 (1982).
6. M. Hegems and H. C. Montgomery, J Phys. Chem Solids **34**, 885 (1973).
7. C. Wang and R. F. Davis, Appl. Phys. Lett. **63**, 990 (1993).
8. M. Asif Khan, J.N. Kuznia, A.R. Bhattarai, and D.T. Olson, Appl. Phys. Lett. **62**, 1786 (1993).

9. M. Asif Khan, J.M. Van Hove, J.N. Kuznia, and D.T. Olson, Appl. Phys. Lett. **58**, 2408 (1991).
10. M. Asif Khan, J. N. Kuznia, J. M. Van Hove, N. Pan, and J. Carter, Appl. Phys. Lett. **60**, 3027 (1992).
11. M. Asif Khan, A. R. Bhattarai, J. N. Kuznia, and D. T. Olson, Appl. Phys. Lett. **63**, 1214 (1993).
12. M. Asif Khan, J.N. Kuznia, D.T. Olson, W.J. Schaff, J.W. Burm, and M.S. Shur, Appl. Phys. Lett. **65**, 1121 (1994).
13. M. Asif Khan, M. S. Shur, J. N. Kuznia, Q. Chen, J. W. Burm, and W. J. Schaff, Appl. Phys. Lett. **66**, 1083 (1995).
14. S. C. Binari, L. B. Rowland, W. Kruppa, G. Kelner, K. Doverspike, and D. K. Gaskill, Electronics Lett. **30**, 1248 (1994).
15. S. C. Binari, L. B. Rowland, G. Kelner, W. Kruppa, H. B. Dietrich, K. Doverspike, and D. K. Gaskill, Proc. 21st Int. Symp. on Compound Semiconductors, September 1994, San Diego.
16. R. J. Shul, A. J. Howard, S. J. Pearton, C. R. Abernathy, C. B. Vartuli, P. A. Barnes, and M. J. Bozack, J. Vac. Sci. Technol. B **13**, 2016 (1995).
17. G. F. McLane, L. Casas, S. J. Pearton, and C. R. Abernathy, Appl. Phys. Lett. **66**, 3328 (1995).
18. S. J. Pearton, C. B. Vartuli, J. C. Zolper, C. Yuan, and R. A. Stall, Appl. Phys. Lett. **67**, 1435 (1995).
19. H. C. Casey, G. G. Fountain, R. G. Ailey, B. P. Keller, Appl. Phys. Lett. **68**(13), 1850 (1996).
20. Y. P. Tsividis, *Operation and Modeling of the MOS Transistor*, McGraw Hill Book Co., New York, 1987.
21. E. H. Nicollian, J. R. Brews, *MOS (Metal Oxide Semiconductor) Physics and Technology*, John Wiley & Sons, New York, 1982.

XXI. Distribution List

Mr. Max Yoder Office of Naval Research Electronics Division, Code: 312 Ballston Tower One 800 N. Quincy Street Arlington, VA 22217-5660	3
Administrative Contracting Officer Office of Naval Research Regional Office Atlanta 101 Marietta Tower, Suite 2805 101 Marietta Street Atlanta, GA 30323-0008	1
Director, Naval Research Laboratory ATTN: Code 2627 Washington, DC 20375	1
Defense Technical Information Center Bldg. 5, Cameron Station Alexandria, VA 22304-6145	2